

Microfluidic Platforms for the Study of Bacterial Metabolism and Antimicrobial Susceptibility Testing

Présentée le 18 février 2021

Faculté des sciences et techniques de l'ingénieur
Laboratoire de microsystemes 2
Programme doctoral en microsystemes et microélectronique

pour l'obtention du grade de Docteur ès Sciences

par

Yang LIU

Acceptée sur proposition du jury

Prof. C. Guiducci, présidente du jury
Prof. M. Gijs, Dr T. Lehnert, directeurs de thèse
Prof. J. Lammertyn, rapporteur
Prof. W. Metsola van der Wijngaart, rapporteur
Prof. Ph. Renaud, rapporteur

“I should like to say two things, one intellectual and one moral. The intellectual thing I should want to say is this: When you are studying any matter, or considering any philosophy, ask yourself only what are the facts and what is the truth that the facts bear out. Never let yourself be diverted either by what you wish to believe, or by what you think would have beneficent social effects if it were believed. But look only, and solely, at what are the facts. That is the intellectual thing that I should wish to say.

The moral thing I should wish to say... I should say love is wise, hatred is foolish. In this world which is getting more closely and closely interconnected we have to learn to tolerate each other, we have to learn to put up with the fact that some people say things that we don't like. We can only live together in that way and if we are to live together and not die together we must learn a kind of charity and a kind of tolerance which is absolutely vital to the continuation of human life on this planet.”

— Bernard Russell

This thesis is dedicated to my parents ...

Acknowledgments

I am grateful to all the people I met during the 4-year Ph.D. study. I express my sincere gratitude to all the people that have contributed to this important personal and professional achievement. I would like to express my thanks for their advice and encouragement.

First and foremost, my acknowledgment goes to my advisor **Prof. Martin Gijs** for giving me the opportunity to conduct research in the Laboratory of Microsystems (LMIS2). Thank you, Martin, for giving me a chance to pursue a Ph.D. in this great university and this beautiful city. You have always been very supportive of me, especially during the difficult times of the doctoral studies. Meanwhile, you gave me full permissions to make decisions by myself: exploring and developing the ideas. Your active involvement in the discussion, patient guidance, and scientific competence carry me through the research work and keep me on the right scientific track.

My deepest appreciation also goes to my co-advisor **Dr. Thomas Lehnert**. Thank you, Thomas, for your tremendous help from the paper writing to the thesis redaction. With your critical questions and patience, we have improved our work together and the work rhythm was always ideal. I learned from you how to be a qualified researcher even though I am still aiming for.

I would also like to thank the professors at **ESPCI Paris**. The knowledge that I have learned at ESPCI is a great treasure for me. My special thank goes to **Prof. Stéphane Descroix** and **Prof. Marie-Caroline Jullien** for the kind help when I am confused about my career. I also would like to thank my advisor **Prof. WANG Xiaoliang** at **Nanjing University** for the guidance at the beginning of my academic career.

I would like to express my gratitude to the jury members of my thesis: the president **Prof. Carlotta Guiducci**; **Prof. Philippe Renaud**, **Prof. Wouter van der Wijngaart** and **Prof. Jeroen Lammertyn** for accepting to read and evaluate my thesis.

Special thanks goes to **Melis** and **Lucie**. I still remember the first day when I came here. Your professional and kind help made the administration work accomplished within 1 day, what an efficient country! You were always helpful during these 4 years. I wish you and your family all the best.

I am deeply grateful to all my colleagues at **LMIS2**. All former members **Raphael**, **Cristina**, **Gergely**,

Acknowledgments

Matteo, Fabien, XIANG Rongrong, LIU Zhentao, and ZHANG Jingwei, I wish you success in your career in either academia or industry. My special thanks go to joint-team member **Roger**, whose creativity inspired me a lot. I remember **Baris** for our late-work time that we aimed for better research results. I appreciate very much your dedication and intelligence. I thank all my roommates **Tuan, Muaz, and Parham**. Our discussions about the research will always be remembered. **Muaz** and **Parham**, the two newest and maybe last Ph.D. students in our lab, I wish you a great Ph.D. study experience and I believe your hard work will be returned with wonderful results. I thank also my student **Terry** for his contribution to the oxygen project. I thank my collaborator **SUN Lin** and wish your Ph.D. goes well. I also thank another collaborator **Dr. Jonas** for his help in the muscle cell metabolic measurements. I am thankful to **Jalil** for the support and our fruitful French talk. Assisting the cleanroom practical session under your direction was a good start for me to tutor the student. My stay at LMIS2 is along with **Vittorio**. We climbed Mount Xiang in Taipei City in China together just like we are now climbing in the Ph.D. journey together. I wish you in advance a successful defense. My closest "ally" in the lab **Farzad**, our discussions about languages, philosophy, politics, history, and the world will always be a good memory. I hope you go through all the difficulties with your passion, creativity, and diligence. You will be a great researcher, just believe it and implement it.

I also thank the colleagues on the same floor in BM Building especially **LMIS1** and **LMIS4**; special thanks go to **Dr. Arnaud, Joan, Thomas, Henry, Dr. WANG Ya, YANG Zhiwei, Chris, ...** for the kind help when we use some machines in your labs. I also thank the **ATMX, ATPR, AFA, and ACI** workshop engineers: **Mr. Despont, Mr. Rougnon, Mr. Alfred, Mr. Schneider, Mr. Leitos, and Mr. Brühlmeier** for their high-quality mechanical, 3D-Printing, and PCB manufacturing work.

The Ph.D. thesis is kindly supported by the European Union H2020 **New Diagnostics for Infectious Diseases (ND4ID)** program. I am very grateful to be a part of this program. I thank all the principal investigators in this project: **Prof. M.-Pilar Marco, Prof. Lluisa Vilaplana, Prof. Xavier Muñoz, Prof. Aman Russom, Prof. Mats Nilsson, Prof. Dragana Spasic, Prof. Karen Vanhoorelbeke, Prof. Nick Geukens, ...** I thank especially **Dr. Pieter Moons** for the project coordination and fantastic work. I also thank **Kitty, Stalin, and Catherine** for the microbiological training in Antwerp. A special thank goes to **Prof.Dr. Herman Goossens** and **Prof.Dr.Dr. Alex van Belkum** for your continuous encouragement and kind suggestions. Your dedication to the career in combating antimicrobial resistance impresses me and the spirit will always raise me up when facing challenges. I thank all the students in the program, we have spent very happy times together: **Aida, Andreu, Ahmad, Emre, Felix, Jiri, Juan-Pablo, Ismail, Matilda, Mattia, Michael, Saba, Sara, Sharif**. I thank specially **Weijin** for the mutual support during all the ND4ID meetings. I wish you soon being **Prof. Guo**.

As a part of the ND4ID project, a special thank goes to my secondment host **Prof. Arben Merkoçi's** laboratory. I spend a very happy time with the friends at ICN2 in Barcelona: **YANG Qiuyue, ZHAO Lei, HU Liming, WANG Kai, LIU Yang, CHEN Yu, HAN Xu, ZHANG Songbai, Amadeo, Enric, Duy, Dr. Giulio, Miguel Ángel, José, ...** Your great kindness helped me survived in an unfamiliar city and created a lot of good memories. Wish you all get your Ph.D. successfully!

I am deeply grateful to all my friends (colleagues) in the Chinese Student & Scholars Association in Lausanne. With all your help, I could serve my term 2018-2019 to the students and scholars in Lausanne: **Dr. LIU Yuanlong, LIU Runzhe, Dr. HE Guosheng, ZHANG Tianchu, CHEN Zhe, ZHANG Ruixi, WEI Shupeng, TAO Yuyu, LU Jiawei, CHEN Danxuan, WANG Yuteng, ZENG Yaling, XIAO Yiqing, WANG Zhen, ZHENG Siqi, Dr. YIN Ting, WANG Ziqi, ZHOU Ling, LV Wenyuan, Dr. LU Qinli, Dr. ZHOU Ruofan, WU Yu, YANG Jian, XIE Yuqing, GUO Jinhui, NIE Shiyue, Dr. SHEN Jiayun, ...** We should be proud of what we have achieved. This valuable experience and what I have learned will always be beneficial all my life.

I think I am more or less one of the most constant participants in Badminton sport as an amateur in Lausanne. When I came to Lausanne, I was a junior while now I was almost the most senior player. Time flies. Once per week play in the badminton playground with all you guys brought about lots of fun: **Dr. ZOU Junwen, ZHOU Jiande, WANG Zhengchao, MA Wei, Dr. XU Tao, YI Xiangli, LIU Sijie, ZHANG Tao, LIU Lulu, Dr. LIU Xiaowang, ...** A special list goes to the **Ultimate 4: HUANG Xiangwei, Dr. LI Rujin, LEI Shengzhao, LIN Tao**. Our matches in the slots of COVID-19 relieved my pressure on the thesis redaction and graduation.

I am sincerely grateful to all my other friends in Lausanne: **FU Changfa, ZHANG Yueyun, CHENG Shiyu, WANG Qiao, DI Yao, ZHAO Yanfei, HU Yi, WU Xingyu, ZHANG Junrui, JIANG Yueting, LU Jin, Dr. YIN Binglun, Dr. MENG Di, Dr. WANG Lei, Dr. LI XiaoKang, Dr. LI Hao, Dr. LIU Junqiu, Dr. WANG Jian, JI Wencheng, QIU Huajian, SU Zhehuan, WANG Taifang, M. Jacques Sturm, Mme Marie-Laure Sturm, ...** I also thank all the friends in other regions in Switzerland: **Dr. YANG Huayan, Dr. XIE Tianwu, YANG Rujia, CHEN Xi, Dr. SUN Qingnan, ZHANG Chumin, ...** and friends in France: **CHEN Dong, ZHANG Shimin, WU Yunxiao, GU Shiyi, YUAN Zhifei, WANG Han, WANG Wendi, WU Yirong, Sopheasith, Dr. Minh-Chau, Dr. Jean-Baptiste, ...** . It is a great pleasure to meet all of you.

I owe my deepest gratitude to all the family members. I would like to express my thanks to my **aunt** and **uncle** in Beijing. You picked me up every time at the airport and took care of me when I went back home. I thank **grandmas, uncles, aunts, brothers, and sisters**, it was a pity that I could not visit you very often. Your cares for me support me go through these years of abroad study. Whenever I encounter difficulties, you all are there. This is the first thing that we should care about in our life. I am deeply thankful to my parents. With your support, I am able to obtain the degree. Your greatest love gives me courage, persistence, and protection. I dedicate this thesis to you two: **my mother and my father**.

Lausanne, January 27, 2021

LIU Yang

Abstract

Fast spreading antimicrobial resistance (AMR) is an emerging major public health issue. New therapeutic and diagnostic paradigms must be implemented to counteract this evolution. In this respect, fast antimicrobial susceptibility testing (AST) plays an important role by enabling optimum antibiotic prescriptions to improve the therapeutic efficiency on the one hand and to avoid excessive consumption of antibiotics on the other hand. Eventually, this could slow down AMR progression and extend the lifespan of current antibiotics. This thesis explores routes towards innovative fast AST technologies from 3 perspectives, using *E. coli* as a model organism: (i) microbial metabolic heat production, (ii) oxygen consumption assessment in response to antimicrobial exposure, and (iii) bacterial motility analysis after incubation without and with antibiotics.

In the first project, we propose a chip-based isothermal nanocalorimeter, enabling reliable bacterial metabolic heat flow measurements. Main components of the nanocalorimeter platform include a microincubator positioned on a Si chip-based heat flow sensor, combined with a custom PID controlled thermostat and an integrated fluidic handling system. The platform's high sensitivity enables bacterial growth detection within only a few hours of culture. The measured heat flow in bacterial growth correlates to the lost energy in terms of heat generation during the central metabolic process. Heat flow curves reflect growth rate and lag phase variations under different bacterial culture conditions and in the presence of antibiotics. At the first stage, for instance, we assessed bacterial heat flow in 3 different culture media, and we found that the overall heat production (*i.e.* heat flow integrated over time) depends on the availability of nutrients. More importantly, using heat as a viability indicator, we were able to perform AST on *E. coli* within only several hours. In these assays, growth inhibition due to antibiotic activity was revealed by a decrease or the absence of the metabolic heat signal. Furthermore, we found that antimicrobial stress resulted in metabolic energy spilling by the bacteria. As a proof-of-concept, we conducted a metabolic heat AST study based on 3 clinically relevant antibiotics featuring different functional mechanisms. The presence of antibiotics at sub-MICs (minimum inhibitory concentrations) leads to slower growth rates and lag phase elongation. MIC ranges could be determined with our system and were found to correspond well to established MIC values.

In a parallel approach, we adapted the nanocalorimeter platform to develop an on-chip bacterial oxygen consumption measurement system as an indirect calorimetric method. We focused on the aerobic metabolic activity of *E. coli* in the early phase of bacterial growth. A nanoparticle-based

Abstract

sensor allows correlating the concentration of dissolved oxygen in the culture medium with a phase shift in the fluorescent signal response. We established a model to evaluate the oxygen consumption rate (OCR) and bacterial doubling time based on exponential bacterial growth. Antibiotic exposure above MIC suppresses bacterial growth as well as oxygen consumption.

In the third project, we further explored the properties of bacteria cultures facing antimicrobial stress. We performed an extensive motility study at single-bacterium resolution under different culture conditions. We developed a protocol using a composite microfluidic chip with UV-curable optical adhesive (OA)-patterned microchannels. The rigid OA-based chip provides several advantages over conventional PDMS chips in certain applications. The 4- μm high microfluidic channels confine bacterial suspensions in a quasi-2D space to facilitate high-resolution time-lapse imaging. We developed a high-content image processing protocol to analyze both the static and dynamic properties of on-chip bacterial cultures. In particular, we studied collective bacterial migration, appearing as "traveling bands" in the microchannel. Such collective behavior occurs as a chemotactic response to self-generated nutrient gradients of confined bacterial populations. For instance, we found that different inoculum sizes of isogenic bacteria result in heterogeneous swimming phenotypes. Interestingly, the collective migration properties were altered by the presence of antibiotics. We investigated this phenotypic diversity by quantifying bacterial motility based on parameters such as swimming velocity, tumble bias, and effective diffusion. We propose that the observation of the presence/absence of traveling bands may be used as an alternative AST method. Based on the quantification of bacterial morphological information, we also found that the bacterial elongation effect varied depending on the antimicrobial mechanism.

In summary, the scope of this thesis was to take advantage of microfluidic technologies to assess the impact of antimicrobial exposure on *E. coli* from several aspects: metabolic heat flow, oxygen consumption, and swimming/motility behavior. The different platforms presented in this work are new tools enabling innovative protocols for fast *in vitro* diagnostics and general metabolism-related biological investigations.

Keywords

Antimicrobial resistance (AMR), antimicrobial susceptibility testing (AST), bacterial metabolism, metabolic heat flow, microfluidics, minimum inhibitory concentration (MIC), nanocalorimetry, on-chip bacterial culture, thermopile, oxygen consumption rate (OCR), chemotaxis, bacterial motility analysis, collective bacterial migration, image processing and analysis, microbial phenotypic diversity, traveling bands, tumble bias (TB).

Résumé

La résistance aux antimicrobiens (AMR) à propagation rapide est un problème de santé publique majeur émergent. Nouveaux paradigmes thérapeutiques et diagnostiques doivent être mis en œuvre pour contrer cette évolution. A cet égard, les tests rapides de sensibilité aux antimicrobiens (AST) jouent un rôle important en permettant des prescriptions d'antibiotiques optimales pour améliorer l'efficacité thérapeutique d'une part et éviter une consommation excessive d'antibiotiques d'autre part. À terme, cela pourrait ralentir la progression de la AMR et prolonger la durée de vie des antibiotiques actuels. Cette thèse explore les voies vers des technologies AST rapides innovantes à partir de 3 perspectives, en utilisant *E. coli* comme organisme modèle : (i) la production de chaleur métabolique microbienne, (ii) l'évaluation de la consommation d'oxygène en réponse à une exposition aux antimicrobiens, et (iii) l'analyse de la motilité bactérienne après incubation sans et avec antibiotiques.

Dans le premier projet, nous proposons un nanocalorimètre isotherme à puce, permettant des mesures fiables du flux de chaleur métabolique bactérien. Les principaux composants de la plateforme nanocalorimétrique comprennent un microincubateur positionné sur un capteur de flux de chaleur basé sur Si, combiné à un thermostat contrôlé par PID et un système de gestion fluide intégré. La haute sensibilité de la plateforme permet la détection de la croissance bactérienne en seulement quelques heures de culture. Le flux de chaleur mesuré dans la croissance bactérienne est corrélé à l'énergie perdue en termes de génération de chaleur pendant le processus métabolique central. Les courbes de flux de chaleur reflètent le taux de croissance et les variations de phase de latence dans différentes conditions de culture bactérienne et en présence d'antibiotiques. À la première étape, par exemple, nous avons évalué le flux de chaleur bactérienne dans 3 milieux de culture différents, et nous avons constaté que la production de chaleur globale (c'est-à-dire le flux de chaleur intégré dans le temps) dépend de la disponibilité des nutriments. Plus important encore, en utilisant la chaleur comme indicateur de viabilité, nous avons pu effectuer l'AST sur *E. coli* en quelques heures seulement. Dans ces essais, l'inhibition de la croissance due à l'activité antibiotique a été révélée par une diminution ou l'absence du signal thermique métabolique. De plus, nous avons constaté que le stress antimicrobien entraînait un déversement d'énergie métabolique par les bactéries. En guise de preuve de concept, nous avons mené une étude d'AST thermique métabolique basée sur 3 antibiotiques cliniquement pertinents présentant différents mécanismes fonctionnels. La présence d'antibiotiques à des sous-MIC (concentrations minimales inhibitrices) entraîne des taux de croissance plus lents et un

allongement de la phase de latence. Les gammes de MIC ont pu être déterminées avec notre système et se sont avérées bien correspondre aux valeurs de MIC établies.

Dans une approche parallèle, nous avons adapté la plateforme du nanocalorimètre pour développer un système de mesure de la consommation bactérienne d'oxygène sur puce en tant que méthode calorimétrique indirecte. Nous nous sommes concentrés sur l'activité métabolique aérobie d'*E. coli* dans la phase précoce de la croissance bactérienne. Un capteur à base de nanoparticules permet de corrélérer la concentration d'oxygène dissous dans le milieu de culture avec un déphasage dans la réponse du signal fluorescent. Nous avons établi un modèle pour évaluer le taux de consommation d'oxygène (OCR) et temps de doublement basé sur la croissance bactérienne exponentielle. L'exposition aux antibiotiques au-dessus de la MIC supprime la croissance bactérienne ainsi que la consommation d'oxygène.

Dans le troisième projet, nous avons exploré plus en détail les propriétés des cultures de bactéries exposées au stress antimicrobien. Nous avons réalisé une étude approfondie de la motilité avec une résolution à une seule bactérie dans différentes conditions de culture. Nous avons développé un protocole utilisant une puce microfluidique composite avec des microcanaux à base d'un adhésif optique durcissable aux UV (OA). La puce à base OA rigide offre plusieurs avantages par rapport aux puces PDMS classiques dans certaines applications. Les canaux microfluidiques de 4 μm de haut confinent les suspensions bactériennes dans un espace quasi-2D pour faciliter l'imagerie time-lapse avec haute résolution. Nous avons développé un protocole de traitement d'images à haut contenu pour analyser les propriétés statiques et dynamiques des cultures bactériennes sur puce. En particulier, nous avons étudié la migration bactérienne collective, apparaissant comme des «bandes mobiles» dans le microcanal. Un tel comportement collectif se produit comme une réponse chimiotactique à des gradients de nutriments auto-générés par des populations bactériennes confinées. Par exemple, nous avons constaté que différentes tailles d'inoculum de bactéries isogéniques entraînent des phénotypes de natation hétérogènes. Fait intéressant, les propriétés de migration collective ont été modifiées par la présence d'antibiotiques. Nous avons étudié cette diversité phénotypique en quantifiant la motilité bactérienne en fonction de paramètres tels que la vitesse de nage, le biais de tumble et la diffusion effective. Nous proposons que l'observation de la présence / absence de bandes mobiles puisse être utilisée comme méthode AST alternative. Sur la base de la quantification des informations morphologiques bactériennes, nous avons également constaté que l'effet d'élongation bactérienne variait en fonction du mécanisme antimicrobien.

En résumé, le but de cette thèse était de tirer parti des technologies microfluidiques pour évaluer l'impact de l'exposition aux antimicrobiens sur *E. coli* sous plusieurs angles : flux de chaleur métabolique, consommation d'oxygène et comportement de natation et de motilité. Les différentes plateformes présentées dans ce travail sont de nouveaux outils permettant des protocoles innovants pour des diagnostics *in vitro* rapides et des investigations biologiques liées au métabolisme en général.

Mots clés

Résistance aux antimicrobiens (AMR), test de sensibilité aux antimicrobiens (AST), métabolisme bactérien, flux de chaleur métabolique, microfluidique, concentration minimale inhibitrice (MIC), nanocalorimétrie, culture bactérienne sur puce, thermopile, taux de consommation d'oxygène (OCR), chimiotaxie, analyse de la motilité bactérienne, migration bactérienne collective, traitement et analyse d'images, diversité phénotypique microbienne, bandes mobiles, biais de tumble (TB).

Contents

Acknowledgments	i
Abstract (English/Français)	v
List of figures	xv
List of tables	xix
List of symbols	xxi
List of abbreviations	xxiii
1 Introduction	1
1.1 Scope of the thesis	1
1.2 Thesis outline	2
1.3 Antimicrobial resistance (AMR) and persistence	3
1.3.1 AMR facts and challenges	3
1.3.2 AMR mechanisms	4
1.4 Microfluidic technology	6
1.5 Antimicrobial susceptibility testing (AST)	8
1.5.1 Definition of AST	8
1.5.2 From hospitalization to AST	8
1.5.3 Conventional methods	9
1.5.4 Recent commercialized methods	10
1.5.5 Microfluidic methods	10
1.6 Bacterial metabolism	12
1.6.1 Metabolic pathways	12
1.6.2 Bacterial growth	14
1.6.3 Antimicrobial effect on the metabolic activity	14
1.7 Swimming of <i>E. coli</i>	15
	xi

Contents

2	Theory of calorimetry	23
2.1	Heat transfer phenomena	23
2.2	The classical calorimeter	25
2.2.1	Simplified calorimeter model	25
2.2.2	Different heat exchange principles	26
2.2.3	Possible descriptions of calorimeters	27
2.3	Heat flux calorimeter	28
2.3.1	The thermoelectric effect	28
2.3.2	Theory of heat flux sensors	30
3	State of the art of modern chip-based calorimeters	39
3.1	Thermopile-based calorimeter	39
3.2	Cantilever-based heat sensing	43
3.3	Thermistor-based calorimeters	45
3.4	Commercial calorimeters	46
3.5	Applications of direct calorimetry	46
4	A nanocalorimetry platform for fast AST	53
4.1	Introduction	53
4.2	Platform design and characterization	55
4.3	Experimental	58
4.3.1	Microincubator fabrication and sensor calibration	58
4.3.2	Preparation of microbial sample and antimicrobial solutions	58
4.3.3	Platform sterilization and heat flow measurement protocol	60
4.3.4	Statistical analysis and baseline correction	61
4.4	Results	61
4.4.1	Analysis of microbial metabolic heat profiles	61
4.4.2	Metabolic activity of <i>E. coli</i> for different culture conditions	63
4.4.3	AST based on metabolic heat assays	66
4.4.4	Energy spilling of <i>E. coli</i> due to antimicrobial stress	67
4.5	Discussion	71
4.6	Conclusion	75
5	Microbial oxygen consumption	83
5.1	Introduction	83
5.2	Current approaches for measuring oxygen consumption rate (OCR)	84
5.2.1	Titration method	84
5.2.2	Electrochemical methods	84

5.2.3	Spectroscopic method	84
5.2.4	Commercial respirometry	85
5.2.5	Luminescence-based oxygen sensing	85
5.3	Experimental	88
5.3.1	OCR measurement set-up	88
5.3.2	Materials and methods	88
5.4	Results	89
5.4.1	Oxygen consumption	89
5.4.2	Modelization of the oxygen consumption	90
5.4.3	Aerobic metabolism assessment	92
5.4.4	AST based on OCR measurements	94
5.4.5	Oxygen consumption <i>vs</i> heat production	95
5.5	Discussion	96
5.6	Conclusion	98
6	Bacterial motility analysis	101
6.1	Introduction	101
6.2	Experimental	103
6.2.1	Material and chemicals	103
6.2.2	Sample preparation	104
6.2.3	Coverslip surface cleaning	104
6.2.4	Microfluidic chip fabrication	105
6.2.5	Working principle	106
6.2.6	Video recording and image processing	108
6.2.7	Statistical analysis	109
6.3	Results	110
6.3.1	Morphological analysis	110
6.3.2	Bacteria traveling bands	112
6.3.3	Motility analysis for different inoculum sizes	117
6.3.4	Motility analysis for different antimicrobials	120
6.4	Discussion	122
6.5	Conclusion	128
7	Conclusion and outlook	135
7.1	Conclusion	135
7.1.1	Project summary	135
7.1.2	Technology readiness	137
7.2	Outlook	137

Contents

7.2.1	High-throughput calorimeters with increased sensitivity	137
7.2.2	Why not performing AST with blood samples?	138
7.2.3	The metabolic perspective	139
7.2.4	Microbial co-culture	139
7.2.5	Bacterial motility	139
7.2.6	Development of new antimicrobials	140
A	Additional technical notes	143
A.1	Environmental effect on the baseline drift	143
A.2	PID controller	144
A.3	ADC resolution	147
A.4	Sensor datasheet	147
B	Software program	151
B.1	LabVIEW program	151
B.2	MATLAB and Python code	151
C	Heat transfer simulations	155
	Curriculum Vitae	159

List of figures

1.1	Thesis outline.	3
1.2	The reality of antimicrobial resistance (AMR).	4
1.3	From hospitalization to AST.	9
1.4	Conventional AST methods.	10
1.5	Commercial AST methods.	11
1.6	Innovative AST methods.	13
1.7	Bacterial metabolic pathways and growth curve.	14
1.8	Swimming of <i>E.coli</i> and random walks.	16
2.1	Schematic representation of the thermal circuit of a classical calorimeter.	26
2.2	Examples of historical calorimeters.	27
2.3	Thermoelectric effect.	29
2.4	Thin film-based <i>vs</i> p-n type thermopile sensor.	30
3.1	Membrane-based calorimeters with open chambers.	40
3.2	Different types of microfluidic calorimeters.	41
3.3	Cantilever beam calorimeters (CBCs).	44
3.4	Thermistor-based calorimeters.	45
3.5	Commercial calorimeters.	46
4.1	Isothermal nanocalorimetry platform.	56
4.2	Temperature stabilization of the INCfAST platform.	57
4.3	Control experiments without bacteria.	57
4.4	Schematic cross-sectional view of a sensor unit with fluidic system.	58
4.5	Thermopile power/voltage coefficient calibration.	59
4.6	Heat flow baseline correction.	61
4.7	Metabolic heat assessment.	62
4.8	Assessment of metabolic features for different growth conditions.	64
4.9	OD600 results of different culture media.	65

List of figures

4.10 OD600 for bacterial culture at different temperatures.	66
4.11 AST with the nanocalorimetry platform.	68
4.12 OD600 for AST experiments.	69
4.13 Energy spillage (heat/OD600).	70
5.1 State-of-the-art system for respirometry.	86
5.2 Sensing principles of photoluminescence oxygen concentration measurements. . .	87
5.3 Oxygen consumption measurement set-up.	89
5.4 Metabolic heat and oxygen consumption measurements.	90
5.5 Modelization of oxygen consumption curve.	91
5.6 OCR curves.	92
5.7 Oxygen consumption for different culture media and temperatures.	93
5.8 Oxygen consumption for AST experiments.	94
5.9 Oxygen consumption <i>vs</i> heat production for different culture media and temperatures.	96
5.10 Oxygen consumption <i>vs</i> heat production for different ASTs.	97
6.1 Chip fabrication and design for quasi-2D confinement of bacterial populations. . .	106
6.2 Optimization of the channel height.	107
6.3 Heat transfer simulation by COMSOL Multiphysics®.	108
6.4 Automated image stack processing and data analysis.	110
6.5 Screenshot of an example video sequence after image processing showing bacterial swimming with trajectories.	111
6.6 Bacterial morphological analysis.	113
6.7 <i>E. coli</i> growth and growth rate curves based on OD600 measurements.	114
6.8 Time dependent bacterial density profiles.	115
6.9 Bacterial number in the FOV as a function of time for different experimental conditions.	116
6.10 Bacterial motility analysis for different inoculum size.	119
6.11 Mean swimming speed or diffusion coefficient <i>vs</i> tumble bias.	121
6.12 Motility and tumble bias analysis for bacterial growth with different antimicrobials.	123
6.13 D_{eff} , and TB distribution for bacteria in the different antimicrobials.	124
A.1 Environmental effect on heat flow.	144
A.2 Examples for calorimeters with multi-layer thermostats.	145
A.3 Schematic representation and pictures of the INCfAST system and the measurement set-up.	146
A.4 Schematic representation of the PID program.	146
A.5 Datasheet of the sensor XEN-NCM9924.	148
A.6 Photo of the thermopile sensor chip with PGA connector (XEN-NCM9924).	149

B.1	LabVIEW program and instruments used in this work.	152
B.2	LabVIEW program interface.	153
B.3	Mindmap of codes.	154
B.4	MATLAB program.	154
C.1	COMSOL Multiphysics® simulation snapshots.	156
C.2	2-D heat transfer simulation results.	157

List of tables

1.1	Examples of commercial AST methods.	12
3.1	Performance of thermopile-based chip calorimeters.	43
3.2	Heat power for cells and living organisms.	48
4.1	Nutrient content of different culture media.	64
4.2	MIC of INCfAST.	69
4.3	Calorimeters applied for microbiological investigations.	74
5.1	Estimation of doubling time and OCR/inoculum size for different culture media and temperatures.	93
5.2	Estimation of doubling time and OCR/inoculum size for AST experiments.	95

List of symbols

The following list describes symbols that will be later used within the body of the document.

α	Seebeck coefficient
χ	Chemotactic coefficient
Δt	Time interval
η	Viscosity
κ	Thermal diffusion coefficient
λ	Thermal conductivity
\mathbf{f}	External force density
\mathbf{v}	Flow field
μ	Bacterial diffusion coefficient due to Brownian motion
ω	Angular frequency
Φ	Phase shift
ρ	Mass density
σ	Stefan-Boltzmann constant
τ	Time constant
ε	Emissivity
A	Surface area
C	Heat capacity
c_p	Specific heat capacity
D_{eff}	Effective diffusion coefficient
E	Energy

List of tables

F_{th}	Sensitivity threshold
I	Amplitude
L	Length
P	Heat power
p	Pressure
Q	Heat
q_A	Heat flow
q_s	Heat flux
R	Thermal resistance
S	Sensitivity
S_A	Power sensitivity [V/W]
S_T	Temperature sensitivity [V/K]
T	Temperature
t	Time
U	Voltage
V	Volume
v_0	Speed for one swimming trajectory
v_{mean}	Mean speed
W	External work
Re	Reynolds number

List of abbreviations

C. elegans *Caenorhabditis elegans*.

E. coli *Escherichia coli*.

S. aureus *Staphylococcus aureus*.

2D two-dimension.

3D three-dimension.

AME aminoglycoside modifying enzyme.

AMR antimicrobial resistance.

AST antimicrobial susceptibility testing.

ATCC American type culture collection.

ATP adenosine triphosphate.

BFC brown fat cell.

BHI brain heart infusion broth.

BMD broth micro dilution.

BSI blood stream infection.

CAT chloramphenicol acetyltransferase.

CBC cantilever beam calorimeter.

CCW counter-clockwise.

CFU colony-forming unit.

CheA chemotaxis protein A.

CheA-P phosphorylated CheA.

CLSI Clinical & Laboratory Standards Institute.

COC cyclic olefin copolymer.

COVID-19 coronavirus disease 2019.

CW clockwise.

DHFR dihydrofolate reductase.

DI deionized.

DSC differential scanning calorimetry.

ECAR extracellular acidification rate.

EPR electron paramagnetic resonance.

EUCAST European Committee on Antimicrobial Susceptibility Testing.

List of abbreviations

FEA finite element analysis.

FISH fluorescent in situ hybridization.

FOV field of view.

H1N1 influenza A virus subtype H1N1.

HMDSO hexamethyldisiloxane.

INCfAST isothermal nanocalorimetric platform for fast antimicrobial susceptibility testing.

LB Lysogeny broth.

LOD limit of detection.

MALDI-TOF matrix assisted laser desorption ionization - time of flight.

MCP methyl-accepting chemotaxis protein.

MEMS micro-electro-mechanical-system.

MH Mueller Hinton broth.

MIC minimum inhibitory concentration.

MRSA methicillin-resistant *S. aureus*.

MSSA methicillin-susceptible *S. aureus*.

NAD nicotinamide adenine dinucleotide.

NADH nicotinamide adenine dinucleotide hydride.

NE noradrenaline.

OA optical adhesive.

OC oxygen consumption.

OCR oxygen consumption rate.

OD600 optical density, measured at 600 nm wavelength.

OPA ortho-phthalaldehyde.

OSTE+ off-stoichiometry thiol-ene-epoxy.

PBP penicillin-binding protein.

PC polycarbonate.

PCB printed circuit board.

PCR polymerase chain reaction.

PDE partial differential equation.

PDMS poly(dimethylsiloxane).

PFHC perfluorinated hydrocarbon.

PGA pin grid array.

PID proportional integral derivative.

PMMA poly(methyl methacrylate).

RMS root mean square.

RPP ribosomal protection protein.

RTD resistance thermometer.

SARS severe acute respiratory syndrome.

SD standard deviation.

SE standard error.

TB tumble bias.

TCA cycle tricarboxylic acid cycle.

TMCS Trimethylchlorosilane.

UV ultraviolet.

1 Introduction

1.1 Scope of the thesis

Escherichia coli (*E. coli*) is one of the oldest organisms on earth and one of the most intensively studied models in biological and biophysical research. Most *E. coli* strains are benign to the human and their presence in the human gut is even beneficial, especially for preventing the invasion of fungi and other hazardous microorganisms. Specific types of *E. coli* strains, however, may bring about serious infectious diseases. A major breakthrough in fighting microbial infections was the discovery of penicillin by Sir Alexander Fleming in 1928,^[1] which has been widely used in public healthcare since 1942 after mass production of the compound was achieved by Howard Florey and Ernst B. Chain. Almost at the same time, in a 1945 interview with *The New York Times*, Sir Fleming warned that the misuse of antimicrobials could result in the selective proliferation of resistant bacterial strains.^[2] In the following half century, a bloom in antimicrobial discovery led to the illusion that humans were invulnerable to bacteria/fungi-caused infectious diseases. However, alarming reports on continuously increasing and spreading antimicrobial resistance (AMR) quickly rectified this optimistic vision.

Although the veil of most infectious diseases has been lifted by biomedical research, and above all, by the development of molecular biology, human beings continue facing serious challenges, in particular related to viral infections. People benefit tremendously from globalization but, in the meanwhile, this facilitates the spreading of pathogens. Since 2000, several serious public health emergencies occurred, such as the outbreak of the SARS epidemic in 2003, H1N1 outbreak in 2009, *Ebola* outbreak in 2014-2016 and the COVID-19 pandemic in 2020. Global outbreaks of bacterial infectious diseases could be prevented so far due to the massive administration of antibiotics. However, facing a context where, on the one hand, more and more bacteria develop multi-drug resistance, and, on the other hand, research and discovery of new antimicrobials is stagnating, this apparently safe situation might change rapidly. Rapid diagnosis of bacterial infections combined with fast and accurate antimicrobial susceptibility testing (AST) appear as keys to counteract AMR progression and to prolong the lifespan of currently existing antimicrobials.

1.2 Thesis outline

In this thesis, we will present three microfluidic-assisted methods to assess the bacterial metabolic activity, including metabolic heat flow measurements, quantification of microbial oxygen consumption and the study of bacterial motility. *E. coli* will be used as model organism in this study. The thesis comprises an introduction chapter (Chapter 1), an overview on theoretical aspects and principles of calorimetry (Chapter 2), a state of the art of modern chip-based calorimeters (Chapter 3), the three major research projects on microbial metabolism and motility (Chapter 4 to Chapter 6), and a final conclusion with outlooks (Chapter 7). The appendices provide additional technical and software-related information.

Chapter 1 (this chapter) prepares the background knowledge on AMR and AST, including not only the gold standard methods used currently in clinical settings, but also innovative methods and commercial technologies. The impact of microfluidic technology in this field will be addressed, as well as fundamental aspects of bacterial metabolism, growth and motility of *E. coli*.

Chapter 2 gives an overview on the theoretical background and recent advances on calorimetry. We presented briefly the heat transfer theory, classifications and principles of calorimeters, and milestones in the development of classical calorimetry. A specific theoretical analysis of the thermopile-based heat flow calorimeter will be introduced.

Chapter 3 presents the state of the art of modern calorimeters and discusses recent advances in the field brought about by MEMS technology and microfluidic integration. Representative examples of chip-based micro- and nanocalorimeters based on different material combinations and operating principles, such as open chamber or flow-through devices, are shown.

Chapter 4 addresses the development and characterization of our isothermal nanocalorimetric platform (INCfAST) and its application to perform fast AST. As a proof-of-concept study, we have demonstrated metabolic heat measurements of *E. coli* in the presence of three clinically relevant antibiotics. By combining heat flow assessment and growth curves recorded by optical density measurements, we revealed that antimicrobials might induce energy spillage in the bacterial metabolism.

Chapter 5 presents oxygen consumption (OC) measurements performed with a modified INCfAST platform (also called indirect calorimetry). Oxygen sensing is based on the fluorescence detection by means of a nanoparticle sensor. For facultative anaerobic bacteria like *E. coli*, oxygen consumption may be used as an indicator of viability and thus also as a new method to perform AST. OC results can be correlated with heat measurements to assess the metabolic state at different growth phases.

Chapter 6 provides an extensive on-chip microbial motility study. Microfluidic technology and time-lapse imaging enables recording and analysis of bacterial swimming with single-cell resolution. We took advantage of an optical adhesive-based microfluidic chip to confine bacteria populations in a quasi-2D channel. We analyzed the collective chemotactic microbial migration behavior and found that genetically identical bacteria may lead to different swimming phenotypes. Interestingly, the swimming behavior may also be altered by the presence of antibiotics.

As is outlined in Figure 1.1, we intended to study bacterial metabolic activity and behavior on different time and dimensional scales, eventually allowing us to correlate single-bacterial features with community patterns. The microfluidic platforms developed in this work provide new toolboxes for performing fast AST and to study antimicrobial effects on bacteria from a more holistic perspective.

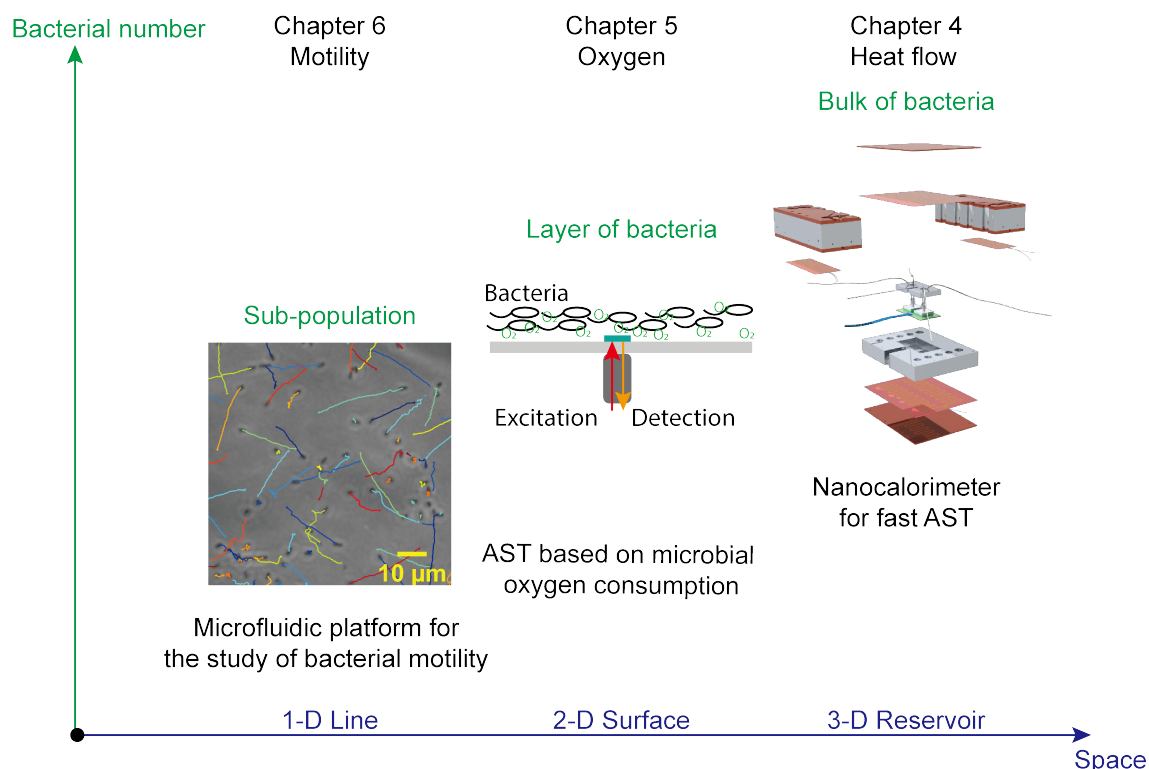


Figure 1.1 – Thesis outline presented on a 2-dimensional parameter space: feature of the bacterial number and experimental space dimension. Metabolic heat was recorded on larger bacteria populations in a micro-chamber and from a growth-related point of view. Indirect calorimetry by oxygen consumption was performed on sedimented bacterial layers near the sensing spot. Motility properties of quasi-2D populations, were derived from trajectories obtained by single-bacteria tracking based on videos recorded for tens of seconds.

1.3 Antimicrobial resistance (AMR) and persistence

1.3.1 AMR facts and challenges

Fast spreading of antimicrobial resistance (AMR) has been considered as one of the most challenging problems for global public health. Antibiotics as "magical weapons" have hidden the potential danger and high mortality related to infectious diseases. However, seven decades of antibiotics use and misuse triggered a strong selective pressure that promotes the proliferation of pathogens harboring antimicrobial resistance genes. Clinically relevant bacteria increasingly show single-drug

Chapter 1. Introduction

and multiple-drug resistance. Wrong administration and overprescription of antibiotics are major driving forces for AMR spreading.

An often cited AMR review report, based on detailed scenario analyses of the impact of AMR spreading on healthcare and macroeconomics, estimated to 10 million the number of deaths per year attributable to AMR in 2050, *i.e.* more than for most of the other major causes of disease-related death like cancer and diabetes (Figure 1.2a). [3] Moreover, since the 1980s, no new class of antibiotics has been discovered (Figure 1.2b), whereas the reported resistances increase steadily. [4] Obviously, this situation will have dramatic consequences, if no urgent measures are taken to reverse this trend.

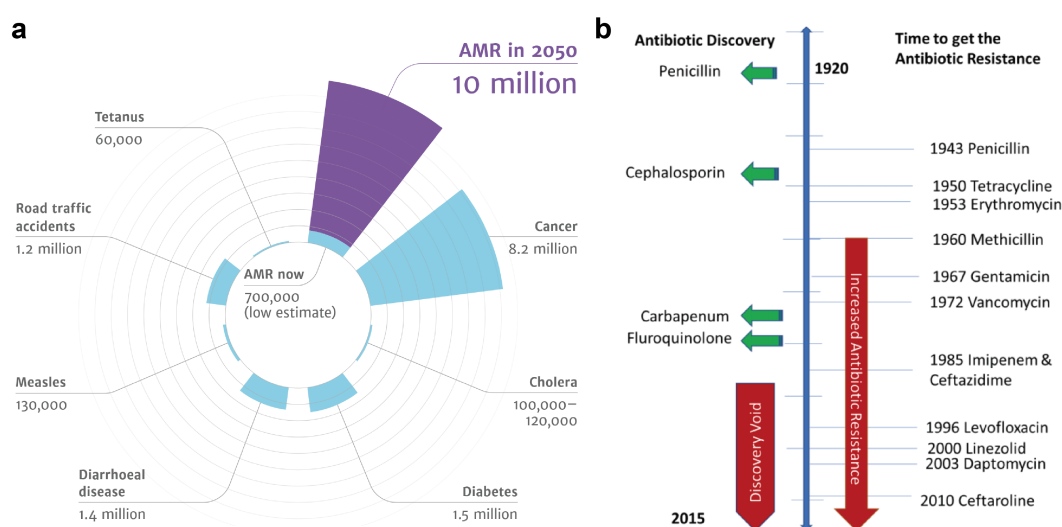


Figure 1.2 – The reality of antimicrobial resistance (AMR). (a) Estimation of deaths caused by AMR compared to other major diseases by 2050 if no effective actions are taken. (b) Antimicrobial discovery roadmap and the reported resistances. Adapted from [3, 4].

1.3.2 AMR mechanisms

Bacterial AMR is an inevitable natural selection process, that may occur faster or slower. AMR exhibited by bacteria has several sources: intrinsic, acquired or adaptive. [5] Intrinsic resistance is related to some inherent properties of the bacterium without exchange of genetic material. Acquired resistance means that an initially sensitive bacterium acquires resistance either by a mutation or the acquisition of new genetic material from horizontal gene transfer. Horizontal gene transfer occurs by transformation, transduction and conjugation. In this way, the selected resistance gene may be spread through the bacterial population. For both of these two sources, natural selection is a critical process, thus the misuse or overuse of antibiotics is highly responsible to promote AMR. Adaptive resistance by the modulations in gene expression is induced by environmental changes. This complicated process allows fast bacterial response to the antibiotic challenge.

In contrast to antimicrobial resistance, bacterial persistence refers to different concepts. Instead

1.3. Antimicrobial resistance (AMR) and persistence

of acquiring resistance genes, bacterial persisters switch the phenotype enabling survival without growth in the presence of antimicrobials.[6] Persisters serve as noticeable reservoir of chronic and recurring infections.

Antibiotic resistance mechanisms are diverse and can be classified into antibiotic destruction, antibiotic modification, target alteration, efflux and global adaptation.[7]

1. Antibiotic destruction

The most classical example is that β -lactamases destroy the amide bond of the β -lactam type antibiotics in order to turn them ineffective. Best known β -lactam antibiotics include penicillin derivatives (including ampicillin), cephalosporin, carbapenems, etc. Other examples include AmpC enzymes and carbapenemases.

2. Antibiotic modification

As an example, the invalidation of clinically relevant aminoglycoside (*e.g.* gentamicin) is often caused by the enzymatic modification of the antibiotic. Aminoglycoside modifying enzymes (AMEs) turn aminoglycoside to be less effective by acetylation, phosphorylation or adenylation. Similarly, chloramphenicol acetyltransferase (CAT) is another example targeting on chloramphenicol.

3. Modification of antibiotic activating enzymes

Mutations in nitroreductase genes *nfsA* and *nfsB* hinder the formation of toxic intermediate compounds which are required for the activity of nitrofurantoin.

4. Target alteration

(a) Target replacement

The β -lactam resistance in *Streptococcus pneumoniae* and methicillin resistance in *Staphylococcus aureus* are mainly caused by the replacement of the bacterial penicillin-binding proteins (PBPs).

(b) Target site alteration

Mutations in genes encoding the domain V of the 23S rRNA are the most common mechanism of linezolid resistance. Quinolone (*e.g.* ciprofloxacin) resistance is caused by the mutations in the bacterial gyrase and/or topoisomerase IV genes.

(c) Target site protection

Ribosomal protection proteins (RPPs) by acting as a DNA analogue and reducing the interaction of the bacterial gyrase and topoisomerase IV with DNA reduces the available binding sites of quinolone to achieve resistance.

(d) Target overproduction

As an example, overproduction of dihydrofolate reductase (DHFR) leads to resistance to trimethoprim in *E. coli*.

5. Decreased permeability of the bacterial outer membrane

The outer membrane of gram-negative bacteria serves as a permeability barrier for antibiotics. Mutations on the function of porins serving as route of entry will effectively reduce the cell susceptibility to certain hydrophilic antibiotics.

6. Efflux pumps

Efflux pumps on the cytoplasmic membrane, which are energy-dependent complex bacterial systems, are capable of pumping toxic molecules like antibiotics out of the cell,

7. Changes in cell regulation

Apart from the previous mechanisms, AMR may be due to a global adaptive response. For example, daptomycin kills the bacterial cell by altering cell membrane homeostasis. In *Enterococci*, mutations in genes encoding regulatory systems controlling cell envelope homeostasis and genes involved in phospholipid metabolism have been associated with the development of daptomycin resistance.

The investigation of mechanisms underlying AMR plays an important role in the development of new antimicrobials and also with respect to new therapeutic protocols based on the combinatorial utilization of antibiotics.[8]

1.4 Microfluidic technology

Microfluidic technology based on soft lithography has been widely used in the biological research works since 2000.[9] George Whitesides forecasted in 2006 that microfluidic technology will boom in the field of fundamental studies and analytical applications.[10] Indeed nowadays, reliable microfluidic toolboxes are getting more and more available to the scientific community, for healthcare settings and for industrial applications. Miniaturization of bio-analytical systems, also called lab-on-a-chip, enable high-throughput and precise manipulation of biological/biochemical samples and small organisms, thus also opening new frontiers in analytical applications. In this thesis, microfluidic-assisted protocols will be used for nanocalorimetric microbial metabolic studies and for bacterial motility analysis.

In general, a fluidic flow field for an incompressible Newtonian fluid is described by the Navier-Stokes equation

$$\rho (\partial_t \mathbf{v} + (\mathbf{v} \cdot \nabla) \mathbf{v}) = -\nabla p + \eta \nabla^2 \mathbf{v} + \mathbf{f} \quad (1.1)$$

where t , ρ , \mathbf{v} , p , η , and \mathbf{f} stands for the time, the fluid density, the velocity field, the pressure, the kinematic viscosity, and the external force density, respectively. To characterize the flow regime, the Reynolds number (Re) expresses the ratio between the inertial force $\rho(\mathbf{v} \cdot \nabla)\mathbf{v}$ and viscous force $\eta \nabla^2 \mathbf{v}$, which leads to

$$\text{Re} = \frac{\rho V_0 L_0}{\eta} \quad (1.2)$$

where L_0 and V_0 stand for the characteristic length and velocity of the system, respectively.

For a microfluidic channel (filled with water), L_0 is typically in the range of $\sim 100 \mu\text{m}$ and a value of $\sim 30 \mu\text{m/s}$ can be used as indication for V_0 , resulting in $\text{Re} = 3 \times 10^{-3}$. In general, Re numbers do not exceed $\sim 10^{-1}$ in a microfluidic system. Consequently, viscous forces dominate and the flow is laminar given that the transition to turbulent flow generally occurs in the range of Reynolds number

2000. In this case, the Navier-Stokes equation is simplified to Stokes equation (1.3) by neglecting the inertial forces (stationary condition without external force).^[11]

$$\eta \nabla^2 \mathbf{v} - \nabla p = 0 \quad (1.3)$$

For pressure driven flow in a microchannel (Poiseuille flow), a parabolic flow profile is observed. The laminar flow regime at low Re numbers, however, implies that different fluidic components can not be easily mixed as in turbulent flow. Active or passive microfluidic mixers have been developed to solve this issue.^[12]

The most common material used in microfluidics is poly(dimethylsiloxane) (PDMS), which is an optically transparent elastic polymer. PDMS is bio-compatible and allows easy prototyping. Taking advantage of the elastic property, on-chip pressure-driven valves and peristaltic pumps have been developed, *e.g.* the pioneering work for microfluidic large-scale integration by Unger *et al.*^[13] Following these developments, droplet technology on microfluidic chips has enabled high-throughput and single-cell based analysis.^[14] Microfluidic-assisted biological research is used nowadays for a broad range of applications, including devices classified as cell-on-a-chip,^[15] blood-on-a-chip,^[16] organ-on-a-chip, or even patient-on-a-chip.^[17] Among these, the emerging field of organ-on-a-chip or tissue-on-a-chip systems, designed as predictive human tissue models with sophisticated tissue assembly, draws more and more attention.^[18] This technology aims to explore dynamic cell environments and cellular communication to mimic organ functions. This approach may also be important to fill the gap between cell culture-based drug screening and drug testing on animals.

Moreover, microfluidic technology has expanded the frontiers of microbiological studies.^[19] Microfluidic chip-assisted time-lapse imaging allows unprecedented characterization of bacterial behavior in specific environments.^[20] The image analysis as a subsequent work step enables single-cell growth, motility and morphological analysis. The software ImageJ was invented to assist the engineers and biologists to extract useful information for the biological studies.^[21] By controlling chemical compound distributions on-chip, bacterial chemotaxis can be specifically studied in a more controlled microenvironment.^[22] In the presence of an external electric or magnetic system, bacterial taxis can be investigated from different perspectives and used for bacterial separation. Other examples are aerotaxis, rheotaxis, pH taxis, thermotaxis, and phototaxis.^[23] Controlling bacterial distributions or locally confining sub-populations on-chip opens the way to advanced studies of quorum sensing in bacterial communities.^[24] As bacteria are abundant in the natural environment, microfluidic chips can help creating a well controlled system to mimic a small snapshot of ecological processes.^[19]

Microfluidics also became increasingly influential in chemical synthesis and some industrial studies.^[25] Chemists can benefit from the advantages of on-chip protocols, such as continuous synthesis, tight control of reaction parameters, small-size, automation and high-throughput.^[26] However, in the extreme conditions required for some chemical processes, such as high temperature or high pressure, microfluidic technology may be less applicable. Microfluidic models have helped in different branches of science such as medicine, genetics, liquid channeling and

enhanced oil recovery. In the latter case, for instance, micromodels can be made to represent a microversion of a partially saturated rock with crude oil.[27]

1.5 Antimicrobial susceptibility testing (AST)

1.5.1 Definition of AST

AST refers to protocols that aim to determine to which specific compound (in particular antibiotics) a specific bacterial strain or fungus is sensitive. Currently in hospital settings or clinical laboratories, AST is mainly performed based on bacterial culture in liquid media or on agar plates. AST leads to qualitative or quantitative results. The qualitative results simply indicate whether the bacteria are sensitive or resistant to a specific antimicrobial. The quantitative results in this context mainly refer to the minimum inhibitory concentration (MIC), which is defined as the lowest concentration of a chemical that prevents visible bacterial growth (typically within 16-20 hours). For the clinical standards, the Clinical & Laboratory Standards Institute (CLSI) and the European Committee on Antimicrobial Susceptibility Testing (EUCAST) are the most important institutions, respectively in US and Europe, that provide guidelines for the practice.[28]

1.5.2 From hospitalization to AST

To emphasize the importance of fast AST, which is one of the core topics of this thesis, we first discuss a typical current clinical timeline from hospitalization to the availability of the AST results. Figure 1.3 shows a schematic referring to a blood stream infection (BSI) as an example that may be applied likewise to urine infections, respiratory tract infections and others.[29, 30] The hospitalization and logistics are the starting point of this workflow. A delay of 2-3 days is necessary from blood sample collection to AST results if traditional blood culture routines are pursued. Once a positive blood culture is identified, a purification step of the pathogens follows. Pathogen identification can be performed by gram-staining, fluorescent in situ hybridization (FISH),[31] matrix assisted laser desorption ionization - time of flight (MALDI-TOF) mass spectrometry,[32] etc. At this stage, the patient is normally treated according to an empirical antibiogram of the identified pathogen. In the meantime, AST can be performed on the purified pathogen culture in order to obtain an experimental antibiogram that allows to refine the therapeutic protocol. In this thesis our focus was to propose a method that may reduce considerably this additional delay in order to provide an optimum antimicrobial administration protocol as a first option for treatment of infections, immediately after identification of a positive culture.

Figure 1.3 indicates another option based on molecular diagnostics to identify microbial resistance to antibiotics. Based on genome sequencing technology or PCR amplification for certain types of genes in the clinical sample, both the bacteria strain identification and the presence of resistance genes can be performed.[33, 34] This routine has high sensitivity and the read-out time is significantly reduced with respect to culture-based methods. However, a pre-established gene database is necessary. Nevertheless, for the time being, molecular diagnosis is still the most

promising of the emerging AST technologies and it is more and more accepted by the clinical facilities.

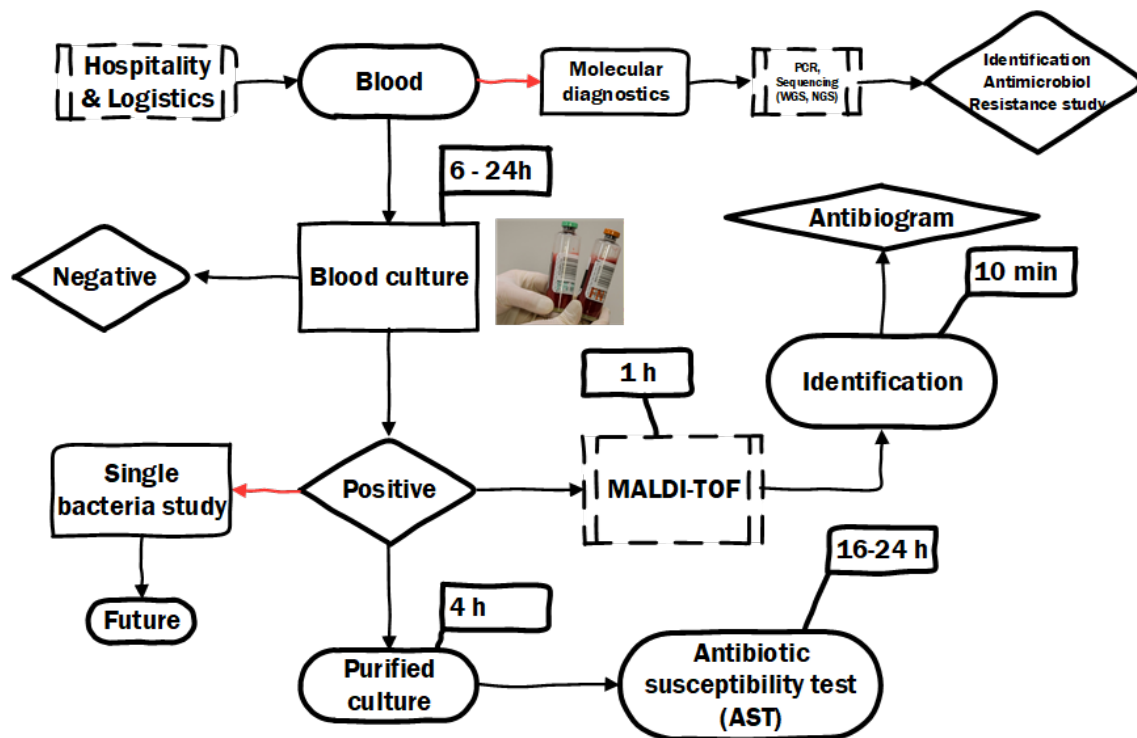


Figure 1.3 – A typical workflow for blood stream infection (BSI) from hospitalization to AST results. The traditional routine comprises blood culture, pathogen purification and AST. The new routines (red arrow) include molecular diagnostics and single-bacteria analysis. The typical time required for each step is indicated in the figure. [29].

1.5.3 Conventional methods

The most widely used AST methods in clinical laboratories are the broth micro dilution (BMD) method and the disk diffusion method (Figure 1.4a and 1.4b), which are considered as gold standard by CLSI and by EUCAST, respectively.[28] Standardized protocols are a pre-requisite for reliable treatments. For instance, MIC values may depend on the initial bacterial concentration, which is called inoculum effect.[35] The above-mentioned methods need overnight culture to monitor whether bacterial growth occurs or not. BMD consists of a labor-intensive protocol for the preparation of antibiotic solutions with different concentrations to determine MIC values quantitatively based on the presence of bacterial growth in the well-plate. Disk diffusion, performed on agar plates spread with bacteria, only provides qualitative results using the categories “susceptible”, “intermediate”, or “resistant” depending on the inhibition zone diameter. bioMérieux commercialized the E-test, a relative new method based on the same principle as disk diffusion (Figure 1.4c). E-test strips already contain antibiotics at different concentrations based on the intersection of the concentration scale with colony growth/no-growth borderline.[36]

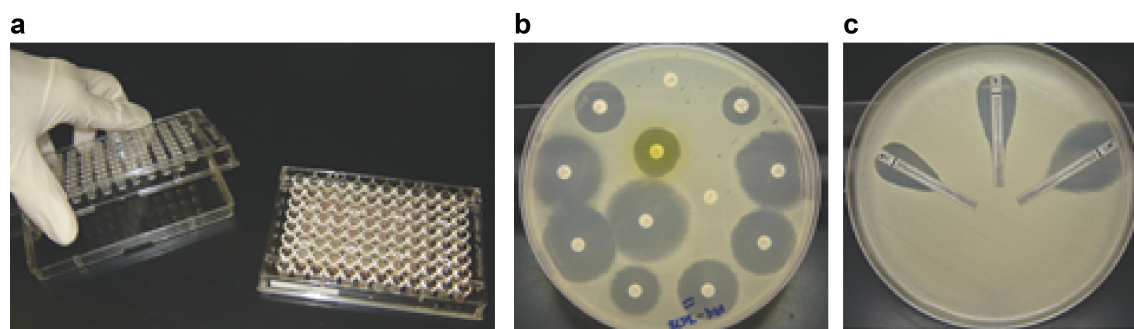


Figure 1.4 – Conventional AST methods in current clinical setting. (a) Broth micro dilution (BMD). The visual formation of bacterial colony in each well is inspected to determine the MIC values. (b) Disk diffusion. The diameter of the inhibition zone around the antimicrobial disk is measured to determine whether the bacteria are "sensitive", "resistant" or "intermediate" to the antimicrobial. (c) E-Test (bioMérieux). The intersection of growth and non-growth areas defines the MIC value, which is indicated on the strip. Adapted from [28].

1.5.4 Recent commercialized methods

From a market perspective, traditional culture-based methods, such as agar plate and BMD, still dominate the market, but it is expected that the impact of these methods will decrease gradually. Competitors in the AST market include established companies, also called unicorns, such as BD and bioMérieux, and start-ups, *e.g.* as Symcel, Astrego Diagnostic AB, Accelerate Diagnostics, Milidrop or oCelloScope. The unicorns mostly developed automated machines based on optical density (*i.e.* turbidity) measurements to monitor bacterial growth as shown in Figure 1.5.[37, 38] Their product is usually equipped with the sample preparation module. Looking at more recent developments, the start-up Symcel uses the detection of microbial heat flow to realize fast AST.[39] This technology is comparable to the approach discussed in the frame of this thesis. Astrego Diagnostic AB declares a 30 min read-out time lapse based on single bacterial growth monitoring, thus being the fastest among all companies.[40] Accelerate Diagnostics performs AST based on bacterial morphological information and species identification with FISH.[41] Milidrop proposes a microfluidic droplet technology with high throughput.[42] oCelloScope produced an automatic microscopy to monitor the growth of individual bacteria or small groups of bacteria.[43] Besides these technologies, there are also products based on gene sequencing technologies, for instance the Biofire® Filmarray® system from bioMérieux.[44] Table 1.1 summarizes the previously mentioned technologies based on the data disclosed by the companies.

1.5.5 Microfluidic methods

Innovative AST methods have been developed based on various principles. The main objective is to minimize the AST time to result without losing accuracy of the final results. Improving the throughput is another objective. In this context, microfluidic-assisted technologies take an important part for developing options for high-content analysis of small sample volumes in a

1.5. Antimicrobial susceptibility testing (AST)

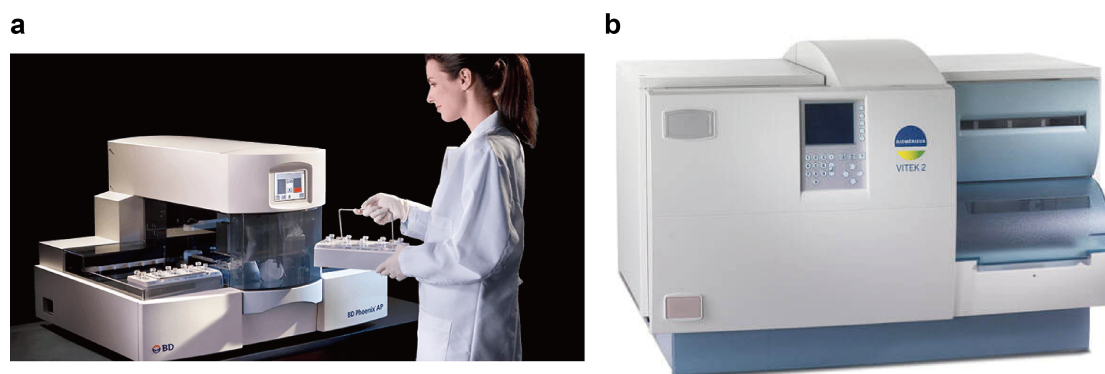


Figure 1.5 – Commercial AST methods. (a) BD Phoenix TM®. (b) bioMérieux Vitek-2®. Adapted from [45, 46].

parallel high-throughput manner. Different detection and characterization methods based on different physical or biological parameters have been demonstrated.

Figure 1.6 shows four examples of microfluidic-based fast AST approaches. Droplet microfluidics (see Milidrop in Table 1.1) enables monitoring bacterial growth and MIC evaluation in individual droplets, in which the bacterial concentration and antimicrobial concentration is quantified by two types of fluorescent molecules (Figure 1.6a).[42] As shown in Figure 1.6b, Baltekin *et al.* took advantage of confined microchannels, for monitoring single bacterial growth when nutrients and drugs are flushed through the system (see Astrego Diagnostic AB in Table 1.1).[40] Based on the biomass change for each individual channel, bacterial susceptibility to the antimicrobial can be analyzed. Choi *et al.* immobilized bacteria in agarose in chip compartment where antimicrobials could diffuse in (Figure 1.6c). The susceptibility algorithm was based on both the bacterial growth and the morphological analysis.[47]. Fredborg *et al.* (see oCelloScope in Table 1.1) developed an imaging technology combined with well plate format to render bacterial morphological and growth information for high-throughput, low-cost and fast AST.[43]

Some other principles may be explored to perform AST. For example, ultrasensitive electrical transduction techniques for detecting nanomechanical movements of bacteria in a microchannel may indicate the bacterial viability.[48]. In another approach, impedance spectroscopy monitored the electrical response of bacteria captured on flexible plastic-based microchips with printed electrodes in the presence and absence of antibiotics.[49] Syal *et al.* demonstrated rapid AST by tracking bacterial motion on the sub- μm scale with an optical imaging technique. The dose-dependent motion provided reliable MIC results.[50] Raman spectroscopy on a dielectrophoresis chip has been introduced to identify antimicrobial susceptibilities and determine MIC values within only 2 h.[51] More work in this field is reported in recent reviews.[52, 53]

Table 1.1 – Examples of commercial available AST platforms.

TECHNOLOGY	DESCRIPTION	TIME TO READ-OUT	COMMENTS
bioMérieux Vitek-2	French company; AST based on the optical density measurement and identification based on Advanced Colorimetry®.	5-24 hours	Sample preparation; high throughput; coherent with the gold standard method; database for identification.
BD Phoenix™ – BD EpiCenter™	American company; based on the optical density measurement.	5-18 hours	Sample preparation; fully automation possible; identification module; data management.
Symcel calScreener	Swedish start-up; based on nanocalorimetry.	6 hours	High throughput; sample loading by pipetting.
Astrego Diagnostic AB	Swedish start-up; based on microscopy imaging of bacteria in a microfluidic chip.	30 min	High throughput; visibility of bacterial growth.
Accelerate Diagnostics	American start-up; based on the morphological analysis of bacterial growth and division.	7 hours	Species identification with FISH; complicated image analysis algorithm.
Milidrop	French start-up; microfluidic droplet-based technology.	7 hours	High throughput; fluorescent dye in the droplets.
oCelloScope	Dutch start-up; based on time-lapse imaging and image processing.	2-6 hours	High throughput; visibility of bacterial number.
INCfAST Platform	Current study of the thesis	5-7 hours	150 μ L sample volume; microfluidic sample delivery system; throughput to be improved.

1.6 Bacterial metabolism

1.6.1 Metabolic pathways

Metabolism refers to all biochemical reactions that occur in a cell or organism. The uptake of nutrients by a cell can be converted to energy to maintain the cellular processes, which is known as catabolism. The produced energy will be used to synthesize bio-molecules (cell walls, proteins, fatty acids, nucleic acids), which is known as anabolism. Most bacteria, including all pathogens, belong to heterotroph organisms and therefore rely on the oxidation of organic compounds in

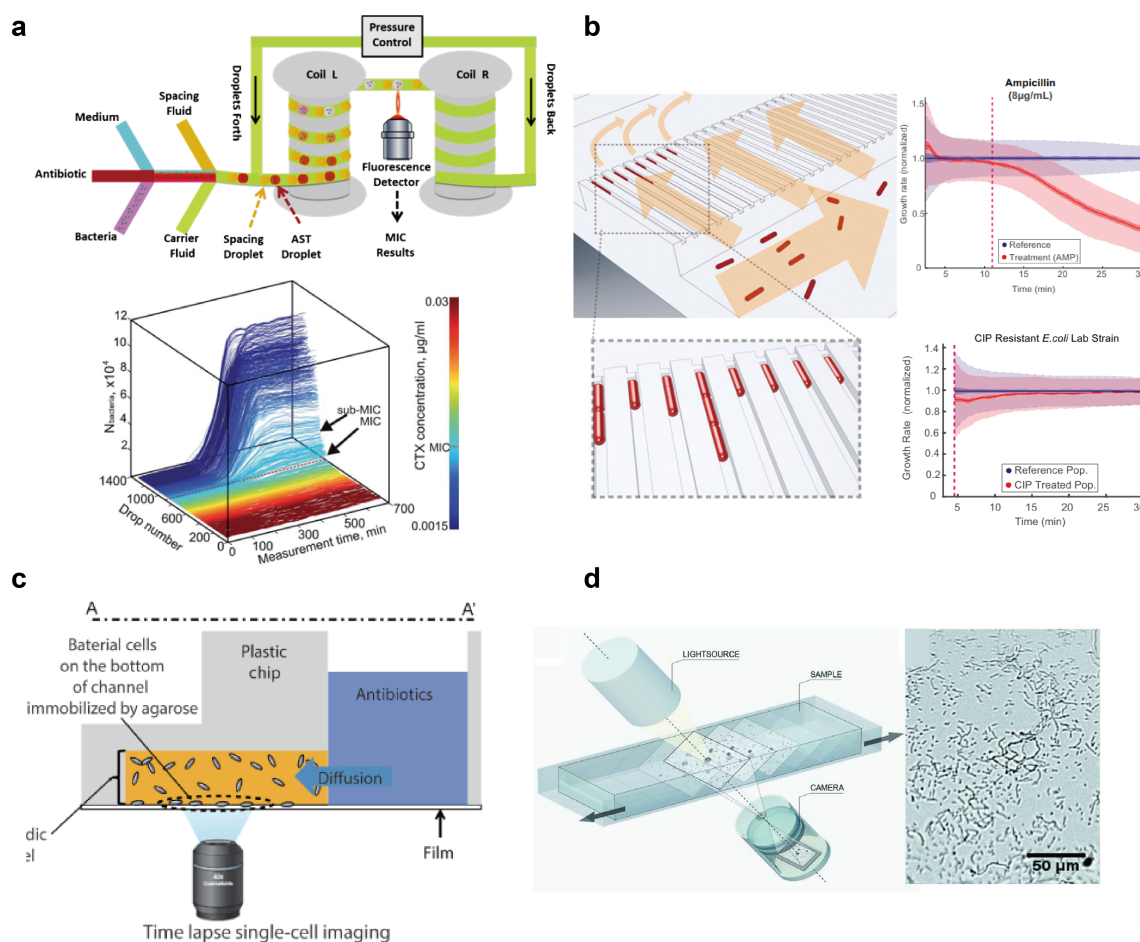


Figure 1.6 – Innovative AST methods. (a) Droplet technology,[42] (b) the bacterial "mother machine", [40] (c) bacterial morphology analysis,[47] and (d) analysis based on images obtained by automatic optical microscopy.[43] Adapted from the corresponding papers.

the food sources. The oxidizable compounds include carbohydrates (in particular glucose), lipids and proteins. The metabolites are converted via several pathways to one common intermediate compound, named pyruvic acid.[54]

Bacterial metabolic pathways mainly includes fermentation, aerobic respiration or anaerobic respiration (Figure 1.7a). Aerobic respiration is a type of heterotrophic metabolism that uses oxygen and in which 38 moles of ATP are derived from the oxidation of 1 mole of glucose with 308,000 cal energy loss as heat, where the energy efficiency is 55%. In the presence of oxygen, the pyruvic acid produced from glycolysis and other substrates may be completely oxidized to H_2O and CO_2 using the Krebs cycle, also called tricarboxylic acid (TCA) cycle. Whereas, in fermentation, another type of heterotrophic metabolism, an organic compound rather than oxygen is the terminal electron acceptor to recycle NADH to NAD. Most bacteria use the one-step conversion of pyruvic acid to lactic acid. Less energy is generated from this incomplete form of glucose oxidation. Anaerobic respiration uses other terminal electron acceptors, such as nitrate bonding to NH_4^+ , sulfate or

molecular sulfur to H_2S , or ferric ion to ferrous ion. Less ATP is produced for each NADH than during aerobic respiration, because the reduction-oxidation potential is lower for these reactions.

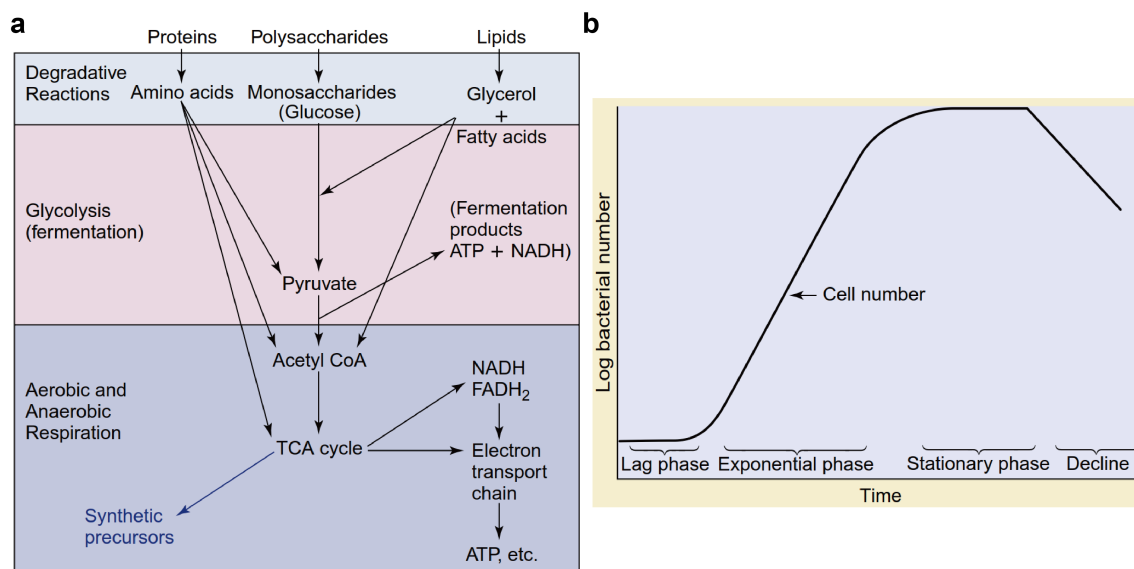


Figure 1.7 – (a) Bacterial metabolic pathways and (b) a typical bacterial growth curve. Adapted from [54].

1.6.2 Bacterial growth

If enough metabolites are available to support synthesis of the bacterial components, especially the nucleotides for DNA synthesis, bacterial growth can occur. The bacterial replication is a coordinated process, in which two identical daughter cells are produced. A typical bacterial growth curve is represented in Figure 1.7b. When alive bacteria are added to the culture medium, a certain time is required for bacteria to adapt to the new environment. This delay is known as the lag phase of growth. Hereafter, bacteria will grow and divide with a characteristic doubling time, resulting in a logarithmic or exponential growth phase. The initial number of bacteria increases by 2^n , where n is the number of generations (doubling). Eventually, metabolite depletion occurs in the culture medium and/or toxic substances may be produced, forcing bacterial growth to stop and enter a stationary phase. Finally the population declines due to death. In the stationary phase and even in the dead phase, some bacteria remain viable but not metabolically active.

1.6.3 Antimicrobial effect on the metabolic activity

Bacterial metabolic homeostasis is often an important consequence of antimicrobial treatment that targets energy-consuming processes. The antimicrobial activity and bacterial metabolism are mutually influenced. Not only the antimicrobials will alter the metabolic state of bacteria, but also the metabolic state will influence their susceptibility to antibiotics.[55, 56] These effects depend on whether the antimicrobial is bactericidal or bacteriostatic.

Recent studies revealed that *E. coli* and *S. aureus* show increasing basal respiration rates via deletion of the alpha subunit of the F_1 complex of ATP synthase (atpA).^[57] However, bacteriostatic antibiotics simultaneously decrease central carbon metabolism and increase the abundance of associated intracellular metabolites. It has been shown that bacterial persisters endure the metabolic repression and display decreased susceptibility to bactericidal agents.^[58]

1.7 Swimming of *E. coli*

Antonie van Leeuwenhoek was the first scientist who observed the motion of *E. coli* under a microscope in the 17th century. Today, not only individual bacteria but also their flagella can be observed under optical microscopes.^[59] Beyond swimming in a liquid phase, bacteria also show specific motility features on a humid surface, including swarming, twitching, gliding and sliding.^[60] Motility on surfaces also plays an important role in bacterial colonization.

The development of molecular biology revealed the molecular machinery that controls swimming of *E. coli*. *E. coli* uses a tumble/run strategy to navigate in the microenvironment. A coordinated protein system senses a chemical gradient and orientates swimming towards optimum environmental conditions.^[61, 62] As shown in Figure 1.8a, the protein network includes a chemical sensing system and a motor system. The sensing and processing of chemotactic stimuli is performed by complexes consisting of attractant-specific chemoreceptors — the methyl-accepting chemotaxis proteins (MCPs) in the cytoplasmic membrane. Apart from the chemoreceptors, the complexes also comprise a histidine kinase CheA (chemotaxis protein A) and an adaptor protein CheW. The responses to the ligand binding events are mediated by methylation or demethylation of chemoreceptors on four specific glutamate residues by the methyltransferase CheR or the methylesterase CheB. CheA senses changes through transmembrane chemoreceptors, which induce the trans-autophosphorylation of dimeric CheA to form CheA-P. The phosphoryl group of CheA-P is competed by two response regulator: CheY and CheB. Therefore, the main output of the signaling network is the level of phosphorylated response regulator CheY (CheY-P). The binding of CheY-P to the switch protein FliM on the flagella motor promotes clockwise (CW) flagella rotation, which causes the cell to tumble and change directions. An increased attractant binding to chemoreceptors inhibits the autophosphorylation of CheA, which reduces the concentration of CheY-P and therefore the frequency of motor switching. This causes the bacterium to swim in a positive direction for longer time by the counter-clockwise (CCW) rotation of the flagella motor, which is called run. Rapid dephosphorylation of CheY-P is ensured by the phosphatase CheZ. An additional negative feedback is provided by CheA-dependent CheB phosphorylation as it also competes for the phosphoryl group from CheA-P, which controls the adaptation of the chemoreceptors. Phosphorylated CheB (CheB-P) results in an increased methylesterase activity and an increased demethylation of the MCPs. Demethylated MCPs have a reduced ability to induce CheA autophosphorylation, so the rate of CheA autophosphorylation and the rate of CheY-P formation are decreased.

As shown in Figure 1.8b, CCW rotation of flagella motors leads to straight swimming runs and CW rotation of flagella motors results in tumbles. Without chemical gradient, bacterial swimming

corresponds to a random walk model.[63] In the presence of a gradient, the CCW rotation is promoted once bacteria sense the attractant gradient, which results in directional bacterial swimming towards the attractant (Figure 1.8c).

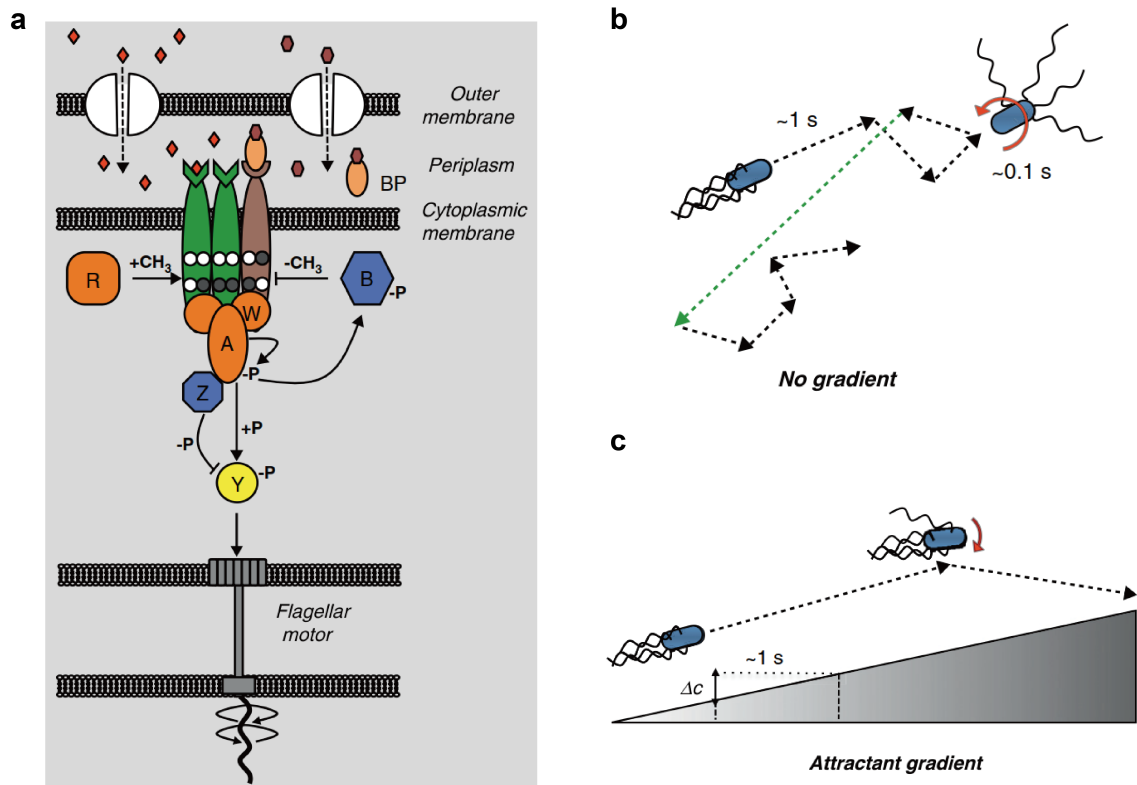


Figure 1.8 – (a) Protein system generating the "tumble/run" swimming strategy of *E. coli*, including a chemical sensing module and a motor module. (b) Swimming of *E. coli* without gradient showing random walks. CCW flagella rotation leads to straight runs and CW rotation leads to bacterial tumbling, which allow the bacteria to adjust the swimming direction. (c) Chemotactic swimming towards higher attractant concentrations. Adapted from [62].

References

1. Fleming, A. On the Antibacterial Action of Cultures of a *Penicillium*, with Special Reference to Their Use in the Isolation of *B. Influenzæ*. *British journal of experimental pathology* **10**, 226–236 (June 1929) (cit. on p. 1).
2. Podolsky, S. H. The Evolving Response to Antibiotic Resistance (1945–2018). *Palgrave Communications* **4**, 124 (Dec. 2018) (cit. on pp. 1, 135, 140).
3. O'Neill, J. *Tackling Drug-Resistant Infections Globally: Final Report and Recommendations. The Review on Antimicrobial Resistance, Chaired by Jim O'Neill* (May 2016) (cit. on pp. 4, 53).
4. Zaman, S. B. *et al.* A Review on Antibiotic Resistance: Alarm Bells Are Ringing. *Cureus* **9**, e1403 (June 28, 2017) (cit. on pp. 4, 53).
5. Lee, J.-H. Perspectives towards Antibiotic Resistance: From Molecules to Population. *Journal of Microbiology* **57**, 181–184 (Mar. 2019) (cit. on p. 4).
6. Balaban, N. Q., Merrin, J., Chait, R., Kowalik, L. & Leibler, S. Bacterial Persistence as a Phenotypic Switch. *Science* **305**, 1622–1625 (Sept. 10, 2004) (cit. on pp. 5, 126).
7. Christaki, E., Marcou, M. & Tofarides, A. Antimicrobial Resistance in Bacteria: Mechanisms, Evolution, and Persistence. *Journal of Molecular Evolution* **88**, 26–40 (Jan. 1, 2020) (cit. on p. 5).
8. León-Buitimea, A., Garza-Cárdenas, C. R., Garza-Cervantes, J. A., Lerma-Escalera, J. A. & Morones-Ramírez, J. R. The Demand for New Antibiotics: Antimicrobial Peptides, Nanoparticles, and Combinatorial Therapies as Future Strategies in Antibacterial Agent Design. *Frontiers in Microbiology* **11**. doi:[10.3389/fmicb.2020.01669](https://doi.org/10.3389/fmicb.2020.01669) (2020) (cit. on p. 6).
9. Xia, Y. & Whitesides, G. M. Soft Lithography. *Annual Review of Materials Science* **28**, 153–184 (1998) (cit. on p. 6).
10. Whitesides, G. M. The Origins and the Future of Microfluidics. *Nature* **442**, 368–373 (July 27, 2006) (cit. on p. 6).
11. Tabeling, P. *Introduction to Microfluidics* 312 pp. (OUP Oxford, Nov. 25, 2005) (cit. on p. 7).
12. Lee, C.-Y., Chang, C.-L., Wang, Y.-N. & Fu, L.-M. Microfluidic Mixing: A Review. *International Journal of Molecular Sciences* **12**, 3263–3287 (May 18, 2011) (cit. on p. 7).
13. Unger, M. A., Chou, H.-P., Thorsen, T., Scherer, A. & Quake, S. R. Monolithic Microfabricated Valves and Pumps by Multilayer Soft Lithography. *Science* **288**, 113–116 (Apr. 7, 2000) (cit. on pp. 7, 125).
14. Shang, L., Cheng, Y. & Zhao, Y. Emerging Droplet Microfluidics. *Chemical Reviews* **117**, 7964–8040 (June 28, 2017) (cit. on p. 7).
15. El-Ali, J., Sorger, P. K. & Jensen, K. F. Cells on Chips. *Nature* **442**, 403–411 (July 27, 2006) (cit. on p. 7).
16. Toner, M. & Irimia, D. Blood-on-a-Chip. *Annual Review of Biomedical Engineering* **7**, 77–103 (July 8, 2005) (cit. on p. 7).

17. Caballero, D., Reis, R. L. & Kundu, S. C. in *Biomaterials- and Microfluidics-Based Tissue Engineered 3D Models* (eds Oliveira, J. M. & Reis, R. L.) 43–64 (Springer International Publishing, Cham, 2020). doi:[10.1007/978-3-030-36588-2_4](https://doi.org/10.1007/978-3-030-36588-2_4) (cit. on p. 7).
18. Zhang, B. & Radisic, M. Organ-on-a-Chip Devices Advance to Market. *Lab on a Chip* **17**, 2395–2420 (2017) (cit. on p. 7).
19. Rusconi, R., Garren, M. & Stocker, R. Microfluidics Expanding the Frontiers of Microbial Ecology. *Annual Review of Biophysics* **43**, 65–91 (May 6, 2014) (cit. on pp. 7, 102).
20. Eland, L., Wipat, A., Lee, S., Park, S. & Wu, L. in *Methods in Microbiology* 69–111 (Elsevier, 2016). doi:[10.1016/bs.mim.2016.10.002](https://doi.org/10.1016/bs.mim.2016.10.002) (cit. on p. 7).
21. *ImageJ* <https://imagej.nih.gov/ij/index.html> (2020) (cit. on p. 7).
22. Wu, F. & Dekker, C. Nanofabricated Structures and Microfluidic Devices for Bacteria: From Techniques to Biology. *Chem. Soc. Rev.* **45**, 268–280 (2016) (cit. on pp. 7, 102).
23. Gurung, J. P., Gel, M. & Baker, M. A. B. Microfluidic Techniques for Separation of Bacterial Cells via Taxis. *Microbial Cell* **7**, 66–79 (Mar. 2, 2020) (cit. on pp. 7, 102).
24. Miller, M. B. & Bassler, B. L. Quorum Sensing in Bacteria. *Annual Review of Microbiology* **55**, 165–199 (Oct. 1, 2001) (cit. on p. 7).
25. Elvira, K. S., i Solvas, X. C., Wootton, R. C. R. & deMello, A. J. The Past, Present and Potential for Microfluidic Reactor Technology in Chemical Synthesis. *Nature Chemistry* **5**, 905–915 (11 Nov. 2013) (cit. on p. 7).
26. Liu, Y. & Jiang, X. Why Microfluidics? Merits and Trends in Chemical Synthesis. *Lab on a Chip* **17**, 3960–3978 (Nov. 21, 2017) (cit. on p. 7).
27. Gogoi, S. & Gogoi, S. B. Review on Microfluidic Studies for EOR Application. *Journal of Petroleum Exploration and Production Technology* **9**, 2263–2277 (Sept. 1, 2019) (cit. on p. 8).
28. Jorgensen, J. H. & Ferraro, M. J. Antimicrobial Susceptibility Testing: A Review of General Principles and Contemporary Practices. *Clinical Infectious Diseases* **49**, 1749–1755 (Dec. 2009) (cit. on pp. 8–10, 104, 127).
29. Jordi, V. *Lecture on "Current Methods of Rapid Diagnosis in Clinical Microbiology-Gaps and Needs"* 2017 (cit. on pp. 8, 9).
30. Vila, J., Gómez, M. D., Salavert, M. & Bosch, J. Métodos de diagnóstico rápido en microbiología clínica: necesidades clínicas. *Enfermedades Infecciosas y Microbiología Clínica* **35**, 41–46 (Jan. 1, 2017) (cit. on p. 8).
31. Kempf, V. A. J., Trebesius, K. & Autenrieth, I. B. Fluorescent In Situ Hybridization Allows Rapid Identification of Microorganisms in Blood Cultures. *Journal of Clinical Microbiology* **38**, 830–838 (Feb. 2000) (cit. on p. 8).
32. Murray, P. R. What Is New in Clinical Microbiology—Microbial Identification by MALDI-TOF Mass Spectrometry. *The Journal of Molecular Diagnostics : JMD* **14**, 419–423 (Sept. 2012) (cit. on p. 8).

33. Buchan, B. W. & Ledeboer, N. A. Emerging Technologies for the Clinical Microbiology Laboratory. *Clinical Microbiology Reviews* **27**, 783–822 (Oct. 1, 2014) (cit. on p. 8).
34. Greatedorex, J., Ellington, M. J., Köser, C. U., Rolfe, K. J. & Curran, M. D. New Methods for Identifying Infectious Diseases. *British Medical Bulletin* **112**, 27–35 (Dec. 1, 2014) (cit. on p. 8).
35. Lenhard, J. R. & Bulman, Z. P. Inoculum Effect of Beta-Lactam Antibiotics. *Journal of Antimicrobial Chemotherapy* **74**, 2825–2843 (Oct. 1, 2019) (cit. on p. 9).
36. Balouiri, M., Sadiki, M. & Ibnsouda, S. K. Methods for in Vitro Evaluating Antimicrobial Activity: A Review. *Journal of Pharmaceutical Analysis* **6**, 71–79 (Apr. 2016) (cit. on pp. 9, 54, 71).
37. Ligozzi, M. *et al.* Evaluation of the VITEK 2 System for Identification and Antimicrobial Susceptibility Testing of Medically Relevant Gram-Positive Cocci. *Journal of Clinical Microbiology* **40**, 1681–1686 (May 1, 2002) (cit. on p. 10).
38. Carroll, K. C. *et al.* Evaluation of the BD Phoenix Automated Microbiology System for Identification and Antimicrobial Susceptibility Testing of Enterobacteriaceae. *Journal of Clinical Microbiology* **44**, 3506–3509 (Oct. 1, 2006) (cit. on p. 10).
39. Wadsö, I. *et al.* A Well-Plate Format Isothermal Multi-Channel Microcalorimeter for Monitoring the Activity of Living Cells and Tissues. *Thermochimica Acta* **652**, 141–149 (June 2017) (cit. on pp. 10, 55, 74).
40. Baltekin, Ö., Boucharin, A., Tano, E., Andersson, D. I. & Elf, J. Antibiotic Susceptibility Testing in Less than 30 Min Using Direct Single-Cell Imaging. *Proceedings of the National Academy of Sciences*, 201708558 (Aug. 8, 2017) (cit. on pp. 10, 11, 13, 54, 102, 127, 137).
41. Ullberg, M. & Özenci, V. Identification and Antimicrobial Susceptibility Testing of Gram-Positive and Gram-Negative Bacteria from Positive Blood Cultures Using the Accelerate Pheno™ System. *European Journal of Clinical Microbiology & Infectious Diseases* **39**, 139–149 (Jan. 1, 2020) (cit. on p. 10).
42. Baraban, L. *et al.* Millifluidic Droplet Analyser for Microbiology. *Lab on a Chip* **11**, 4057 (2011) (cit. on pp. 10, 11, 13).
43. Fredborg, M. *et al.* Real-Time Optical Antimicrobial Susceptibility Testing. *Journal of Clinical Microbiology* **51**, 2047–2053 (July 1, 2013) (cit. on pp. 10, 11, 13).
44. Leber, A. L. *et al.* Multicenter Evaluation of BioFire FilmArray Respiratory Panel 2 for Detection of Viruses and Bacteria in Nasopharyngeal Swab Samples. *Journal of Clinical Microbiology* **56**. doi:10.1128/JCM.01945-17 (June 2018) (cit. on p. 10).
45. BD Phoenix™ AP Instrument
<https://www.bd.com/en-us/offerings/capabilities/microbiology-solutions/identification-and-susceptibility-testing/bd-phoenix-automated-identification-and-susceptibility-testing-system/bd-phoenix-ap-instrument> (2020) (cit. on p. 11).
46. VITEK® 2: Healthcare bioMérieux. <https://www.biomerieux-usa.com/vitek-2> (2020) (cit. on p. 11).

47. Choi, J. *et al.* A Rapid Antimicrobial Susceptibility Test Based on Single-Cell Morphological Analysis. *Science translational medicine* **6**, 267ra174–267ra174 (2014) (cit. on pp. 11, 13).
48. Kara, V. *et al.* Microfluidic Detection of Movements of Escherichia Coli for Rapid Antibiotic Susceptibility Testing. *Lab on a Chip* **18**, 743–753 (2018) (cit. on p. 11).
49. Safavieh, M. *et al.* Rapid Real-Time Antimicrobial Susceptibility Testing with Electrical Sensing on Plastic Microchips with Printed Electrodes. *ACS Applied Materials & Interfaces* **9**, 12832–12840 (Apr. 12, 2017) (cit. on p. 11).
50. Syal, K. *et al.* Rapid Antibiotic Susceptibility Testing of Uropathogenic *E. Coli* by Tracking Submicron Scale Motion of Single Bacterial Cells. *ACS Sensors*. doi:[10.1021/acssensors.7b00392](https://doi.org/10.1021/acssensors.7b00392) (Aug. 8, 2017) (cit. on p. 11).
51. Kirchhoff, J. *et al.* Simple Ciprofloxacin Resistance Test and Determination of Minimal Inhibitory Concentration within 2 h Using Raman Spectroscopy. *Analytical Chemistry* **90**, 1811–1818 (Feb. 6, 2018) (cit. on p. 11).
52. Leonard, H., Colodner, R., Halachmi, S. & Segal, E. Recent Advances in the Race to Design a Rapid Diagnostic Test for Antimicrobial Resistance. *ACS Sensors* **3**, 2202–2217 (Nov. 26, 2018) (cit. on p. 11).
53. Dietvorst, J., Vilaplana, L., Uria, N., Marco, M.-P. & Muñoz-Berbel, X. Current and Near-Future Technologies for Antibiotic Susceptibility Testing and Resistant Bacteria Detection. *TrAC Trends in Analytical Chemistry* **127**, 115891 (June 1, 2020) (cit. on p. 11).
54. Murray, P. R., Rosenthal, K. & Pfaller, M. in. 9th ed., 152–167 (Elsevier, 2020) (cit. on pp. 13, 14).
55. Stokes, J. M., Lopatkin, A. J., Lobritz, M. A. & Collins, J. J. Bacterial Metabolism and Antibiotic Efficacy. *Cell Metabolism* **30**, 251–259 (Aug. 2019) (cit. on p. 14).
56. Belenky, P. *et al.* Bactericidal Antibiotics Induce Toxic Metabolic Perturbations That Lead to Cellular Damage. *Cell Reports* **13**, 968–980 (Nov. 2015) (cit. on p. 14).
57. Lobritz, M. A. *et al.* Antibiotic Efficacy Is Linked to Bacterial Cellular Respiration. *Proceedings of the National Academy of Sciences* **112**, 8173–8180 (July 7, 2015) (cit. on p. 15).
58. Brauner, A., Fridman, O., Gefen, O. & Balaban, N. Q. Distinguishing between Resistance, Tolerance and Persistence to Antibiotic Treatment. *Nature Reviews Microbiology* **14**, 320–330 (5 May 2016) (cit. on p. 15).
59. Turner, L., Ping, L., Neubauer, M. & Berg, H. C. Visualizing Flagella While Tracking Bacteria. *Biophysical Journal* **111**, 630–639 (Aug. 2016) (cit. on p. 15).
60. Harshey, R. M. Bacterial Motility on a Surface: Many Ways to a Common Goal. *Annual Review of Microbiology* **57**, 249–273 (Oct. 2003) (cit. on p. 15).
61. Wadhams, G. H. & Armitage, J. P. Making Sense of It All: Bacterial Chemotaxis. *Nature Reviews Molecular Cell Biology* **5**, 1024–1037 (Dec. 2004) (cit. on pp. 15, 101, 102).
62. Sourjik, V. & Wingreen, N. S. Responding to Chemical Gradients: Bacterial Chemotaxis. *Current Opinion in Cell Biology. Cell Regulation* **24**, 262–268 (Apr. 1, 2012) (cit. on pp. 15, 16).

63. Berg, H. C. *Random Walks in Biology* (Princeton University Press, Princeton, New Jersey, 1993) (cit. on pp. 16, 101).

2 Theory of calorimetry

Calorimetry is a classical method in physical chemistry. The famous ice calorimeter experiment performed by Lavoisier and Laplace marked the birth of modern calorimetry.[64] Today, MEMS technology and new synthesized thermoelectric materials[65] provide enhanced versatility for innovate calorimeter research and technology. The wide range of applications covers chemical, biological[66], food-related research[67], and industrial needs. Design aspects of calorimeters comprise heat transfer simulations, sensor technology and signal processing protocols. In this chapter, theoretical aspects related to calorimetry will be outlined and different principles will be discussed, mainly from the perspective of heat exchange. We then focus on heat flux calorimeters based on thermopile temperature sensors, which corresponds to the concept of the isothermal nanocalorimeter for fast antimicrobial susceptibility testing (INCfAST) presented in this thesis.

2.1 Heat transfer phenomena

Heat transfer is one of the most studied transport phenomenon, which comprises three parts: heat conduction, convection and radiation.[68] Understanding the heat transfer theory, described by well-established partial differential equations (PDE), is a prerequisite for developing the calorimetric platform.

The energy transport equation is obtained from the conservation of mass and energy. To do so, we consider a system with a volume V [m³] and a system boundary defined by a surface A [m²]. The variation of energy within V is equal to the heat flux crossing the surface A . The global conservation of energy E [J · m⁻²] in the system can be described as

$$\frac{dE}{dt} = q_{D_{in}} - q_{D_{out}} + q_{C_{in}} - q_{C_{out}} + q_R - W \quad (2.1)$$

where $q_{D_{in}}$ and $q_{D_{out}}$ represent the inward and outward heat flux by conduction (diffusion). Correspondingly, $q_{C_{in}}$ and $q_{C_{out}}$ represent the heat flux by convection. q_R represents the heat exchange by radiation. The last term corresponds to the work W carried out by the system.

The transfer of kinetic energy between atoms or molecules leads to heat conduction. The collisions between molecules in gases, lattice vibrations in solids and an intermediate behavior in liquids

Chapter 2. Theory of calorimetry

result in different heat conductivities depending on the media. In a homogeneous environment, heat conduction is described mathematically by the Fourier law

$$q_D = -\lambda \nabla T \quad (2.2)$$

where the heat flux q_D in $[\text{J} \cdot \text{s}^{-1} \cdot \text{m}^{-2}]$ is proportional to the temperature gradient ∇T in $[\text{K}]$. λ $[\text{W} \cdot \text{K}^{-1} \cdot \text{m}^{-2}]$ is the thermal conductivity of the system, which is a positive value. The minus "–" sign in the equation accounts for heat transport from high to low temperature (the second law of thermodynamics).

Heat may also be transported by convection if the system consists of liquid or gas phase enduring a flow field \mathbf{u} . Flow can be generated naturally by buoyancy effects or by external forces. Heat flux by convection is expressed by the following equation

$$\mathbf{q}_C = \mathbf{u} \rho c_p T \quad (2.3)$$

where ρ $[\text{kg} \cdot \text{m}^{-3}]$ is the mass density and c_p $[\text{J} \cdot \text{kg}^{-1} \cdot \text{K}^{-1}]$ is the specific heat capacity. $\rho \mathbf{u}$ is the mass flow density that carries the heat quantity $c_p T$ at a temperature T $[\text{K}]$.

The Stefan-Boltzmann law describes the total energy radiated per unit surface area per unit time of a black body. If the hot object is radiating energy to its cooler surroundings, the net radiation loss rate takes the form

$$q_R = \varepsilon \sigma (T_s^4 - T_e^4) \quad (2.4)$$

where ε is the emissivity of the object's surface, σ is the Stefan-Boltzmann constant ($5.669 \times 10^{-8} \text{ W} \cdot \text{m}^{-2} \cdot \text{K}^{-4}$), T_s $[\text{K}]$ is the object's temperature, and T_e $[\text{K}]$ is the temperature of the surrounding environment.

Partial differential equations for heat transport

If only the heat conduction (diffusion) q_D and convection q_C are considered, energy conservation in a system with volume V can be written as

$$\int_V \frac{\partial E}{\partial t} dV = \int_A \lambda \nabla T \cdot \mathbf{n} dA - \int_A \rho c_p T \mathbf{u} \cdot \mathbf{n} dA \quad (2.5)$$

where \mathbf{n} is the vector normal to the surface element dA . For a constant volume, the energy variation dE is related to the temperature variation $dE = \rho c_p dT$ and the energy conservation can be expressed as

$$\int_V \frac{\partial T}{\partial t} dV = \frac{\lambda}{\rho c_p} \int_A \nabla T \cdot \mathbf{n} dA - \int_A T \mathbf{u} \cdot \mathbf{n} dA \quad (2.6)$$

The divergence theorem allows us to rewrite the previous equation

$$\int_V \left[\frac{\partial T}{\partial t} - \frac{\lambda}{\rho c_p} \nabla^2 T + \nabla \cdot (T \mathbf{u}) \right] dV = 0 \quad (2.7)$$

If we assume an incompressible system ($\rho = \text{const}$, $\nabla \mathbf{u} = 0$), we obtain the following partial differential equation

$$\frac{\partial T}{\partial t} + \mathbf{u} \cdot \nabla T = \kappa \nabla^2 T \quad (2.8)$$

where $\kappa = \lambda / \rho c_p$ is the thermal diffusivity in $[\text{m}^2 \cdot \text{s}^{-1}]$. Without flow ($\mathbf{u} = 0$), Eqn. 2.8 can be simplified to the classical heat equation

$$\partial_t T = \kappa \nabla^2 T \quad (2.9)$$

where ∇^2 signifies the Laplace operator.

2.2 The classical calorimeter

Thermal analysis is the study of a specific sample property as a function of its temperature upon heating or cooling in a controlled manner. Calorimeters, some of the most important tools in thermal analysis, are used to characterize the heat information of a system for different conditions. Heat information such as temperature, heat and heat power is measured in an absolute or relative way.[69]

2.2.1 Simplified calorimeter model

A simplified calorimeter model is illustrated in Figure 2.1. The system comprises the sample and its container. We assume a good thermal contact inside the system with a temperature T_{Sys} . The system is thermally connected to the surrounding environment at a temperature T_{Env} through a thermal resistance R_{SystoEnv} . R_{SystoEnv} includes the thermal resistance to the thermostat R_{SystoTS} and the resistance to the measurement unit R_{SystoMU} . The heat quantity transferred through each thermal pathway depends on the relative value of these thermal resistances. In addition, as the measuring unit is not fully thermally isolated, heat passing from the sample to the measurement unit will eventually go to the thermostat or the environment as well. This heat transfer path also has a resistance R_{MUtoTS} . Most of the calorimeters, even if their design is based on different principles, can be described by this simplified model. Historically, calorimeters are classified based on different criteria.[70]

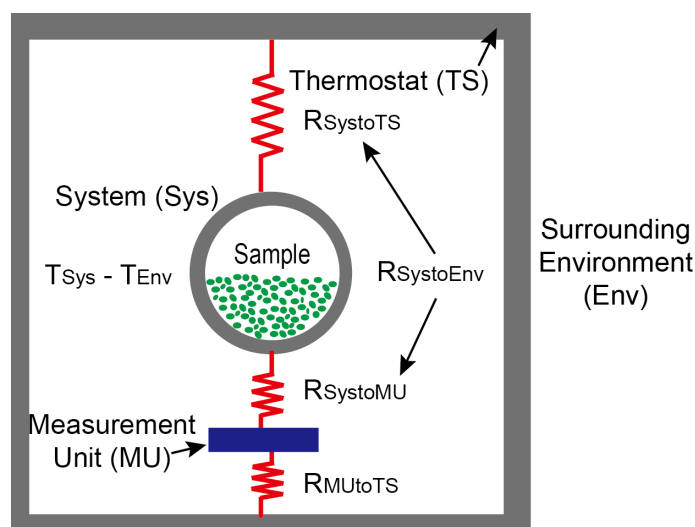


Figure 2.1 – Schematic representation of the thermal circuit of a classical calorimeter composed of a sample in a container (system), a measuring unit, the thermostat and the surrounding environment. Thermal resistances indicate pathways for heat transport.

2.2.2 Different heat exchange principles

Adiabatic and diathermal calorimeters

Based on whether a heat exchange exists between the system and the thermostat, two broad families of calorimeters can be distinguished: adiabatic and diathermal. For the adiabatic type, no heat exchange occurs between the system and thermostat. In this way, heat stored in the system is maximized and measured *in situ* by a temperature change. Heat production and absorption influence the temperature being measured. On the contrary, in diathermal calorimeters heat exchange between the system and surrounding thermostat is enhanced. The heat exchange will influence the temperature of the surrounding environment, which can be controlled by the experimental set-up.

Passive and active modes of operation

Adiabatic or diathermal can be designed based on passive control using appropriate thermal resistances R_{th} or with the help of active electronic control.

For adiabatic calorimeters, heat exchange between the system and the surrounding thermostat can be minimized by two routes: (i) in a passive manner, by increasing the thermal resistance $R_{SystoTS}$ with appropriate thermal insulation, or (ii) actively by decreasing the temperature difference between the system and the surrounding $T_{Sys} - T_{TS}$ (considering the thermostat temperature is the same as the surrounding environment). Infinite thermal resistances $R_{SystoTS}$ and R_{MUtoTS} do not exist in reality, so heat leak always occurs between the system and surroundings. Therefore, passive adiabatic calorimeters are often called quasi-adiabatic or isoperibol calorimeters historically.

"Water calorimeters", for which the samples are in good contact with a water bath that collects the heat produced, are a type of passive adiabatic calorimeters. The Berthelot calorimeter (Figure 2.2b) is a typical water calorimeter. Passive adiabatic designs may also be used in sophisticated modern calorimeters. Instead of maximizing thermal resistance and insulation, the active adiabatic calorimeter approach may be more convenient by implementing servo-controlling of the thermostat temperature T_{TS} to follow the sample T_{Sys} . By combining the advantage of thermal insulation and temperature control, heat phenomena can usually be followed over much longer time than with passive calorimeter.

Passive diathermal calorimeters monitor the heat transferred from the sample to the thermostat by taking advantage of good thermal conduction. As shown in Figure 2.2c, the Tian-Calvet calorimeter is a typical passive diathermal set-up. Heat is not stored in the sample or system but will pass through a thermopile to the thermostat.[71] The heat can also be measured by a quartz microbalance, phase transitions or peripheral liquid flow. The Lavoisier ice calorimeter (Figure 2.2a) was based on the observation of a phase transition in the surrounding thermostat. Passive diathermal calorimeters are also called heat flowmeters and thermal conductive calorimeters. The calorimeter developed in this thesis also belongs to this category. The working principle of active diathermal calorimeters is opposite to the active adiabatic calorimeter, as here the system temperature is servo-controlled in order to follow the thermostat temperature. In this way, good heat exchange is simulated. Heat compensation can be achieved by Joule effect if the phenomenon is endothermic or by Peltier effect if it is exothermic.

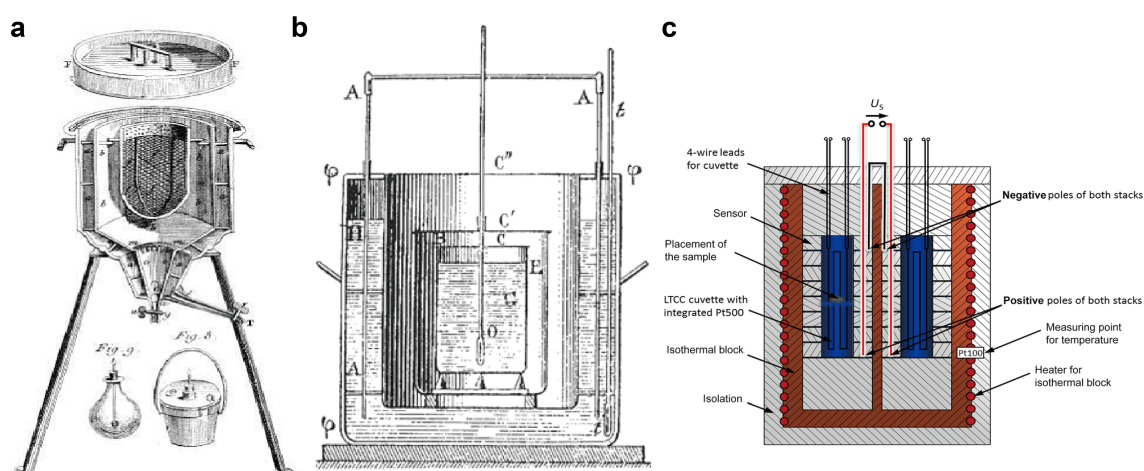


Figure 2.2 – Examples of historical calorimeters. (a) Ice calorimeter developed by Lavoisier.[64] (b) Typical passive adiabatic calorimeter developed by Berthelot.[70] (c) Tian-calvet calorimeter as an example for a passive diathermal calorimeter.[71] Adapted from [70–72].

2.2.3 Possible descriptions of calorimeters

The previous nomenclature classifies most calorimeters. Other nomenclatures have been proposed to illustrate different working principles. For example, Hemminger and Hohne in 1984 proposed

various types of classifications depending on criteria, including measurement principles, mode of operation, and construction principle. [73, 74]

Measurement principles

1. Heat compensation: Calorimetry with compensation of the thermal effects: (i) by phase transition, for example the ice calorimeter, (ii) by electric effects (Joule effect, Peltier or Seebeck effects), or by chemical heat of reaction.
2. Heat-accumulating principle (temperature difference): The heat capacity and heat leaks must be considered to design a reliable calorimeter. This includes most of the adiabatic and quasi-adiabatic calorimeters.
3. Heat conduction: Such calorimeters usually make use of a thermopile as a sensor of heat flow.

Operation mode

The operation mode can be static (isothermal, isoperibol, adiabatic) or dynamic (scanning of surroundings, isoperibol scanning, adiabatic scanning).

Construction principle

Single measuring systems, twin systems or differential measuring systems may be used.

2.3 Heat flux calorimeter

Thermopile-based calorimeters represent a large part of modern systems based on heat conduction. Moreover, the development of MEMS-based sensors and new thermoelectric materials has become the driving force for innovative calorimeter design. In the present thesis, we used thermopile sensors to measure the metabolic heat production of bacteria.

2.3.1 The thermoelectric effect

Thermopile sensors are based on the thermoelectric effect, *i.e.* the direct conversion of temperature differences to electric voltage and vice versa via a thermocouple (a junction of two different metals). Two effects may be distinguished, known as Seebeck effect and Peltier effect, which will be discussed in the following. The nanocalorimeter developed in this thesis is based on the Seebeck effect.

The Seebeck effect describes that a temperature gradient across an isolated conducting material generates an electromotive effect (voltage). The effect was discovered by Thomas J. Seebeck in the 1900s. As shown in Figure 2.3a, the temperature difference ΔT between the hot junction T_{hot} and the cold junction T_{cold} of a thermocouple (TC) induces electric voltage difference U_{TC} . The two junctions are separated by a layer of medium with a given thermal resistance. U_{TC} is proportional to

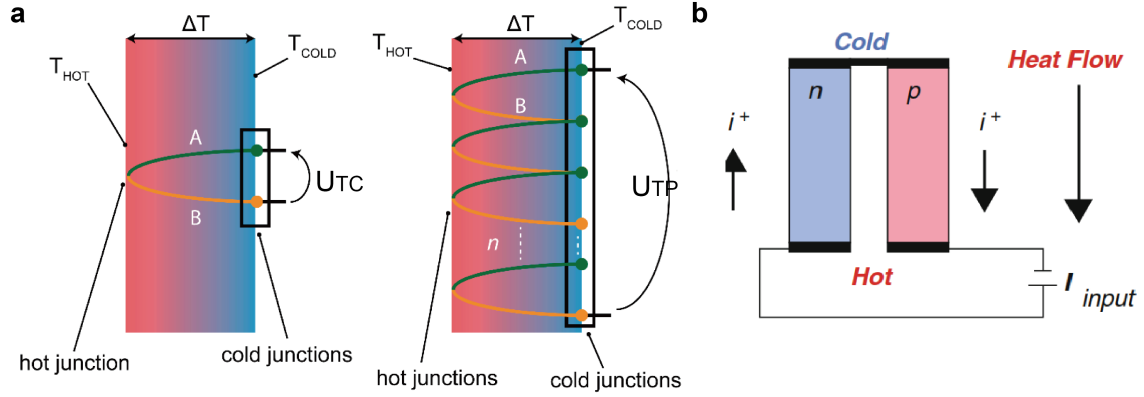


Figure 2.3 – Thermoelectric effect. (a) Seebeck effect. Thermocouple (left) and thermopile (right). (b) Peltier effect illustrated by a p-n junction.

the temperature difference and depends on the material properties of the thermocouple described by the Seebeck coefficient α .

$$U_{TC} = \alpha \cdot \Delta T \quad (2.10)$$

where $\Delta T = T_{hot} - T_{cold}$. α represents the thermal electromotive force for a temperature difference of 1 K. Material properties fundamentally influence the heat flux sensor performance. The output signal may be amplified by connecting N thermocouples in series to form a thermopile (TP), resulting in U_{TP}

$$U_{TP} = N \cdot \alpha \cdot \Delta T \quad (2.11)$$

The traditional copper-constantan thermocouple has a Seebeck coefficient of about $50 \mu V \cdot K^{-1}$. The thin-film sensor chip used in the present work is based on p-type silicon-aluminum thermocouples (Figure 2.4a), which has a considerably higher Seebeck coefficient ($\sim 300 \mu V \cdot K^{-1}$). Emerging semiconductor thermoelectric modules may have further higher Seebeck coefficients of more than $1500 \mu V \cdot K^{-1}$ like $Pb_{0.3}Ge_{0.39}Se_{0.58}$ (Figure 2.4b).^[75]

The Peltier effect is of the same nature as the Seebeck effect but describes the temperature difference generated at the junction of dissimilar conductors upon the passage of an electric current. It is the basis for thermoelectric coolers. As shown in Figure 2.3b, the consumption of electrical energy maintains the temperature difference between the cold and hot side of the device. Heat absorption or production dQ_P per time (Equation 2.12) depends on the direction of the current i [A] and a material property $C_{peltier}$ [V]. The Peltier coefficient $C_{peltier}$ represents how much heat is carried per unit charge.

$$dQ_P = C_{peltier} i dt \quad (2.12)$$

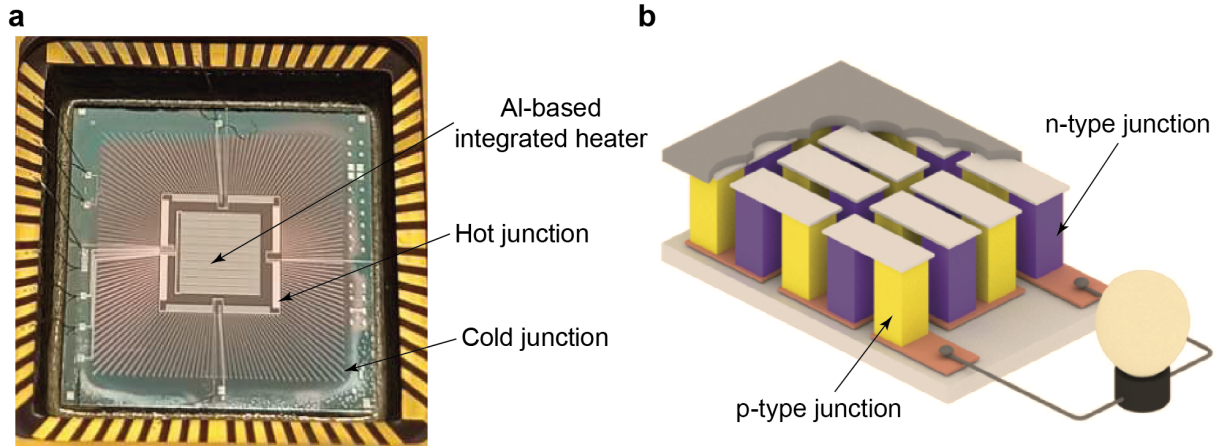


Figure 2.4 – Thin film-based *vs* p-n type thermopile sensor. (a) Themopile made of a series of p-type silicon-aluminum thermocouples on a thin SiO₂ membrane. (b) Schematic of semiconductor thermoelectric modules.

2.3.2 Theory of heat flux sensors

2.3.2.1 Sensor sensitivity

Heat flux q_s [$\text{W} \cdot \text{m}^{-2}$] (or heat flow density) is the quantity of heat transported through an isothermal surface per unit time and unit area. Modern sensors measure a heat flux from $10^{-3} \text{ W} \cdot \text{m}^{-2}$ to the order of $10^7 \text{ W} \cdot \text{m}^{-2}$. The operating principle of most heat flux sensors may be described by a theoretical model, which was elaborated by Schmidt in the 1900s. An "additional wall" with a known thermal conductivity λ is located in the path of the heat flux q to be measured. The reciprocal value of λ is the thermal resistance R_{th} . The temperature difference ΔT between the wall sides is proportional to the amount of the total heat flux q_A [W] (also called heat flow) through a surface A . At a known thermal resistance of the sensor, ΔT is created by the heat flow q_A from the hot junction to the cold junction.[75]

$$\Delta T = R_{th} \cdot q_A \quad (2.13)$$

The heat flux q_s [$\text{W} \cdot \text{m}^{-2}$] through a surface A perpendicular to its direction is given by

$$q_s = q_A / A \quad (2.14)$$

The sensitivity S_s [$\text{V} \cdot \text{W}^{-1} \cdot \text{m}^2$] of a heat flux sensor is defined by the ratio of the electrical sensor signal U [V] to the heat flux q_s ,

$$S_s = \frac{U}{q_s} \quad (2.15)$$

Correspondingly, the integral sensitivity S_A [$V \cdot W^{-1}$] is the ratio of U to the heat flow q_A through the surface A ,

$$S_A = \frac{U}{q_A} = \frac{U}{q_s \cdot A} = \frac{S_s}{A} \quad (2.16)$$

Combing with the previous equations, the voltage signal U can be expressed in the following way

$$U = N \cdot \alpha \cdot R_{th} \cdot q_A \quad (2.17)$$

Thus the power sensitivity S_A is expressed as:

$$S_A = \frac{U}{q_A} = N \cdot \alpha \cdot R_{th} \quad (2.18)$$

2.3.2.2 Tian's equation

For a model system including the reaction vessel, sample, thermopile and heat sink, the net heat flow may be expressed by two parts, considering the configuration of a calorimeter shown in Figure 2.1. Here the measurement unit is a thermopile sensor. We define q_{sample} as the heat flow generated by the sample in the system (Sys). In the heat flow balance, q_{sample} is set equal to the sum of two parts: (1) the heat flow $q_{SystoMU}$ from the hot junction to the cold junction through the thermopile (*i.e.* the measuring unit MU) with a corresponding thermal resistance $R_{SystoMU}$, and (2) the heat flow q_{loss} dissipated to the thermostat (TS) through $R_{SystoTS}$ (here we use "loss" assuming the sample has a higher temperature).

$$q_{sample} = q_{SystoMU} + q_{loss} \quad (2.19)$$

According to Eqn. 2.13, $q_{SystoMU}$ and q_{loss} can be expressed as

$$q_{SystoMU} = \frac{\Delta T_{Sys}}{R_{SystoMU}} \quad (2.20)$$

$$q_{loss} = \frac{\Delta T_{Sys}}{R_{SystoTS}} \quad (2.21)$$

For an isothermal platform, we assume that eventually the temperature at the cold junction is equal to the temperature of the heat sink, thus $\Delta T_{Sys} = \Delta T_{hot-cold}$. Another approach considers a heat capacity C_{Sys} for the system including the sample container, sample and half of the thermopile wall. The total heat loss Q_{loss} [J] can be expressed by the temperature change of the measuring unit ΔT_{Sys} .

$$Q_{loss} = C_{Sys} \Delta T_{Sys} \quad (2.22)$$

Chapter 2. Theory of calorimetry

Thus q_{loss} is a function of the temperature change rate.

$$q_{loss} = C_{Sys} \frac{d\Delta T_{Sys}}{dt} \quad (2.23)$$

with Eqn. 2.13 and 2.17, we find Eqn. $\Delta T_{Sys} = U/(N \cdot \alpha)$ which we substitute in Eqn. 2.20 and Eqn. 2.23. We obtain

$$q_{SystoMU} = \frac{U}{N \cdot \alpha \cdot R_{SystoMU}} \quad (2.24)$$

$$q_{loss} = \frac{C_{Sys}}{N \cdot \alpha} \frac{dU}{dt} \quad (2.25)$$

According to Eqn. 2.19 and by using Eqn. 2.24 and Eqn. 2.25, we can establish a relation between the measured voltage signal U and the heat flow q_{sample} . This relation is called Tian's equation. [76]

$$q_{sample} = \epsilon \left(U + \tau_{sensing} \frac{dU}{dt} \right) \quad (2.26)$$

where $\tau_{sensing}$ is the sensing time constant defined by $\tau_{sensing} = R_{SystoMU} C_{sys}$. ϵ [W·V⁻¹] corresponds to the inverse integral sensitivity S_A and can be written as

$$\epsilon = 1/(N \cdot \alpha \cdot R_{SystoMU}) = 1/S_A \quad (2.27)$$

In the ideal case, $q_{sample} \simeq q_{SystoMU}$ where all the heat flow generated by the system is transported through the thermopile, the second term in Eqn. 2.26 can be neglected and the equation simplifies to

$$q_{sample} = U/S_A \quad (2.28)$$

2.3.2.3 Noise analysis

The first term in the Tian's equation corresponds to the electrical heat compensation. The second term accounts for the transient state for an instant sample temperature change. Using a thermopile as heat flux sensor, the measurement can be classified as a fast or a slow process. Fast reaction occurs on a time scale smaller than the sensing time constant and slow processes have a longer time scale. Mixing of two liquids is typically a fast reaction, whereas biological processes like bacterial growth usually are slow.

In the case of fast temperature variations, the nanocalorimeter works almost in adiabatic mode, as the heat flow through the membrane may be neglected. In such conditions, the signal-to-noise

ratio (SNR) may be calculated in the following manner

$$SNR_{fast} = \frac{U_{TP}}{U_{noise}} = \frac{S_T \Delta T_{ad}}{U_{noise}} = \frac{S_T}{U_{noise}} \cdot \frac{Q}{C} = \frac{S_T}{U_{noise}} \frac{cV\Delta H}{\rho c_p V + C_a} \approx \frac{S_T}{U_{noise}} \frac{c\Delta H}{\rho c_p} \quad (2.29)$$

for $C_a \ll \rho c_p V$

where U_{TP} [V] is the measured signal, U_{noise} [V] is the voltage noise, S_T [V·K⁻¹] is the temperature sensitivity of the nanocalorimeter, ΔT_{ad} [K] is the adiabatic temperature change, Q [J] is the heat generated by the sample, C [J·K⁻¹] is the total heat capacity, c [mol·m⁻³] is the reactant concentration, V [m³] is the sample volume, ΔH [J·mol⁻¹] is the reaction enthalpy, ρ [kg·m⁻³] is the sample density, c_p [J·kg⁻¹·K⁻¹] is the specific heat capacity of the sample, and C_a [J·K⁻¹] is the heat capacity of the nanocalorimeter excluding the sample. As can be seen on the right-hand side of Eqn. 2.29, for a heat capacity C_a of the nanocalorimeter being very small ($C_a < 1$ mJ/K), the volume of the sample drops out and does not directly affect SNR, which mainly depends on the temperature sensitivity S_T of the device. For this reason, this type of nanocalorimeter is suitable for very small sample volumes, down to the nL volume range and below.

The calculation of the SNR for slow processes, instead, may be reported as follows:

$$SNR = \frac{U_{TP}}{U_{noise}} = \frac{S_A q_{sample}}{U_{noise}} = \frac{S_A}{U_{noise}} \cdot rV\Delta H \quad (2.30)$$

where S_A [V·W⁻¹] is the heat power sensitivity, q_{sample} [J·s⁻¹] is the heat power generated by the sample, and r [mol·m⁻³·s⁻¹] is the reaction rate. In this case, the SNR is proportional to the sample volume, making extreme reduction of sample volumes less advantageous. In the specific case of the nanocalorimeter developed in the present work, our main interest focuses on the investigation of slow biological processes.

In fact, the sensing time constant $\tau_{sensing}$ of a previous version of the current nanocalorimeter was about 10 s [77], which is much smaller than the reaction time of typical metabolic processes, which are in the order of minutes. In this case, it is possible to neglect the transient term and to write the simplified version of Tian's equation (Eqn. 2.28). Specifically, the documented temperature sensitivity S_A for the commercial nanocalorimeter (XEN-NCM 9924 chip, Xensor Integration) used in this work is 50 mV/K as shown in Appendix A.4.[78] Additionally, sample volumes of around 150 μ L have been used in order to obtain good SNR.

Thermal noise (Johnson–Nyquist noise)

The SNR and thus U_{noise} are very critical for the performance of a calorimeter. An important component of the total noise is the thermal noise or Johnson-Nyquist noise, generated by the thermal agitation of electrons inside an electronic conductor. Similar to photodetectors, the usual parameters also apply to the heat flux sensors: electrical thermal noise U_{ET}^2 , sensitivity threshold F_{th} , NEP (noise-equivalent power), and detectivity D^* . Electrical thermal noise is expressed in the

following way:

$$U_{ET}^2 = 4k_B \cdot T \cdot ACR \cdot \Delta f \quad (2.31)$$

where k_B is the Boltzmann constant, T is the sensor average temperature, ACR is the sensor resistance, and Δf is the frequency band in which the measurements are done.

The sensitivity threshold F_{th} [$\text{W} \cdot \text{cm}^{-1} \cdot \text{Hz}^{1/2}$] is the value of the heat flux causing a sensor output voltage equal to the root mean square (RMS) noise voltage. Sensitivity threshold with reference to the unit pass band and unit area of the sensor is expressed as

$$F_{th} = \frac{\sqrt{U_{ET}^2}}{S_A \sqrt{A \Delta f}} \quad (2.32)$$

where S_A is the power sensitivity [V/W] and A is the sensor working area in [cm^2].

NEP [$\text{W} \cdot \text{Hz}^{-1/2}$] is the sensor parameter characterizing the minimum detectable radiation power in a 1 Hz bandwidth causing a sensor signal equal to RMS noise.

$$NEP = \frac{\sqrt{U_{ET}^2}}{S_A} \quad (2.33)$$

The reciprocal value of the sensitivity threshold F_{th} is the detectivity D^* [$\text{cm} \cdot \text{Hz}^{1/2} \cdot \text{W}^{-1}$].

$$D^* = 1/F_{th} = \frac{\sqrt{A}}{NEP} = \frac{S_A \sqrt{A}}{\sqrt{4k_B T \cdot ACR}} \quad (2.34)$$

Electronic thermal noise can be minimized by averaging a series of continuous data points considering the time scale of our experiment. In our study, the baseline drift caused by the temperature variations is more critical for the platform's performance.

Thermostat temperature fluctuation

Apart from the Johnson–Nyquist noise, the thermostat temperature fluctuation also contributes to the noise performance of the calorimetric system. The influence on the signal is dependent on the heat capacity C of the sample and the microincubator as well as the thermal time constant. Assuming white temperature noise of bandwidth ω_B , the relationship between voltage noise U_n and temperature noise T_n can be expressed as follows [79]

$$U_n \simeq \frac{1}{\sqrt{3}} S_A C \omega_B T_n \quad (2.35)$$

It is realistic to aim at a heat power resolution level near 10 – 15 nW by decreasing the temperature noise down to 10 μK . [80] Noise related to temperature fluctuations can be minimized by

embedding the measurement system in a highly stable thermostat and adequate thermal insulation. Thermostat temperature fluctuation is the dominant source of noise if we don't consider baseline drift for a long-term experiment. Further improvement of the temperature control system can reduce this noise.

Baseline drift

For a long term measurement, the baseline drift due to the environmental influence of the voltage output of the nanocalorimeter can be considered as another main source to affect the limit of detection. Although the thermostat is maintained at a constant temperature, the measuring units still possess a certain temperature distribution. Ideally, this temperature distribution is constant, thus the resulting heat transfer through the thermopile will generate a constant background signal. In the experiment, the temperature of the thermostat is controlled by probing the temperature near the thermopile unit. Although the temperature is maintained at a constant level by a closed PID controller, this does not necessarily imply that the temperature distribution is constant. In fact, the thermostat's heater power will change, if the environmental temperature is varying. This leads to a change in the background heat transfer and temperature distribution, which causes the baseline drift. For a short-term experiment, the baseline drift may not be obvious. However, for a long-term experiment (several hours), this baseline drift must be considered and reduced to obtain optimal results. Additional data analysis can be found in the Appendix A.1. The baseline drift caused by the environmental influence in the current context is the main source of noise when considering the SNR to determine the LOD.

References

64. Lavoisier, A.-L. & marquis de Laplace, P. S. in *Histoire de l'Académie royale des sciences* 355 (1780) (cit. on pp. 23, 27).
65. He, R., Schierning, G. & Nielsch, K. Thermoelectric Devices: A Review of Devices, Architectures, and Contact Optimization. *Advanced Materials Technologies* **3**, 1700256 (Apr. 2018) (cit. on pp. 23, 138).
66. Wang, S., Sha, X., Yu, S. & Zhao, Y. Nanocalorimeters for Biomolecular Analysis and Cell Metabolism Monitoring. *Biomicrofluidics* **14**, 011503 (Jan. 1, 2020) (cit. on p. 23).
67. Wadsö, L. & Gómez Galindo, F. Isothermal Calorimetry for Biological Applications in Food Science and Technology. *Food Control* **20**, 956–961 (Oct. 1, 2009) (cit. on pp. 23, 48).
68. Fermigier, M. *Lecture Notes on "Phénomènes de Transports"* 2014 (cit. on p. 23).
69. Zielenkiewicz, W. & Margas, E. *Theory of Calorimetry* doi:[10.1007/0-306-48418-8](https://doi.org/10.1007/0-306-48418-8) (Springer Netherlands, 2002) (cit. on p. 25).
70. Rouquerol, J., Wadsö, I., Lever, T. & Haines, P. in *Handbook of Thermal Analysis and Calorimetry. Vol. 5: Recent Advances, Techniques and Applications* (eds Brown, M. E. & Gallagher, P. K.) 1st ed, 13–54 (Elsevier, Amsterdam, 2008) (cit. on pp. 25, 27).
71. Schubert, F., Gollner, M., Kita, J., Linseis, F. & Moos, R. Optimization of a Sensor for a Tian–Calvet Calorimeter with LTCC-Based Sensor Discs. *Journal of Sensors and Sensor Systems* **5**, 381–388 (Nov. 8, 2016) (cit. on p. 27).
72. 2016, A. S. J. *Laplace's Calorimeter* Chemistry World. <https://www.chemistryworld.com/opinion/laplaces-calorimeter/1010082.article> (2020) (cit. on p. 27).
73. *Calorimetry: Fundamentals, Instrumentation and Applications* | Wiley Wiley.com. <https://www.wiley.com/en-au/Calorimetry%3A+Fundamentals%2C+Instrumentation+and+Applications-p-9783527327614> (2020) (cit. on p. 28).
74. Wadsö, I. Trends in Isothermal Microcalorimetry. *Chemical Society Reviews* **26**, 79–86 (1997) (cit. on p. 28).
75. Gromov, G. in *Advanced Micro and Nanosystems* (eds Dávila Pineda, D. & Rezania, A.) 1st ed., 233–282 (Wiley, Sept. 25, 2017). doi:[10.1002/9783527698110.ch11](https://doi.org/10.1002/9783527698110.ch11) (cit. on pp. 29, 30, 138).
76. Jesús, C., Socorro, F. & Rodríguez de Rivera, M. New Approach to Tian's Equation Applied to Heat Conduction and Liquid Injection Calorimeters. *Journal of Thermal Analysis and Calorimetry* **110**, 1523–1532 (Dec. 1, 2012) (cit. on p. 32).
77. Padovani, R., Lehnert, T., Trouillon, R. & Gijs, M. A. M. Nanocalorimetric Platform for Accurate Thermochemical Studies in Microliter Volumes. *RSC Adv.* **5**, 97133–97142 (2015) (cit. on p. 33).
78. *Datasheet of "Liquid Nanocalorimeters XEN-NCM9924 / -LCM2506 / -LCMquad"* 2016 (cit. on pp. 33, 148, 149).

79. Lerchner, J., Wolf, A., Wolf, G. & Fernandez, I. Chip Calorimeters for the Investigation of Liquid Phase Reactions: Design Rules. *Thermochimica Acta. Honour Issue on the Retirement of Prof. W. Hemminger* **446**, 168–175 (July 1, 2006) (cit. on p. 34).
80. Lerchner, J., Maskow, T. & Wolf, G. Chip Calorimetry and Its Use for Biochemical and Cell Biological Investigations. *Chemical Engineering and Processing: Process Intensification* **47**, 991–999 (June 2008) (cit. on p. 34).

3 State of the art of modern chip-based calorimeters

Advances in MEMS technology and material science promote the development of modern calorimeters. In this chapter, representative examples for modern chip-based calorimetry approaches will be presented. Chip calorimeters based on different sensing principles, including thermopiles, cantilevers and thermistors, will be discussed. Finally, two examples of commercially available systems will be shown.

3.1 Thermopile-based calorimeter

Thermopile-based calorimeters are an important category in modern calorimetry. Historically, a distinction between microcalorimeters and nanocalorimeters was made. In principle, these calorimeters measure heat power in the μW range or nW range, respectively. Nowadays, these categories may be somewhat obsolete, as some of the microcalorimeters are able to obtain heat signal limit of detection (LOD) in the hundreds of nW range, when the electrical controlling components are updated. However, the design principles of some older calorimeters may still be used for modern calorimeters. Today, nanocalorimeters usually correspond to a miniaturized MEMS-based format, thus they are often referred as chip calorimeters. Table 3.1 summarizes the performance of the thermopile-based calorimeters discussed in the following.

Open chamber devices

Johannessen *et al.* developed a thermopile sensor on an 800-nm thick silicon nitride membrane.^[81] As shown in Figure 3.1a, the thermopile is made of 10 gold-nickel thermocouples, which are radially positioned with respect to an open polyimide sample microchamber on the top of the membrane. The resulting temperature sensitivity is $220 \mu\text{V/K}$ and the limit of detection is 15 nW. The microchamber has a diameter of $200 \mu\text{m}$ and a volume of 700 pL. The calibration is performed with an integrated nickel heater on the thin film. The authors investigated the heat production of brown adipocytes upon the treatment with noradrenaline (NE). NE is a hormone released by the cold- or diet-stimulated sympathetic nervous system, which induces thermogenesis in the adipocytes. The average metabolic heat production of NE-stimulated brown adipocytes is around

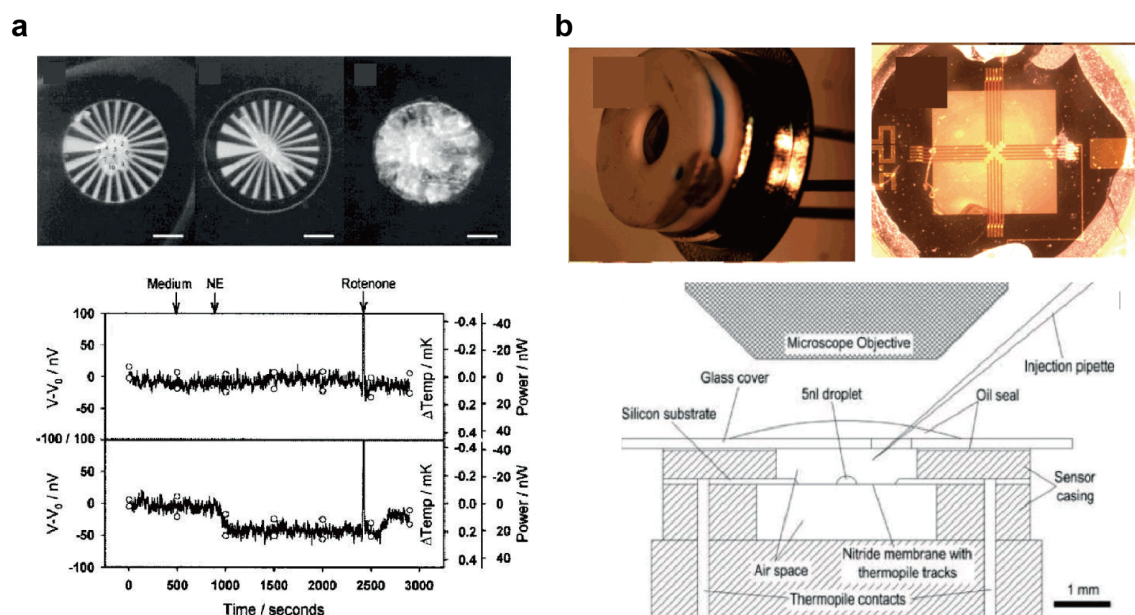


Figure 3.1 – Membrane-based calorimeters with open chambers. (a) Nanocalorimeter developed by Johannessen *et al.* Upper panel: Top view of the microchamber with samples placed on the thermopile sensors. Lower panel: Heat measurement of brown adipocytes upon the treatment with noradrenaline (NE) and rotenone. The two curves show the control and the drug test on cells, respectively.[81] (b) Nanocalorimeter developed by Xu *et al.*. Upper left: Photo of the commercial thermopile sensor (S25 silicon-based thermopile sensor from Dexter Research Center, Inc., Dexter, MI). Upper right: Photo of the thermopile inside the housing. Lower panel: Schematic representation showing the working principle of the device, where a 50 nL droplet was positioned on the suspended nitride membrane. The microchamber is sealed to prevent evaporation.[82]

1.6 nW per cell. Xu *et al.* developed an open chamber titration calorimeter based on a commercial suspended thin-film thermopile sensor that is placed on a 1.5 μm thick silicon membrane (Figure 3.1b).[82] A small number of cells suspended in a sample volume of ~ 50 nL is pipetted on the membrane. The power sensitivity of ~ 2.9 V/W is calibrated by a chemical reaction between H_2SO_4 and NaOH. Two thermal shields without temperature controlling system reduce the thermal noise and a LOD of 22 nW is reported. The chamber is closed with a cover glass and the samples are covered locally by oil to prevent evaporation of the small liquid volume. An updated version of this platform further reduced the sample volume to 2.5 nL, resulting in an improved power sensitivity of 60 V/W.[83]

Closed chamber chip calorimeters

Figure 3.2a and 3.2b are two examples of passive diathermal chip calorimeters with closed chambers. Lerchner *et al.* built a heat flow chip calorimeter for samples in the μL range (Figure 3.2a).[84] This calorimeter was used for a wide range of applications, from enzymatic assays to metabolic activity of biofilms.[88–91] The thin film thermopile is fabricated on a 1 μm silicon nitride membrane on

3.1. Thermopile-based calorimeter

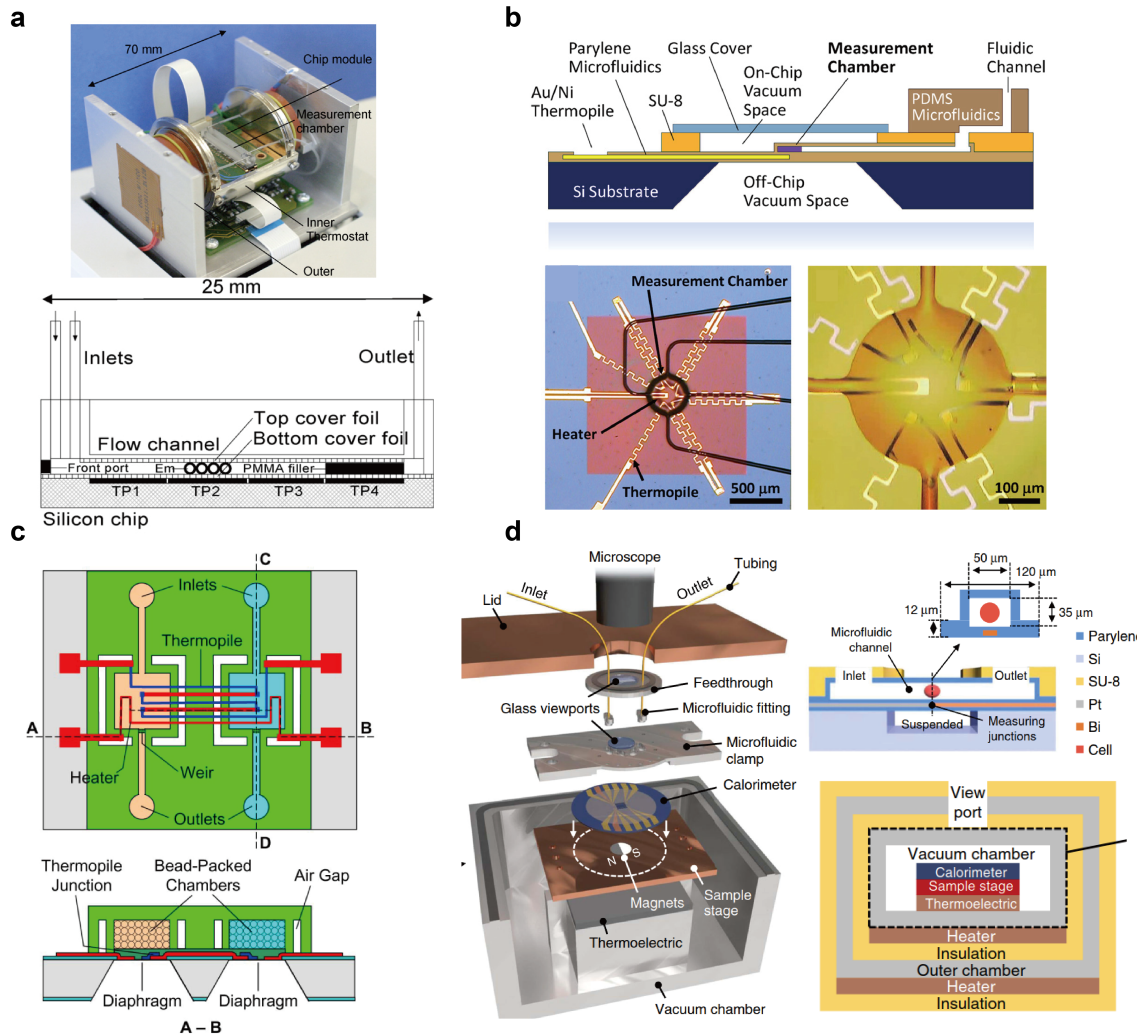


Figure 3.2 – Different types of microfluidic calorimeters. (a) Top: Photo of a flow-through chip calorimeter with two embedded thermostats developed by Lerchner *et al.* [84] Bottom: Cross-sectional view of the calorimeter with four thermopiles (TP) positioned along a PMMA channel, which is sealed with a thin PMMA film (50 μm) on the bottom. (b) Chip calorimeter with MEMS technology developed by Lee *et al.* [85] Top: Cross-sectional view showing the different components of the nanocalorimeter, including parylene and PDMS microfluidics. The vacuum space for thermal isolation is indicated. Bottom: Gold-nickel thermopile on the parylene membrane (red square) and enhanced view of the parylene microchamber with access channels. (c) Differential microfluidic calorimeter developed by Wang *et al.* featuring two parallel flow-through chambers. [86] (d) Calorimeter for heat measurements of single cells developed by Hong *et al.* [87] The calorimeter is equipped with several embedded thermostats and insulation layers. The cell which intakes iron oxide nanoparticles can be immobilized by magnetic focusing.

which 118 bismuth-antimony thermocouples and a nickel-chromium resistive heater are patterned. Four identical thermopile sensors are aligned along the fluidic channel enabling 4 consecutive measurements on samples that flow through the channel. A removable poly(methyl methacrylate) (PMMA) channel (20 mm in length, 1 mm in width and 0.5 to 1.2 mm in height) is positioned on the thermopile sensor and separated from it by a 50 μm PMMA foil. An additional thin paraffin film was used to enhance the thermal contact between the PMMA foil and the sensor. A high-precision thermostat enabled a temperature stability better than $\pm 100 \mu\text{K}$. A more recent version of this platform used a so-called segmented flow mode, where sequential processing of sample separated by immiscible inert segments was performed.[91, 92]

Lee *et al.* implemented a parylene-based microfluidic chip calorimeter combined with other materials for studying the heat production of nL-volume samples and reagents (Figure 3.2b).[85] The sample chamber is thermally isolated from the surrounding by an on-chip vacuum space to maximize the heat transfer through the sensor. A thermopile of 5 gold-nickel thermocouples is arranged around of the 3.5-nL sample chamber on top of the 2- μL parylene membrane. This chip calorimeter has a power sensitivity of 7.1 V/W, an estimated thermal conductance of 16 $\mu\text{W/K}$ and a power resolution of 4.2 nW. As a proof-of-concept the authors demonstrated its application for measuring the heat of urea hydrolysis reaction catalyzed by urease.

Differential measurements

Wang *et al.* developed a differential calorimeter integrated with a microfluidic chip (Figure 3.2c).[86, 93, 94] The thermopile sensor is made of 50 nickel-chromium thermocouples on a 5 μm thick SU-8 membrane. The temperature sensitivity is around 35 μK . Two parallel PDMS microfluidic channels are located above the hot and the cold junction, respectively, with the thermopile unit spanning the space in between. This configuration enabled differential measurements between the sample and the reference chamber. In a flow-through mode, the heat production of a glucose oxidation reaction was analyzed by prefilling the sample chamber with enzyme modified beads while blank beads were used in the reference chamber. The resulted power sensitivity is 1.2 V/W.

Multi-thermostat set-up and single-cell study

Most recently, Hong *et al.* developed a flow-through microfluidic-assisted calorimeter for single-cell measurements (Figure 3.2d).[87] The noise can be reduced dramatically thanks to the high temperature stability and 3 thermal insulation and thermostat layers. The temperature stability can be maintained within 80 μK for more than 10 h and the resolution was as low as 0.2 nW, enabling the single-cell metabolic heat measurements. Cells are introduced through the vacuum-isolated microfluidic channel and an embedded magnetic-based focusing system minimizes the cell movement. A Bi-Pt based thermopile was fabricated on a parylene layer underneath the microfluidic channel. The authors proposed that the heat production fits to the following power

relationship[95]

$$B = B_0 V^{3/4} \quad (3.1)$$

where B is the basal metabolic rate, B_0 is the normalization coefficient, and V is the body size.

Table 3.1 – Performance of thermopile-based chip calorimeters.

Name [Ref]	Resolution	Sample volume	Temperature stability	Power sensitivity
TAM-IV system (TA Instrument)[96]	200 nW	1-20 mL	$\pm 100 \mu\text{K}$	N/A
Johannessen <i>et al.</i> [97]	13 nW	700 pL	N/A	1.1 V/W
Lee <i>et al.</i> [85]	4.2 nW	3.5 nL	$\pm 500 \text{ mK}$ (1 h)	7.1 V/W
Lerchner <i>et al.</i> [89]	50 nW	10 μL	$\pm 100 \mu\text{K}$	N/A
Hong <i>et al.</i> [87]	0.2 nW	0.2 μL	$\pm 40 \mu\text{K}$	88 V/W
Liu <i>et al.</i> [98]	750 nW	150 μL	$\pm 250 \mu\text{K}$	1.14 V/W

3.2 Cantilever-based heat sensing

Cantilever beam calorimeters (CBCs) have been demonstrated to be a sensitive and reliable thermomechanical sensing tool for chemical and biological heat detection. A CBC usually works in deflection or resonant mode. In both modes, the extracted parameters can be correlated to the temperature change of the cantilever. The materials used for the fabrication are silicon or silicon nitride and thin metallic films such as gold or aluminum.[99] In the deflection mode, the temperature change will cause the bending of the cantilever metal/silicon bimorph structure due to their different thermal expansion coefficients. Barnes *et al.* were the first to adapt an AFM cantilever for femtojoule-level heat measurements.[100] As an example for biological applications, Sato *et al.* measured the heat production of brown fat cells (BFCs) with the cells placed on a fine movable needle (Figure 3.3a). When the needle approaches the cantilever, the produced heat causes the deflection of the cantilever tip. By recording the cantilever tip displacement, the small temperature difference caused by BFCs is measured. In comparison, for the resonant mode, a temperature change will shift the vibration frequency of the cantilever beam. Inomata *et al.* presented a cantilever calorimeter based on the resonant principle.[102, 103] A microfluidic channel is integrated with the set-up to assist sample delivery (Figure 3.3b). The sample is captured near the cantilever with a filter structure and the generated heat is conducted to the sensor in vacuum. The temperature change is measured by the change of vibration frequency.

Etayash *et al.* fabricated a bimaterial microcantilever (BMC) with an integrated microfluidic channel (Figure 3.3c).[104] 100 cells per 100 μL could be detected in this study. The authors developed 3 different modes of detection and both deflections and resonant frequencies were measured simultaneously. This BMC was used to monitor the bacterial response to antimicrobials. Alive and dead bacteria can be differentiated based on the resonance frequency shift, whereas different metabolic activities were monitored in the deflection mode. In addition to this, using

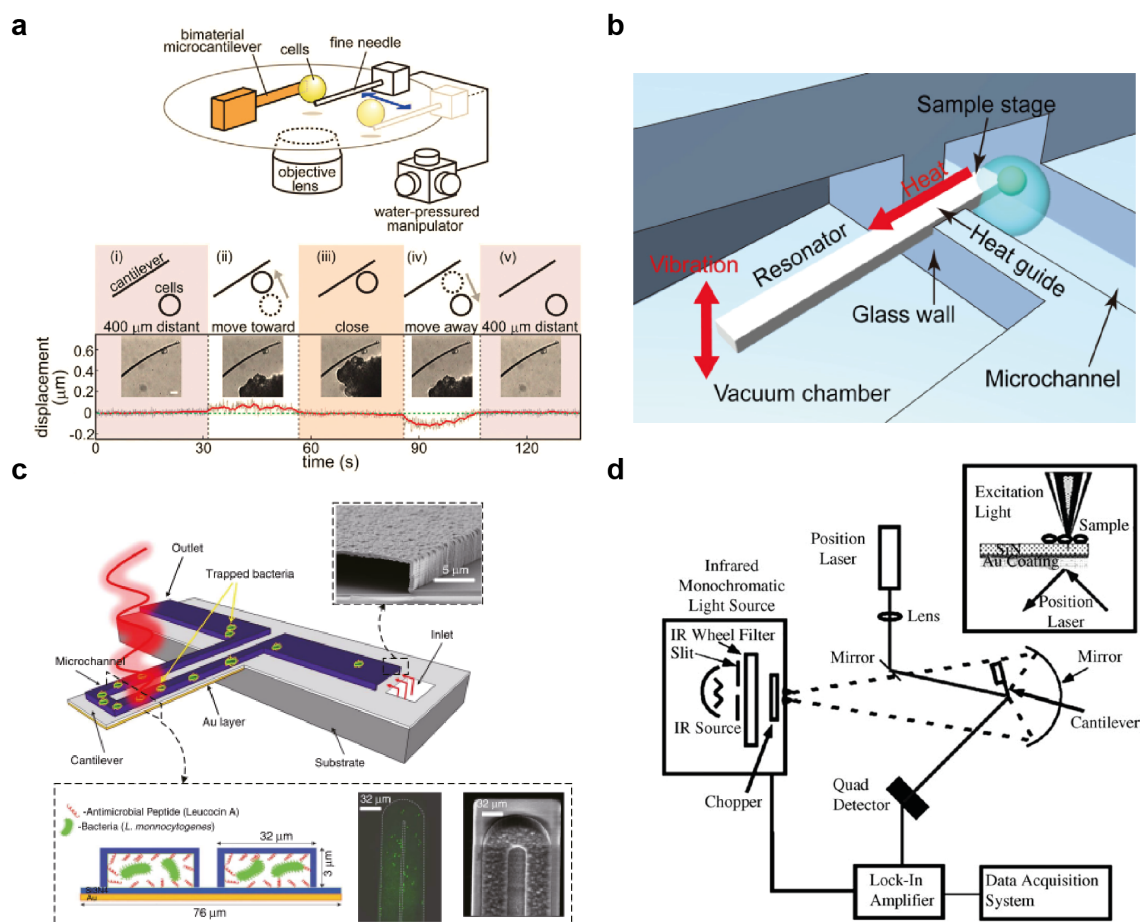


Figure 3.3 – Cantilever beam calorimeters (CBCs). (a) CBC based on deflection measurements.[104] Top: Schematic representation of the measurement principle with a sample positioned on a fine needle. Bottom: During approach and withdrawal of the cell sample, heat-induced deflections of the cantilever are recorded. (b) CBC based on frequency measurements.[105] The heat flow produced from the biological sample attached to one end of the cantilever causes a shift of the resonance frequency. (c) Cantilever for fast AST. The bacterial viability is correlated to the cantilever deflection and frequency shift. Bacterial identification can be performed by the selective absorption of IR light.[104] (d) Set-up of the cantilever-based photothermal spectroscopy. The cantilever deflection is strongly correlated to the reference spectroscopic absorption peaks.[105] Adapted from the corresponding papers.

microchannels with a chemically or physically functionalized internal surface, such as AMP (Leucocin A)-coated BMC, different strains could be detected. A third mode of detection is based on IR-induced nanobending, for microbial identification, due to the selective absorption of certain wavelengths. This principle was first introduced by the same group to identify *Bacillus anthracis* and *Bacillus cereus* with a set-up show in Figure 3.3d.[105]

Measuring metabolic heat induced stress is also the core principle of another cantilever-based device.[106] This technology enables rapid AST and is currently developed towards a commercial

product by the EPFL spin-off Resistell.[107]

3.3 Thermistor-based calorimeters

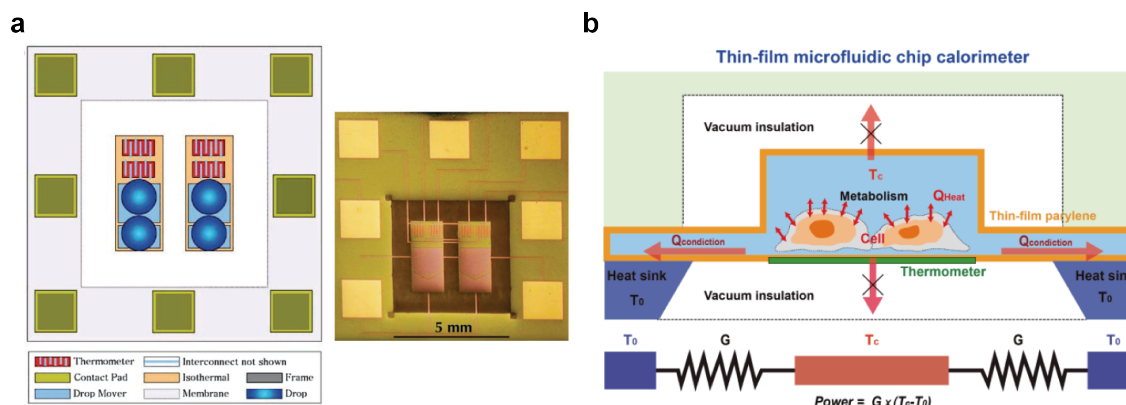


Figure 3.4 – Thermistor-based calorimeters. (a) Droplets with different compounds are mixed by electrostatic actuation on an enthalpy array.[108] The temperature change is detected by the thermistor unit beneath the droplet. (b) Thermistor-based calorimeter with microfluidic modules for cell metabolism measurements.[109] The parylene measurement chamber is isolated from the environment by vacuum and the V_2O_5 thermistor is placed below the chamber. Adapted from the corresponding papers.

Thermistors may be used to measure the absolute temperature in an adiabatic situation. Torres *et al.* developed a thermistor-based nanocalorimeter working in a differential mode (Figure 3.4a).[108] This so-called "enthalpy array" based on a suspended membrane is designed to study the molecular interactions. The two thermistor sensing units were connected through a Wheatstone bridge. The parylene layer provided the hydrophobicity for electrostatic sample handling to realize mixing and merging. A chemical reaction and a temperature change occurs when two droplets of ~ 250 nL are mixed on-chip. A temperature difference of $500 \mu\text{K}$ could be detected based on a reference reaction producing 250 ncal of heat in 500 nL volume. As a proof-of-concept, the heat production of protein-ligand binding interactions was measured. The device sensitivity was further increased in an updated version, where vanadium oxide was used as the thermistor material instead of silicon.[110, 111] In a similar way, Kim *et al.* developed a thermistor-based calorimeter to measure the heat production of tumor cells.[109, 112] As shown in Figure 3.4b, the set-up is based on a vacuum-insulated thin-film parylene chamber connected with multilayer PDMS microfluidic valves. The vanadium pentoxide (V_2O_5) thin-film thermistor allowed a temperature resolution of $\sim 15 \mu\text{K}$.

3.4 Commercial calorimeters

Here, we introduce two commercial calorimeters that are widely used in biological research. Commercial products usually are equipped with a high-performance thermostat providing long-term temperature stability. As shown in Figure 3.5a, the TAM IV system (TA Instrument) has a heat power precision of ± 100 nW and uses 1 mL sample ampoules. The device is inspired by the thermopile-based Tian-Clavet calorimeter (see Figure 2.2c in the previous chapter). Increased sensitivity can be achieved by subtraction of a reference signal from the sample signal. Another version, the TAM-48 system (TA Instrument) measures up to 48 samples in parallel. The calScreener (Symcel AB) entered the market (Figure 3.5b). Initially, the company focused on heat measurements of cells upon stimuli. Nowadays, they shifted to microbiological studies, especially to AST based on heat flow measurements.[113] The samples need to be pipetted into the vials, which are placed on top of the thermopile sensors array in the platform.

Besides these two products, two more systems, the C80 by Setaram (Caluire-et-Cuire, France)[114], and the μ RC by Thermal Hazard Technology (Bletchley, England)[115] are available on the market. The working principle of these machines is similar to the TAM IV.

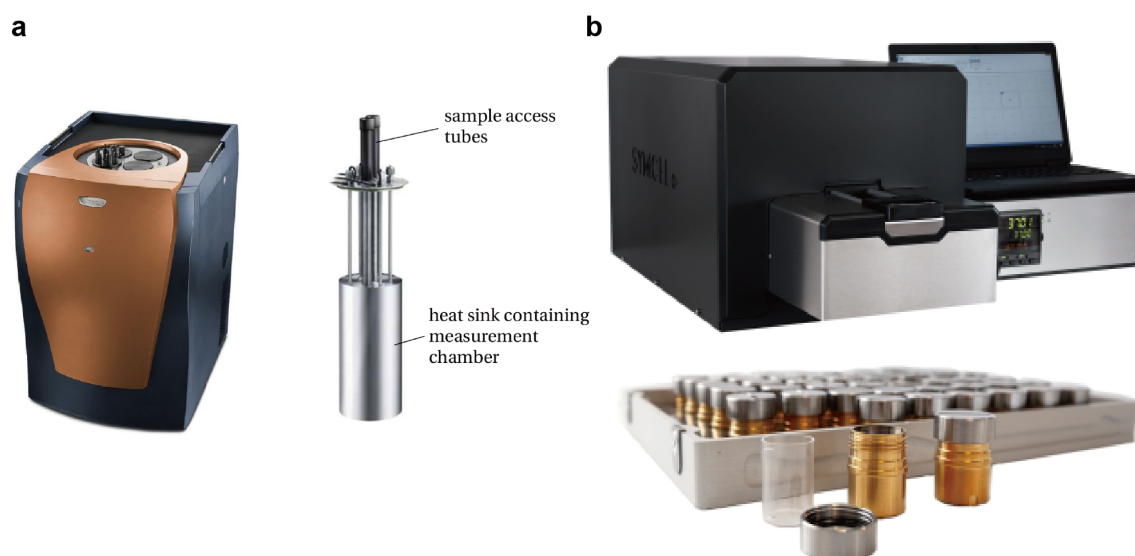


Figure 3.5 – Commercial calorimeters. (a) Photograph of TAM IV system (TA Instrument) and a single measuring unit with two access tubes for introducing the 1 mL sample ampoule and the reference ampoule (hidden on the backside), respectively.[96] (b) The calScreener system (Symcel) with an array of sample vials and the holding plate.[116] Adapted from [96, 116].

3.5 Applications of direct calorimetry

As summarized in the following, direct calorimetry has several advantages and disadvantages that determine their range of applications.

Advantages

1. Label-free: Heat generated by *in vitro* (bio-)chemical reaction or *in vivo* by small organisms is directly recorded by the calorimeter. Thus no labeling chemicals are required.
2. Non-invasive: Measurements are performed in a non-invasive way as usually nothing hazardous is added to the system. Therefore, after each experiment, the samples can be collected for further analysis.
3. Versatility: Calorimetry can be used for many applications. In particular, the method is not limited by the shape or optical properties of the sample.
4. Accuracy: With an appropriate design, long term temperature stability and high resolution can be achieved. The best commercial product can reach a temperature stability of $\pm 100 \mu\text{K}$ over 24 h and a LOD of $0.2 \mu\text{W}$.[\[96\]](#)

Disadvantages

1. Non-specificity: Heat is a non-specific signal. The omnipresence of thermochemical phenomena in nature may cause misinterpretation of the recorded thermal signal.
2. Temperature stabilization: Sophisticated thermostat designs are required to avoid excessive thermal equilibration times, during which, in the worst case, the sample heat signal may be lost. Environmental temperature variations may disturb the system.
3. Sample environment alteration: For biological application, heat accumulation may change the temperature of the culture medium. Waste accumulation in a closed system has to be considered as well. Specific types of calorimeter can meditate this issue.
4. Size: Commercial high-precision calorimeters are usually equipped with a bulky thermostat and peripheral electronic controllers, thus cannot be designed as portable devices.
5. Cost: High equipment and operation cost, due to sophisticated components and uniquely designed consumables, may be an issue.

Applications

Miniaturized calorimetry is the future trend to solve some of the disadvantages stated above. Smaller size may enable portable platform formats. Sensor arrays can be readily implemented in order to increase throughput. Cost per unit may be reduced through convenient large-scale wafer-based fabrication of the sensor chips. Small sample size increases the range of possible applications involving, for instance, rare biological cells or expensive samples such as certain proteins. Regarding the non-specificity, it has been shown that recording bacterial heat flow profiles may be a potential way for identification[\[117\]](#).

Applications of calorimetry are found in various fields in scientific research and industrial applications. Examples in the field of biological research include heat measurement of single cells [\[87\]](#) and multi-cellular organisms[\[118, 119\]](#). Commercial systems have proven to be reliable tools for microbiological[\[120\]](#) and antimicrobial susceptibility studies[\[113\]](#). In this context, Table 3.2 shows an outline of heat power level produced by different cell types or small organisms. The

enthalpy of chemical reactions can also be measured with calorimeters. As a thermal analysis tool, calorimetry became a valuable and necessary tool for material characterization.[121] Quantitative applications include the measurement of heat of fusion and the extent of crystallization of a material. Specially, differential scanning calorimetry (DSC) is a useful tool for determining glass transition temperatures and melting points of polymer materials.[122] In addition to this, calorimetry is also widely used in environmental science[123] and food science[67].

Table 3.2 – Heat power for cells and living organisms.

Living cell or organism	Heat power	Refs
<i>Escherichia coli</i>	1 pW/bacterium	[124]
<i>Staphylococcus aureus</i>	3 pW/bacterium	[124]
3T3 mouse fibroblasts	17 pW/cell	[125]
HeLa-53G	31 pW/cell	[125, 126]
Rat white adipocytes	40 pW/cell	[125, 127]
Human melanoma H1477	80 pW/cell	[125, 128]
Hamster brown adipocytes	110 pW/cell	[125, 129]
Keratinocytes	134 pW/cell	[125, 130]
Rat hepatocytes	329 pW/cell	[125, 131]
Human myocardial cells	2 nW/cell	[124]
<i>C. elegans</i> nematodes	13 nW/worm	[132]

References

67. Wadsö, L. & Gómez Galindo, F. Isothermal Calorimetry for Biological Applications in Food Science and Technology. *Food Control* **20**, 956–961 (Oct. 1, 2009) (cit. on pp. 23, 48).
81. Johannessen, E. A. *et al.* Micromachined Nanocalorimetric Sensor for Ultra-Low-Volume Cell-Based Assays. *Analytical Chemistry* **74**, 2190–2197 (May 2002) (cit. on pp. 39, 40, 55).
82. Xu, J., Reiserer, R., Tellinghuisen, J., Wikswo, J. P. & Baudenbacher, F. J. A Microfabricated Nanocalorimeter: Design, Characterization, and Chemical Calibration. *Analytical Chemistry* **80**, 2728–2733 (Apr. 15, 2008) (cit. on p. 40).
83. Lubbers, B. & Baudenbacher, F. Isothermal Titration Calorimetry in Nanoliter Droplets with Subsecond Time Constants. *Analytical Chemistry* **83**, 7955–7961 (Oct. 15, 2011) (cit. on p. 40).
84. Lerchner, J. *et al.* Nano-Calorimetry of Small-Sized Biological Samples. *Thermochimica Acta* **477**, 48–53 (Oct. 2008) (cit. on pp. 40, 41, 147).
85. Lee, W., Fon, W., Axelrod, B. W. & Roukes, M. L. High-Sensitivity Microfluidic Calorimeters for Biological and Chemical Applications. *Proceedings of the National Academy of Sciences* **106**, 15225–15230 (2009) (cit. on pp. 41–43, 55).
86. Wang, L., Sipe, D. M., Xu, Y. & Lin, Q. A MEMS Thermal Biosensor for Metabolic Monitoring Applications. *Journal of Microelectromechanical Systems* **17**, 318–327 (Apr. 2008) (cit. on pp. 41, 42).
87. Hong, S. *et al.* Sub-Nanowatt Microfluidic Single-Cell Calorimetry. *Nature Communications* **11**, 2982 (Dec. 2020) (cit. on pp. 41–43, 47, 143, 145, 147).
88. Lerchner, J. *et al.* A New Micro-Fluid Chip Calorimeter for Biochemical Applications. *Thermochimica Acta* **445**, 144–150 (June 2006) (cit. on p. 40).
89. Lerchner, J. *et al.* Miniaturized Calorimetry — A New Method for Real-Time Biofilm Activity Analysis. *Journal of Microbiological Methods* **74**, 74–81 (Aug. 2008) (cit. on pp. 40, 43, 55).
90. Ahmad, L., Towe, B., Wolf, A., Mertens, F. & Lerchner, J. Binding Event Measurement Using a Chip Calorimeter Coupled to Magnetic Beads. *Sensors and Actuators B: Chemical* **145**, 239–245 (Mar. 4, 2010) (cit. on p. 40).
91. Hartmann, T. *et al.* Thermopile Chip Based Calorimeter for the Study of Aggregated Biological Samples in Segmented Flow. *Sensors and Actuators B: Chemical* **201**, 460–468 (Oct. 2014) (cit. on pp. 40, 42).
92. Wolf, A. *et al.* Toward High-Throughput Chip Calorimetry by Use of Segmented-Flow Technology. *Thermochimica Acta* **603**, 172–183 (Mar. 2015) (cit. on p. 42).
93. Wang, L., Wang, B. & Lin, Q. Demonstration of MEMS-Based Differential Scanning Calorimetry for Determining Thermodynamic Properties of Biomolecules. *Sensors and Actuators B: Chemical* **134**, 953–958 (Sept. 25, 2008) (cit. on p. 42).

94. Wang, B. & Lin, Q. Temperature-Modulated Differential Scanning Calorimetry in a MEMS Device. *Sensors and Actuators B: Chemical. Transducers 2011* **180**, 60–65 (Apr. 1, 2013) (cit. on p. 42).
95. West, G. B., Woodruff, W. H. & Brown, J. H. Allometric Scaling of Metabolic Rate from Molecules and Mitochondria to Cells and Mammals. *Proceedings of the National Academy of Sciences* **99**, 2473–2478 (suppl 1 Feb. 19, 2002) (cit. on p. 43).
96. TAM IV-48 TA Instruments. <http://www.tainstruments.com/tam-48/> (2017) (cit. on pp. 43, 46, 47).
97. Johannessen, E. A., Weaver, J. M. R., Cobbold, P. H. & Cooper, J. M. Heat Conduction Nanocalorimeter for Pl-Scale Single Cell Measurements. *Applied Physics Letters* **80**, 2029 (2002) (cit. on p. 43).
98. Liu, Y., Lehnert, T. & Gijs, M. A. M. Fast Antimicrobial Susceptibility Testing on *Escherichia coli* by Metabolic Heat Nanocalorimetry. *Lab on a Chip* **20**, 3144–3157 (Aug. 26, 2020) (cit. on pp. 43, 53, 74, 83, 127).
99. Toda, M., Inomata, N., Ono, T. & Voiculescu, I. Cantilever Beam Temperature Sensors for Biological Applications. *IEEE Transactions on Electrical and Electronic Engineering* **12**, 153–160 (2017) (cit. on p. 43).
100. Barnes, J. R., Stephenson, R. J., Welland, M. E., Gerber, C. & Gimzewski, J. K. Photothermal Spectroscopy with Femtojoule Sensitivity Using a Micromechanical Device. *Nature* **372**, 79–81 (6501 Nov. 1994) (cit. on p. 43).
101. Sato, M. K. *et al.* Temperature Changes in Brown Adipocytes Detected with a Bimaterial Microcantilever. *Biophysical Journal* **106**, 2458–2464 (June 3, 2014) (cit. on p. 43).
102. Inomata, N., Toda, M., Sato, M., Ishijima, A. & Ono, T. Pico Calorimeter for Detection of Heat Produced in an Individual Brown Fat Cell. *Applied Physics Letters* **100**, 154104 (Apr. 9, 2012) (cit. on pp. 43, 55).
103. Inomata, N., Toda, M. & Ono, T. Highly Sensitive Thermometer Using a Vacuum-Packed Si Resonator in a Microfluidic Chip for the Thermal Measurement of Single Cells. *Lab on a Chip* **16**, 3597–3603 (2016) (cit. on p. 43).
104. Etayash, H., Khan, M. F., Kaur, K. & Thundat, T. Microfluidic Cantilever Detects Bacteria and Measures Their Susceptibility to Antibiotics in Small Confined Volumes. *Nature Communications* **7**, 12947 (Oct. 4, 2016) (cit. on pp. 43, 44).
105. Wig, A., Arakawa, E. T., Passian, A., Ferrell, T. L. & Thundat, T. Photothermal Spectroscopy of Bacillus Anthracis and Bacillus Cereus with Microcantilevers. *Sensors and Actuators B: Chemical* **114**, 206–211 (Mar. 30, 2006) (cit. on p. 44).
106. Longo, G. *et al.* Rapid Detection of Bacterial Resistance to Antibiotics Using AFM Cantilevers as Nanomechanical Sensors. *Nature Nanotechnology* **8**, 522–526 (7 July 2013) (cit. on p. 44).
107. Resistell AG - Developing Leading Rapid AST Solution <https://resistell.com/> (2021) (cit. on p. 45).

108. Torres, F. E. *et al.* Enthalpy Arrays. *Proceedings of the National Academy of Sciences* **101**, 9517–9522 (June 29, 2004) (cit. on pp. 45, 55).
109. Kim, J., Nam, S. M., Kim, J., Seo, S. & Lee, W. *High-Sensitivity Parylene Microfluidic Chip Calorimeters for Measurements of Cellular Metabolic Heat* in 2019 IEEE 32nd International Conference on Micro Electro Mechanical Systems (MEMS) 2019 IEEE 32nd International Conference on Micro Electro Mechanical Systems (MEMS) (IEEE, Seoul, Korea (South), Jan. 2019), 544–546. doi:[10.1109/MEMSYS.2019.8870722](https://doi.org/10.1109/MEMSYS.2019.8870722) (cit. on pp. 45, 55).
110. Recht, M. I. *et al.* Enthalpy Array Analysis of Enzymatic and Binding Reactions. *Analytical Biochemistry* **377**, 33–39 (June 2008) (cit. on p. 45).
111. Recht, M. I. *et al.* Measurement of Enzyme Kinetics and Inhibitor Constants Using Enthalpy Arrays. *Analytical Biochemistry* **388**, 204–212 (May 15, 2009) (cit. on pp. 45, 55).
112. Koh, J., Lee, W. & Shin, J. H. High-Sensitivity Chip Calorimeter Platform for Sub-Nano Watt Thermal Measurement. *Sensors and Actuators A: Physical* **241**, 60–65 (Apr. 15, 2016) (cit. on p. 45).
113. Braissant, O. *et al.* Isothermal Microcalorimetry Accurately Detects Bacteria, Tumorous Microtissues, and Parasitic Worms in a Label-Free Well-Plate Assay. *Biotechnology Journal* **10**, 460–468 (Mar. 2015) (cit. on pp. 46, 47, 74).
114. *Calvet Calorimeters* SETARAM. <https://setaramsolutions.com/product/calvet> (2020) (cit. on p. 46).
115. *Micro Reaction Calorimeter | Thermal Hazard Technology* <https://www.thermalhazardtechnology.com/chemical-products/micro-reaction-calorimeter> (2020) (cit. on p. 46).
116. *Product Suite of Symcel* Symcel. <https://symcel.com/calscreener/product-suite/> (2020) (cit. on p. 46).
117. Boling, E. A., Blanchard, G. C. & Russell, W. J. Bacterial Identification by Microcalorimetry. *Nature* **241**, 472–473 (5390 Feb. 1973) (cit. on pp. 47, 138).
118. Krenger, R., Lehnert, T. & Gijs, M. A. M. Dynamic Microfluidic Nanocalorimetry System for Measuring *Caenorhabditis Elegans* Metabolic Heat. *Lab on a Chip* **18**, 1641–1651 (2018) (cit. on pp. 47, 56, 147).
119. Hur, S., Mittapally, R., Yadlapalli, S., Reddy, P. & Meyhofer, E. Sub-Nanowatt Resolution Direct Calorimetry for Probing Real-Time Metabolic Activity of Individual C. Elegans Worms. *Nature Communications* **11**, 2983 (Dec. 2020) (cit. on pp. 47, 143, 145).
120. Trampuz, A., Salzmann, S., Antheaume, J. & Daniels, A. U. Microcalorimetry: A Novel Method for Detection of Microbial Contamination in Platelet Products. *Transfusion* **47**, 1643–1650 (Sept. 2007) (cit. on pp. 47, 54).
121. Koshy, O., Subramanian, L. & Thomas, S. in *Thermal and Rheological Measurement Techniques for Nanomaterials Characterization* (eds Thomas, S., Thomas, R., Zachariah, A. K. & Mishra, R. K.) 109–122 (Elsevier, Jan. 1, 2017). doi:[10.1016/B978-0-323-46139-9.00005-0](https://doi.org/10.1016/B978-0-323-46139-9.00005-0) (cit. on p. 48).

122. Rieger, J. The Glass Transition Temperature T_g of Polymers—Comparison of the Values from Differential Thermal Analysis (DTA, DSC) and Dynamic Mechanical Measurements (Torsion Pendulum). *Polymer Testing* **20**, 199–204 (Oct. 1, 2001) (cit. on p. 48).
123. Rong, X.-M., Huang, Q.-Y., Jiang, D.-H., Cai, P. & Liang, W. Isothermal Microcalorimetry: A Review of Applications in Soil and Environmental Sciences¹ ¹Project Supported by the National Natural Science Foundation of China (No. 40571084). *Pedosphere* **17**, 137–145 (Apr. 1, 2007) (cit. on p. 48).
124. Maskow, T. *et al.* Potentials and Limitations of Miniaturized Calorimeters for Bioprocess Monitoring. *Applied Microbiology and Biotechnology* **92**, 55–66 (Oct. 2011) (cit. on p. 48).
125. Kemp, R. Calorimetric Studies of Heat Flux in Animal Cells. *Thermochimica Acta* **193**, 253–267 (Dec. 1991) (cit. on p. 48).
126. McGuinness, S. M., Roess, D. A. & Barisas, B. G. Acute Toxicity Effects of Mercury and Other Heavy Metals on HeLa Cells and Human Lymphocytes Evaluated via Microcalorimetry. *Thermochimica Acta* **172**, 131–145 (Dec. 1, 1990) (cit. on p. 48).
127. Nilsson-Ehle, P. & Nordin, G. Microcalorimetric Studies on the Total Metabolic Activity of Fat Cells. *International Journal of Obesity* **9 Suppl 1**, 169–172 (1985) (cit. on p. 48).
128. Görman Nordmark, M., Laynez, J., Schön, A., Suurkuusk, J. & Wadsö, I. Design and Testing of a New Microcalorimetric Vessel for Use with Living Cellular Systems and in Titration Experiments. *Journal of Biochemical and Biophysical Methods* **10**, 187–202 (Dec. 1, 1984) (cit. on p. 48).
129. Nedergaard, J., Cannon, B. & Lindberg, O. Microcalorimetry of Isolated Mammalian Cells. *Nature* **267**, 518–520 (5611 June 1977) (cit. on p. 48).
130. Reichert, U. & Schaarschmidt, B. Heat Evolution of Cultured Human Keratinocytes. *Experientia* **42**, 173–174 (Feb. 15, 1986) (cit. on p. 48).
131. Nässberger, L., Jensen, E., Monti, M. & Florén, C.-H. Microcalorimetric Investigation of Metabolism in Rat Hepatocytes Cultured on Microplates and in Cell Suspensions. *Biochimica et Biophysica Acta (BBA) - General Subjects* **882**, 353–358 (July 16, 1986) (cit. on p. 48).
132. Braeckman, B. P., Houthoofd, K., De Vreese, A. & Vanfleteren, J. R. Assaying Metabolic Activity in Ageing *Caenorhabditis Elegans*. *Mechanisms of Ageing and Development* **123**, 105–119 (Jan. 2002) (cit. on p. 48).

4 A nanocalorimetry platform for fast AST

Fast spreading of AMR is now considered to be a major global health threat. New technologies are required, enabling rapid diagnostics of bacterial infection combined with fast AST for evaluating the efficiency and dosage of antimicrobial compounds *in vitro*. This chapter presents an integrated chip-based isothermal nanocalorimetry platform for direct microbial metabolic heat measurements and evaluates its potential for fast AST. Direct detection of the bacteria-generated heat allows monitoring of metabolic activity and antimicrobial action at subinhibitory concentrations in real-time. The platform's high heat sensitivity enables bacterial growth detection within only a few hours of culture, whereas growth inhibition upon administration of antibiotics is revealed by a decrease or the absence of the heat signal. Antimicrobial stress results in lag phase extension and metabolic energy spilling. Optical density measurements provide a more holistic insight of the metabolic state and the evolution of bacterial biomass. As a proof-of-concept, a metabolic heat-based AST study on *E. coli* as model organism with three clinically relevant antibiotics is performed and the MIC values could be determined.

This chapter is adapted from the following paper: Liu, Y., Lehnert, T. & Gijs, M. A. M. Fast Antimicrobial Susceptibility Testing on *Escherichia coli* by Metabolic Heat Nanocalorimetry. *Lab on a Chip* **20**, 3144–3157 (Aug. 26, 2020)

4.1 Introduction

Steadily increasing AMR of medically relevant microorganisms is an important threat to global health[4, 133, 134]. Multi-drug resistance of common pathogens, such as *Staphylococcus aureus*, *Enterobacteriaceae* and *Pseudomonas aeruginosa*, brings about severe therapeutic challenges, associated with elevated morbidity and mortality rates.[135] An often cited AMR review report, based on detailed scenario analyses of the impact of AMR spreading on healthcare and macroeconomics, estimated to 10 million the number of deaths per year attributable to AMR in 2050, *i.e.* more than for most of the other major causes of disease-related death.[3] An European cross-national database study established a correlation between AMR and outpatient antibiotic use.[136] Moreover, clinical studies revealed a high percentage of unnecessary prescriptions of antibiotics for therapeutic and prophylactic purposes. This fact has been recognized as one of the

main causes of emerging AMR. In many cases prescribed drugs are broad-spectrum antimicrobial agents, which further promotes AMR development and spreading.

Rapid diagnosis of bacterial infection combined with fast and accurate AST is one of the keys to counteract AMR progression, in particular by optimizing and personalizing the therapeutic management of infected patients.[137] AST *in vitro* techniques aim to predict the efficiency of an antimicrobial compound for treating an infection. Ideally, an AST protocol should provide the MIC for microbial growth, *i.e.* the lowest drug concentration that inhibits bacterial growth after overnight incubation.[138] Standard AST methods in clinical microbiological diagnosis, in particular the disk diffusion method and broth microdilution, are based on established, robust and often manual protocols. A commercial diffusion-based gradient method (Etest®, bioMérieux) may be used for MIC determination.[36] Current clinical protocols, however, suffer from important limitations, in particular extended time to result or the requirement for relatively large amounts of viable microorganisms. Automated AST systems based on turbidity measurements aim to reduce time to result, typically to below 24 h.[139] Moreover, a range of new AST technologies is under development to tackle the AMR problem,[139, 140] either in a 96-well plate or microfluidic format, including molecular diagnostic tools to detect the presence of resistance genes[141] and fast AST assays based on single-cell imaging, for instance.[40] Nevertheless, most of these technologies still face major barriers with respect to general acceptance by the healthcare system and market penetration.[137]

In this context, we explore microbial heat production as a direct indicator of metabolic activity and viability of bacterial populations. Metabolic heat/heat flow curves provide real-time information on microbial growth dynamics and can be used for detecting bacterial growth inhibition in the presence of antimicrobials *in vitro*. The potential of isothermal microcalorimetry (IMC) for microbial activity monitoring, metabolic studies and drug assays has already been demonstrated by means of commercial devices. The latter use sealed mL-size sample ampoules and have very low heat power detection limits, typically in the range of a few μW down to 0.2 μW . [142, 143] For instance, different metabolic phases of *E. coli* bacterial growth have been identified by analyzing heat flow profiles.[144] Highly sensitive and fast detection of bacterial contamination ($\geq 1 - 10$ CFU/mL) was also demonstrated by recording heat flow of artificially contaminated blood platelets samples.[120] The potential of IMC for rapid differentiation between methicillin-resistant *S. aureus* (MRSA) and methicillin-susceptible *S. aureus* (MSSA) was evaluated by von Ah *et al.* by using the antibiotics cefoxitin and oxacillin.[145] Subsequently, Baldoni *et al.* reported a study using a 48-channel batch calorimeter for the detection of methicillin-resistance in *S. aureus* including genetically distinct clinical isolates.[146] MRSA isolates were correctly identified after 5 h by testing against cefoxitin, however, very high bacterial inocula (McFarland turbidity of 5) were used to reduce time to result. Yang *et al.* analyzed the growth rate of *E. coli* and the time to maximum heat power as a function of concentration for two different cephalosporins.[147] The two antibiotics tested affected the heat power curves in a clearly different manner. A more extensive AST study was performed by von Ah *et al.*, analyzing heat flow curves for reference strains of *E. coli* and *S. aureus* for 12 different antibiotics. The results have been grouped by mode of antimicrobial action, revealing different thermal signatures for each compound family.[148]

Different microfabricated and microfluidic integration formats have been proposed for high-sensitivity nanocalorimeters. A miniaturized chip-based calorimeter, similar to the one presented in the present work, has been developed earlier by Higuera-Guisset *et al.*. The authors studied the effect of two different growth media and of the culture temperature on the metabolic heat curves of *E. coli*. [149] Another group used a flow-through chamber chip module, enclosed by two high-precision thermostats, for the study of biofilm inactivation by predatory bacteria and for monitoring biofilm eradication with antibiotics. [89, 150, 151] Johannessen *et al.* implemented a sub-nL open-reservoir assay for heat measurements on a small number of isolated living cells. [81] Torres *et al.* reported the microfabrication of 96-detector enthalpy arrays on polyimide membranes and implemented rapid electrostatic merging/mixing of droplets. [108] The technology enabled studying kinetic parameters of enzyme-catalyzed reactions. [111] Lee *et al.* proposed a more complex closed-chamber microfluidic approach with precise nL sample manipulation capabilities for measuring the heat of reaction of urea hydrolysis, for instance. [85] Inomata *et al.* developed a picocalorimeter for detection of heat produced by a brown fat cell attached to a Si microstage connected to a cantilevered Si sensor. Heat is sensed by the resulting shift in the resonant frequency. [102] An ultrasensitive micro-DSC (differential scanning calorimeter) for liquid protein sample characterization was demonstrated by Wang *et al.*. The device is based on vanadium oxide thermistors and a microfluidic dual-chamber calorimeter design. [152] Kim *et al.* recently reported a thin-film parylene microfluidic calorimeter with on-chip vacuum insulation. Measurement of cellular metabolic power changes upon controlled stimuli was demonstrated. [109] A more recent commercial microcalorimetry instrument (Symcel AB®) uses a well-plate format for tracking the activity of living cells and biological processes. [39]

In this work, we present an isothermal nanocalorimetry platform designed for monitoring microbial growth dynamics with high sensitivity, thus enabling fast AST based on metabolic heat measurements. Our system is operated in a microincubator format and was optimized with respect to high thermal stability, a prerequisite for fast detection of bacterial infection or establishing accurate antibiograms. We evaluated microbial heat generation under different culture conditions. More importantly, we performed a proof-of-concept study comprising metabolic heat AST assays of *E. coli* exposed to three commonly used antimicrobial drugs (ciprofloxacin, ampicillin and gentamicin). Specific features of the metabolic heat/heat flow curves showed clear variations as a function of the antimicrobial concentration and MIC values could be determined for the tested compounds. This offered a more detailed phenotypic fingerprint of the microbial metabolic activity upon drug exposure, while optical density measurements over time of the bacterial cultures provided additional insight in the development of bacterial biomass.

4.2 Platform design and characterization

The nanocalorimetry platform is constructed around a sensing unit comprising a microincubator for bacterial culture and a thermopile sensor chip that detects heat flow corresponding to the metabolic heat power generated by the microbial sample during incubation. A dual chip arrangement allows increasing assay throughput or differential/control measurements. Several

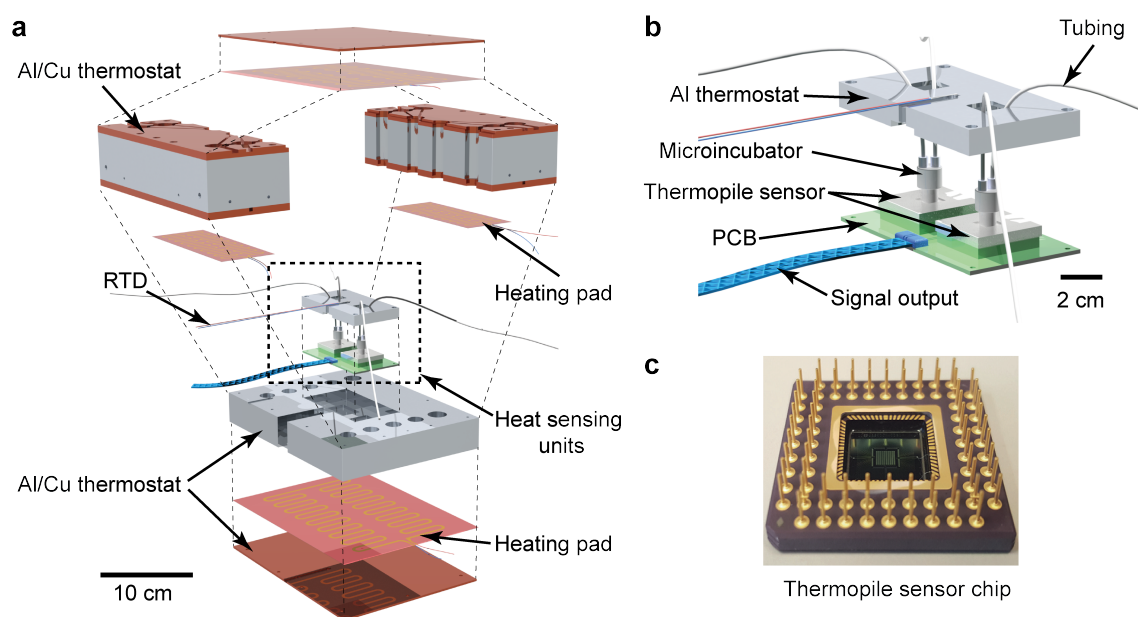


Figure 4.1 – The isothermal nanocalorimetry platform. (a) Exploded 3D view of the integrated platform with two thermopile-based sensing units. The Al/Cu thermostat is based on a PID controller, using several heating pads and a resistance temperature detector (RTD) sensor (Pt1000). (b) Enlarged view of the twin heat sensing unit including a parallel arrangement of two microincubators ($2 \times 150 \mu\text{L}$). (c) Photograph of one thermopile sensor chip and pin grid array (Xensor Integration, XEN-NCM9924). The hot junctions of the thermopile and a thin-film Al heating element are located on the sensitive central part ($3 \text{ mm} \times 3 \text{ mm}$) of the Si membrane. The cold junctions are in thermal contact with the Si frame situated at the edge of the chip ($10 \text{ mm} \times 10 \text{ mm}$).

important modifications have been implemented with respect to a previous version of the system,^[118] mainly aiming at improving specific requirements for allowing high-sensitivity detection and accurate recording of metabolic heat profiles. These features include high thermal stability and fluidic integration suitable for fast thermalization of the sample and drug solutions. Figure 4.1a shows an exploded 3D view of the INCfAST platform. Sensor chip and microincubator are inserted in the central part of the Al/Cu thermostat. A proportional–integral–derivative (PID) temperature control system with several heating pads provides uniform temperature distribution and stabilization at the sample location within $\pm 250 \mu\text{K}$ at 37°C (Figure 4.2, mK-range for the previous version of the platform ^[118]). Consequently, a limit of detection (LOD) for heat power of microbial suspensions as low as 750 nW was achieved (Figure 4.3). The core of the platform comprises the dual chip system with microincubators, fluidic connections and electrical read-out for independent parallel measurements (4.1b). Voltage signals generated by the thermal sensors are recorded by a two-channel nanovoltmeter (34420A, Keysight, USA). Commercially available sensor chips were used in this study (XEN NCM9924, Xensor Integration, Delft, The Netherlands) (Figure 4.1c, datasheet in Appendix A.4). The sensing mechanism is based on a thin-film thermopile distributed around the center region of a Si membrane. The relatively thick membrane ($45 \mu\text{m}$

according to the data sheet) provides sufficient robustness for liquid nanocalorimetry applications.

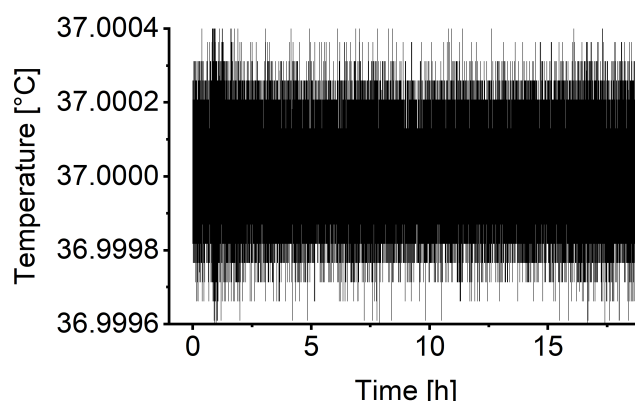


Figure 4.2 – Temperature stabilization of the INCfAST platform. The plot indicates that the temperature fluctuation is about $\pm 250 \mu\text{K}$ around the set point of 37°C for the duration of a typical metabolic assay. The temperature was measured with the RTD sensor of the platform, which is located close to the microincubator.

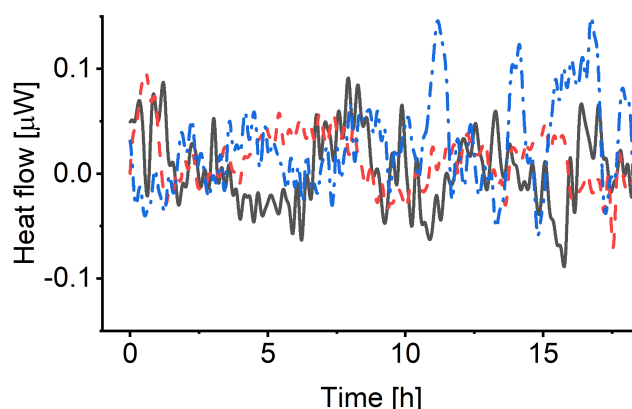


Figure 4.3 – Control experiments without bacteria. In order to evaluate the efficiency of the cleaning and sterilization protocol applied to the fluidic system of the platform, control curves have been recorded with pure Mueller-Hinton broth (no bacteria, $n = 3$). Heat flow signals fluctuate around zero-level (after baseline correction) for the time scale of typical assays, indicating that the microincubator is well sterilized and that the recorded metabolic heat signals are not generated by any contamination with other bacteria. An average filter was firstly applied to process these curves. From these recordings we derive a maximum noise level of 200-250 nW, resulting in a conservative LOD estimate of $\sim 750 \text{ nW}$ for metabolic heat measurements (corresponding to $\text{SNR} \approx 3$).

More details of the integrated system are shown in Figure 4.4. The microincubator that receives the bacterial suspension is bonded onto the sensor surface. The liquid sample is in direct contact with the Si sensor membrane (no polymer membrane on the bottom of the microincubator), thus maximizing heat transfer to the sensing elements. The microincubator has one sample inlet and one waste outlet. The corresponding reservoirs are located outside the thermostat at room temperature for convenient operation. Nevertheless, thermalization of compound solutions and bacterial

suspensions during injection is fast and not limiting the performance of the platform for the present application involving relatively slow heat signal variations. Optionally, the reservoirs could be placed inside the thermostat for reducing thermal stabilization time. Placing the whole setup inside a foam/polystyrene housing (not shown) further reduced perturbations due to environmental temperature variations.

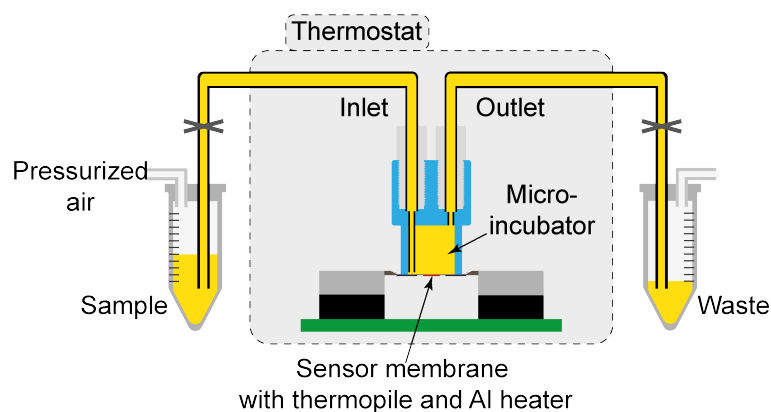


Figure 4.4 – Schematic cross-sectional view of a sensor unit with fluidic system (yellow). The microincubator is positioned directly on the chip membrane and connected to external sample and waste reservoirs, respectively. Bacterial suspensions are injected into the microincubator by pressure control of the sample reservoir.

4.3 Experimental

4.3.1 Microincubator fabrication and sensor calibration

Polycarbonate microincubators ($V = 150 \mu\text{L}$, $\varnothing = 5.7 \text{ mm}$, height = 6 mm) fabricated by micromilling were employed for the metabolic heat assays on the INCfAST platform. Polycarbonate offers good mechanical stability and high chemical resistance with respect to the sterilization protocols applied for the experiments.

Sensor calibration was performed by means of the Al thin-film resistive heater on the sensing area of the chip membrane. A deionized (DI) water-filled microincubator was positioned on the sensor during calibration in order to simulate actual assay conditions. Calibration of the thermopile voltage output was performed by generating defined heat power signals via an external electrical power source. We determined a *power/voltage* coefficient of 0.88 W/V for the present system configuration (Figure 4.5). The reciprocal value of this coefficient is the power sensitivity, 1.14 V/W.

4.3.2 Preparation of microbial sample and antimicrobial solutions

Assays in this work were carried out using the *E. coli* ATCC 25922 strain (*E. coli* WDCM 00013 VitroidsTM, Sigma-Aldrich). This organism is a typical AST control strain. We used a standard broth micro dilution (BMD) protocol for bacterial culture and sample preparation. *E. coli* inoculum was

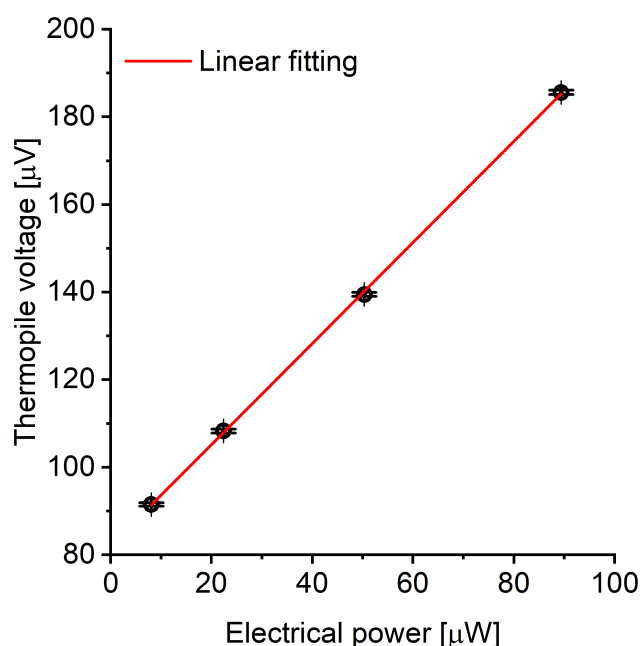


Figure 4.5 – Calibration of the heat power/thermopile voltage conversion coefficient. The conversion coefficient was obtained by means of an Al thin-film resistor deposited on the sensitive part of the thermopile chip membrane (see Figure 4.1c and 4.4). A power/voltage conversion coefficient of 0.88 W/V was determined by linear regression of the thermopile voltage output *vs* the applied electrical power ($n = 3$). Calibration was carried out with a deionized (DI) water-filled microincubator positioned on the sensor membrane.

first introduced into liquid Mueller-Hinton (MH) culture medium and incubated overnight at 37 °C. Subsequently, 10 μ L of this suspension was cultured on MH agar plates (Thermo Scientific, CM0337) and diluted by streaking. Single colonies were picked to prepare a bacterial suspension with an Optical density (OD) value of 0.2 measured at 600 nm (0.5 McFarland standard), *i.e.* a concentration of $\sim 1 \times 10^8$ CFU/mL. By dilution in pure culture medium we obtained the primary samples for the heat flow assays with an initial bacterial concentration of $2.8 \pm 0.5 \times 10^5$ CFU/mL for all experiments (confirmed by 3 serial quality control experiments). A purity, viability and concentration check prior to each measurement series was carried out by inoculation on a non-selective agar plate (after further 100-fold dilution) and colony counting after overnight culture. With our quality control experiments we determined a concentration of $3.7\text{--}5.5 \times 10^8$ CFU/mL for 1.0 OD600 (Optical density, measured at 600 nm wavelength), which is consistent with the value given by Stevenson *et al.* [153]. The bacterial suspension was stored in a small flask and used within 15 min as inoculum on the INCfAST platform. For some of the metabolic heat assays in this work different culture media were compared, including Brain Heart Infusion (BHI) (Thermo Scientific, CM1135), Mueller-Hinton (MH) (Thermo Scientific, CM0405), and Lysogeny broth (LB) (Sigma Aldrich, L3522). All culture media and agar plates were prepared according to the recommended protocols and concentrations. Microbial suspensions and antimicrobial solutions for OD600 measurements were prepared in the same way as for the heat assays. We performed OD600 measurements on a plate reader (24-well

plate, inoculum $2.8 \pm 0.5 \times 10^5$ CFU/mL, 37 °C). The microbial suspension in each well was sealed with 500 μ L mineral oil (Sigma-Aldrich, M8410) to prevent evaporation.

Ciprofloxacin, ampicillin sodium salt, and gentamicin were purchased from Sigma-Aldrich. Ampicillin sodium salt and gentamicin are soluble in DI water. 1 mol/L hydrogen chloride solution was used for ciprofloxacin. Ciprofloxacin, ampicillin, and gentamicin stock solutions were prepared with a concentration of 25.5 mg/mL, 51.9 mg/mL and 36.0 mg/mL, respectively. Stock solutions were stored at 4 °C and used within maximum 1 week to avoid a risk of declining activity. Prior to the measurements stock solutions were thermalized at room temperature and gradually diluted in DI water to prepare a series of concentrations according to the potency of each antibiotic (10 times higher than the final target concentrations). Test solution aliquots were prepared by further 10-fold dilution in MH. Target concentrations were chosen according to the range suggested by EUCAST. The bacterial inoculum was added to the test solutions immediately before sample injection into the microincubator.

4.3.3 Platform sterilization and heat flow measurement protocol

In order to avoid damage of the fragile sensor membrane during operation, different key components, in particular the microincubator and the sensor, were generally reused in successive measurements. After each experiment, a cleaning and sterilization protocol was applied to the whole fluidic circuit of the nanocalorimetry platform, including tubing, the microincubator and the sensor surface. First, the circuit was thoroughly rinsed with ethanol in order to remove and elute most of the bacteria in the system, followed by soaking all exposed surfaces in RAPICIDETM OPA/28 High-Level Disinfectant (Cantel Medical Corp.) for 20 min for sterilization and repeated washing with sterilized DI water. Control experiments without bacterial inoculum confirmed the efficiency of this protocol (no microbial heat signal was detected for ≤ 15 h, Figure 4.3). The platform and all auxiliary devices were kept under a biosafety cabinet to avoid contamination from the environment during the experiment.

Metabolic heat generation of *E. coli* ATCC 25922 was studied under different culture conditions, and upon exposure to antimicrobial compounds. First, the microincubator was installed in the platform and connected to the reservoirs for the bacterial sample/drug suspension and waste, respectively (Figure 4.4). The platform was then stabilized to the temperature set point (normally 37 °C) and kept at that temperature for consecutive measurements. The sample solution was injected into the microincubator by pressure control of the sample reservoir (Fluigent MFCS pressure pump). The microincubator was then isolated by closing the valves in the inlet/outlet tubing and recording of the heat flow curves was started. Different assay conditions were successively tested by changing the external sample reservoir and refilling the microincubator after applying the cleaning/sterilization protocol described above. The platform thermalization was not interrupted. From the initial part of the experimental recordings, we found that thermal stabilization of the injected solution and the sensor can be safely achieved within 30 min. On the heat flow curves $P(t)$ and heat curves $Q(t)$ shown in this paper, $t = 0$ h defines the time point when signal recording was actually started, *i.e.* 30 min after solution injection. Heat flow curves were generally recorded through the whole culture

cycle (sampling frequency 0.5 Hz) until no heat signal could be detected anymore (up to 20 h).

4.3.4 Statistical analysis and baseline correction

All nanocalorimetric experiments shown in the paper were performed 3 times with identical conditions. Heat flow $P(t)$ raw data was first filtered by an average filter to minimize the noise level. Mean values are indicated by lines on the figures and the shaded regions correspond to the standard error (SE), calculated using OriginLab® software. For baseline correction of the $P(t)$ curves, a spline fit was generated by the baseline correction function of the OriginLab® software (Figure 4.6). OD measurements were performed 3 times as well.

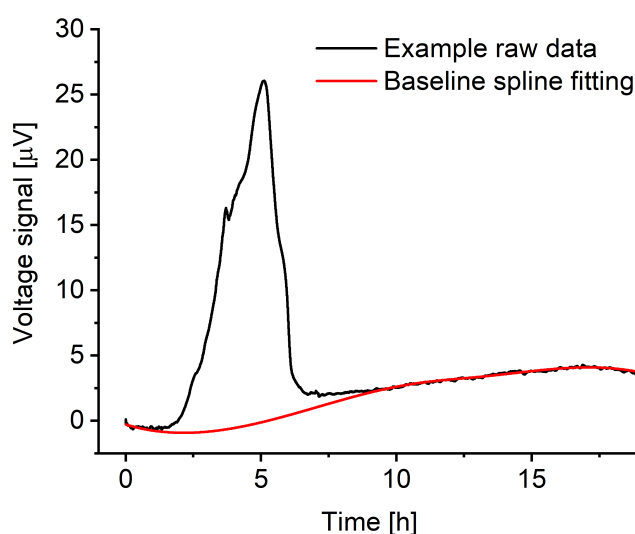


Figure 4.6 – Heat flow baseline correction. The figure shows a representative example for the baseline correction applied in the present experiments. The black curve represents the raw data of a heat flow measurement (voltage signal in μV). A baseline spline fit (red curve) was generated by OriginLab® software based on 3 separated points in the initial flat region and 3 points in the region after 11 h. The raw data is corrected by subtracting this baseline.

4.4 Results

4.4.1 Analysis of microbial metabolic heat profiles

Figure 4.7a (black curve) shows a representative metabolic heat flow curve (*i.e.* heat power $P(t)$ [W]) for *E. coli* in Mueller-Hinton broth (MH) recorded on the INCfAST platform ($V = 150 \mu\text{L}$, inoculum size $2.8 \pm 0.5 \times 10^5$ CFU/mL, 37°C). The $P(t)$ curve displays the time-dependent metabolic heat flow generated by the bacterial population in the center region of the Si chip membrane towards the Si bulk edge, thus depends on the actual number of viable cells and their metabolic activity. In the initial segment the signal is below LOD, corresponding to an apparent lag phase or delay time ($t_{\text{delay}} \sim 1.5$ h) associated with low biomass and/or low metabolic activity. Subsequently,

exponential growth generated a rapidly rising signal up to a transient maximum rate of heat production P_{max} (at ~ 5 h, $21.3 \pm 2.5 \mu\text{W}$) followed by a sharp decline. Assay curves have been recorded up to 20 h, however only the most relevant time interval [0, 7 h] is shown in Figure 4.7a. At longer incubation times (10 - 11 h) metabolic heat production ceased due to nutrient and/or oxygen depletion in the microincubator. At this stage, most of the bacteria are still alive as revealed by optical microscopy inspection or are possibly in a dormant state. The aggregate metabolic heat curve (energy $Q(t)$ [J]) was obtained by integration of the heat flow curve over time (Figure 4.7a, red curve). Accordingly, the $Q(t)$ curve features three phases, namely the initial lag phase, the exponential growth region (for $t \sim [1.5 \text{ h} ; 5.5 \text{ h}]$) and a stationary phase (for $t \gtrsim 7 \text{ h}$), in which the total heat does not increase any more ($Q_{max} \pm 15 \text{ mJ}$). For the metabolic assays discussed below, the $P(t)$ and $Q(t)$ curves shown in Figure 4.7a were used as reference for normal culture conditions on the INCfAST platform.

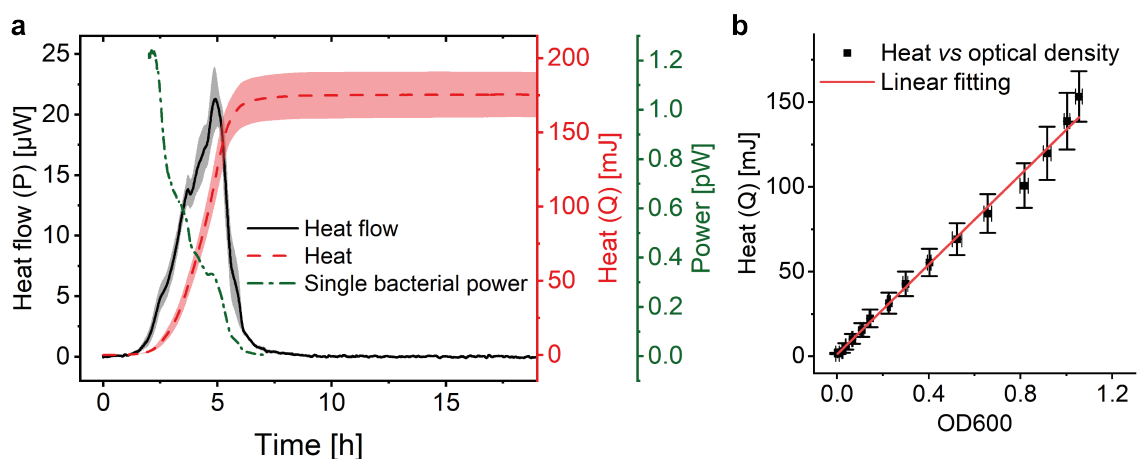


Figure 4.7 – Metabolic heat measurements performed on the nanocalorimetry platform. (a) Metabolic heat flow curve $P(t)$ (black) for *E. coli* ATCC 25922 with typical incubation conditions on the INCfAST platform (Mueller-Hinton broth (MH), 37 °C). The heat power signal was obtained by read-out of the thermopile sensor voltage output after calibration. Integration of the heat flow curve over time provides the corresponding metabolic heat curve $Q(t)$ (red). The single bacteria heat power (green curve) was estimated by normalization of $Q(t)$ by the biomass at a given time point, as determined from optical density (OD600) measurements. (b) Plot of the metabolic heat signal *vs* OD600 of a bacterial suspension up to the exponential growth phase (using data shown in (a) and Figure 4.9a for $t = [0, 5 \text{ h}]$). The proportional relationship (coefficient 134 mJ/1.0 OD600) indicates that the heat signal is directly related to the amount of bacteria in this regime. All curves represent mean \pm SE ($n = 3$).

We performed optical density measurements (OD600, *i.e.* at 600 nm) under culture conditions comparable to the BMD method on a plate reader. As shown in Figure 4.9 for culture in MH, the exponential phases of the $Q(t)$ and the OD600 curves overlap well. A scaling or heat/OD600 conversion coefficient of 134 mJ/1.0 OD600 for MH was determined by linear regression of the $Q(t)$ *vs* OD600 plot shown in Figure 4.7b. This observation indicates that heat curves recorded with our system can be safely correlated with bacterial growth or the actual biomass density in the

microincubator, respectively. Mean slopes Q/t in the exponential region may be considered as indicative for bacterial growth rates, whereas heat flow profiles $P(t)$ are more sensitive to transient phenomena of the growth behavior. Furthermore, $P(t)$ can be normalized with respect to biomass simply by dividing through the converted $Q(t)$. The resulting curve (Figure 4.7a, green curve), showing a continuous decline (~ 0 pW for $t > 7$ h), provides a rough estimate of the time evolution of the metabolic heat production per bacterium for the specific culture conditions. For the calculation we applied a conversion equivalence of 1.0 OD600 corresponding to 5×10^8 CFU/mL.[153]

4.4.2 Metabolic activity of *E. coli* for different culture conditions

Assessment of the metabolic activity of *E. coli* in different culture media (Figure 4.8a and 4.8b), as well as for several culture temperatures (Figure 4.8c and 4.8d), was performed as a first evaluation of the INCfAST platform performance. Heat flow curves have been recorded in BHI, MH and LB (Figure 4.8a). These media have different compositions and amounts of nutrients (Table 4.1), affecting growth rate and metabolic activity of the bacteria. We found that rich media, in particular BHI, promotes transient metabolic heat production reflected by the P_{max} values of the heat flow curves, yielding $31.3 \pm 1.2 \mu\text{W}$ in BHI (highest amount of carbon compounds), $21.3 \pm 2.5 \mu\text{W}$ in MH (intermediate nutrient level) and $18.7 \pm 1.4 \mu\text{W}$ in LB (low amount of nutrients) (Figure 4.8a). Consequently, culture in BHI also enhanced the total heat generated during incubation ($Q_{max} \approx 252 \pm 10$ mJ in Figure 4.8b), whereas $Q(t)$ reached comparable levels for MH and LB in the stationary phase (175 ± 15 mJ and 157 ± 32 mJ, respectively).

For all media, the OD600 curves, recorded separately on a plate reader, overlap well with the corresponding heat curves in the exponential region (after y-axis scaling and time synchronization, Figure 4.9a-c). OD600 measurements reveal that the increase of the bacterial biomass is fastest in BHI compared to MH or LB. As already shown in Figure 4.7b for MH, heat/OD600 coefficients were determined by linear regression in the exponential region for all media tested (Figure 4.9d). These coefficients vary for the different culture media (BHI 84 mJ/1.0 OD600, MH 134 mJ/1.0 OD600 and LB 162 mJ/1.0 OD600), indicating that heat curves cannot be converted to growth curves based on biomass in a universal manner for all conditions. Considering the P_{max} values stated above, maximum growth rates of 1.9×10^5 CFU/s for BHI, 8.1×10^4 CFU/s for MH and 6.0×10^4 CFU/s for LB, respectively, can be derived for culture in the microincubator of the INCfAST platform (1.0 OD600 = 5.0×10^8 CFU/mL). Incubation of *E. coli* in BHI yields the fastest growth rate but the lowest heat production rate per unit weight. This finding is in agreement with a previous statement in literature, claiming that the heat production rate per unit weight is inversely proportional to the growth rate in the exponential phase.[154] Interestingly, for all 3 media conditions in the microincubator Q_{max} values are reached on the same time scale (at $t \approx 6$ h, Figure 4.8b).

We also compared the effect of culture temperature in MH on the heat flow curves (Figure 4.8c) and the heat curves (Figure 4.8d). As expected, bacterial populations show the highest transient growth rate (heat production rate) under most favorable conditions (37 °C, $P_{max} \approx 21.3 \pm 2.5 \mu\text{W}$) and lower values for higher (42 °C) or lower temperatures (in particular for 27 °C with $P_{max} \approx 10.3 \pm 1.8 \mu\text{W}$). The apparent lag phase t_{delay} (~ 1.5 h at 37 °C) is shortest for 42 °C ($t_{delay} < 1$ h)

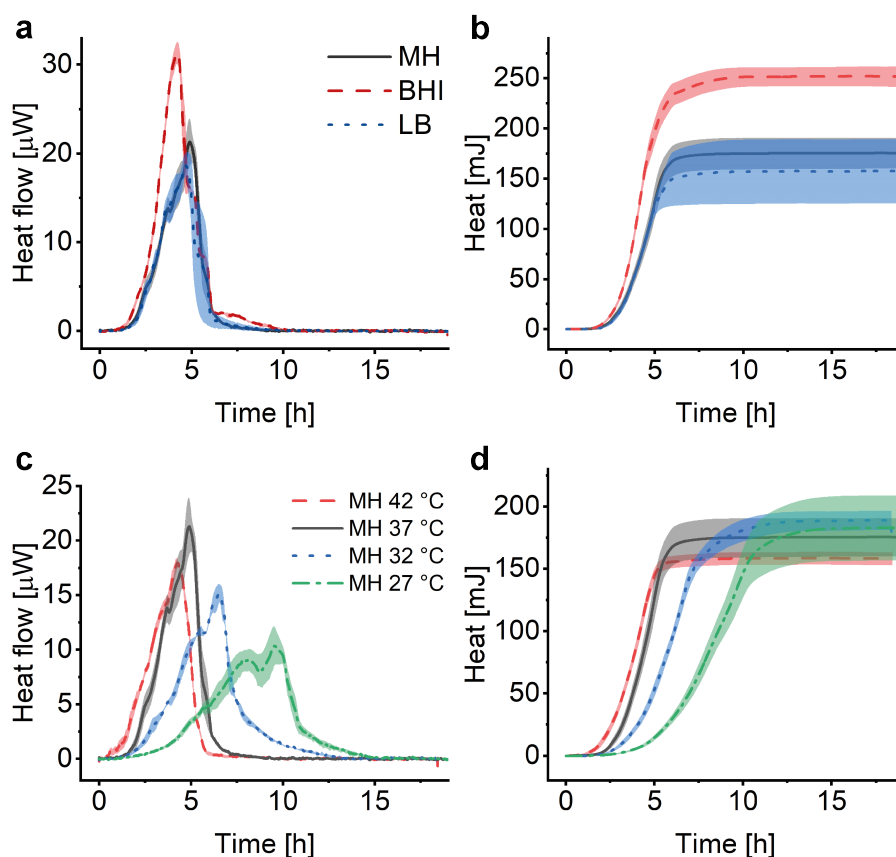


Figure 4.8 – Assessment of metabolic features for different growth conditions of *E. coli* ATCC 25922. (a) Metabolic heat flow $P(t)$ for different culture media at 37 °C. Rich medium (Brain Heart Infusion medium (BHI), black curve) enhances the maximum bacterial heat production rate compared to media containing less nutrients (Mueller-Hinton broth (MH), red curve, or Lysogeny broth (LB), blue curve). (b) Corresponding heat curves $Q(t)$ obtained by time integration of the curves in (a). The maximum total heat value increases with the amount of nutrients provided by the medium (BHI > MH \geq LB). (c) Heat flow curves for different culture temperatures in MH. The maximum peak value for heat flow decreases in the lower temperature range and secondary peaks are more pronounced. The apparent lag phase elongates significantly at 27 °C (green curve). (d) Heat curves obtained by integrating the curves in (c), indicating comparable stationary phase end levels Q_{max} , but reached at different time scales. All curves represent mean \pm SE ($n = 3$).

Table 4.1 – Nutrient content of different culture media.

Brain Heart Infusion medium (BHI)	Mueller-Hinton broth (MH)	Lysogeny broth (LB)
12.5 g/L Brain infusion solids		
5.0 g/L Beef heart infusion solids		
10.0 g/L Proteose peptone	2.0 g/L Beef dehydrated infusion	5 g/L Yeast extract
2.0 g/L Glucose	17.5 g/L Casein hydrolysate	10 g/L Tryptone
5.0 g/L Sodium chloride	1.5 g/L Starch	10 g/L NaCl
2.5 g/L Disodium phosphate		

* according to data sheets available on www.oxoid.com and www.sigmaaldrich.com

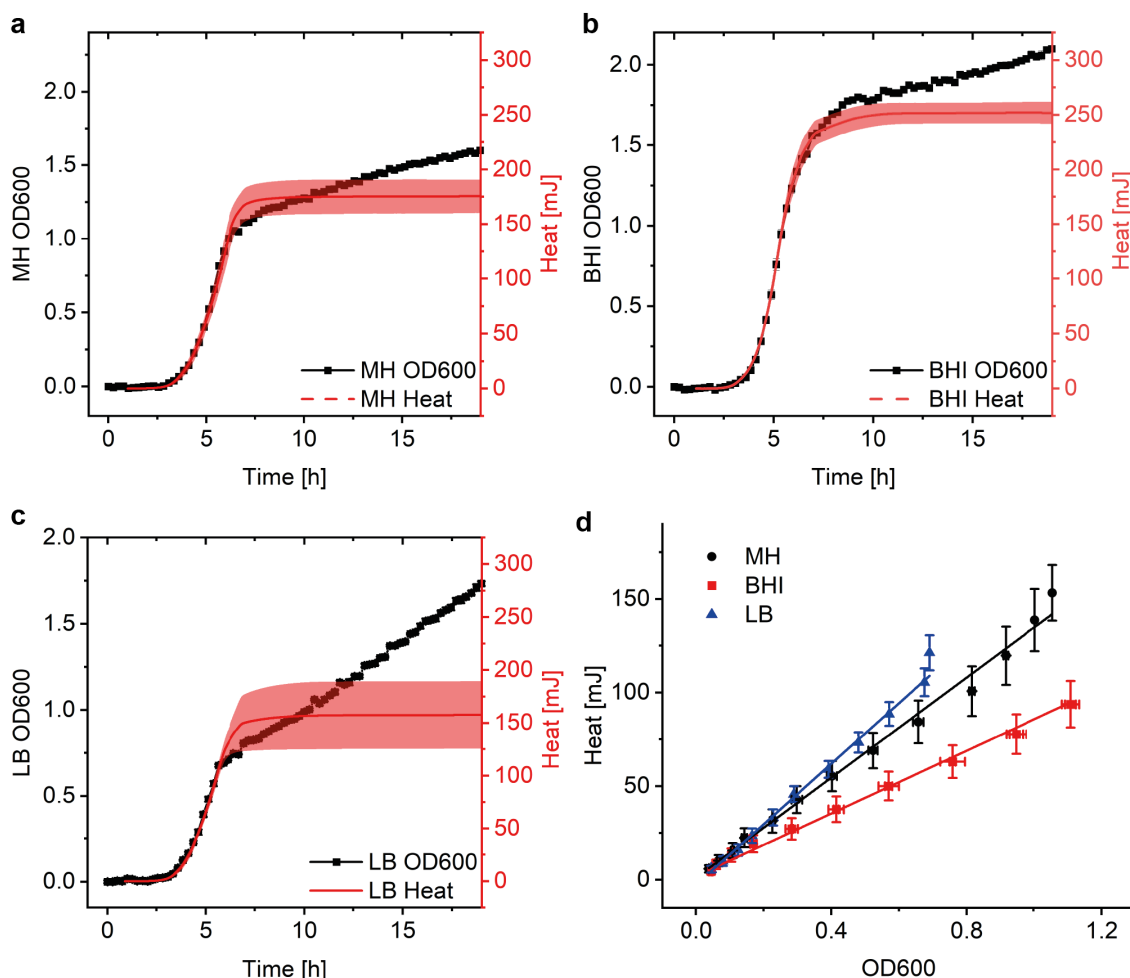


Figure 4.9 – Comparison of metabolic heat curves with optical density measurements in different culture media (*E. coli* ATCC 25922). (a) MH, (b) BHI, and (c) LB at 37 °C, respectively. OD600 curves have been recorded using a plate reader (PerkinElmer VICTOR 3®). Heat signal and OD600 curves overlap well in the exponential growth regions (*i.e.* up to $t \approx 5$ h - 6 h), after time synchronization and scaling with the heat/OD600 coefficients derived from (d). Time synchronization is required as initial delay times t_{delay} depend on the exact culture conditions and thus are different for OD600 and heat curves. Time synchronization was carried out by manually adjusting the midpoint of the exponential growth region, *i.e.* by shifting the heat curve in order to overlap with the OD600 curve. (d) Bacterial growth in different culture media affects the metabolic heat production. In the exponential growth phase, a specific heat/OD600 coefficient could be determined for each medium by linear regression of the heat signal *vs* OD600 data points (134 mJ/1.0 OD600 for MH, 84 mJ/1.0 OD600 for BHI and 162 mJ/1.0 OD600 for LB, respectively). This proportionality indicates that the heat curves recorded with the INCfAST platform can be understood as growth curves after calibration with respect to biomass. In contrast to heat curves, OD600 curves continue increasing in a roughly linear way above the exponential growth phase in all cases (Figure 4.9, 4.10, 4.12), however this region is not relevant for the present analysis. The continuous OD600 increase may be attributed to ongoing oxygen replenishment due to shaking of the culture plates on the plate reader, whereas oxygen is depleted in the microincubator. All curves represent mean \pm SE ($n = 3$).

and becomes more important for decreasing temperatures (~ 3 h at 27°C). Further alterations of the heat flow curves, comprising a general broadening or flattening of the profiles and emerging secondary transient peaks, is observed for culture at low temperatures (Figure 4.8c, 32°C and 27°C). $P(t)$ broadening also results in lower mean slopes Q/t in the exponential phase (Figure 4.8d, in particular at 27°C). Heat signals reach comparable Q_{max} levels for all culture temperatures (160 - 190 mJ), but on longer time scales for decreasing temperature. Corresponding OD curves evolve similarly (Figure 4.10).

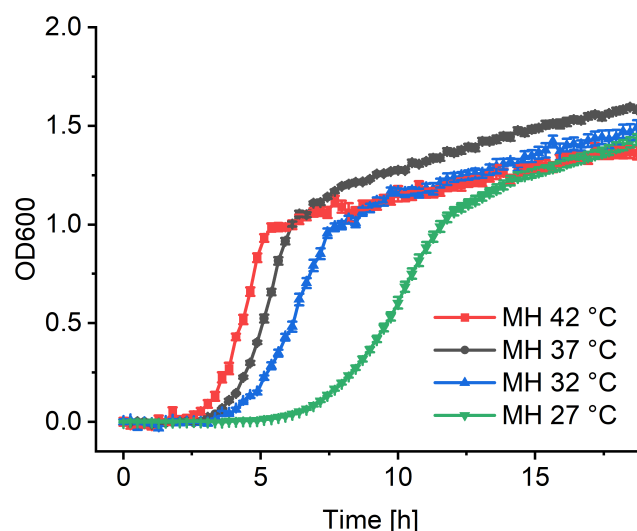


Figure 4.10 – Bacterial growth curves based on optical density measurements for culture at different temperatures in MH (*E. coli* ATCC 25922). Lag phase elongation for decreasing culture temperatures, in particular for 27°C , can be observed in accordance to the heat curves shown in Figure 4.8d. The biomass after overnight culture approaches comparable levels for all conditions. OD600 measurements have been carried out on a plate reader (PerkinElmer VICTOR 3®). All curves represent mean \pm SE ($n = 3$).

4.4.3 AST based on metabolic heat assays

The INCfAST platform was primarily designed for probing the efficacy of antimicrobial drugs and possibly for monitoring specific modes of action by means of metabolic heat assays. The presence or absence of a heat signal during a preset incubation period provides information on antimicrobial susceptibility or resistance of a bacterial strain. We performed AST on *E. coli* ATCC 25922 by analyzing the metabolic heat profiles for a selection of clinically relevant antibiotics and estimated MIC values. Heat flow curves $P(t)$ for ciprofloxacin, ampicillin and gentamicin are shown in Figure 4.11a, 4.11c and 4.11e and the corresponding heat curves $Q(t)$ in Figure 4.11b, 4.11d and 4.11f, respectively. $P(t)$ and $Q(t)$ reference curves without antibiotic (0 mg/L, MH, 37°C) are the same as for the previous assays (Figure 4.7a and Figure 4.8). In the low drug concentration range and for all 3 antimicrobial agents tested, heat flow curves approximately maintain a shape similar to culture in pure medium (Figure 4.11a, 4.11c and 4.11e, black and red curves, respectively), indicating normal

exponential bacterial growth in the microincubator. A decrease of the maximum heat power P_{max} values and the appearance of bump-like features may be noted. Stronger alterations occur with increasing drug concentrations, especially for values approaching MICs. Heat signals disappear at concentrations above MIC (Figure 4.11a, 4.11c and 4.11e, purple curves).

For ciprofloxacin, for instance, heat flow curves are relatively confined for drug concentrations ≤ 0.004 mg/L, whereas at concentrations ≥ 0.015 mg/L heat production is inhibited (Figure 4.11a). In the intermediate concentration range, *i.e.* for 0.008 mg/L in this case, the heat flow curve flattens significantly and secondary transient structures become more apparent. On the corresponding heat curve the mean slope Q/t in the exponential growth region decreases (Figure 4.11b, green curve). The total heat signal disappears at ≥ 0.015 mg/L for the assay duration of 20 h. Moreover, a clear prolongation of the apparent lag phase t_{delay} from ~ 1.5 h at 0 mg/L to ~ 4 h at 0.008 mg/L occurs. Based on this series of experiments, we assume that the MIC value for ciprofloxacin falls into the concentration interval $0.008 \text{ mg/L} < \text{MIC} \leq 0.015 \text{ mg/L}$. Clinical reference values established by the *European Committee on Antimicrobial Susceptibility Testing* (EUCAST) are summarized in Table 4.1 for the antibiotics studied in this work. [155] EUCAST provides a MIC range of 0.004 mg/L - 0.016 mg/L for ciprofloxacin, thus the INCfAST result overlaps well with the reference range.

We performed similar AST assays for ampicillin (Figure 4.11c and Figure 4.11d) and gentamicin (Figure 4.11e and Figure 4.11f). Ampicillin heat flow curves showed prolonged lag phase and a strongly modified profile at 2.4 mg/L (*i.e.* close to MIC). Secondary transient structures are not visible in this case. The mean slope Q/t in the exponential growth region decreases strongly for this concentration (Figure 4.11d, blue curve). Heat production was inhibited for higher concentrations (≥ 4.7 mg/L) providing an INCfAST interval of $2.4 \text{ mg/L} < \text{MIC} \leq 4.7 \text{ mg/L}$, which falls within the EUCAST reference value range 2 mg/L - 8 mg/L (Table 4.2). Heat profiles for bacterial culture with increasing concentrations of gentamicin evolved in a similar way as for ciprofloxacin. Interestingly, close to MIC the secondary $P(t)$ transient features are strongly pronounced but the mean slope Q/t in the exponential growth region seems to be less affected (Figure 4.11e and 4.11f, green curve). In case of gentamicin, however, the INCfAST interval $1.1 \text{ mg/L} < \text{MIC} \leq 2.2 \text{ mg/L}$ was just above the EUCAST range (Table 4.2). As a control, we performed AST using the BMD method on a plate reader (Figure 4.12). OD600 results for ciprofloxacin and ampicillin are consistent with heat measurements in terms of MIC values. The OD600 interval $0.55 \text{ mg/L} < \text{MIC} \leq 1.1 \text{ mg/L}$ for gentamicin is lower compared to the heat assay and overlaps well with the EUCAST range of 0.25 mg/L - 1 mg/L.

4.4.4 Energy spilling of *E. coli* due to antimicrobial stress

OD600 growth curves recorded with the BMD method on a plate reader show that the overall biomass density decreases for increasing antimicrobial concentration in the observed assay duration for the 3 compounds tested (Figure 4.12), whereas observing a systematic behavior of the heat signals Q_{max} is less obvious (Figure 4.11b, 4.11d and 4.11f). This observation implies that the metabolic heat production per biomass unit may be enhanced under antimicrobial stress. In order to analyze the correlation of heat production and biomass in the presence of antimicrobials more accurately, we measured OD600 values of samples directly collected from the microincubator at

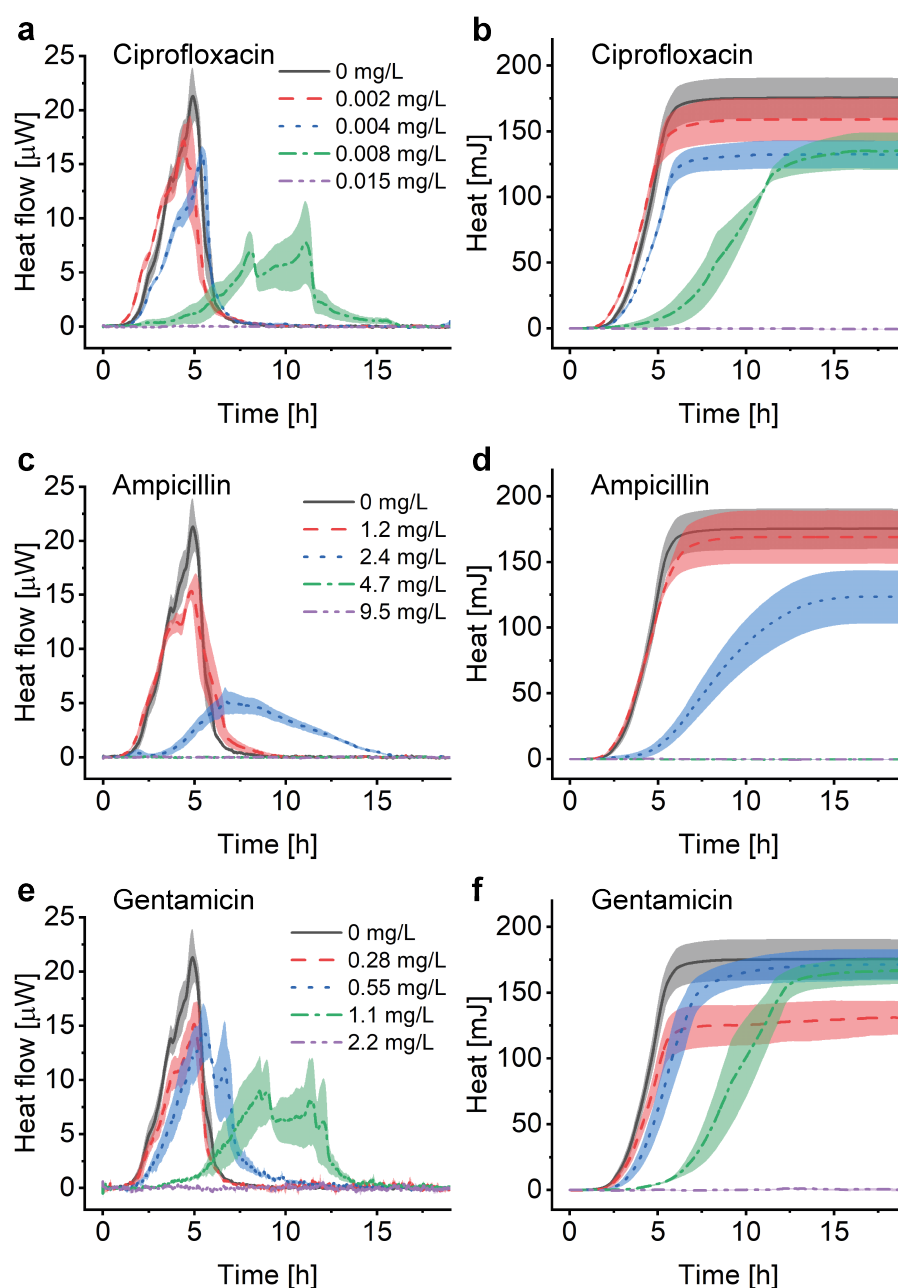


Figure 4.11 – Antimicrobial susceptibility testing with the nanocalorimetry platform. Heat flow curves for *E. coli* ATCC 25922 (MH, 37 °C) recorded in the presence of different antibiotics and concentrations: (a) ciprofloxacin, (c) ampicillin, and (e) gentamicin. In all cases, a strong impact on the growth dynamics could be observed for antimicrobial concentrations approaching the MIC values. The MIC value for a specific antibiotic falls into the concentration interval, where complete suppression of the bacterial heat production occurs first. Corresponding heat curves are shown in (b), (d) and (f), respectively. In accordance to the heat flow curves, a general tendency of lag phase elongation is observed with increasing drug concentration. The absence of heat production above MIC is clearly observed. All curves represent mean \pm SE ($n = 3$).

Table 4.2 – MIC obtained with the nanocalorimetry platform compared to standard EUCAST* values (*E. coli* ATCC 25922). Our metabolic heat experiments (INCfAST platform) allow defining intervals, into which actual MIC values fall. For ciprofloxacin and ampicillin these intervals overlap well with the MIC range established by EUCAST. For gentamicin, the resulting MIC interval is slightly higher, possibly due to reduced activity after oxygen depletion in the microincubator. (*The European Committee on Antimicrobial Susceptibility Testing)

Antibiotic	INCfAST MIC interval (mg/L)	EUCAST MIC range (mg/L)
Ciprofloxacin	$0.008 < \text{MIC} \leq 0.015$	0.004 - 0.016
Ampicillin	$2.4 < \text{MIC} \leq 4.7$	2 - 8
Gentamicin	$1.1 < \text{MIC} \leq 2.2$	0.25 - 1

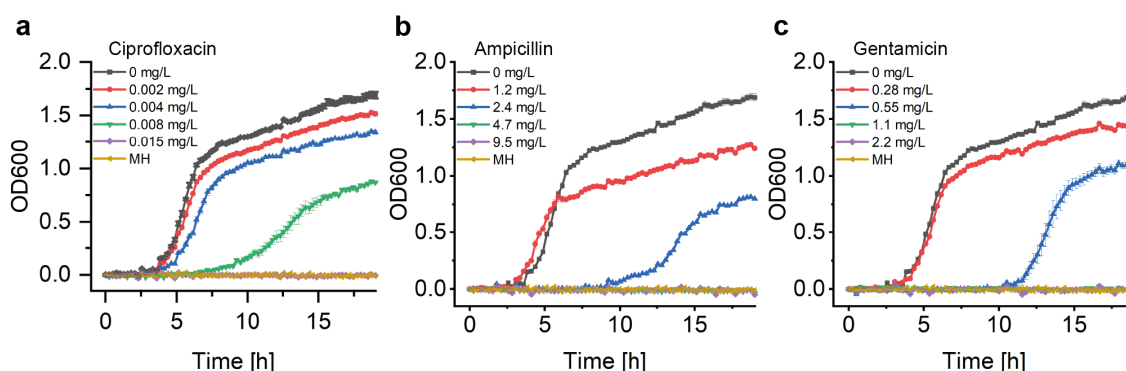


Figure 4.12 – Growth curves based on optical density measurements for bacterial cultures with different antimicrobial conditions in MH (*E. coli* ATCC 25922). OD600 measurements have been carried out on a plate reader (PerkinElmer VICTOR 3®) during bacterial growth in the presence of (a) ciprofloxacin, (b) ampicillin and (c) gentamicin. OD600 measurements reveal a systematic lag phase elongation with antimicrobial exposure comparable to the heat experiments. OD600 MIC intervals for ciprofloxacin and ampicillin are consistent with those derived from the corresponding heat flow measurements and overlap with the EUCAST range. The OD600-based interval for gentamicin $0.55 \text{ mg/L} < \text{MIC} \leq 1.1 \text{ mg/L}$ also overlaps well with the EUCAST range (Table 4.2), in contrast to the heat measurement result (Figure 4.11f). In (a), (b) and (c), OD600 values of bacterial growth under antimicrobial stress decrease gradually with increasing drug concentration. All curves represent mean \pm SE ($n = 3$). “MH” in the graphs corresponds to pure medium without bacteria.

the end of each metabolic heat assay (at $t = 20 \text{ h}$). By this means, we may evaluate precisely the Q_{max} to OD600 ratio of the final bacterial suspension, thus providing an average value resulting from the incubation process on the INCfAST platform. Figure 4.13a summarizes the heat/OD600 coefficients for different antimicrobial exposures below MIC and compares these values to bacterial growth without antibiotics ($98 \pm 12 \text{ mJ}/1.0 \text{ OD600}$ for MH, dashed line). The plot indicates that for ciprofloxacin and gentamicin the bacterial heat production per biomass unit is strongly promoted by antimicrobial stress, reaching a more than 9-fold enhancement close to MICs ($931 \pm 64 \text{ mJ}/1.0 \text{ OD600}$ at 0.008 mg/L for ciprofloxacin and $970 \pm 243 \text{ mJ}/1.0 \text{ OD600}$ at 1.1 mg/L for gentamicin, respectively). The effect is much less pronounced for ampicillin. These values, taken at the end of the assay, are indicative for comparing the impact of the different antibiotics,

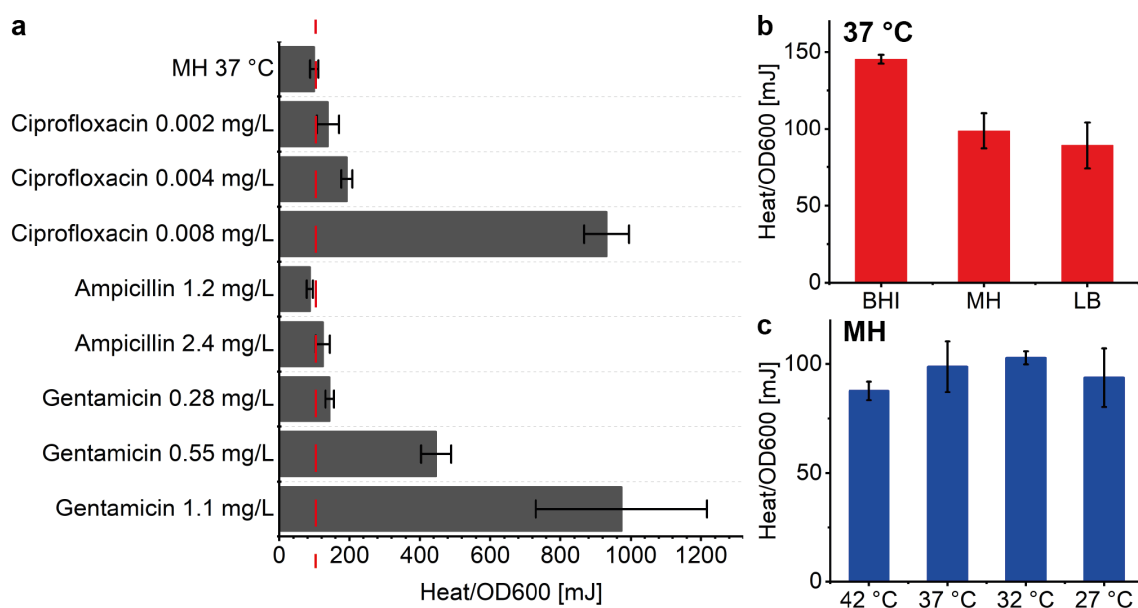


Figure 4.13 – Metabolic heat production *vs* optical density measurements of *E. coli* for different conditions. The plots show heat/OD600 coefficients, *i.e.* the ratio of total heat Q_{max} to the corresponding OD600 value. Both values were determined using the same sample at the endpoint of each assay after incubation on the INCfAST platform ($t = 20$ h). (a) Coefficients for different antimicrobial exposures with respect to the reference value obtained for bacteria inoculated in the microincubator in pure MH (98 mJ/1.0 OD600, dashed line). The bar chart indicates that bacterial heat production per biomass unit is promoted by antimicrobial stress (except for ampicillin 1.2 mg/L). (b) heat/OD600 coefficients for different culture media yielding the highest value for the richest media (BHI) at the endpoint. (c) Bacterial culture at different temperatures did not significantly change the heat/OD600 coefficients. All bars show mean \pm SE ($n = 3$).

but absolute heat/OD600 coefficients may be different if taken during the growth phase at an earlier time point than in the stationary phase, as the biomass may still evolve.

A similar analysis based on assay endpoint detection of OD600 and Q_{max} has been done for different culture media (Figure 4.13b). In this case, the heat/OD600 coefficients decreased from BHI, MH to LB, corresponding to the order of the respective nutrient levels (98 \pm 12 mJ/1.0 OD600 for MH). This was not the case with the coefficients derived previously by linear regression during the exponential growth phase (Figure 4.7b and Figure 4.9d, 134 \pm 3 mJ/1.0 OD600 for MH). OD600 values have been determined either with a sample retrieved from the closed microincubator (Figure 4.13b) or cultured by BMD on a shaking plate reader (Figure 4.7b and Figure 4.9d). Both methods evaluate the heat/OD600 coefficients in a methodically different way, with focus on averaging over the assay duration or on the exponential growth region, respectively. As outlined above, the endpoint method is better suited for evaluating energy spilling over the whole assay duration. For the average heat per biomass at different culture temperatures in MH, no significant differences were observed (Figure 4.13c).

4.5 Discussion

Current AST protocols in clinical microbiological laboratories generally require several incubation cycles for preparing standardized inoculums of isolated microorganisms and/or for pathogen identification. Reliable detection of growth inhibition typically again takes up to ~ 20 h, or even longer depending on the bacterial species. As a consequence, AST results may be available to clinicians only after several days.[36, 139] Hence, in order to improve antimicrobial prescription and treatment practice, there is a clear need for implementing new technologies enabling fast and fully automated AST protocols.[137, 139, 140]

IMC has high potential for biomedical applications in general and for microbial studies in particular.[142–144] In this view, IMC may also be considered as one of the near-future alternatives for AST in clinical settings.[140] For instance, among other specific advantages, calorimetric assays can in principle be performed directly with opaque clinical samples, thus reducing significantly time to result. The non-specificity of the heat signal, however, requires carefully designed protocols in order to extract the information of interest and interpretation of calorimetric data in terms of meaningful microbiological parameters.[143] Despite their performance, commercial IMC systems have drawbacks related to the use of sealed mL-size ampoules, requiring relatively large inoculum size and impeding fluidic manipulations during the assay. The chip-based nanocalorimetry platform developed in this work aims to overcome such bottlenecks, mainly through miniaturization and improved fluidic integration. The INCfAST platform was designed for direct injection of bacterial suspensions or drug solutions into the isothermal microincubator. This feature reduces delay times (only the small sample/drug volume needs to be thermalized), enables automated operation and eventually enhances assay versatility. Minimizing thermal time constants by reducing sample volumes and thermostat size, combined with high sensitivity, is a prerequisite for implementing fast AST protocols.

In the present proof-of-concept study, AST assays were performed on purified samples with volumes of only $150\ \mu\text{L}$. In order to estimate the lower limit of time to detection, we consider the LOD of $750\ \text{nW}$ of the platform, corresponding to $\sim 10^6$ CFU (assuming $1.1\ \text{pW}$ per *E. coli* bacterium). For an inoculum size of 4.2×10^4 CFU (2.8×10^5 CFU/mL) and taking a typical doubling time of 15 - 20 min for *E. coli* in laboratory conditions, the limit of quantification (*i.e.* $3 \times \text{LOD} \approx 2.2\ \mu\text{W}$ or $\sim 2.2 \times 10^6$ CFU per microincubator) should be reached after ~ 2 h. In our study, heat flow was indeed reliably detectable after a time lapse of ~ 2 h (corresponding to $\sim 2\ \mu\text{W}$) under normal culture conditions (MH, no antibiotics, $37\ ^\circ\text{C}$) (Figure 4.7a). An additional conservative time lapse of 30 min for thermalization was allowed after the injection before starting data recording of each experimental curves. This estimation is based on a fast-growing laboratory strain of *E. coli* as bacterial model.

Based on the heat flow curves in Figure 4.11, AST on *E. coli* ATCC 25922 with ampicillin, ciprofloxacin and gentamicin could be safely performed in approximately 5-6 hours using the INCfAST platform. After this incubation duration, a significant difference between the heat flows of the lag phase with antibiotic and the “no growth” of cultures at the MIC occurs in all 3 cases. Nevertheless we have to consider that most clinical isolates, for instance *Klebsiella pneumoniae*, [156] *Acinetobacter*

baumannii,^[157] and *Pseudomonas aeruginosa*^[158] have doubling times in the range of 40 to 140 min, *i.e.* longer than the *E. coli* strain in the present study. Accordingly, the amount of microbials required for reliable detection might only be reached on a longer time scale. On the other hand, the heat power per bacterium also varies for different species. Higher heat power relieves partly the adverse effect of slow growth in terms of time to result. Further investigations will be needed to evaluate the performance of the present approach in real clinical settings and to determine actual realistic time scales of the metabolic heat AST assays.

Compared to other AST techniques, the thermal profiles of metabolic heat assays reveal significantly more information on the mode and kinetics of action of antimicrobial compounds. In the frame of this study, we observed clear variations of growth-related patterns in the presence of antibiotics. One important parameter is the time lapse to reach a detectable heat signal t_{delay} (apparent lag phase). Extension of t_{delay} , in particular for concentrations close to MICs, was observed for the 3 compounds tested (Figure 4.11). This feature may be interpreted as a transient bacteriostatic effect, especially in the case of ciprofloxacin and gentamicin, where the mean growth rate Q/t in the delayed exponential phase is less affected than for ampicillin. On the other hand, ciprofloxacin, ampicillin and gentamicin are bactericidal antibiotics and in principle two reasons may be considered for longer apparent lag phases: (i) the drug compound kills most of the bacteria population, but a small amount of surviving cells (persisters) can be detected only with delay,^[159] or (ii) elongation of the lag phase of the bacterial growth cycle attributed to enzymatic adaptations or genetic regulations in response to changing micro-environmental biochemical conditions.^[160, 161] Single-cell analysis would be necessary for discriminating between these two possibilities. It has been shown previously that lag phase extension in the presence of antibiotics is an important criterion that has to be taken into account, in addition to MIC or IC₅₀ (concentration at 50 % growth inhibition) values, in order to evaluate the efficacy of a drug.^[162] For instance, bacterial strains were found to increase the lag time as a strategy for developing compound tolerance in response to antibiotic stress.^[163] Such findings are important for the clinical evaluation of antimicrobial treatments. As outlined above, the high sensitivity of the INCfAST platform allows bacterial growth detection using a standard inoculum size in pure medium after only ~ 2.5 h for *E. coli*. Detection of infection in clinical samples should in principle be possible on the same time scale. Lag phase extension in the presence of antibiotics, however, counteracts this advantage. Nevertheless, even if antimicrobial action delays the onset of metabolic heat production, heat signals could still be detected as early as ~ 4 h just below MICs for the specific conditions of our assays (Figure 4.11). However, actual time windows in clinical settings for differentiation between growth/growth inhibition based on standard methods are set to 16-20 h. For implementing a new AST approach this time frame has to be reconsidered in order to take full advantage of the new technology, but also for defining an acceptable minimum assay time with respect to reliability of the results from the clinician's point of view.

Antimicrobial action not only delays the onset of heat production, but also has a significant impact on the transient features of the heat flow curves. Progressively emerging secondary peaks and a general broadening of the curves with increasing antimicrobial concentration is most evident in Figure 4.11a and 4.11e for ciprofloxacin and gentamicin, in particular close to MICs (green curves).

Similar features were also observed in heat profiles without drug exposure and are generally attributed to metabolic transitions. Metabolizing sequentially two different carbon sources results in successive growth cycles with multiple exponential phases, possibly separated by a phase with reduced growth rate or transient growth inhibition, giving rise to diauxic shifts.[164, 165] As observed in Figure 4.8c, such effects may be enhanced at low culture temperatures, possibly due to reduced cellular enzymatic activity. Transitions between respiration and a fermentation states (Figure 4.7a, black curve) may also generate more or less pronounced features or peaks, depending on the respective time scales.[166] It was noted previously that deconvolution of heat profiles yields individual Gaussians that can be used to estimate the metabolic heat produced by different mechanisms.[144]

Comprehensive understanding of the dynamic growth behavior at subinhibitory concentrations revealed by specific metabolic heat flow profiles might enable anticipation of antimicrobial efficacy and possibly extrapolation to MIC values, provided that quantification of growth parameters through adequate growth models can be applied.[148, 167] Interestingly, it was demonstrated by von Ah *et al.*, based on an IMC study with 12 antibiotics on *E. coli* and *S. aureus* that it could be possible to distinguish between different modes of antimicrobial action. In addition to alterations of transient features, variations in t_{delay} and mean growth rates Q/t were observed. The 3 antibiotics tested in our nanocalorimetric study have different modes of action. Ciprofloxacin targets topoisomerase II (DNA gyrase), which inhibits bacterial DNA synthesis, ampicillin inhibits cell wall synthesis and gentamicin inhibits bacterial protein synthesis through binding to the A site of 16S ribosomal RNA.[168] As discussed before, we observed a strong impact on the heat profiles for all compounds. Nevertheless, no conclusions can be drawn from our results with respect to different mode of actions. Heat flow curves for ciprofloxacin (Figure 4.11a) and gentamicin (Figure 4.11e) close to MIC are very similar, for ampicillin (Figure 4.11c) the overall shape is different. A more systematic study is necessary for further going interpretations. Investigation of bactericidal and bacteriostatic modes of action would also be of interest.

Total heat curves $Q(t)$ as integrals of heat flow curves allow a better evaluation of mean growth rates Q/t in the exponential region. The aggregated heat value Q_{max} in the stationary phase is determined by growth-limiting factors, such as oxygen/nutrient depletion and waste production in the microincubator. Interestingly, comparing heat curves (Figure 4.11) and OD600 values of samples after incubation in the microincubator revealed that the metabolic heat production may be enhanced under antimicrobial stress (Figure 4.13), an observation that can be understood as energy spilling. Inefficient use or spilling of adenosine triphosphate (ATP) as energy source is known as a possible survival strategy for many bacterial species. In *E. coli*, energy spilling could be mediated by a futile cycle of potassium or ammonium ions.[169] As far as can be deduced from our nanocalorimetric assays (Figure 4.13a), ciprofloxacin and gentamicin induced strong energy spillage close to MICs, whereas the effect was only weakly pronounced for ampicillin.

Table 4.3 – Calorimeters applied for microbiological investigations.

Name [Ref]	Calorimeter	Application	Performance of the platform				Novelty
			LOD [μ W]	Read-out time [h]	Volume [mL]	Specific sensitivity [$\text{mW} \cdot \text{L}^{-1}$]	Temperature stabilization [μ K]
von Ah <i>et al.</i> [148]	TA Instrument TAM-48	AST	2×10^{-1}	24 (CLSI standard)	1-4	$\sim 1.3 \times 10^{-1}$	$\pm 1 \times 10^2$
MICs; Similar heat patterns were identified for antibiotics with similar mechanism.							
Braissant <i>et al.</i> [39, 113, 170]	Syncel calScreener	Microbial metabolic activity and AST	6×10^{-1}	8 - 18 (AST)	6×10^{-1}	~ 1	N/A
Microbial lag phase investigation; MICs.							
Cooney <i>et al.</i> [171]	Commercial products	Fermentation, heat and oxygen consumption measurement	N/A	N/A	9×10^3	N/A	$\pm 2.5 \times 10^5$
Heat per oxygen consumption was determined during the bacterial fermentation process.							
Birou <i>et al.</i> [172]	BSC 81 heat-flux calorimeter	Aerobic metabolic activity monitoring	3×10^5	N/A	1.5×10^3	2×10^2	N/A
Simultaneously determines heat, biomass and oxygen consumption.							
Liu <i>et al.</i> [98]	INCfAST (Current study)	AST	7.5×10^{-1}	5-7	1.5×10^{-1}	~ 5	$\pm 2.5 \times 10^2$
MICs; Energy spillage from heat perspective; Quasi-simultaneous measurement of heat and oxygen. (<i>E. coli</i> as model)							

Previously, an initial increase of the heat production rate upon antibiotic exposure was observed in *Pseudomonas putida* biofilms and related to energy-dependent resistance mechanisms.[173] In addition, there is evidence that antibiotics can perturb bacterial respiration and central metabolism. A recent publication demonstrated that antibiotic-induced adenine limitation increases purine biosynthesis and ATP demand, which might relate antimicrobial stress to enhanced bacterial heat production.[174]

Calorimetry, and more specifically microcalorimetry, is an established method for investigating the microbial metabolic activity. Table 4.3 provides a comparison of the current study and several representative calorimeters for microbiological investigations. Based on this table, we consider that our platform has a technical performance comparable with existing devices. The TA-48 from TA instruments shows the best overall technical performance, providing a balance between the required sample volume and the LOD. Cooney *et al.* attempted to study the heat and oxygen consumption simultaneously, however the required sample volume was high and the device was bulky.[171] Birou *et al.* improved the set-up and the performance.[172] Comparing to other systems, we could further reduce the required sample volume. In the current mode of operation of the INCfAST platform, the microincubator serves as both the bioreactor and the measurement chamber, with the sample being isolated from the environment. In principle, our system can also be operated in a different way, using the (external) sample reservoir (see Figure 4.4) as a bioreactor for bacterial culture. In this case the following features could be implemented: (i) performing sequential heat measurements by periodically injecting small sample volumes into the microincubator, and (ii) metabolic heat measurements on highly aerobic bacteria (*e.g. Mycobacterium tuberculosis*) as adequate growth conditions can be provided by oxygen replenishment and agitation of the medium in the sample reservoir. This mode of operation also enables the possibility to work with samples of low bacterial concentration, for instance samples from patient with suspected blood infection. An added value of the INCfAST platform is that oxygen consumption measurements as an indirect calorimetric method can be performed using the same fluidic configuration with only minor modifications of the platform (described in Chapter 5). In view of the AST application, all cited methods attempted to reduce the read-out time, however, the actual assay duration depends on the investigated bacterial species, applied antimicrobials and, at least for the time being, AST results must be evaluated and compared with respect to the time scale of the standard protocol defined by CLSI (~ 20 h).

4.6 Conclusion

There is a general consensus among healthcare actors involved in infectious diseases management and microbiologists that the implementation of new technologies aiming to reduce the time to result of current clinical AST protocols is a key issue in combatting the increasingly important global health problem related to AMR of clinically important bacterial strains. In this regard, we developed a miniaturized isothermal nanocalorimetry platform (INCfAST) providing a direct method for measuring bacterial metabolic heat of *E. coli*. Considering bacterial heat production as a new phenotype opens the way to a more comprehensive understanding of fundamental metabolic

processes, especially upon drug exposure. High heat detection sensitivity and signal stability enabled detection of bacterial growth in the microincubator under normal conditions after only ~ 2-3 hours. Eventually infection in clinical samples could be monitored on a similar time scale. The integrated fluidic design facilitates sample handling and the implementation of automated assay protocols. The versatility of the method was first demonstrated by analyzing metabolic heat profiles for various culture conditions over extended durations. More importantly, we could demonstrate that our nanocalorimetry platform has high potential for evaluating the efficacy and activity of antimicrobial compounds, in particular with respect to the implementation of fast AST protocols. Based on our experimental heat flow curves, AST could be performed in 5-6 hours using a fast-growing laboratory strain of *E. coli* as bacterial model. Heat flow profiles provided a detailed real-time insight of the dynamics of antimicrobial effects for all 3 antibiotics tested (ciprofloxacin, ampicillin and gentamicin). We observed notable lag phase extensions close to MICs and alterations of transient features in the heat flow curves. MIC values obtained with the INCfAST platform are consistent with accepted clinical values for *E. coli* in the case of ciprofloxacin and ampicillin. Gentamicin showed a slightly higher value range, most likely due to its oxygen-dependent activity. In contrast to the standard BMD method, the calorimetric approach does not rely on optical parameters, in principal raw patient samples could therefore be used, omitting culture steps for sample purification. Discrimination between growth/growth inhibition in the presence of antibiotics was possible on a time scale of only a few hours. In this view, we anticipate that with the present nanocalorimetry approach, AST assays can be performed on a faster time scale and with enhanced information content than current conventional clinical methods.

References

3. O'Neill, J. *Tackling Drug-Resistant Infections Globally: Final Report and Recommendations. The Review on Antimicrobial Resistance, Chaired by Jim O'Neill* (May 2016) (cit. on pp. 4, 53).
4. Zaman, S. B. *et al.* A Review on Antibiotic Resistance: Alarm Bells Are Ringing. *Cureus* **9**, e1403 (June 28, 2017) (cit. on pp. 4, 53).
36. Balouiri, M., Sadiki, M. & Ibnsouda, S. K. Methods for in Vitro Evaluating Antimicrobial Activity: A Review. *Journal of Pharmaceutical Analysis* **6**, 71–79 (Apr. 2016) (cit. on pp. 9, 54, 71).
39. Wadsö, I. *et al.* A Well-Plate Format Isothermal Multi-Channel Microcalorimeter for Monitoring the Activity of Living Cells and Tissues. *Thermochimica Acta* **652**, 141–149 (June 2017) (cit. on pp. 10, 55, 74).
40. Baltekin, Ö., Boucharin, A., Tano, E., Andersson, D. I. & Elf, J. Antibiotic Susceptibility Testing in Less than 30 Min Using Direct Single-Cell Imaging. *Proceedings of the National Academy of Sciences*, 201708558 (Aug. 8, 2017) (cit. on pp. 10, 11, 13, 54, 102, 127, 137).
81. Johannessen, E. A. *et al.* Micromachined Nanocalorimetric Sensor for Ultra-Low-Volume Cell-Based Assays. *Analytical Chemistry* **74**, 2190–2197 (May 2002) (cit. on pp. 39, 40, 55).
85. Lee, W., Fon, W., Axelrod, B. W. & Roukes, M. L. High-Sensitivity Microfluidic Calorimeters for Biological and Chemical Applications. *Proceedings of the National Academy of Sciences* **106**, 15225–15230 (2009) (cit. on pp. 41–43, 55).
89. Lerchner, J. *et al.* Miniaturized Calorimetry — A New Method for Real-Time Biofilm Activity Analysis. *Journal of Microbiological Methods* **74**, 74–81 (Aug. 2008) (cit. on pp. 40, 43, 55).
98. Liu, Y., Lehnert, T. & Gijs, M. A. M. Fast Antimicrobial Susceptibility Testing on *Escherichia coli* by Metabolic Heat Nanocalorimetry. *Lab on a Chip* **20**, 3144–3157 (Aug. 26, 2020) (cit. on pp. 43, 53, 74, 83, 127).
102. Inomata, N., Toda, M., Sato, M., Ishijima, A. & Ono, T. Pico Calorimeter for Detection of Heat Produced in an Individual Brown Fat Cell. *Applied Physics Letters* **100**, 154104 (Apr. 9, 2012) (cit. on pp. 43, 55).
108. Torres, F. E. *et al.* Enthalpy Arrays. *Proceedings of the National Academy of Sciences* **101**, 9517–9522 (June 29, 2004) (cit. on pp. 45, 55).
109. Kim, J., Nam, S. M., Kim, J., Seo, S. & Lee, W. *High-Sensitivity Parylene Microfluidic Chip Calorimeters for Measurements of Cellular Metabolic Heat* in 2019 IEEE 32nd International Conference on Micro Electro Mechanical Systems (MEMS) 2019 IEEE 32nd International Conference on Micro Electro Mechanical Systems (MEMS) (IEEE, Seoul, Korea (South), Jan. 2019), 544–546. doi:[10.1109/MEMSYS.2019.8870722](https://doi.org/10.1109/MEMSYS.2019.8870722) (cit. on pp. 45, 55).
111. Recht, M. I. *et al.* Measurement of Enzyme Kinetics and Inhibitor Constants Using Enthalpy Arrays. *Analytical Biochemistry* **388**, 204–212 (May 15, 2009) (cit. on pp. 45, 55).

113. Braissant, O. *et al.* Isothermal Microcalorimetry Accurately Detects Bacteria, Tumorous Microtissues, and Parasitic Worms in a Label-Free Well-Plate Assay. *Biotechnology Journal* **10**, 460–468 (Mar. 2015) (cit. on pp. 46, 47, 74).
118. Krenger, R., Lehnert, T. & Gijs, M. A. M. Dynamic Microfluidic Nanocalorimetry System for Measuring *Caenorhabditis Elegans* Metabolic Heat. *Lab on a Chip* **18**, 1641–1651 (2018) (cit. on pp. 47, 56, 147).
120. Trampuz, A., Salzmann, S., Antheaume, J. & Daniels, A. U. Microcalorimetry: A Novel Method for Detection of Microbial Contamination in Platelet Products. *Transfusion* **47**, 1643–1650 (Sept. 2007) (cit. on pp. 47, 54).
133. Cantas, L. *et al.* A Brief Multi-Disciplinary Review on Antimicrobial Resistance in Medicine and Its Linkage to the Global Environmental Microbiota. *Frontiers in Microbiology* **4** (2013) (cit. on p. 53).
134. Sugden, R., Kelly, R. & Davies, S. Combatting Antimicrobial Resistance Globally. *Nature Microbiology* **1**, 16187 (Oct. 2016) (cit. on p. 53).
135. Lowy, F. D. Antimicrobial Resistance: The Example of Staphylococcus Aureus. *The Journal of Clinical Investigation* **111**, 10 (2003) (cit. on p. 53).
136. Goossens, H., Ferech, M., Vander Stichele, R., Elseviers, M. & ESAC Project Group. Outpatient Antibiotic Use in Europe and Association with Resistance: A Cross-National Database Study. *Lancet (London, England)* **365**, 579–587 (Feb. 12, 2005–18) (cit. on p. 53).
137. Van Belkum, A. *et al.* Developmental Roadmap for Antimicrobial Susceptibility Testing Systems. *Nature Reviews Microbiology* **17**, 51–62 (Jan. 2019) (cit. on pp. 54, 71, 102).
138. Andrews, J. M. Determination of Minimum Inhibitory Concentrations. *Journal of Antimicrobial Chemotherapy* **48**, 5–16 (2001) (cit. on p. 54).
139. Puttaswamy, S., Gupta, S. K., Regunath, H., Smith, L. P. & Sengupta, S. A Comprehensive Review of the Present and Future Antibiotic Susceptibility Testing (AST) Systems. *Archives of Clinical Microbiology* **9**, 83 (2018) (cit. on pp. 54, 71).
140. Van Belkum, A. & Dunne, W. M. Next-Generation Antimicrobial Susceptibility Testing. *Journal of Clinical Microbiology* **51**, 2018–2024 (July 1, 2013) (cit. on pp. 54, 71).
141. Athamanolap, P., Hsieh, K., Chen, L., Yang, S. & Wang, T.-H. Integrated Bacterial Identification and Antimicrobial Susceptibility Testing Using PCR and High-Resolution Melt. *Analytical Chemistry* **89**, 11529–11536 (Nov. 7, 2017) (cit. on p. 54).
142. Braissant, O., Wirz, D., Göpfert, B. & Daniels, A. Biomedical Use of Isothermal Microcalorimeters. *Sensors* **10**, 9369–9383 (Oct. 18, 2010) (cit. on pp. 54, 71).
143. Braissant, O., Bachmann, A. & Bonkat, G. Microcalorimetric Assays for Measuring Cell Growth and Metabolic Activity: Methodology and Applications. *Methods* **76**, 27–34 (Apr. 2015) (cit. on pp. 54, 71).

144. Braissant, O., Wirz, D., Göpfert, B. & Daniels, A. U. Use of Isothermal Microcalorimetry to Monitor Microbial Activities. *FEMS Microbiology Letters* **303**, 1–8 (Feb. 2010) (cit. on pp. 54, 71, 73).
145. Von Ah, U., Wirz, D. & Daniels, A. U. Rapid Differentiation of Methicillin-Susceptible *Staphylococcus Aureus* from Methicillin-Resistant *S. Aureus* and MIC Determinations by Isothermal Microcalorimetry. *Journal of Clinical Microbiology* **46**, 2083–2087 (June 1, 2008) (cit. on p. 54).
146. Baldoni, D., Hermann, H., Frei, R., Trampuz, A. & Steinhuber, A. Performance of Microcalorimetry for Early Detection of Methicillin Resistance in Clinical Isolates of *Staphylococcus Aureus*. *Journal of Clinical Microbiology* **47**, 774–776 (Mar. 1, 2009) (cit. on p. 54).
147. Yang, L. N., Xu, F., Sun, L. X., Zhao, Z. B. & Song, C. G. Microcalorimetric Studies on the Antimicrobial Actions of Different Cephalosporins. *Journal of Thermal Analysis and Calorimetry* **93**, 417–421 (Aug. 2008) (cit. on p. 54).
148. Von Ah, U., Wirz, D. & Daniels, A. Isothermal Micro Calorimetry – a New Method for MIC Determinations: Results for 12 Antibiotics and Reference Strains of *E. Coli* and *S. Aureus*. *BMC Microbiology* **9**, 106 (2009) (cit. on pp. 54, 73, 74).
149. Higuera-Guisset, J. *et al.* Calorimetry of Microbial Growth Using a Thermopile Based Microreactor. *Thermochimica Acta* **427**, 187–191 (Mar. 2005) (cit. on p. 55).
150. Buchholz, F. *et al.* Chip-Calorimetry Provides Real Time Insights into the Inactivation of Biofilms by Predatory Bacteria. *Biofouling* **28**, 351–362 (Mar. 2012) (cit. on p. 55).
151. Mariana, F. *et al.* Chip-Calorimetric Monitoring of Biofilm Eradication with Antibiotics Provides Mechanistic Information. *International Journal of Medical Microbiology* **303**, 158–165 (Apr. 2013) (cit. on p. 55).
152. Wang, S. *et al.* Micro-Differential Scanning Calorimeter for Liquid Biological Samples. *Review of Scientific Instruments* **87**, 105005 (Oct. 2016) (cit. on p. 55).
153. Stevenson, K., McVey, A. F., Clark, I. B. N., Swain, P. S. & Pilizota, T. General Calibration of Microbial Growth in Microplate Readers. *Scientific Reports* **6**, 38828 (Dec. 2016) (cit. on pp. 59, 63, 104).
154. Rosenberg, E. & Zilber-Rosenberg, I. Do Microbiotas Warm Their Hosts? *Gut Microbes* **7**, 283–285 (July 3, 2016) (cit. on p. 63).
155. EUCAST. "The European Committee on Antimicrobial Susceptibility Testing. Routine and Extended Internal Quality Control for MIC Determination and Disk Diffusion as Recommended by EUCAST. Version 9.0, 2019. <http://www.eucast.org>." (2019) (cit. on pp. 67, 104).
156. Regué, M. *et al.* A Gene, Uge, Is Essential for *Klebsiella Pneumoniae* Virulence. *Infection and Immunity* **72**, 54–61 (Jan. 2004) (cit. on p. 71).

157. Moffatt, J. H. *et al.* Colistin Resistance in *Acinetobacter Baumannii* Is Mediated by Complete Loss of Lipopolysaccharide Production. *Antimicrobial Agents and Chemotherapy* **54**, 4971–4977 (Dec. 2010) (cit. on p. 72).
158. Yang, L. *et al.* In Situ Growth Rates and Biofilm Development of *Pseudomonas Aeruginosa* Populations in Chronic Lung Infections. *Journal of Bacteriology* **190**, 2767–2776 (Apr. 15, 2008) (cit. on p. 72).
159. Harms, A., Maisonneuve, E. & Gerdes, K. Mechanisms of Bacterial Persistence during Stress and Antibiotic Exposure. *Science* **354**, aaf4268 (Dec. 16, 2016) (cit. on p. 72).
160. Swinnen, I. Predictive Modelling of the Microbial Lag Phase: A Review. *International Journal of Food Microbiology* **94**, 137–159 (July 2004) (cit. on p. 72).
161. Rolfe, M. D. *et al.* Lag Phase Is a Distinct Growth Phase That Prepares Bacteria for Exponential Growth and Involves Transient Metal Accumulation. *Journal of Bacteriology* **194**, 686–701 (Feb. 1, 2012) (cit. on p. 72).
162. Li, B., Qiu, Y., Shi, H. & Yin, H. The Importance of Lag Time Extension in Determining Bacterial Resistance to Antibiotics. *The Analyst* **141**, 3059–3067 (2016) (cit. on p. 72).
163. Fridman, O., Goldberg, A., Ronin, I., Shores, N. & Balaban, N. Q. Optimization of Lag Time Underlies Antibiotic Tolerance in Evolved Bacterial Populations. *Nature* **513**, 418–421 (Sept. 2014) (cit. on p. 72).
164. Loomis, W. F. & Magasanik, B. Glucose-Lactose Diauxie in *Escherichia Coli*. *Journal of bacteriology* **93**, 1397–1401 (1967) (cit. on p. 73).
165. Solopova, A. *et al.* Bet-Hedging during Bacterial Diauxic Shift. *Proceedings of the National Academy of Sciences* **111**, 7427–7432 (May 20, 2014) (cit. on p. 73).
166. Johansson, P. & Wadsö, I. An Isothermal Microcalorimetric Titration/Perfusion Vessel Equipped with Electrodes and Spectrophotometer. *Thermochimica Acta* **342**, 19–29 (Dec. 1999) (cit. on p. 73).
167. Braissant, O., Bonkat, G., Wirz, D. & Bachmann, A. Microbial Growth and Isothermal Microcalorimetry: Growth Models and Their Application to Microcalorimetric Data. *Thermochimica Acta* **555**, 64–71 (Mar. 2013) (cit. on p. 73).
168. Kohanski, M. A., Dwyer, D. J. & Collins, J. J. How Antibiotics Kill Bacteria: From Targets to Networks. *Nature Reviews Microbiology* **8**, 423–435 (June 2010) (cit. on pp. 73, 125).
169. Russell, J. B. The Energy Spilling Reactions of Bacteria and Other Organisms. *Journal of Molecular Microbiology and Biotechnology* **13**, 1–11 (2007) (cit. on p. 73).
170. Tellapragada, C. *et al.* Isothermal Microcalorimetry Minimal Inhibitory Concentration Testing in Extensively Drug Resistant Gram-Negative Bacilli: A Multicentre Study. *Clinical Microbiology and Infection* **26**, 1413.e1–1413.e7 (Oct. 1, 2020) (cit. on p. 74).
171. Cooney, C. L., Wang, D. I. C. & Mateles, R. I. Measurement of Heat Evolution and Correlation with Oxygen Consumption during Microbial Growth. *Biotechnology and Bioengineering* **11**, 269–281 (1969) (cit. on pp. 74, 75, 95).

172. Birou, B., Marison, I. W. & Stockar, U. V. Calorimetric Investigation of Aerobic Fermentations. *Biotechnology and Bioengineering* **30**, 650–660 (Oct. 5, 1987) (cit. on pp. 74, 75, 95).
173. Buchholz, F. *et al.* Chip Calorimetry for Fast and Reliable Evaluation of Bactericidal and Bacteriostatic Treatments of Biofilms. *Antimicrobial Agents and Chemotherapy* **54**, 312–319 (Jan. 1, 2010) (cit. on p. 75).
174. Yang, J. H. *et al.* A White-Box Machine Learning Approach for Revealing Antibiotic Mechanisms of Action. *Cell* **177**, 1649–1661.e9 (May 2019) (cit. on p. 75).

5 Microbial oxygen consumption

Aerobic respiration is a fundamental aspect of bacterial metabolic activity. For facultative anaerobic bacteria like *E. coli*, oxygen uptake can be considered as a viability indicator from the metabolic perspective. Here, we propose a photoluminescence-based oxygen sensing system for analyzing microbial oxygen consumption rates (OCR). By adapting the INCfAST platform, oxygen consumption and metabolic heat production could be measured in a quasi-synchronized way. We measured OCR as a function of different parameters, in particular for microbial exposure to different antibiotics and performed AST by quantification of consumed oxygen.

Part of the experimental results shown in this chapter have been presented in the following paper: Liu, Y., Lehnert, T. & Gijs, M. A. M. Fast Antimicrobial Susceptibility Testing on *Escherichia coli* by Metabolic Heat Nanocalorimetry. *Lab on a Chip* **20**, 3144–3157 (Aug. 26, 2020)

5.1 Introduction

Oxygen is associated to aerobic metabolic activity. As the main carbohydrate, glucose is converted to pyruvate by the process of glycolysis in the cytoplasm. In eukaryotes and in the presence of oxygen, mitochondria couple the oxidation of pyruvate to the production of a high amount of adenosine triphosphate (ATP) by the electron transport chain (ETC) when oxygen is present.[175] Under aerobic respiration, using oxygen as the electron acceptor, pyruvate is metabolized and ATP is formed with energy loss in terms of heat. Without the presence of oxygen, pyruvate undergoes a fermentation process in which energy can be produced, however some toxic compounds such as lactic acid, ethanol, or mixed acids can be generated as well, depending on the bacterial species.[175] Measuring the oxygen consumption and the dissolved oxygen is important to better evaluate the bacterial metabolic activity. Various technologies have been developed,[176] in particular, nanomaterial-based sensors for quantifying concentrations of dissolved the oxygen concentration in a microfluidic system.[177] In the previous chapter, we evaluated the metabolic activity from the perspective of heat production. We modified the isothermal nanocalorimetry platform to implement an oxygen measurement system enabling oxygen consumption measurements for identical culture conditions in parallel. Similar to the heat production, bacterial growth under different cultural conditions leads to different OCR footprints. We investigated the

oxygen consumption in different cultural media and at different temperatures. In particular, using oxygen consumption as an indicator, we performed a proof-of-concept AST study with the platform. This AST method is useful to determine the antimicrobial susceptibility of facultative anaerobic bacteria. By combining heat and oxygen measurements, we were able to identify the transition from aerobic to anaerobic or fermentation metabolism. In addition, this method provides a way to evaluate the energy efficiency of the metabolic process by quantifying heat production with respect to oxygen consumption.

5.2 Current approaches for measuring oxygen consumption rate (OCR)

There are various methods to determine oxygen concentrations in different kind of systems, including Winkler titration, electrochemical, pressure-based and optical methods.[178]

5.2.1 Titration method

For Winkler titration, oxygen in the solution is fixed by forming an acid compound, which can be neutralized by titration with a color change.[179, 180] Based on the color change, the amount of titration reagent is determined and the oxygen concentration can be calculated. Winkler titration is precise thus well-suited for calibration, however, it cannot monitor the dissolved oxygen continuously, as is required for a biological study.

5.2.2 Electrochemical methods

For miniaturized applications, small-scale Clark-type electrodes were developed to measure the dissolved oxygen concentration based on an electrochemical approach.[181] Clark-type cells usually comprise a platinum electrode covered with an oxygen-permeable membrane, where oxygen is reduced, if a voltage of about 0.7 V is applied. However, the intrinsic consumption of oxygen at the cathode may diminish the accuracy of the results and the lifespan may be limited due to contamination of the electrodes. In addition, integration in fluidic devices is limited by the physical electrical connections to the sensing electrodes for the current read-out.

5.2.3 Spectroscopic method

The emission of short-live radioisotopes of elements such as oxygen, nitrogen, and carbon can be used for the oxygen sensing in a three-dimensional, non-invasive, and full-body imaging way. This radioisotope technique is, however, far beyond routine applications and expensive.[176] Magnetic resonance methods measure oxygen based on the relaxation time of ^{19}F in perfluorinated hydrocarbons (PFHCs) or ^1H in hexamethyldisiloxane (HMDSO). PFHCs and HMDSO work as contrast agents. This relaxation time is affected by the partial pressure of O_2 , *i.e.* the oxygen concentration.[176] Oxygen sensing can also be based on electron paramagnetic resonance (EPR) since O_2 has a triplet electronic ground state and is paramagnetic. The paramagnetic state of O_2 cannot be rendered in a biological samples due to the broad spectral lines. The normal way is to

5.2. Current approaches for measuring oxygen consumption rate (OCR)

measure indirectly by adding exogenous paramagnetic substances such as nitroxides, which can be metabolized quickly to diamagnetic hydroxylamines. The rate of this process depends on the local O_2 concentration.[176] Spectroscopic methods are expensive, difficult to calibrate, and usually hard to work with biological samples.

5.2.4 Commercial respirometry

Oxygen sensing in living organisms, also called respirometry, is commonly used for metabolic studies. The state-of-the-art in commercial respirometry is the Seahorse Extracellular Flux Analyzer (Seahorse XF, Agilent, USA) as shown in Figure 5.1a.[182]

This device is able to measure cellular oxygen consumption rate (OCR) and extracellular acidification rate (ECAR) in a 96-well plate format (Seahorse XF96). ECAR measures the concentration of H^+ (pH change) in the solution. The fermentation of pyruvate produces lactic acid, which lowers pH value of the solution. The production of CO_2 produced in the tricarboxylic acid cycle (TCA cycle) will further diminish the pH. The device is able to maintain an optimal culture temperature, for instance, 37 °C. Synchronized O_2 and H^+ measurements provide a more holistic view of the metabolic activity. The sensing cartridges are equipped with O_2 and H^+ dependent luminophores (see next section) to correlate the O_2 and H^+ concentrations with the light signal. During the OCR and ECAR measurement, an array of optical fibers is inserted to the well plate as shown in Figure 5.1b. The insertion of fibers confines the sample volume in the well to about 2 μ L and seals the chamber to prevent oxygen diffusion between the culture media and the surrounding air (Figure 5.1b, closed position). Then OCR and ECAR can be determined according to a real-time continuous measurement of the concentration of O_2 and H^+ change for a 5 min. Each individual well is equipped with injection ports allowing sequential introduction of up to four drugs into the well comprising the sample. The optical fiber can be moved up and down to achieve good mixing for the dispensed reagents with the culture media (Figure 5.1b, open position).

5.2.5 Luminescence-based oxygen sensing

Optical sensing technologies are more suitable for microfluidic systems, compared to electrochemical methods. The technology is scalable, non-invasive and requires no external physical connections between the sensing unit and the detector. A sensing unit made of nanoparticles does not get degraded by the sample and does not consume oxygen intrinsically.[178]

The emission of light by a substance upon absorption of light at a specific wavelength is called photoluminescence. Photoluminescence can be categorized into fluorescence and phosphorescence. Fluorescence indicates a light-emitting transition of excited electrons from the lowest excited state to the ground state in a fast process. In contrast, excited electrons in phosphorescence first endure a fast intersystem crossing from a singlet excited state to an energetically favorable triplet excited state, and then re-emit light in a slow way before returning to the relaxed ground singlet state. Luminescence-based oxygen sensors usually take advantage of either fluorescent or

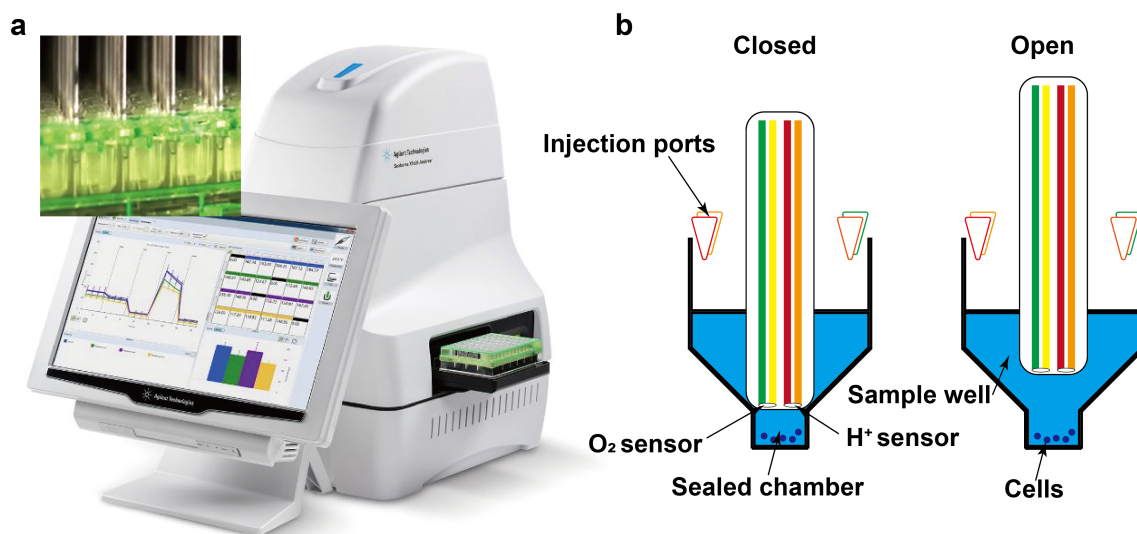


Figure 5.1 – State-of-the-art system for respirometry. (a) Seahorse XF respirometer from Agilent. (b) Schematic of the measuring unit of the commercial Seahorse XFb96. The optical fiber can be used to seal the cell chamber (left) or for mixing of injected compounds with the sample by moving up and down (right). Image adapted and reproduced from [182]

phosphorescent dyes for which the luminescent response is correlated to the surrounding oxygen concentrations. The presence of oxygen usually quenches the luminescence by absorbing the energy when excited electron relax to the ground state.[183]

Mathematically, the Stern-Volmer equation models the quenching behavior.[184]

$$\frac{\tau_0}{\tau} = \frac{I_0}{I} + k_q \cdot \tau_0 \cdot C_{O_2} \quad (5.1)$$

where C_{O_2} is the concentration of dissolved oxygen, k_q is the quenching rate constant, τ and τ_0 are the excited state lifetimes in the presence and absence of oxygen, I and I_0 are the excited state luminescence intensities in the presence and absence of the oxygen. Based on this model, oxygen concentration can be determined by detecting the luminescence intensity or excited state lifetime.

The measurement of photoluminescence intensity after excitation of the sensing dye is easy to implement. However, it is significantly influenced by photobleaching after repeated excitation. Therefore, a correlation between the luminescence lifetime and oxygen concentration is a more robust and reliable sensing method. In the luminescence lifetime-based sensing, a modulated light source is used to excite the sensing dye. Re-emitted luminescence time is measured in the time domain or in the frequency domain (Figure 5.2).

In the time domain, the excitation pulse is a square wave that induces exponential decay. Two acquisition windows at time t_1 and t_2 with duration Δt and amplitude I_1 and I_2 are used to

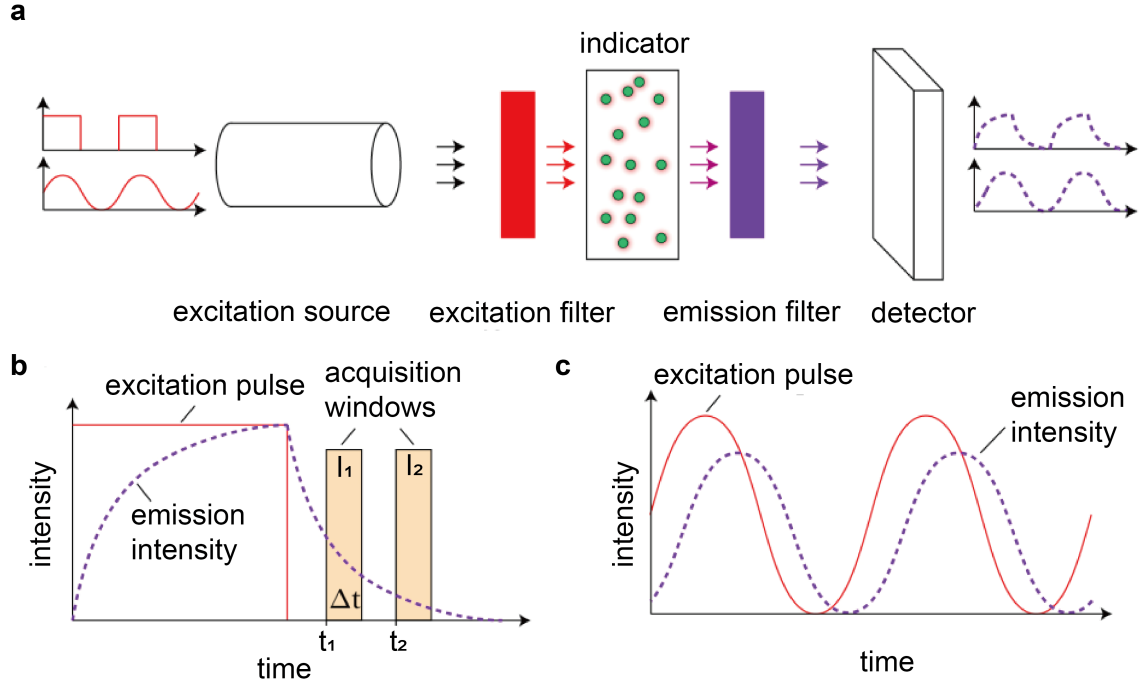


Figure 5.2 – Sensing principles of photoluminescence oxygen measurements. (a) Schematic representation of a measurement set-up for the life-time based sensing of dissolved oxygen, including an excitation source, filters, a photosensitive indicator, and the photodetector. (b) Photoluminescence lifetime detection in the time-domain. The time constant of the exponential decay is calculated based on the signal intensity of two subsequent acquisition windows. (c) Photoluminescence life-time detection in the frequency domain. The lifetime is calculated based on the phase shift of the excitation pulse and the emission pulse.

characterize the decay.

$$\tau = \frac{t_2 - t_1}{\ln(I_1 / I_2)} \quad (5.2)$$

In the frequency domain, the measurement is performed by analyzing the phase shift between the modulated excitation light pulse and the intensity emitted by luminophore. The phase shift Φ can be obtained with the following equation

$$\tau = \omega / \tan \Phi \quad (5.3)$$

where ω is the angular frequency of the modulated excitation pulse.[185]

5.3 Experimental

5.3.1 OCR measurement set-up

One goal of our study was to combine nanocalorimetry with oxygen consumption measurements. The INCfAST platform was therefore modified to enable real-time oxygen consumption/OCR measurements of microbial suspensions under culture conditions that are equivalent to the heat assays. For that purpose, the thermopile sensor was replaced by a glass substrate holding a sputter-deposited thin-film optical oxygen sensor spot. The microincubator was fixed directly over the sensor and optical access was provided from the bottom of the thermostat. A schematic of the modified system is shown in Figure 5.3a. The same thermal control and fluidic systems were used for both platforms, ensuring identical assay conditions. Parallel heat and oxygen measurements could be performed by injecting simultaneously identical bacterial samples into each platform. The integrated sensor detects oxygen-dependent luminescence in the near-infrared (REDFLASH Technology, PyroScience GmbH), based on phase shift measurement in the frequency domain (Figure 5.3b). The photodetector is positioned beneath the glass slide for excitation light emission and recording of fluorescent signals generated by bacteria populations sedimented on the bottom of the microreservoir (Figure 5.3c).

The microincubator made of transparent polycarbonate (PC) was stick to the glass. PC has a gas permeability of $70\text{--}130\text{ cm}^3 \cdot \text{mm}/(\text{m}^2 \cdot \text{day} \cdot \text{bar})$ at $20\text{ }^\circ\text{C}$. [186] In contrast, as a typical gas permeable material, PDMS has a permeability of $\sim 5 \times 10^4\text{ cm}^3 \cdot \text{mm}/(\text{m}^2 \cdot \text{day} \cdot \text{bar})$ [187]. The microincubator itself can therefore be considered as gas non-permeable, thus the oxygen concentration directly reflects the actual oxygen consumption of the bacterial population. The sample incubator was isolated from the sample and waste reservoirs by valves in the fluidic pathway. The microincubator is put into a thermostat to maintain the incubation temperature.

The sensor is calibrated by filling the microincubator with two types of liquids having saturated or depleted dissolved oxygen, respectively. DI water is used to calibrate the saturation point at a certain temperature. Whereas, 0.1 mol/L sodium sulfite (Na_2SO_3) solution is used to calibrate zero point. After each measurement, the chamber is first cleaned with ethanol (3 times) to remove most of the residual bacterial suspension. Then the chamber is soaked with OPA Rapicide 28 for 20 min at $37\text{ }^\circ\text{C}$ to achieve sterilization. After that the system is eluted with sterilized DI water to remove the residual detergent. Sterilization is verified by injecting pure MH broth into the system for overnight incubation to verify that the oxygen concentration is maintained at the initial level, indicating that no bacteria exist in the microincubator after this cleaning protocol. As a remark, initially, we have applied 15% hydrogen peroxide H_2O_2 to sterilize the system, however, we found that H_2O_2 will strongly perturbate the measurement as they can be decomposed into O_2 and H_2O .

5.3.2 Materials and methods

The bacterial strain used in the current study is *E. coli* ATCC 25922, the same as the one we used for the heat flow measurements. The microbial suspensions and antimicrobial solutions are prepared

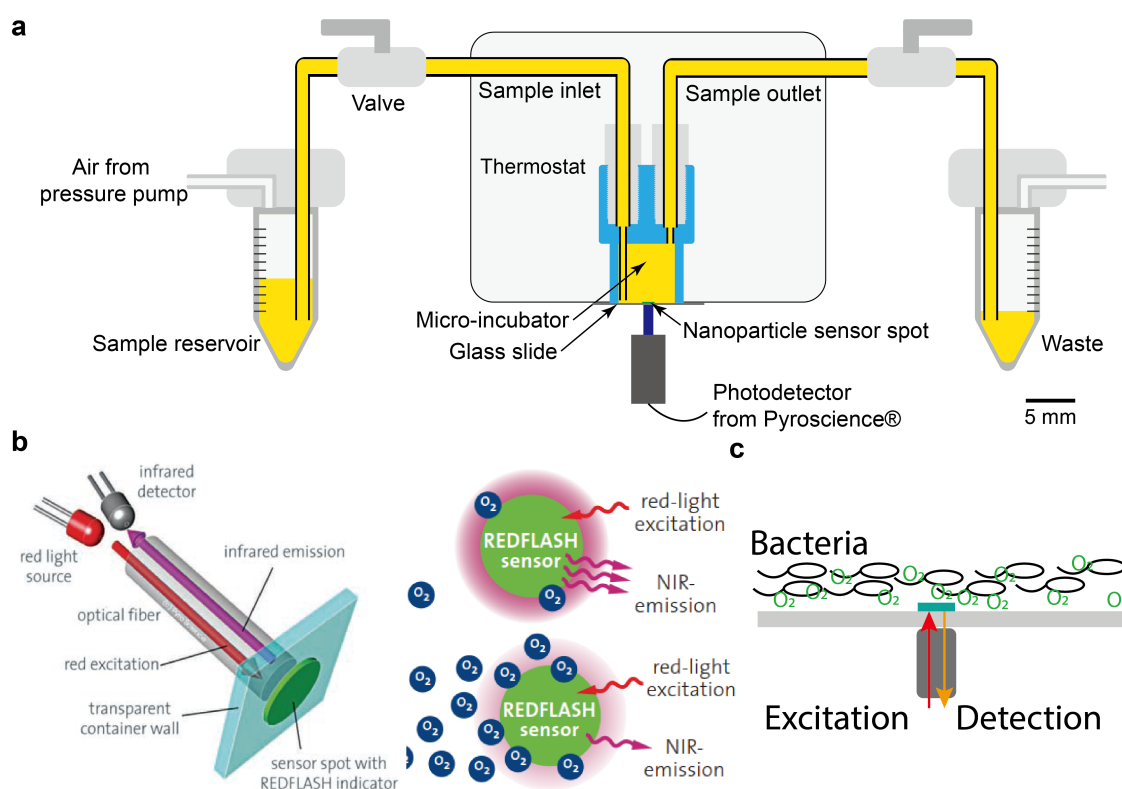


Figure 5.3 – (a) OCR measurement set-up based on a modified INCfAST platform. Schematic cross-sectional view of the oxygen consumption measurement unit with a microincubator reservoir integrated in a set-up similar to the nanocalorimetry platform. The microbial sample is injected to the microincubator by pressurized air. The valves are closed during the measurement to prevent the oxygen diffusion from the environment. (b) Schematic representation of the REDFLASH technology and the sensor spot (image reproduced from Pyroscience).^[188] (c) The thin-film optical sensor spot (green, $\varnothing \sim 1$ mm), which shows oxygen-dependent luminescence in the near-infrared range, is deposited on the glass slide holding the sample reservoir. The oxygen concentration is measured after sedimentation of the bacterial population.

in the same way as described in Section 4.3.2 of the previous chapter.

5.4 Results

5.4.1 Oxygen consumption

For aerobic bacteria such as *E. coli*, oxygen consumption is an important indicator of metabolic activity and viability. In order to further analyze the metabolic phenotype, we measured the oxygen concentration during bacterial growth in the thermalized microincubator. In the case study discussed in Figure 5.4, the oxygen signal started declining sharply at the onset of exponential growth (*i.e.* at ~ 1.5 h) and reached a non-detectable level after 4 h (Figure 5.4, blue curve). Interestingly, the oxygen consumption curve indicates that depletion of oxygen occurs earlier than

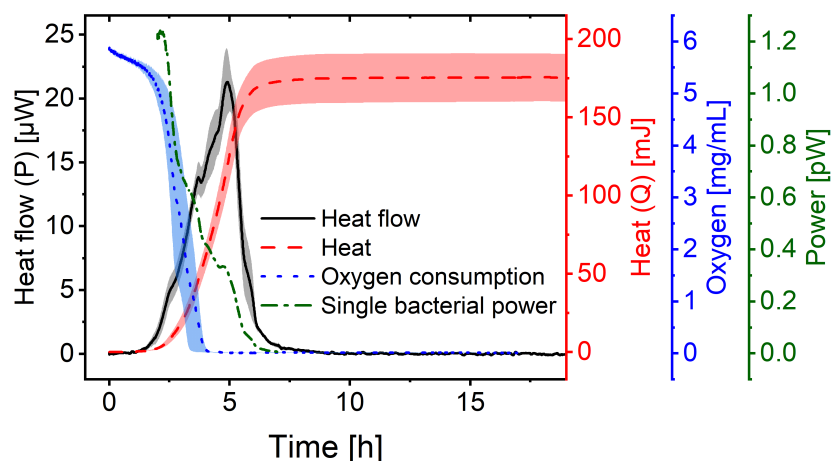


Figure 5.4 – Metabolic heat and oxygen consumption measurements. Heat flow curve $P(t)$ (black), the corresponding heat curve $Q(t)$ (red), and the single bacteria heat power curve (green) for *E. coli* ATCC 25922 with typical incubation conditions on the INCfAST platform (Mueller-Hinton broth (MH), 37 °C). Synchronized parallel on-chip oxygen consumption measurements revealed complete oxygen depletion in the microincubator after 4 h (blue curve), indicating the transition from an aerobic to an anaerobic metabolic state. All curves represent mean \pm SE ($n = 3$).

the time point where heat flow is maximum P_{max} (at ~ 5 h, black curve in Figure 5.4), suggesting that the bacteria population continues growing normally for at least 1 h in an anaerobic metabolic state. As a facultative anaerobic bacterium, *E. coli* thus appears not to be immediately sensitive to oxygen depletion. Indicative heat power/bacterium mid-range values are 1.1 pW (at $t = 2.5$ h) for the aerobic metabolic state and 0.32 pW (at $t = 5$ h) for the anaerobic state, respectively (Figure 5.4, green curve). Transitions between different metabolic states may in principle result in more complex heat flow curves (see section 4.5). In the present case, a small crinkle-like feature can be identified at ~ 3.7 h (Figure 5.4, black curve), possibly corresponding to the transition from aerobic to anaerobic conditions. Nevertheless, no significant impact on the overall shape of the heat flow curve is observed, suggesting a fast shift between the two metabolic states.

5.4.2 Modelization of the oxygen consumption

In a nutrient-rich medium, the growth of bacteria like *E. coli* obeys the exponential model with a certain doubling time t_{db} , as shown in the following equation

$$N(t) = N(t_0)2^{t/t_{db}} \quad (5.4)$$

where $N(t)$ is the number of bacteria at a certain time t with doubling time t_{db} and $N(t_0)$ is the initial number of bacteria.

Based on the exponential growth, we established a model for oxygen consumption in the following

way

$$C_{O_2}(t) = C_{O_2}(t_0) - \frac{\int_{t_0}^t XN(t') dt'}{V}$$

$$= C_{O_2}(t_0) - \frac{\ln 2 t_{db} (XN(t_0) 2^{t/t_{db}} - XN(t_0))}{V} \quad (5.5)$$

$$= C_{O_2}(t_0) - \ln 2 t_{db} X C_{bac}(t_0) (2^{t/t_{db}} - 1) \quad (5.6)$$

where $C_{O_2}(t)$ is the variation of the dissolve oxygen concentration over time with an initial value $C_{O_2}(t_0)$. X is the OCR per bacterium, which we assume to be constant under favorable culture conditions. $C_{bac}(t_0)$ is the initial bacteria concentration (inoculum size) in a sample incubator of volume V . The initial oxygen concentration $C_{O_2}(t_0)$ is usually the maximum oxygen concentration. $XC_{bac}(t_0)$ corresponds to the OCR of the inoculum size at t_0 .

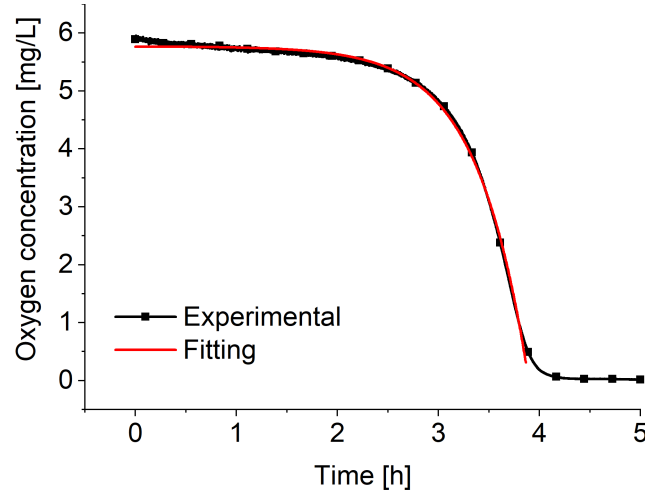


Figure 5.5 – Modelization of the oxygen consumption based on Eqn. 5.6. The black curve is a $C_{O_2}(t)$ curve obtained from growth experiment of *E. coli* with inoculum size of 3×10^5 CFU/mL in MH at 37 °C. The red curve is fitted according to the model Eqn. 5.6.

For the modelization of the oxygen consumption, e.g. the $C_{O_2}(t)$ curve shown in Figure 5.5, we take into account three parameters X , t_{db} , and $C_{O_2}(t_0)$. $C_{O_2}(t_0)$ usually depends only on the temperature and on the type of the culture media. However, X and t_{db} are highly related to the bacterial metabolic activity. Figure 5.5 is an example of the non-linear fitting with the established model. We performed the fitting from the beginning of an experiment at t_0 until the time point before full oxygen depletion. $C_{O_2}(t_0)$ can be derived from the initial plateau region of the oxygen concentration curve. t_{db} determines the characteristic decay time of the exponential curve.

Accordingly, the OCR for a bacterial culture can be expressed as the time derivative of the oxygen consumption curve. The oxygen consumption curve is obtained by subtracting the current oxygen

concentration from the maximum concentration, *i.e.*, $C_{O_2}(t_0) - C_{O_2}(t)$.

$$OCR = -\frac{dC_{O_2}(t)}{dt} = (\ln 2)^2 X C_{bac}(t_0) 2^{t/t_{ab}} \quad (5.7)$$

Figure 5.6 shows an experimental oxygen consumption curve that was obtained from the black curve in Figure 5.5. The corresponding OCR curve derived from the model (Eqn. 5.7) is also shown in Figure 5.6 (red line). Both curves increase exponentially.

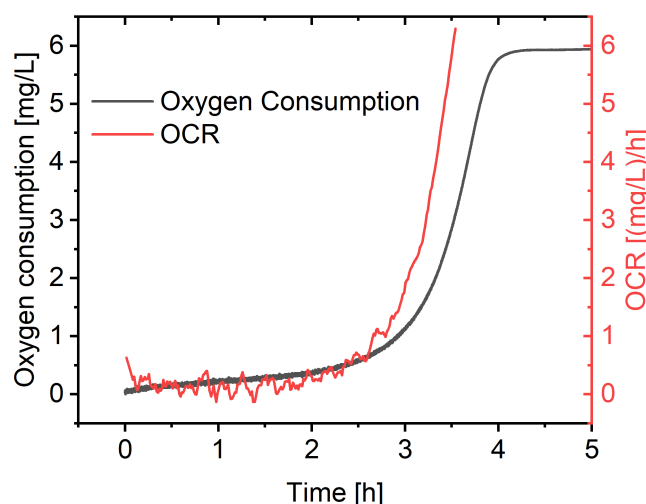


Figure 5.6 – An example of an OCR curve. OCR (red curve) is obtained as the time derivative of oxygen consumption (black curve).

5.4.3 Aerobic metabolism assessment

Bacterial oxygen consumption depends on the nutrient level and temperature, as shown in Figure 5.7a and 5.7b. As summarized in Table 4.1 in the previous chapter, BHI broth has a higher nutrient level than MH and LB. In BHI, the oxygen concentration in the culture medium decreases faster, *i.e.* OCR is higher than in the other two culture media. This corresponds to the observed variations of the *E. coli* metabolic heat flow (Figure 4.8a) and generated heat / growth rate (Figure 4.8b/4.9b). BHI enhanced the maximum bacterial heat production rate compared to media containing less nutrients. Likewise the maximum total heat value increased with the amount of nutrients provided by the medium (BHI > MH ≥ LB, Figure 4.8b). Culture temperature influences the enzymatic efficiency of cellular metabolic reactions. Highest OCR was therefore found at 42 °C, and gradually decreasing values as the culture temperature is lowered (Figure 5.7b). The temperature effect on oxygen consumption, showing a clear delay of oxygen depletion at most unfavorable growth conditions (27 °C, Figure 5.7b), is in line with the heat curves as well (Figure 4.8c). Heat flow and heat curves for different culture temperatures in MH showed a corresponding variation (Figure 4.8c and 4.8d, respectively), with a significant elongation of the apparent lag phase at 27 °C and stationary phase end levels Q_{max} that were comparable for all temperatures but reached on different time scales.

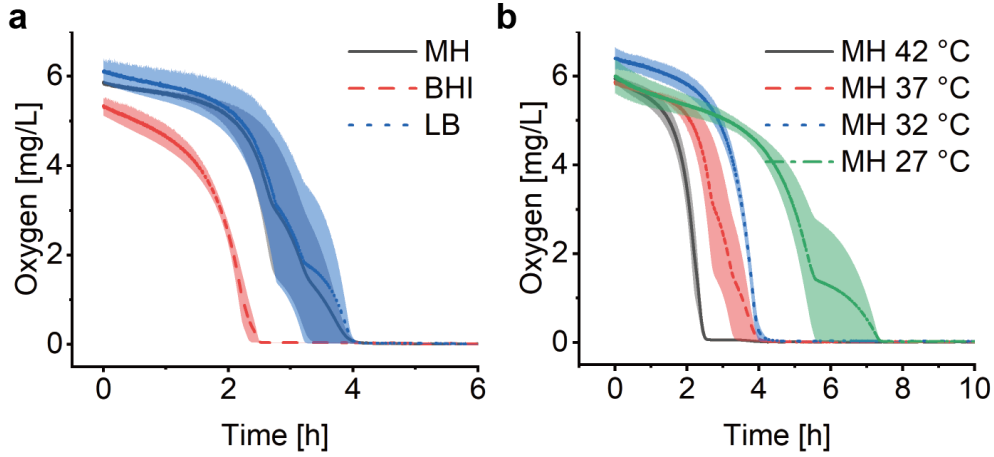


Figure 5.7 – Oxygen consumption measurements for different conditions. (a) Bacterial oxygen consumption in different culture media. Oxygen depletion occurs first in the richest medium (BHI), whereas OCR in MH and LB is very similar. (b) Oxygen consumption of the bacterial populations at different temperatures. Oxygen depletion is fastest at 42 °C and more delayed for decreasing temperatures. Error bars represent mean \pm SE (n=3).

Corresponding modelization results for the growth in different culture media and temperature are shown in Table 5.1. We observe that our model works well to predict the doubling time t_{db} with small errors. Based on the results, we can conclude that, when bacteria cultured at unfavorable temperatures (27 °C), the doubling time is strongly prolonged (48 ± 4.7 min) with respect to more suitable conditions (~ 20 min). The highest $XC_{bac}(t_0)$ values have been found for BHI and LB at 37 °C. However, in all cases, for $XC_{bac}(t_0)$, the error is quite big. We suppose that the main reason resides in the bacterial sample preparation step, as the initial concentration $C_{bac}(t_0)$ can only be guaranteed in a certain range. The current system only supports one test of the bacteria concentration in the beginning of the experiment. An improved platform supporting successive evaluation of the bacteria concentration may help to determine OCR/bacterium more accurately and to reduce systematic errors.

Table 5.1 – Estimation of the microbial doubling time t_{db} and OCR/inoculum size $XC_{bac}(t_0)$ for different culture media and temperatures based on the modelization (mean values \pm SD, n=3).

Condition	Doubling time t_{db} [min]	$XC_{bac}(t_0)$ [$\text{mg} \cdot \text{L}^{-1} \cdot \text{min}^{-1}$]
MH at 37 °C	20 ± 1.2	$5.5 \times 10^{-4} \pm 4.7 \times 10^{-4}$
BHI at 37 °C	26 ± 6	$1.2 \times 10^{-2} \pm 1.2 \times 10^{-2}$
LB at 37 °C	21 ± 3	$3.7 \times 10^{-3} \pm 4.7 \times 10^{-3}$
MH at 27 °C	48 ± 5	$1.3 \times 10^{-3} \pm 9.7 \times 10^{-4}$
MH at 32 °C	30 ± 1.2	$1.2 \times 10^{-3} \pm 2.8 \times 10^{-4}$
MH at 42 °C	17 ± 2	$1.9 \times 10^{-3} \pm 1.2 \times 10^{-3}$

5.4.4 AST based on OCR measurements

Oxygen consumption as a viability indicator can be applied as an interesting method to evaluate metabolic activity and MIC for non-anaerobic bacteria. We have recorded bacterial oxygen consumption curves for the different pharmacological conditions considered in the frame of this work (Figure 5.8). Corresponding AST assays based on metabolic heat flow have been discussed in Chapter 4 (Figure 4.11). MIC reference values are indicated in Table 4.2. For concentrations below MIC, oxygen is gradually consumed and the time to full oxygen depletion in the microincubator increases clearly for concentrations approaching MIC (Figure 5.8). All 3 antibiotics tested are bactericidal, thus the oxygen concentration in the microincubator should remain constant above MIC, as observed for ciprofloxacin (0.015 mg/L, purple curve in Figure 5.8a) and for ampicillin (4.7 mg/L and 9.5 mg/L, Figure 5.8b, green and purple curves, respectively). In the specific case of gentamicin, oxygen consumption at subinhibitory concentrations evolves in principle as for ciprofloxacin and ampicillin, even if delays are more pronounced close to the expected MIC (e.g. green curve in Figure 5.8c, 1.1 mg/L). Surprisingly, oxygen depletion is also observed at a concentration of 2.2 mg/L, *i.e.* above the MIC value range derived from the heat assay. The oxygen concentration in the microincubator decreased sharply only after a prolonged incubation period of ~ 13 h (purple curve in Figure 5.8c), determined by heat flow measurements. This fact suggests that a small population of bacteria was able to survive in the microincubator. The antimicrobial action of gentamicin is based on an oxygen-dependent process.^[189] It is therefore possible that diffusion of oxygen to bacteria clusters attached on the surface of the oxygen sensing spot is limited thus inhibiting temporarily the action of gentamicin.

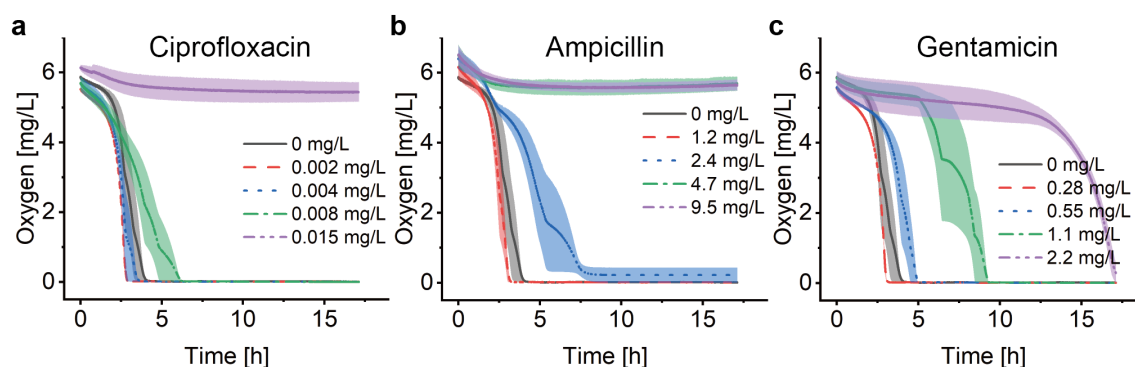


Figure 5.8 – Oxygen consumption for AST experiments with (a) ciprofloxacin (b) ampicillin and (c) gentamicin. Growth and non-growth conditions can be differentiated by oxygen consumption. All three antimicrobials are bactericidal, and the MIC results are coherent with the established MIC range for ciprofloxacin and ampicillin. In gentamicin, oxygen consumption was still observed after a prolonged incubation time above the MIC value determined by heat flow.

Table 5.2 shows the modelization results for oxygen consumption in the presence of different antibiotics with a series of concentrations. A clear prolonged doubling time is observed when the antimicrobial concentration is increasing. However, whether the bacteria upon antimicrobial stress are still dividing in the normal way, *i.e.* by dividing and cell doubling, needs further investigation.

As will be shown in the next chapter, from a microscopic view, antibiotics such as ampicillin may generate a significant filamentation effect, *i.e.* an elongation of the cell body without division, thus bacteria may accumulate biomass without increasing their number. In addition, in this case the bacterial size distribution is larger than for normal growth conditions, where the divided bacteria usually have identical biomass.

Table 5.2 – Estimation of doubling time t_{db} and OCR/inoculum size $XC_{bac}(t_0)$ for AST experiments based on modelization (mean values \pm SD, $n=3$).

Condition	Doubling time t_{db} [min]	$XC_{bac}(t_0)$ [$\text{mg} \cdot \text{L}^{-1} \cdot \text{min}^{-1}$]
Ampicillin 1.2 mg/L	23 ± 3	$5.5 \times 10^{-4} \pm 4.7 \times 10^{-4}$
Ampicillin 2.4 mg/L	100 ± 50	$8.4 \times 10^{-3} \pm 7.6 \times 10^{-3}$
Ciprofloxacin 0.002 mg/L	22 ± 2	$1.8 \times 10^{-3} \pm 5.0 \times 10^{-4}$
Ciprofloxacin 0.004 mg/L	24 ± 1	$2.0 \times 10^{-3} \pm 1.0 \times 10^{-3}$
Ciprofloxacin 0.008 mg/L	79 ± 13	$8.0 \times 10^{-3} \pm 3.2 \times 10^{-3}$
Gentamicin 0.28 mg/L	25 ± 3	$2.0 \times 10^{-3} \pm 7.8 \times 10^{-4}$
Gentamicin 0.55 mg/L	30 ± 9	$9.5 \times 10^{-4} \pm 8.1 \times 10^{-4}$
Gentamicin 1.1 mg/L	28 ± 5	$8.9 \times 10^{-6} \pm 1.1 \times 10^{-5}$
Gentamicin 2.2 mg/L	80 ± 30	$4.6 \times 10^{-5} \pm 7.3 \times 10^{-5}$

5.4.5 Oxygen consumption vs heat production

With our platforms, we were able to study microbial heat production and oxygen consumption under comparable conditions, thus to evaluate and correlate metabolic heat as a function of oxygen consumption. The heat production per oxygen consumption has been reported in some previous works.[171] High correlation of direct heat calorimetry and indirect calorimetry based on oxygen consumption has been demonstrated.[172] Figure 5.9 and Figure 5.10 show plots of the heat *vs* oxygen consumption for the range of experimental conditions described before. For the different culture media, MH and LB generate comparable curves, whereas BHI has a considerably lower heat per oxygen consumption values. The nutrient composition in MH and LB is quite similar and suitable for the growth of most non-fastidious bacteria, whereas BHI as a richer media can support the growth of fastidious bacteria. The high oxygen expenditure in BHI of *E. coli* as a non-fastidious bacteria may be attributed to the high protein content in this medium. In comparison, the heat/oxygen consumption for bacteria growing in MH but under different temperatures shows no clear difference. Heat production rates (Figure 4.8b) and oxygen consumption rates (Figure 5.8) both vary with culture temperature as well as the bacterial growth (Figure 4.10).

Furthermore, we investigated the relation between heat production and oxygen consumption in the presence of antimicrobials. From a growth perspective, bacteria may produce more heat for the synthesis of the same amount of biomass (*i.e.* same OD600 as stated in the previous chapter, section 4.4.4). We called this phenomenon "energy spilling" that revealed that antibiotics do alter the bacterial metabolic activity. However, considering the heat per oxygen consumption curves, no systematic effect is observed. For ciprofloxacin and ampicillin (Figure 5.10a and 5.10b, respectively), increasing antimicrobial concentration may lead to a lower heat production per

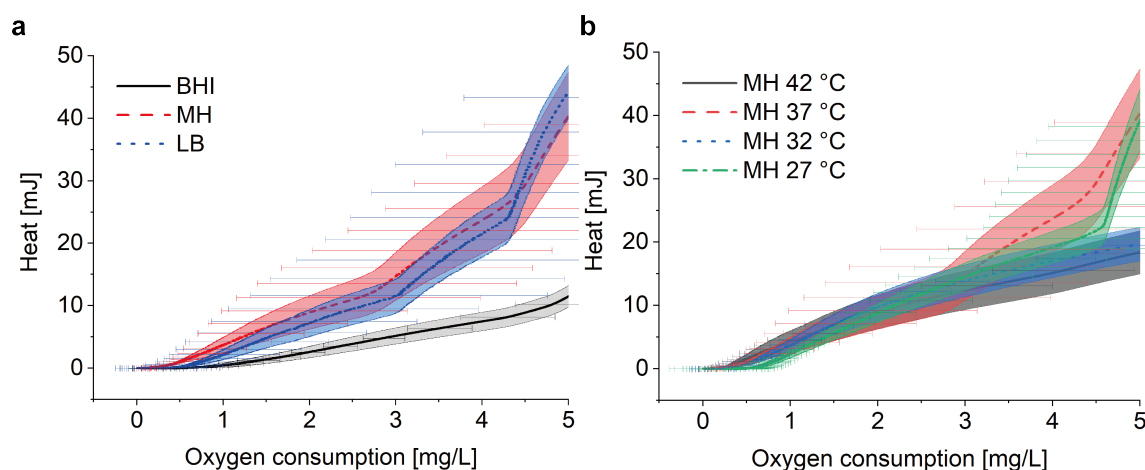


Figure 5.9 – Oxygen consumption *vs* heat production for different culture media and temperatures. For all curves, both for x-axis and y-axis, error bars represent mean \pm SE, n=3.

consumed unit amount of oxygen (lower slope of the curves). However, this effect was not observed for gentamicin. Correlating these two types of measurements results in a big error range, therefore, further improvement of the measurement set-ups might be required for more detailed analysis.

5.5 Discussion

An important aspect of the study of cellular oxygen consumption is that it helps in understanding mitochondrial dysfunction. Mitochondrial dysfunction in eukaryote cells is highly related to metabolic disorders, *e.g.* obesity, diabetes mellitus, but also to cardiovascular disease and neurodegenerative disorders, such as Alzheimer's disease, Parkinson's disease, Huntington's disease and amyotrophic lateral sclerosis.[190, 191] There is evidence that mitochondria in eukaryotes have bacterial origin,[192] thus considering bacteria themselves as a kind of mitochondria, measuring dissolved oxygen concentrations in culture media to evaluate microbial metabolic activity, appears as an important method with possible conclusions on mitochondrial functioning. Oxygen consumption only depends on the bacterial concentration, thus facilitating system miniaturization, unlike heat measurements, which depend on the absolute bacterial quantity to reach to the LOD. Moreover, luminescence-based methods, taking advantage of a wide range of bio-compatible nanomaterials, are a versatile option for optical oxygen sensing in small systems and for assay parallelization.[178] Integration of small photosensitive spots in microsystems, including microfluidic devices, is relatively simple with the photodetector being placed outside of the system.

Combining oxygen consumption measurements with metabolic heat recordings of bacteria under antimicrobial stress provides a more holistic phenotypic characterization of metabolic activity. Time to full oxygen depletion in the microincubator increases clearly close to MIC (Figure 5.8). In our assays, oxygen depletion appeared on a shorter time scale than significant features of the corresponding heat flow profiles (Figure 4.11), *e.g.* earlier than the maximum of heat production P_{max} . Oxygen consumption may therefore be explored as another potential parameter for fast AST

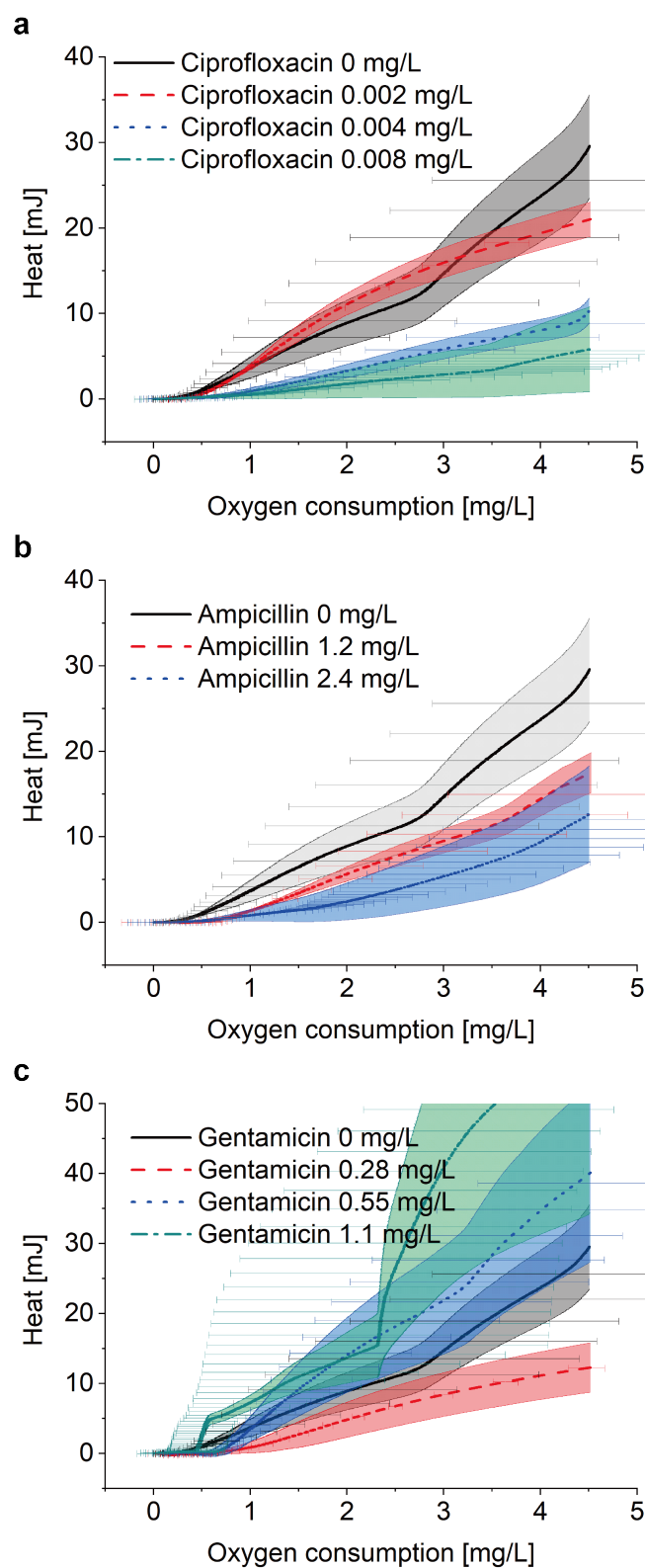


Figure 5.10 – Oxygen consumption *vs* heat production for different antimicrobials. (a) ciprofloxacin, (b) ampicillin, (c) gentamicin. For both x-axis and y-axis, error bars of all curves represent mean \pm SE, n =3.

on aerobic bacteria. Nevertheless, oxygen depletion in the microincubator has to be considered carefully when evaluating the results. For instance, the MIC interval for gentamicin determined with the oxygen sensing platform was above EUCAST reference values (Table 4.2). The oxygen-dependent antimicrobial action of gentamicin may be at the origin of this observation.[189] Progressive oxygen depletion in the microincubator during the assay possibly reduced the antimicrobial efficacy of gentamicin, resulting in somewhat enhanced MIC values with respect to conventional protocols. Accordingly, for OD measurements (Figure 4.12c), where shaking of the plate reader ensures oxygen replenishment of the culture solution, no deviation from the standard MIC range was observed. On the other hand, the enclosed microincubator system might be suitable for performing fast AST on anaerobic bacteria, which can be challenging with the conventional agar-based culture methods.

Most thermoplastic materials, such as PMMA, COC and PC are gas non-permeable. We used PC for the microbial microincubator, the bacterial culture was therefore isolated from oxygen diffusion from the surrounding environment in our case. This feature enabled stable oxygen consumption measurements. In our *E. coli* study, oxygen is not vital for the growth of these facultative anaerobic bacteria. For cell cultures, strictly aerobic bacterial cultures or culture of other small model organisms, however, the material choice can be quite important. PDMS is still the most widely used material for cell culture thanks to its high gas permeability. Other materials may provide interesting alternatives. For instance, Krenger *et al.* applied OSTE+ for an oxygen consumption study of *C. elegans* [193]. As OSTE+ itself may consume the oxygen[194], an oxygen consumption baseline removal had to be performed. Ochs *et al.* have investigated polymethylpentene (PMP), a thermoplastic material with relatively high oxygen permeability, as an option for cell culture.[195]

5.6 Conclusion

Oxygen consumption measurements provide valuable additional information for a more holistic evaluation of the microbial metabolic state. We implemented an on-chip bacterial oxygen consumption measurement system based on a modified isothermal nanocalorimeter platform. The oxygen consumption can be modeled based on the doubling growth of bacteria. We concluded that under unfavorable cultural conditions, microbial doubling times prolong significantly. In a proof-of-concept study we demonstrated that OCR measurements can be used for fast AST of facultative anaerobic bacteria, which represent most of clinically relevant bacteria in blood stream infections. Correlating heat and oxygen consumption provides a method to further evaluate potential metabolic pathways under different cultural conditions. Heat production per oxygen consumption varies in culture media with different nutrient compounds, whereas maintains the same level for different culture temperatures in the same medium. Furthermore, we suggest that bacteria possess a higher heat per oxygen consumption for growth in the presence of low antimicrobial concentrations with respect to high concentrations, especially for ampicillin and ciprofloxacin.

References

98. Liu, Y., Lehnert, T. & Gijs, M. A. M. Fast Antimicrobial Susceptibility Testing on *Escherichia coli* by Metabolic Heat Nanocalorimetry. *Lab on a Chip* **20**, 3144–3157 (Aug. 26, 2020) (cit. on pp. 43, 53, 74, 83, 127).
171. Cooney, C. L., Wang, D. I. C. & Mateles, R. I. Measurement of Heat Evolution and Correlation with Oxygen Consumption during Microbial Growth. *Biotechnology and Bioengineering* **11**, 269–281 (1969) (cit. on pp. 74, 75, 95).
172. Birou, B., Marison, I. W. & Stockar, U. V. Calorimetric Investigation of Aerobic Fermentations. *Biotechnology and Bioengineering* **30**, 650–660 (Oct. 5, 1987) (cit. on pp. 74, 75, 95).
175. Carroll, K., Butel, J. & Morse, S. *Jawetz Melnick & Adelbergs Medical Microbiology 27 E* 27th edition. 864 pp. (McGraw-Hill Education / Medical, New York, Oct. 20, 2015) (cit. on p. 83).
176. Wolfbeis, O. S. Luminescent Sensing and Imaging of Oxygen: Fierce Competition to the Clark Electrode. *BioEssays* **37**, 921–928 (Aug. 2015) (cit. on pp. 83–85).
177. Grist, S. M., Chrostowski, L. & Cheung, K. C. Optical Oxygen Sensors for Applications in Microfluidic Cell Culture. *Sensors* **10**, 9286–9316 (Oct. 15, 2010) (cit. on p. 83).
178. Wang, X.-d. & Wolfbeis, O. S. Optical Methods for Sensing and Imaging Oxygen: Materials, Spectroscopies and Applications. *Chemical Society Reviews* **43**, 3666–3761 (Apr. 22, 2014) (cit. on pp. 84, 85, 96).
179. Winkler, L. W. Die Bestimmung Des Im Wasser Gelösten Sauerstoffes. *Berichte der deutschen chemischen Gesellschaft* **21**, 2843–2854 (1888) (cit. on p. 84).
180. *Dissolved Oxygen by the Winkler Method* Environmental Sampling. https://serc.carleton.edu/microbelife/research_methods/envIRON_sampling/oxygen.html (2020) (cit. on p. 84).
181. Wu, C.-C., Yasukawa, T., Shiku, H. & Matsue, T. Fabrication of Miniature Clark Oxygen Sensor Integrated with Microstructure. *Sensors and Actuators B: Chemical* **110**, 342–349 (Oct. 14, 2005) (cit. on p. 84).
182. SelectScience. *Seahorse XFe Analyzers from Agilent Cell Analysis* | SelectScience <https://www.selectscience.net/products/seahorse-xfe-analyzers/?prodID=196716> (2020) (cit. on pp. 85, 86).
183. Lefebvre, J., Maruyama, S. & Finnie, P. in *Carbon Nanotubes: Advanced Topics in the Synthesis, Structure, Properties and Applications* (eds Jorio, A., Dresselhaus, G. & Dresselhaus, M. S.) 287–319 (Springer, Berlin, Heidelberg, 2008). doi:10.1007/978-3-540-72865-8_9 (cit. on p. 86).
184. DeGraff, B. A. & Demas, J. N. in *Reviews in Fluorescence 2005* (eds Geddes, C. D. & Lakowicz, J. R.) 125–151 (Springer US, Boston, MA, 2005). doi:10.1007/0-387-23690-2_6 (cit. on p. 86).
185. Liebsch, G., Klimant, I., Frank, B., Holst, G. & Wolfbeis, O. S. Luminescence Lifetime Imaging of Oxygen, pH, and Carbon Dioxide Distribution Using Optical Sensors: *Applied Spectroscopy*. doi:10.1366/0003702001949726 (Aug. 31, 2016) (cit. on p. 87).

186. in. *Wikipedia* (Nov. 6, 2020) (cit. on p. 88).
187. Merkel, T. C., Bondar, V. I., Nagai, K., Freeman, B. D. & Pinnau, I. Gas Sorption, Diffusion, and Permeation in Poly(Dimethylsiloxane). *Journal of Polymer Science Part B: Polymer Physics* **38**, 415–434 (2000) (cit. on p. 88).
188. *Optical Oxygen Sensors User Manual* (cit. on p. 89).
189. Walker, P. D. & Shah, S. V. Gentamicin Enhanced Production of Hydrogen Peroxide by Renal Cortical Mitochondria. *American Journal of Physiology-Cell Physiology* **253**, C495–C499 (Oct. 1, 1987) (cit. on pp. 94, 98).
190. Fernyhough, P., Roy Chowdhury, S. K. & Schmidt, R. E. Mitochondrial Stress and the Pathogenesis of Diabetic Neuropathy. *Expert review of endocrinology & metabolism* **5**, 39–49 (Jan. 1, 2010) (cit. on p. 96).
191. Ferreira, I. L., Resende, R., Ferreira, E., Rego, A. C. & Pereira, C. F. Multiple Defects in Energy Metabolism in Alzheimer's Disease. *Current Drug Targets* **11**, 1193–1206 (Oct. 2010) (cit. on p. 96).
192. Pallen, M. J. Time to Recognise That Mitochondria Are Bacteria? *Trends in Microbiology* **19**, 58–64 (Feb. 2011) (cit. on p. 96).
193. Krenger, R., Cornaglia, M., Lehnert, T. & M. Gijs, M. A. Microfluidic System for *Caenorhabditis Elegans* Culture and Oxygen Consumption Rate Measurements. *Lab on a Chip* **20**, 126–135 (2020) (cit. on p. 98).
194. Sticker, D. *et al.* Oxygen Management at the Microscale: A Functional Biochip Material with Long-Lasting and Tunable Oxygen Scavenging Properties for Cell Culture Applications. *ACS Applied Materials & Interfaces* **11**, 9730–9739 (Mar. 13, 2019) (cit. on p. 98).
195. Ochs, C. J., Kasuya, J., Pavesi, A. & Kamm, R. D. Oxygen Levels in Thermoplastic Microfluidic Devices during Cell Culture. *Lab on a Chip* **14**, 459–462 (Dec. 23, 2013) (cit. on p. 98).

6 Bacterial motility analysis

Phenotypic diversity in bacterial flagellar motility leads to non-uniform collective swimming patterns, appearing as traveling bands with transient enhanced local cell densities. Traveling bands emerge as the bacterial chemotactic response to self-generated nutrient gradients during growth in resource-limited microenvironments. In this chapter, we studied *E. coli* collective migration for different parameters, in particular inoculum size and for incubation with three different antibiotics (ampicillin, ciprofloxacin, and gentamicin). We developed on-chip microfluidic assays, based on a poly(methyl methacrylate)(PMMA)-glass hybrid chip with an intermediate optical adhesive layer featuring the microfluidic channel structure. The accurately defined channel height provided a shallow Hele-Shaw cell geometry, enabling high-content imaging of the migration dynamics of single bacterial layers confined in a quasi-2D space. Bacterial motility and on-chip traveling band analysis was performed on individual bacterial trajectories by means of custom-developed algorithms. Moreover, *E. coli* filamentation in the presence of antibiotics was assessed and the impact on motility was evaluated. Quantification of swimming speed, tumble bias and effective diffusion properties allowed to describe the phenotypic heterogeneity resulting in variations of the transient cell density distributions and swimming performance. We found that incubation of identical *E. coli* genotypes with different inoculum sizes eventually generated different swimming phenotypes. Interestingly, incubation with antimicrobials promoted bacterial chemotaxis in specific cases, despite the growth inhibition. Moreover, we propose that the observation of traveling bands can be explored as an innovative alternative to current approaches for fast antimicrobial susceptibility testing.

6.1 Introduction

Bacteria can sense a vast range of environmental signals. Decades of studies on the mechanisms underlying self-propelled oriented bacterial swimming towards preferred niches for colonization, commonly known as chemotaxis, have elucidated pathways of chemosensory signal transduction and response regulation that affects bacterial active motion.[61, 63, 196] Most interestingly, motility and chemotaxis play an important role as virulence factors, as these are essential features for pathogens to colonize hosts and to evade their defense mechanisms.[197] For example, chemotaxis

is shown to guide the human gastric pathogen *Helicobacter pylori* to the mucus lining of the stomach[198] and *Vibrio anguillarum* to the surface of fish.[199] Therefore, from a healthcare perspective, a further more holistic understanding of bacterial motility, in particular of specific collective and coordinated dynamic patterns of migrating bacterial populations, may open the way to explore new disease-preventive or therapeutic paradigms based on unconventional targets. This perspective is of particular importance with respect to the great challenge of fast spreading antimicrobial resistance (AMR) that the public health system is facing for the time being.[200] In this context, fast antimicrobial susceptibility testing (AST), which is essential to provide correct antimicrobial administration, is a key requirement to counteract AMR propagation.[137]

Microfluidic high-throughput platforms incorporating chips with (sub)micrometer features, enabling precise handling and observation of single-cell organisms or small microbial populations, helped to reveal fundamental aspects of microbial life, cell-cell interactions and population dynamics.[19, 22, 201] On-chip control of microenvironmental conditions was used to study microbial taxis with respect to a range of physical parameters, including temperature, magnetic field or light sensitivity.[23] Microfluidic chip assays enable accurate imaging and tracking of bacterial populations with single-cell resolution.[202] The “mother machine”, composed of an array of parallel dead-end microchannels, is a prominent example for monitoring single bacterial growth and rod-shape bacterial division on-chip.[203] Using a similar chip design and by averaging the growth rate response to different antibiotics, Baltekin *et al.* declared an AST read-out time of only 30 min.[40] Motility and chemotaxis studies benefit strongly from a versatile microfluidic toolbox, providing controlled and complex on-chip chemical gradient patterns.[204] As a recent example, Lambert *et al.* engineered a chip featuring an array of 110 μL wells loaded with out-diffusing chemicals to assess the chemotactic behavior of marine microorganism communities.[205, 206]

E. coli is a well characterized model organism for motility studies that uses a run- and tumble-motion strategy by randomly changing the direction of successive straight swimming sections. It performs chemotaxis for exploring optimal environmental conditions by adjusting the duration of straight runs or the frequency of tumbling.[61] The flagellar motor switches from counter-clockwise to clockwise rotation to realize this typical motion pattern, which is controlled by a coordinated protein network. In *E. coli*, the sensitivity of ligand-binding chemoreceptors is mediated by the enzymes CheR and CheB. Chemoreceptor activity is communicated to the flagellar motor via phosphorylation and dephosphorylation of the response regulator CheY regulated by the histidine kinase CheA or the phosphatase CheZ. Phosphorylated CheY (CheY-P) binds to the switch protein FliM on the flagellar motor to trigger clockwise rotation. Local depletion of nutrients and oxygen in the culture media during bacteria colony growth is a driving force of bacterial chemotaxis in seek for energy resources in the microenvironment. Chemotaxis-induced collective *E. coli* migration patterns, appearing in the form of traveling bands, were first observed by Adler in different geometrical setting, such as agar plates or capillary tubes.[207] This phenomenon can be described as collective migration of a dense sub-population of motile *E. coli*, when placed at one end of a capillary tube filled with nutrients. The consumption of attracting nutrients in the culture media drives the bacterial chemotaxis and forms collective traveling band. This has been described mathematically by the Keller-Segel model.[208] However, this model does not describe

the effect of individual variations in swimming behavior that exist in a bacterial population, which was reported firstly by Spudich & Koshland.[209] For the time being the existence of microbial cell-to-cell heterogeneity that does not have genotypic differences is well-known and underlying sources have been extensively studied.[210, 211] Recently, Salek *et al.* used a microfluidic T-maze to expose individual cells to a sequence of chemosensory decisions revealing a phenotypic heterogeneity of bacterial chemotaxis.[212] Phenotypic diversity in chemotactic sensitivity may serve as functional bet-hedging strategy to adapt to local environmental variations. Variability in the expression of motility-related genes is thought to be responsible for maintaining chemotactic performances. For instance, it was found that the degree of phenotypic diversity of a population can be controlled by adjusting the global expression level of CheR and CheB.[213] Fu *et al.* revealed that bacteria are able to migrate as a group by sorting themselves and adapting to the chemical gradient steepness in a traveling band despite the continuum of phenotypic diversity.[214] They have applied a non-genetic diversity indicator named “tumble bias” (the fraction that tumbling time takes in the duration of a whole swimming segment) to evaluate the individuality in bacterial motility.[215]

In this work, we present a study of microbial collective behavior using *E. coli* as the model organism, by investigating the impact of the inoculum size and of antimicrobial action on specific features of bacterial traveling bands. We intend to provide new insight in understanding the effect of these important assay conditions on the phenotypic diversity of the swimming behavior. The bacterial suspension was confined in a Hele-Shaw microfluidic channel to achieve high-precision imaging of a quasi 2-dimensional single bacterial layer. The height of the channel was accurately defined by a patterned optical adhesive (OA) layer. A custom image processing protocol was developed for tracking and quantifying swimming parameters, in particular speed and tumble bias, of coherently migrating bacterial populations at single-cell resolution. We revealed that isogenic bacteria populations growing from different inoculum sizes eventually generated diverse swimming phenotypes. This study was then extended to bacteria populations exposed to different antibiotics and concentrations. Interestingly, we observed that sub-minimum inhibitory concentrations (MIC) promoted the swimming ability in some cases despite considerable antimicrobial growth inhibition. An *in situ* morphological analysis provided complementary information on *E. coli* filamentation, a co-existing effect in the presence of antimicrobials. Finally, we propose that the appearance or absence of traveling bands as a function of antimicrobial concentration may be explored as an interesting alternative for current fast AST approaches.

6.2 Experimental

6.2.1 Material and chemicals

NOA 68 optical adhesive (OA) was purchased from Norland Products (Cranbury, NJ). Sylgard 184 PDMS was acquired from Dow Corning GmbH (Wiesbaden, Germany). 4 inch 550 μm thick Si wafers and AZ1512 HS (MicroChemicals) photoresist were provided by the EPFL Center of MicroNanoTechnology (Lausanne, Switzerland). *E. coli* ATCC 25922 strain (*E. coli* WDCM 00013 VitroidsTM), ciprofloxacin (17850, CAS Number 85721-33-1), ampicillin sodium salt (A0166, CAS

Number 69-52-3), gentamicin (G1264, CAS Number 1405-41-0), sterilized mineral oil (M5310, CAS Number 8042-47-5), and trimethylchlorosilane (TMCS, CAS Number 75-77-4) were purchased from Sigma-Aldrich (Buchs, Switzerland).

6.2.2 Sample preparation

Assays in this work were carried out using the *E. coli* ATCC 25922 strain. This organism is a motile and typical AST control strain. We retrieve bacteria from -20 °C and perform overnight bacterial culture in liquid Mueller Hinton media (MH) without shaking. Culture without shaking might potentially enhance the bacterial motility.[216] Under this condition, the OD600 (optical density measured at 600 nm) of the bacterial suspension will reach ~ 1.0 after overnight culture. We dilute the solution to prepare a bacterial suspension with an OD600 value of 0.2 (*i.e.* 0.5 McFarland standard). Hereafter, a two-step dilution respectively 200-fold and 10-fold in pure culture medium was used to prepare the bacterial suspension for the antibiotic-related experiments. As quality control experiments, a purity, viability and concentration check prior to each measurement series was carried out by inoculation on a non-selective Mueller-Hinton agar plate (after a further 100-fold dilution) and colony counting after overnight culture. Based on 3 serial quality control experiments, the bacterial concentration range for quality control was determined to be $3.1 \pm 0.4 \times 10^3$ CFU/mL. Correspondingly, the bacterial suspension used for antibiotic-related experiments has a concentration of $3.1 \pm 0.4 \times 10^5$ CFU/mL, which is in the recommend range for standard AST.[28] We also determined that 1.0 OD600 corresponds to $2.7 - 3.5 \times 10^8$ CFU/mL in our study, which is coherent with a recent systematic OD and bacterial number study.[153] For the inoculum-size related experiments, we prepared concentrations of 3×10^6 , 3×10^5 , 3×10^4 , and 3×10^3 CFU/mL, respectively, by gradual dilution of the bacterial suspension with OD600 of 0.2. All bacterial suspensions were stored in a small flacon and used within 15 min.

Antimicrobial solutions used in this study were prepared according to the recommended protocols. Ampicillin sodium salt and gentamicin are soluble in DI water. 1 mol/L hydrogen chloride solution was used for ciprofloxacin. Ciprofloxacin, ampicillin, and gentamicin stock solutions were prepared with a concentration of 25 mg/mL, 50 mg/mL and 36 mg/mL, respectively. Stock solutions were stored at 4 °C and used within 1 week to avoid a risk of declining activity. Prior to the measurements, stock solutions were thermalized at room temperature and gradually diluted in DI water to prepare a series of concentrations according to the potency of each antibiotic (10 times higher than the final target concentrations). Test solution aliquots were prepared by further 10-fold dilution in MH with bacterial inoculation. Target concentrations were chosen according to the MIC range suggested by EUCAST.[155]

6.2.3 Coverslip surface cleaning

A glass coverslip forms the bottom part of the OA chip and channels (Figure 6.1a). The coverslip was cleaned prior to the chip assembly by a protocol of successive soaking steps, comprising (i) acetone, (ii) ethanol, (iii) isopropanol and finally (iv) DI water, resulting in a hydrophilic surface

with a contact angle of 12.0 ± 0.3 degrees (measured by Krüss DSA-30E). Each of these steps was carried out in an ultrasonic bath for 10 min at 45 °C. In addition, the glass slide is rinsed with DI water in between each step to remove the residual liquid.

6.2.4 Microfluidic chip fabrication

The microfluidic chip was fabricated using an OA-based protocol that was adapted from previously published papers.[217–220] Unlike these approaches, our chip consists of a glass-OA-PMMA composite structure. We have chosen NOA68, instead of NOA81 as used in the other papers, as the former provides better adhesive properties for plastics.[221] For OA microfluidic chip fabrication, a PDMS mold or stamp was required for patterning the liquid OA (Figure 6.1a). The PDMS stamp in turn was fabricated using a Si mold, that was patterned by standard photolithography (AZ1512 HS resist, thickness 1.6 μm) and by deep reactive ion etching (DRIE). The depth of the Si grooves, corresponding to the final channel height of the OA chip, was adjusted by the duration of the dry etching. The etch rate ($\sim 4 \mu\text{m}/\text{min}$) was determined prior to each Si mold fabrication, to ensure a precise control on the final channel depth. Photoresist was removed by oxygen plasma and TMCS Si surface treatment was applied prior to pouring PDMS (base-to-curing agent ratio 10:1) on the wafer mold. PDMS was degassed and cured at 80 °C for 2 h and subsequently the layer was peeled off from the wafer and cut to form the final stamps for OA layer.

The fabrication steps of the OA microfluidic chip are outlined in Figure 6.1a. First, liquid access holes to the channels are machined in a PMMA slide (25 mm \times 75 mm) by laser cutting. The four edges of the PMMA slide were fixed by tapes to facilitate removal of OA residues on the borders after the stamp patterning. A layer of liquid OA (thickness ≈ 1 mm) was poured manually on the PMMA slide. Big bubbles could be wiped off using a scalpel. The holes were sealed from the bottom by tape to confine the adhesive. At this stage, featuring the predefined channel structures was aligned and pressed into the liquid OA layer. The OA patterns were solidified by partial curing during UV exposure through the PMMA side (dose: 480 mJ/cm^2) and PDMS mold side (dose: 240 mJ/cm^2), respectively. Subsequently the PDMS stamp could be removed and reused for the next chip after simple cleaning with ethanol. Tapes on the edge of the PMMA slide were removed together with overflowing OA and OA-filled holes of the PMMA slide were reopened by punching. A coverslip was brought in contact with the partially cured OA and pressed slightly to seal the chip. Finally, the OA was fully cured by UV light (dose: 1.2 J/cm^2). Adhesion was strong enough to perform liquid manipulations without leakage. Sealing the OA channels with a thin glass coverslip provides a clear advantage for high-resolution imaging using microscope objectives with short working distance. The final microfluidic chip, featuring 30 independent channels (2 rows of 15 channels) is shown in Figure 6.1b, allowing either performing assays under different conditions simultaneously or improving statistical analysis of equal assays.

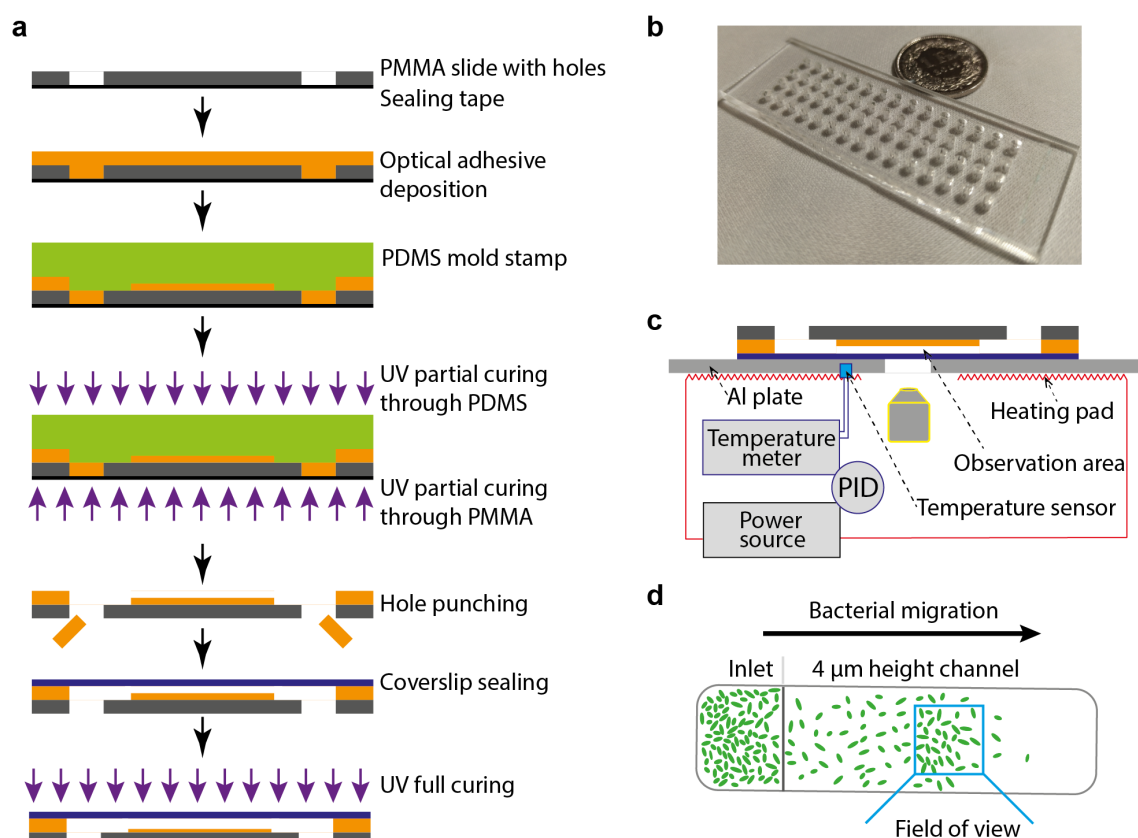


Figure 6.1 – Chip fabrication and design for quasi-2D confinement of bacterial populations. (a) Fabrication process of the shallow microfluidic channels (height: $4\ \mu\text{m}$) defined by imprinting a PDMS stamp into a thin OA layer. A glass coverslip seals the microfluidic channel before complete OA curing. (b) Image of the final chip ($75\ \text{mm} \times 25\ \text{mm}$, top view) showing the fluidic access holes in the PMMA slide to 30 individual parallel OA channels, arranged in two rows. (c) Schematic diagram illustrating the imaging configuration and PID temperature control for on-chip incubation. (d) Bacteria spread out from the inlet into the OA channel after certain time of on-chip incubation (no flow applied). A bacterial traveling band, *i.e.* a transient increase of the bacterial density, may be observed in the field of view.

6.2.5 Working principle

The on-chip array of individual microfluidic channels allows either performing assays under different conditions simultaneously or improving statistical analysis of identical assays. Each channel had a width of $800\ \mu\text{m}$ and a length of $3\ \text{mm}$. We determined an optimal channel height by testing a range of different OA layer thicknesses ($2\ \mu\text{m}$ to $12\ \mu\text{m}$). Bacteria could not be focused on a quasi-2D level when the height exceeded $8\ \mu\text{m}$. On the other hand, bacterial suspensions remained largely confined in the inlet hole if the channel height was too small, eventually resulting in channel clogging (for $< 4\ \mu\text{m}$ in our case). A height of $4\ \mu\text{m}$ was found to be most suitable for the present application (Figure 6.2). The observation region is located in the middle of each channel. An automated x/y-motor stage was used to scan the array of observation windows for imaging

successively all on-chip assays. For bacterial motion tracking discussed in this work, we used an inverted phase contrast microscope with a 40 \times objective (Zeiss LD ACHROPLAN 40 \times /0.60 Korr Ph2, working distance 1.8 mm).

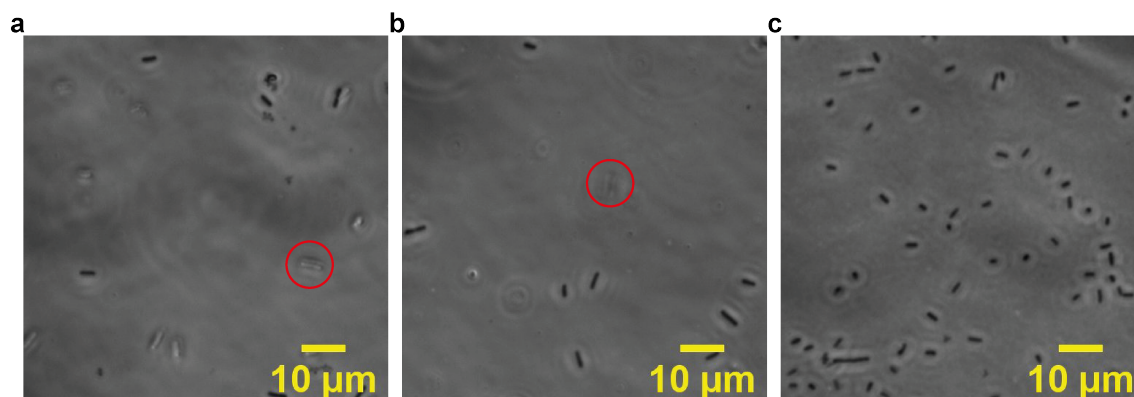


Figure 6.2 – Optimization of the channel height. (a) Height = 12 μm , (b) height = 8 μm , (c) height = 4 μm . The red circles indicate bacteria that are out of focus. All bacteria confined in a 4 μm high channel can be well focused, thus this geometrical parameter was chosen for our microfluidic chip. A chip with a lower OA channel height can be fabricated, however, clogging at the inlet is likely to appear.

Samples were loaded by pipetting 2 μL of bacterial suspension (inoculum) into the inlet of each channel, which then filled autonomously by capillary flow. Eventually, channels and inlets are uniformly filled with bacterial suspension of the same concentration. To prevent evaporation, the inlets and outlets were sealed with sterilized mineral oil (4 μL). The chip was mounted on an Al plate (1.5 mm thick) with a heating pad attached underneath, providing a suitable thermal environment and control for on-chip incubation (Figure 6.1c). The heating pad had two parallel rectangular openings (3 mm \times 60 mm, for each row of channels) for optical access to the imaging region from below. Assays were carried out at 37 $^{\circ}\text{C}$. Temperature regulation was based on a PID closed loop using a Lakeshore 336 temperature controller. The chip temperature was probed with a resistance thermometer (RTD) sensor. According to heat transfer simulations (3D model shown in Figure 6.3a), a stable temperature distribution can already be achieved after a few minutes with a variation of less than ± 0.5 K over the whole chip area, despite the openings in the heating pad (Figure 6.3b and Figure 6.3c). The measured temperature at the RTD sensor location stabilized to 37.0 ± 0.1 $^{\circ}\text{C}$ after 3 min (Figure 6.3d). In reality, the temperature perturbation and air convection in the ambient space that is not fully rendered in the simulation, may influence the temperature stability. Thus, the actual temperature over the Al plate surface was 37 ± 1 $^{\circ}\text{C}$ (measured separately with a movable RTD sensor). Imaging protocols were started 15 min after sample loading to ensure fully stabilized fluidic and thermal conditions.

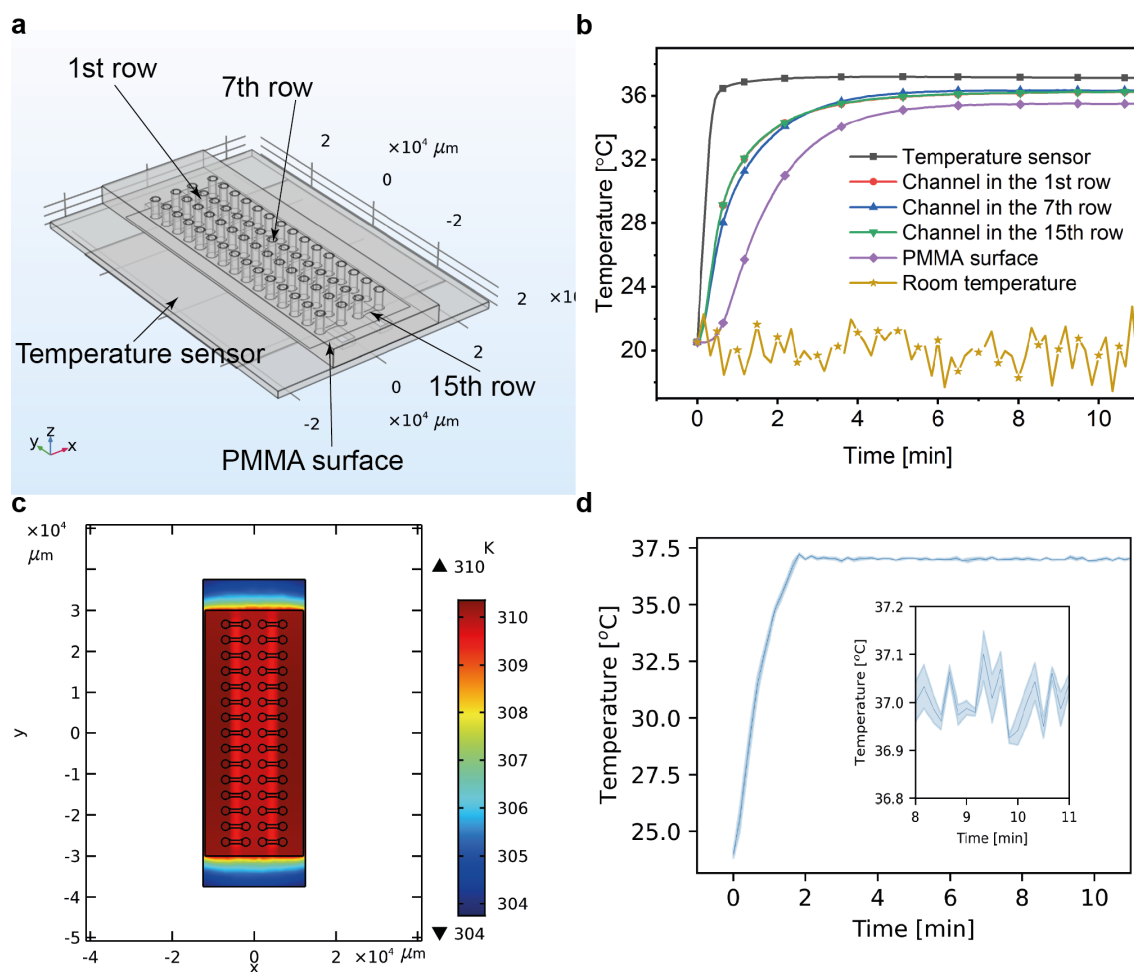


Figure 6.3 – Heat transfer simulation by COMSOL Multiphysics®. (a) 3D model of the microfluidic chip (from top to bottom: PMMA, OA, and coverslip), Al plate and underlying heating pad. (b) Simulated temperature stabilization at different positions of the microfluidic chip: PID temperature sensor location, the channels in the first, seventh, and fifteenth row, and the PMMA top surface, indicated on (a) respectively. (c) Temperature distribution (simulation) of the microfluidic chips after heating for 10 min. The rectangular openings of the heating pads under each channel row result in a slight temperature inhomogeneity with a variation of $\pm 0.5 \text{ K}$. (d) Temperature measured by the RTD (Pt1000) sensor on the Al pad. The temperature stabilization at the sensor spot in the range of $\pm 0.1 \text{ K}$ around the set point $37.0 \text{ }^{\circ}\text{C}$ (insert in Figure 6.3d). The first video acquisition for bacterial recording was done after 15 min to ensure temperature equilibration over the whole microfluidic chip.

6.2.6 Video recording and image processing

Videos of the bacterial on-chip populations were taken by means of a sCMOS camera (PCO. Panda 4.2). Using a high frame rate and resolution (40 fps, $2048 \text{ px} \times 2048 \text{ px}$), bacterial swimming traces could be precisely captured in an area corresponding to an on-chip field of view (FOV) of $340 \mu\text{m} \times 340 \mu\text{m}$. A video sequence was recorded once per hour (10 s corresponding to 400 frames) on each

of the observation windows of the chip array during the whole assay duration (typically 15 h). As shown schematically in Figure 6.1d, traveling bands corresponding to a transient increase of the microbial density could be observed in the observation region, located at the mid-position of each channel after on-chip incubation of several hours.

Automated image and data processing were performed after collecting the experimental raw data. Image processing was implemented with ImageJ software. As shown in Figure 6.4a, the main steps of the protocol are background removal, filtering, image binarization by thresholding, and bacteria boundary detection, respectively. A typical sequence of corresponding microscopy images (Figure 6.4b-e, zoomed in for details) illustrates the different processing steps. In the raw phase contrast image, bacteria are darker than the background or defects. The first step was to perform illumination background subtraction (obtained by taking an image without chip in the optical path of the microscope). Subsequently, an unsharp filter was applied to the image (radius = 10 pixels, intensity = 0.9) to enhance the contrast between bacteria and background (Figure 6.4b). This image is binarized by means of a threshold method (“IsoData”, embedded in ImageJ) as shown in Figure 6.4c. Then the center position and the boundaries of each individual bacterium were determined and highlighted by red lines (Figure 6.4d, using the function “Analyzing the particle” in ImageJ). Furthermore, the skeleton of each bacterium could be analyzed by converting the 2-D white geometry in Figure 6.4c into the skeletonized 1-D line as shown in Figure 6.4e. Occasionally bacteria may stick together forming pairs or small clusters. In principle, they could be separated during image processing (using the “Watershed” tool in Image J). However, in the current study we did not apply this algorithm, as it was not accurate enough to discriminate between cell clusters and cell elongation (filamentation) due to antimicrobial stress (see further).

Datasets of bacterial coordinates were extracted from the processed image stacks. Subsequent data processing was performed by means of MATLAB programs. We used an established tracking algorithm to record the swimming path of individual bacteria in small on-chip populations and to perform trajectory analysis.^[222] An example of a high-resolution image is shown in Figure 6.4f, where trajectories of bacteria have been identified with different colors. This image corresponds to a stack of 40 frames, *i.e.* an observation time of 1 s (zoomed in to a frame of $90\ \mu\text{m} \times 90\ \mu\text{m}$ in this case). In a time lapse of 1 s, bacteria trajectories mainly correspond to straight or slightly bending segments of motion, only a few microbes are tumbling frequently on this time scale. Entire trajectories observed in the full FOV (400 frames, recorded over 10 s) indeed show random sequences of straight runs and tumbling events as shown in the Figure 6.5. Eventually, we were able to characterize different properties of individual bacteria and of their collective behavior, including the cell body elongation under antimicrobial stress (filamentation), transient bacterial density profiles (traveling bands), and swimming parameters, in particular speed and tumble bias distributions.

6.2.7 Statistical analysis

All experiments shown in the work were carried out for 3 parallel assays on the chip. Statistical analysis of the obtained results such as speed, skeleton size, effective diffusion coefficient and

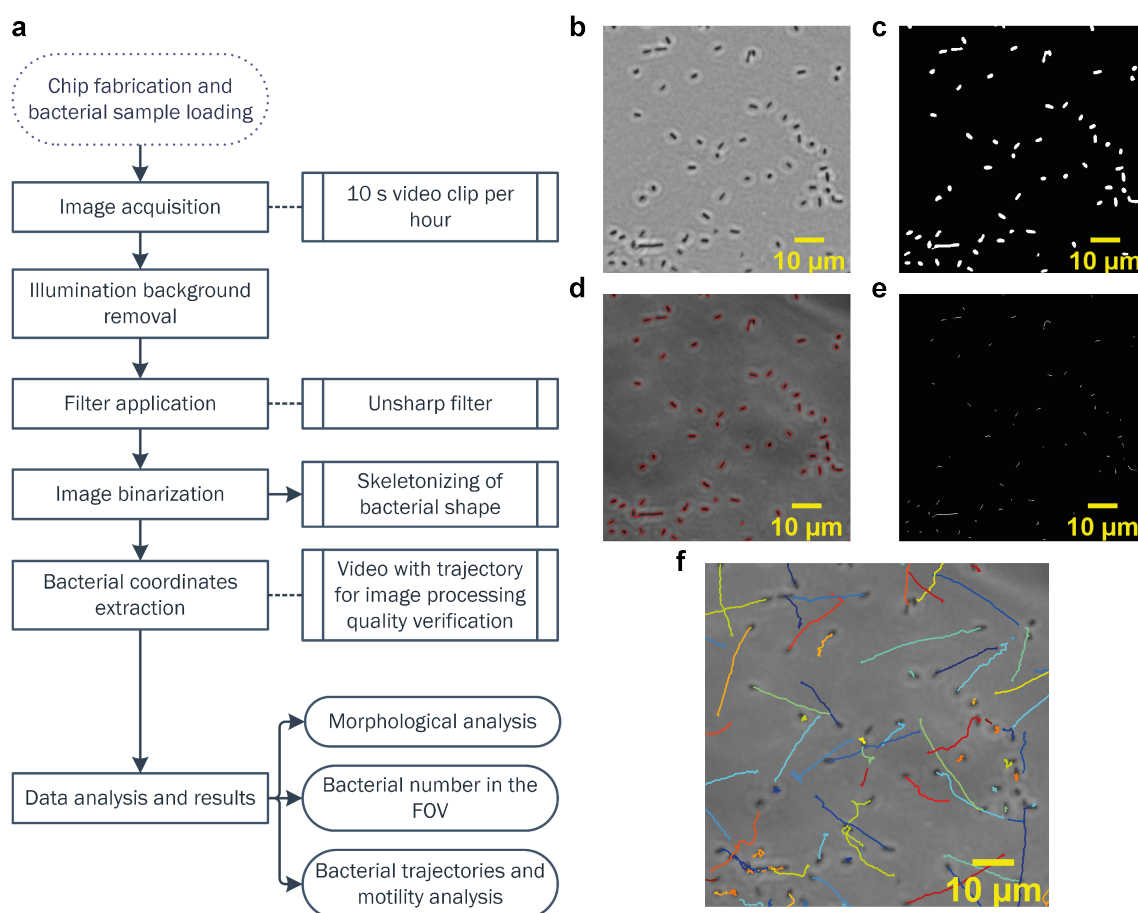


Figure 6.4 – Automated image stack processing and data analysis. (a) Schematic diagram of the workflow for assessing properties of individual bacteria and bacteria populations in the OA chip. Morphological and motility-related information can be extracted for different experimental conditions and time points based on video analysis. (b) Raw phase contrast image of individual *E. coli* bacteria in a quasi-2D population layer confined in the OA channel (40 \times phase contrast objective, FOV $\sim 340 \mu\text{m} \times 340 \mu\text{m}$, the ImageJ software unsharp filter was applied). (c) Binarized images processed by thresholding the image shown in (b). (d) Red contours indicate each identified bacterium. (e) Image showing the skeleton of each bacterium by replacing the 2D bacterial shape in (b) by a 1D line. (f) Bacterial swimming trajectories obtained by attributing an index to each individual bacterium on a consecutive image stack (40 frames, *i.e.* an observation time of 1 s).

tumble bias was performed using MATLAB R2018b® and Python (packages: pandas and SciPy).

6.3 Results

6.3.1 Morphological analysis

At a first stage of our study, we analyzed bacteria morphology on-chip, *i.e.* in the same FOV of the chip, where also traveling bands have been visualized. The analysis considers only the

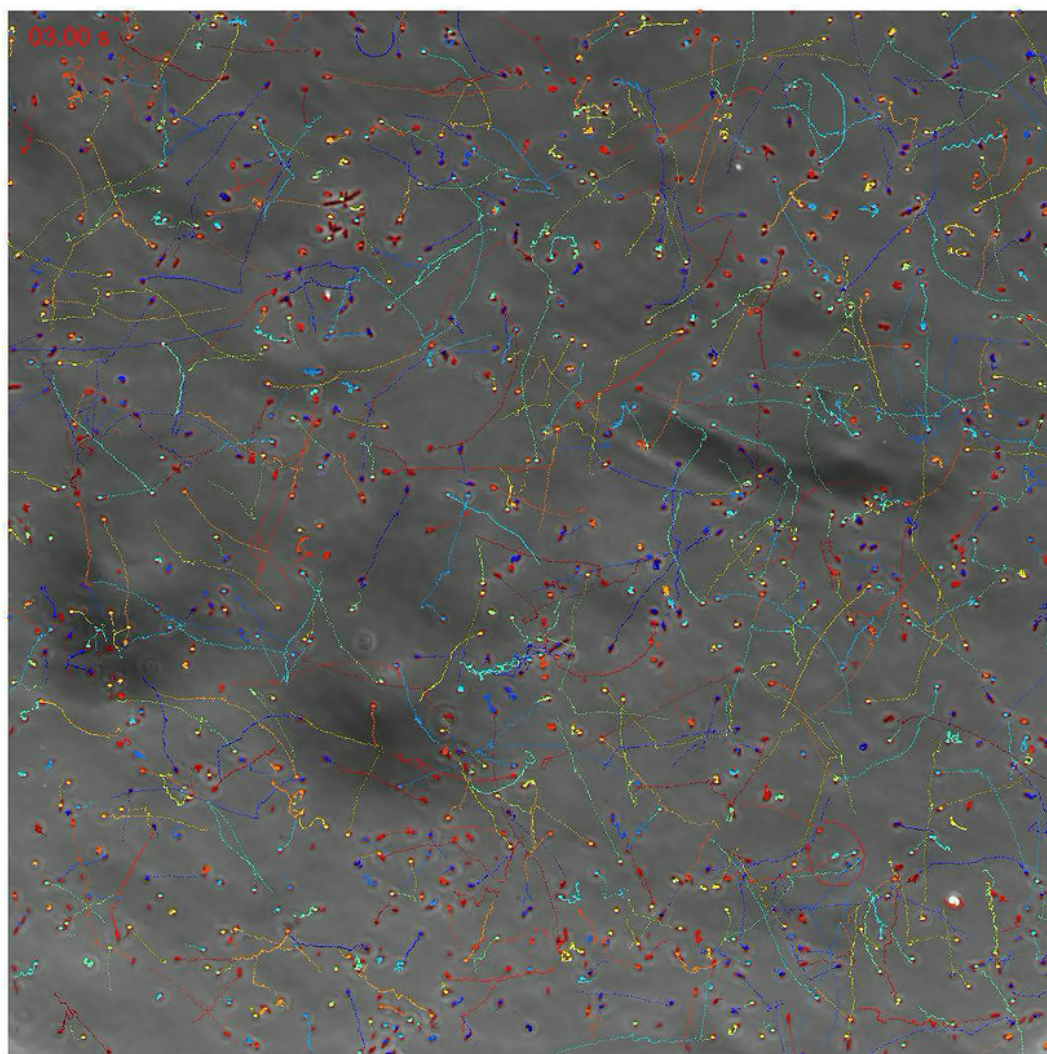


Figure 6.5 – Screenshot of an example of a video sequence after image processing showing bacterial swimming with trajectories in a quasi-2D 4- μm high microfluidic channel (Conditions: bacterial inoculum concentration 5×10^5 CFU/mL observation at 6 h, 40 f/s for 10s with a FOV of $340 \mu\text{m} \times 340 \mu\text{m}$).

motile fraction of the microbial population of interest in this context, excluding the non-migrating population that remained in the channel inlet. Figure 6.6a-c shows the distribution of the skeleton length of *E. coli* as a function of on-chip incubation time in MH with three different antibiotics (ampicillin, ciprofloxacin and gentamicin). For normal bacterial growth conditions (MH without antimicrobials) the average cell body length is $1.43 \pm 0.04 \mu\text{m}$ after 6 h and $1.36 \pm 0.06 \mu\text{m}$ after 12 h, (blue bars in Figure 6.6a). As a reference for assays involving antibiotics in the present work, we determined the following MIC value ranges from *E. coli* OD600 growth curves: (i) $2.5 < \text{MIC} \leq 5.0$ mg/L for ampicillin, (ii) $0.008 < \text{MIC} \leq 0.015$ mg/L for ciprofloxacin, and (iii) $1.1 < \text{MIC} \leq 2.2$ mg/L for gentamicin (Figure 6.7a-c).

Exposure to antimicrobials in the sub-MIC range may have a significant effect on the bacterial morphological development, referred to as filamentation. Strongest elongation of the *E. coli* skeleton with respect to normal growth was observed for ampicillin. Figure 6.6a shows the bacterial size increase and evolution with incubation time for two different ampicillin concentrations (1.2 mg/L orange bars and 2.5 mg/L green bars, respectively; the latter concentration is close to MIC). In both cases elongation of about a factor of 3 to 4 with respect to normal growth was observed. The average size first increased and then decreased due to partial lysis in the later growth phase. This variation over time (6 to 12 h) was more pronounced for the highest concentration in this case (*i.e.* for 2.5 mg/L ampicillin). The variability of bacterial growth, expressed as standard error of the skeleton length (95% confidence interval thus $\pm 2 \times \text{SE}$), is much smaller under normal growth conditions than for the two ampicillin cases, indicating that antimicrobial stress frequently generates non-uniform bacterial divisions. Ciprofloxacin generated a somewhat less pronounced filamentation effect compared to ampicillin (Figure 6.6b). The maximum average skeleton length does not exceed $3.6 \pm 0.6 \mu\text{m}$ (0.015 mg/L at 6 h), in comparison to $7.0 \pm 1.2 \mu\text{m}$ for ampicillin (2.5 mg/L at 8h). However in the case of ciprofloxacin, the average bacterial elongation increased gradually for incubation with higher antimicrobial doses and over the whole assay duration (6 to 12 h). The size uniformity declines strongest at 0.015 mg/L, *i.e.* close to MIC (Figure 6.6b, purple bars). A slight decrease of bacteria length with incubation time was also observed. In contrast to the previous findings, bacteria growth in gentamicin does not show a clear filamentation effect (Figure 6.6c). Although we observe that the bacterial average size in 1.1 mg/L gentamicin (red bars) is slightly higher than for the other concentrations, elongation is far less pronounced than for ampicillin or ciprofloxacin. Correspondingly, bacterial divisions are more uniform (small SE in Figure 6.6c) even for a gentamicin concentration just below MIC.

A more detailed analysis of the filamentation effect in ampicillin is presented in Figure 6.6d, showing the bacterial skeleton length distribution and median values for different ampicillin concentrations after 8-hour on-chip incubation. Figure 6.6e and 6.6f show images of *E. coli* with highlighted skeletons, incubated in MH and an example of a strongly elongated cell in the presence of ampicillin, respectively.

6.3.2 Bacteria traveling bands

Coherent migration of bacteria through the microchannel appearing as traveling bands with locally increased population density were observed in the FOV of the chip after a few hours of on-chip incubation (passive migration by diffusion is not relevant in the present case). At the beginning of each experiment the bacterial density in the microchannel is very low, thus nearly any bacteria can be observed in the FOV. Considering a typical inoculum size of 3×10^5 CFU/mL used in our assays and the low volume of ~ 0.36 nL of the channel portion observed, less than 1 bacterium is expected to be found in the FOV. After on-chip incubation for a few hours, the number of bacteria in the inlet reservoir increases exponentially, resulting in a local depletion of nutrients and other chemical attractants. This self-generated chemical gradient activates chemotaxis and sub-population(s) of more motile bacteria possibly start migrating into the microchannel in a coherent collective

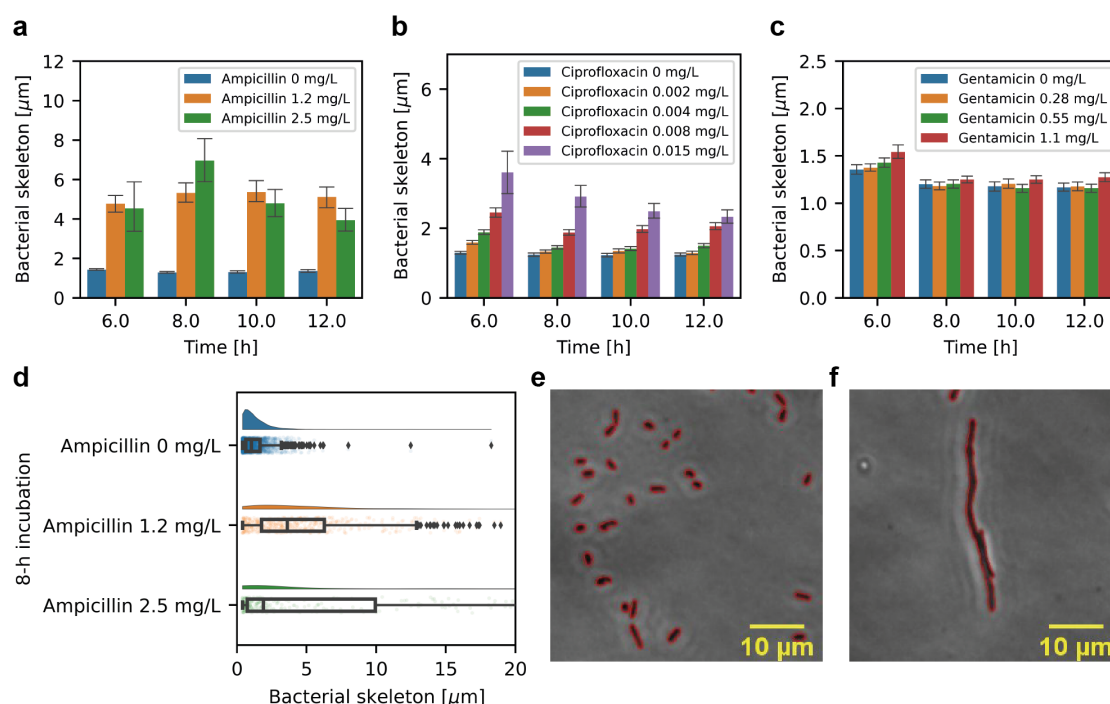


Figure 6.6 – *E. coli* morphological analysis. Mean bacterial skeleton length as a function of incubation time for *E. coli* exposed to ampicillin (a), ciprofloxacin (b) and gentamicin (c), respectively (in MH at 37 °C, error bars represent $\pm 2 \times \text{SE}$). The bacterial skeleton considerably elongates in the presence of ampicillin. The filamentation effect is less pronounced in the presence of ciprofloxacin and nearly invisible with gentamicin. (d) Boxplot of the bacterial skeleton length distribution for bacterium after on-chip incubation for 8 hours with ampicillin at different doses. In the presence of ampicillin, bacterial skeletons show a significantly wider length distribution than with normal growth conditions. (e) Image of *E. coli* cells (indicated by red contours) after on-chip incubation for 8 hours without antimicrobials. (f) Image and contour of a single elongated *E. coli* bacteria after on-chip incubation with 2.5 mg/L ampicillin for 8 hours.

manner. The resulting traveling band(s) may be recorded at the FOV location of the chip as transient peaks in the microbial population density. In the shallow geometry of our microfluidic channel, traveling bands formed in a 2D bacterial layer were observed and analyzed.

We first studied the effect of the *E. coli* inoculum size on the traveling band peak intensity and the peak delay under normal culture conditions in pure MH (Figure 6.8a, inoculum range from 3×10^3 CFU/mL to 3×10^6 CFU/mL). The transient cell density peak has the highest amplitude and shows longest delay (10 h) for the smallest inoculum size (3×10^3 CFU/mL, blue curve in Figure 6.8a). In Figure 6.8a (as well as in Figure 6.8d-f) cell density is defined as the fraction of the total bacterial body area to the area of the FOV, reflecting more accurately the actual biomass. Due to possible filamentation in the presence of antibiotics, the corresponding bacterial number densities (Figure 6.9) may be smaller and not proportional to the integrated cell body area obtained by image analysis, especially in the case of ampicillin (see below, Figure 6.8d and 6.9b). In Figure 6.8a,

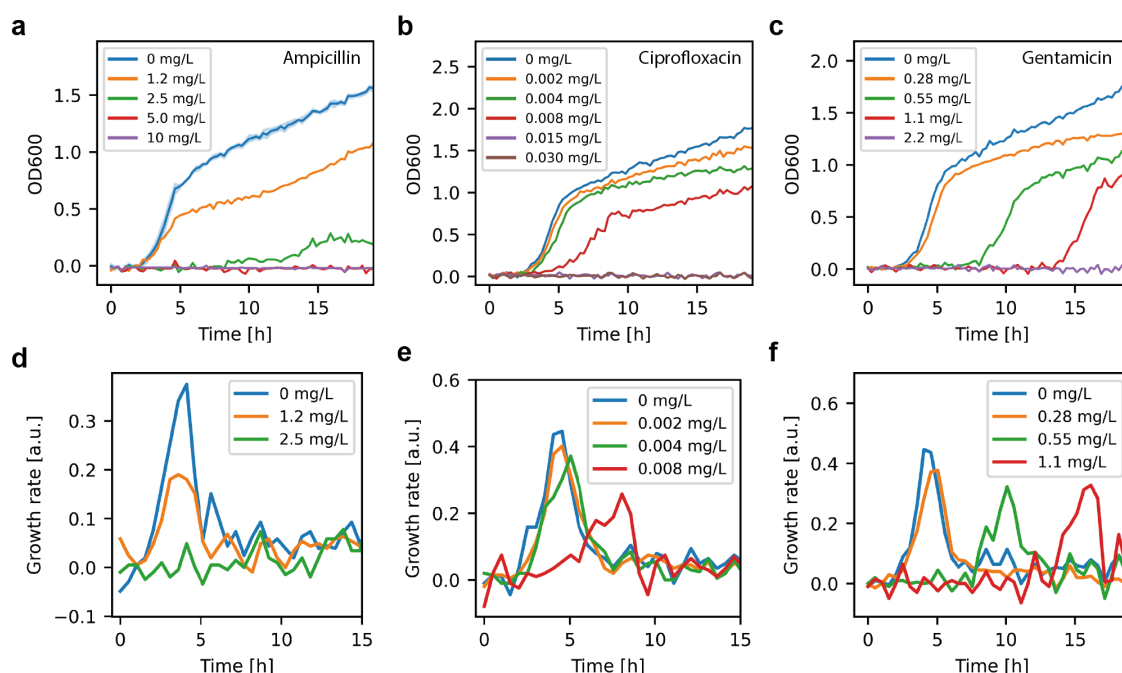


Figure 6.7 – *E. coli* growth and growth rate curves based on OD600 measurements as measured in a well plate. (a-c) Growth curves for *E. coli* exposed to different antibiotics: ampicillin (a), ciprofloxacin (b), gentamicin (c). The error bars (or bands) stand for $\pm 2 \times \text{SE}$. (d-f) Corresponding growth rate curves (time derivatives of a-c): ampicillin (d), ciprofloxacin (e), gentamicin (f). Exposure to antimicrobials with concentrations approaching MIC results in strongly prolonged lag phases, *i.e.* for 2.5 mg/L ampicillin, 0.008 mg/L ciprofloxacin, 0.55 mg/L and 1.1 mg/L gentamicin, indicating progressive inhibition of bacterial growth. No growth can be seen above MIC. We determined the following MIC value ranges from curves a-c: (i) $2.5 < \text{MIC} \leq 5$ mg/L for ampicillin, (ii) $0.008 < \text{MIC} \leq 0.015$ mg/L for ciprofloxacin, and (iii) $1.1 < \text{MIC} \leq 2.2$ mg/L for gentamicin.

delays and peak amplitudes decreased for increasing inoculum size. As nutrient depletion in the inlet generated by exponentially growing bacterial populations is at the origin of the collective chemotactic behavior, the traveling band delay should in principle be related to the bacterial growth. More bacteria mean faster depletion in the inlet, leading to earlier bacterial migration out of the inlet in the form of traveling band. OD600 growth curves measured in a well plate show different lag phases, indicating basically a right-hand shift for decreasing inoculum size, whereas the overall curve shape is conserved (Figure 6.8b). Correspondingly, the maximum growth rate appears to be shifted on the time scale according to lag phase extension (Figure 6.8c, curves are time derivatives of Figure 6.8b). However, the lag phase difference cannot explain the pronounced cell density peak amplitude variation observed in Figure 6.8a. Actually, according to the OD600 curves, cell densities are expected to be very similar at the time when the peak for the corresponding inoculum size is observed in the FOV (*i.e.* ≈ 1.0 OD600 in Figure 6.8b).

Traveling bands generated by bacteria populations incubated with antibiotics are the focus of the second part of our study (Figure 6.8d-f). In the presence of antibiotics, features of traveling bands

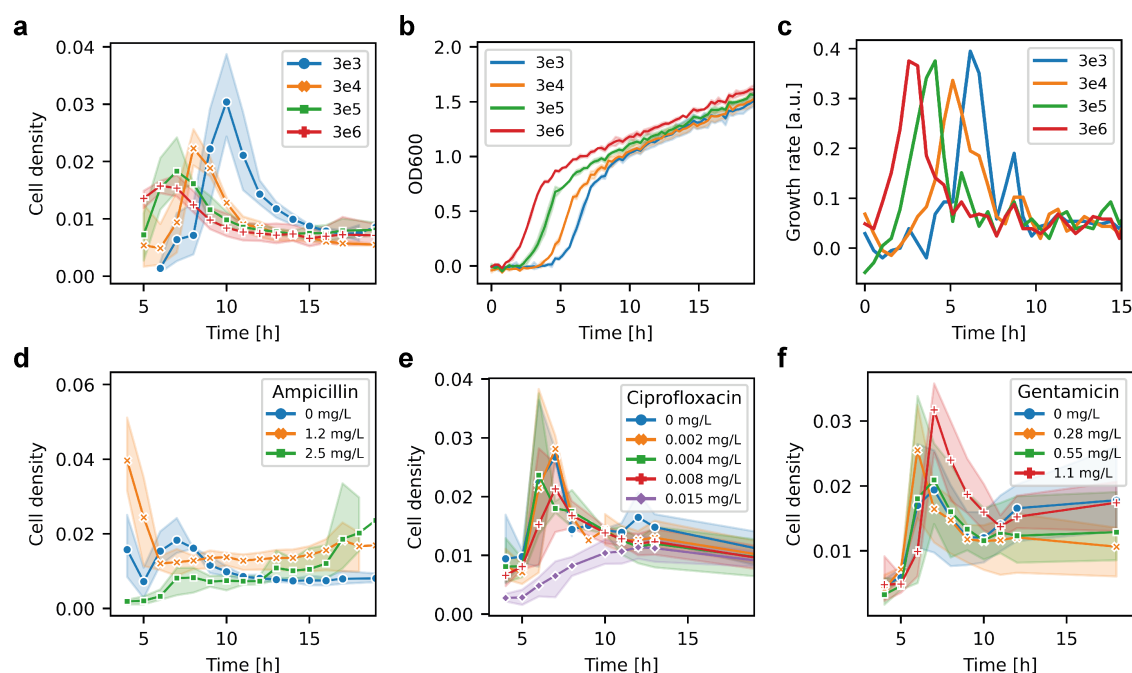


Figure 6.8 – Time dependent bacterial density profiles (traveling bands). A transient increase of the *E. coli* density is generally observed in the FOV of the microchannel after a few hours of on-chip incubation, corresponding to a collective bacterial migration pattern referred to as traveling band. (a) Cell density in the FOV as a function of time for bacterial suspensions originating from different inoculum sizes. Cell density peaks appear in the FOV on different time scales. Strongest delay and cell density increase were observed for the lowest inoculum size. (b) Standard OD600 growth curves obtained on a plate reader. The growth curves indicate that lag phases (below the LOD of the plate reader in this case) prolonged with decreasing inoculum size, corresponding to the peak delays observed in (a). (c) Growth rate curves (time derivatives of Figure 6.8b) show a corresponding shift of the maximum growth rate. (d-f) Traveling bands for *E. coli* subjected to different antimicrobial conditions, *i.e.* ampicillin (d), ciprofloxacin (e), and gentamicin (f). For concentrations below MIC, traveling bands were observed in all cases. For concentrations approaching MIC, bacteria can still be observed in the FOV for ampicillin (green curve, 2.5 mg/L) and ciprofloxacin (purple curve, 0.015 mg/L), but no transient traveling bands occurred. For gentamicin at the concentration tested which was closest to MIC (red curve, 1.1 mg/L), a clear traveling band with the highest peak amplitude occurred. No bacteria were detected in the channel at the next higher concentration tested (2.2 mg/L \geq MIC). The presence or absence of traveling bands is related to growth/motility inhibition and may be explored as an indicator for *E. coli* MIC values. Inoculum concentrations are labeled as $3e^n$ corresponding to 3×10^n CFU/mL. The error bars (or bands) stand for $\pm 2 \times \text{SE}$.

depend on both, on growth inhibition due to the antimicrobials and on possible alterations of the bacterial mobility. At sub-MIC values (according to MIC reference values in Figure 6.7), traveling bands could be observed in the FOV for the three antibiotics tested (ampicillin, ciprofloxacin and gentamicin), whereas no bacteria could be detected above MIC (for $t \leq 19$ h, tested for ampicillin 5.0 mg/L, ciprofloxacin 0.030 mg/L, and gentamicin 2.2 mg/L, results not shown). In the concentration

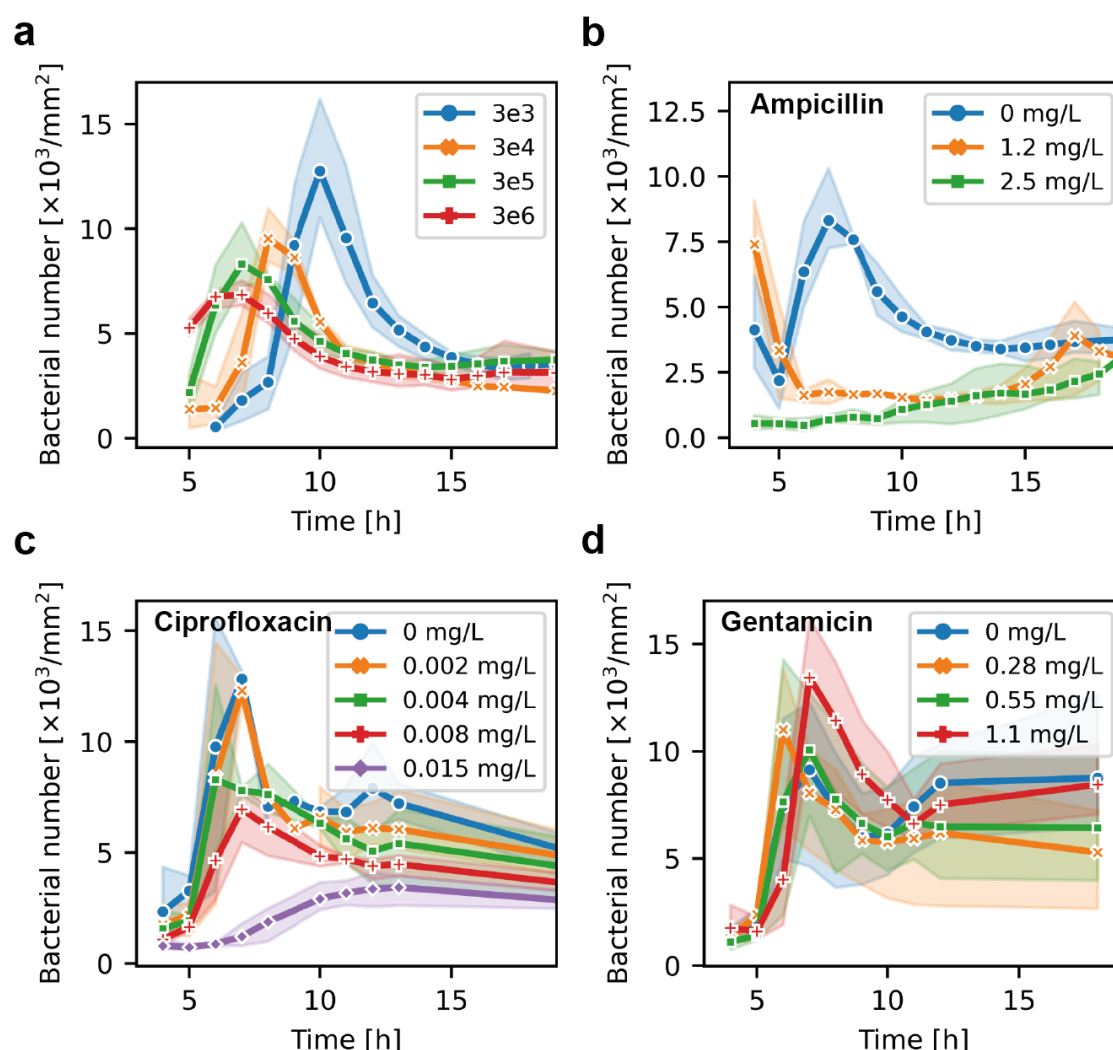


Figure 6.9 – Bacterial number density in the FOV as a function of time for different experimental conditions: inoculum size (a), ampicillin concentration (b), ciprofloxacin concentration (c), and gentamicin concentration (d). Bacterial number curves have the same overall shape as the cell density curves based on the integrated cell area measurements (Figure 6.8), but due to filamentation stimulated by antibiotics, bacterial number curves do not reflect the true biomass. The error bars (or bands) stand for $\pm 2 \times \text{SE}$.

range close to MIC, in particular for 2.5 mg/L ampicillin and 0.015 mg/L ciprofloxacin, enhanced growth inhibition monitored by prolonged lag phases and filamentation effects dominated (Figure 6.7a,b and Figure 6.6a,b, respectively). No dense traveling bands occurred in these cases, however a smoother bacteria population density variation could still be observed, mainly because occasionally migrated bacteria still keep growing in the channel (green curve in Figure 6.8d and purple curve in Figure 6.8e, respectively).

For these two antibiotics, we can therefore determine a lower limit for the *E. coli* MIC value range by

identifying the concentration where clear traveling bands do not appear anymore. These values are coherent with the MIC ranges obtained by OD600 growth curves (Figure 6.7a and b). The situation is somewhat different in the case of gentamicin, where traveling bands appeared for all concentrations shown, including the ones that featured strongest lag phase extensions, *i.e.* from ~ 2 h in pure MH to ~ 7 h at 0.55 mg/L and ~ 13 h at 1.1 mg/L (Figure 6.7c or Figure 6.7f, green and red curves), with nearly normal growth resuming after this lapse of time. The transient peak amplitude was even highest for the concentration that was closest to MIC (*i.e.* for 1.1 mg/L, red curve in Figure 6.8f). No growth occurred at the next higher concentration tested (2.2 mg/L). Interestingly, no pronounced or systematic variation of the delay of the traveling band peaks at sub-MIC concentrations could be observed. Extension of the lag phases for increasing antimicrobial concentrations, as monitored by the OD600 bacterial growth curves (Figure 6.7) does not seem to have a corresponding effect on the transient cell density curves. The peak value for 1.2 mg/L ampicillin appears at ~ 4 h (orange curve in Figure 6.8d, no bacteria visible in the channel at $t \leq 3$ h), which is earlier than for normal growth conditions (blue curve in Figure 6.8d), even though the growth rate peaks appeared at the same time (Figure 6.7d), indicating that growth in the microchannel is not dominating the traveling band dynamics.

For ciprofloxacin, all traveling band peaks appeared nearly at the same time, although the growth rate curves showed a clear time shift for 0.008 mg/L (Figure 6.8e and red curve in Figure 6.7e). This discrepancy is even more pronounced for gentamicin. As mentioned above, OD600 growth curves for 0.55 and 1.1 mg/L indicated that growth under these conditions were not fully inhibited but occurred with a strong delay. However, there was no corresponding time shift in the traveling bands for this concentration range (Figure 6.8f). Unlike to the assays testing different inoculum sizes (Figure 6.8a), where the traveling peak positions shifted according to lag phase extension (Figure 6.8b), such tendency was not observed for incubation with antimicrobials. As will be discussed in the following, exposure to antimicrobials might enhance the chemotactic swimming ability. Moreover, *E. coli* did not show significant filamentation for gentamicin in the sub-MIC concentration range (Figure 6.6c), in contrast to ampicillin and ciprofloxacin, which certainly has a significant impact on the different dynamic migration patterns generated by the three antibiotics.

6.3.3 Motility analysis for different inoculum sizes

We performed a bacterial motility analysis of migrating *E. coli* populations in order to unravel underlying features of coordinated chemotactic behavior and dynamic properties of traveling bands under different conditions. The analysis is performed from several perspectives, namely the swimming speed and the tumble bias (TB) distribution, and the resulting effective microbial diffusion properties. The motility analysis is based on individual swimming trajectories of the bacteria sub-population appearing in the FOV at a given point in time, in particular at the peak of the transient cell density. A MATLAB particle tracking algorithm^[222] was applied to identify specific bacteria and to calculate the set of individual trajectories (see also Figure 6.5). Only trajectories longer than 1 s have been used to improve the reliability of the calculation. Once individual bacterial trajectories are identified, the swimming speed v_0 can be calculated as the trajectory

distance divided by the duration. The mean speed v_{mean} can be obtained based the v_0 of all trajectories that appeared in the videoclip.

As shown in Figure 6.10a, the v_{mean} peak delay and peak amplitude both increased for decreasing inoculum size. This trend is very similar to the transient behavior of the cell density in the FOV (Figure 6.8a). As a validation of the motility analysis based on individual trajectories (Figure 6.10a), we considered the pixel changes in two consecutive binarized image frames (Figure 6.10b). More pixel changes (normalized with respect to the amount of bacteria in the FOV) indicate a higher overall bacterial motility. This classical pixel analysis of an image is relatively simple but does not reveal individual bacterial trajectory properties. The overall shape of the curves obtained with both methods corresponds well.

The effective diffusion properties of an *E. coli* population in the FOV may be assessed by considering the mean square displacement (MSD) as a function of a time interval Δt .

$$MSD(\Delta t) = \frac{1}{N} \sum_{i=1}^N \left((x(t_i + \Delta t) - x(t_i))^2 + (y(t_i + \Delta t) - y(t_i))^2 \right) \quad (6.1)$$

where t_i represents the time lapse for each frame i of the image sequence, and Δt is the full time interval after N frames. In the case of merely passive diffusion due to random Brownian motion, MSD would be proportional to the interval time Δt . However, bacteria are active swimmers, the $MSD(\Delta t)$ relation therefore deviates from the linear relationship. This is emphasized in Figure 6.10c, where a strong parabolic-like increase is observed for Δt values approaching 1.0 s for all inoculum sizes investigated. MSD data analysis, as well as data in Figure 6.10d-f, corresponds to the time point when the peak in the v_{mean} of the corresponding traveling band appeared in the FOV (as observed in Figure 6.10a). Obviously, the MSD of bacteria originating from lower initial inoculum size (e.g. 3×10^3 CFU/mL, blue curve in Figure 6.10c) increased much stronger than for those cultured with higher inoculum size (e.g. 3×10^6 CFU/mL, red curve). Figure 6.10d shows the v_0 distribution of individual bacteria. In all cases two more or less apparent Gaussian distribution profiles could be distinguished, which implies the existence of two distinct bacteria groups traveling with lower and higher speeds, respectively. For inoculum sizes in the range from 3×10^3 CFU/mL to 3×10^5 CFU/mL, the high-speed group is dominating with its peak position shifting to lower values, whereas the density of the low-speed sub-population tends to increase slightly. For the highest inoculum size (3×10^6 CFU/mL), the low-speed group is clearly more pronounced than the high-speed group. This evolution of the v_0 distribution profiles results in decreasing median speed values for increasing inoculum size as shown in Figure 6.10d, or a lower v_{mean} peak value for bigger inoculum size as shown in Figure 6.10a, respectively.

An effective diffusion coefficient can be obtained based on the way proposed by Dufour *et al.* [213]. It is defined as $D_{eff} = (v_0^2 \tau) / d$, where v_0 is the speed of a bacterium, d is the number of dimensions ($d = 2$ for the quasi-2D bacteria confinement in the microchannel), τ is the time scale of the cell directional persistence. The latter is a function of the cell tumble bias, mean tumble angle, and rotational diffusion. Figure 6.10e shows the D_{eff} distribution for all analyzed bacteria trajectories (dots, the density of each value is plotted on the y-scale) and corresponding median values. The

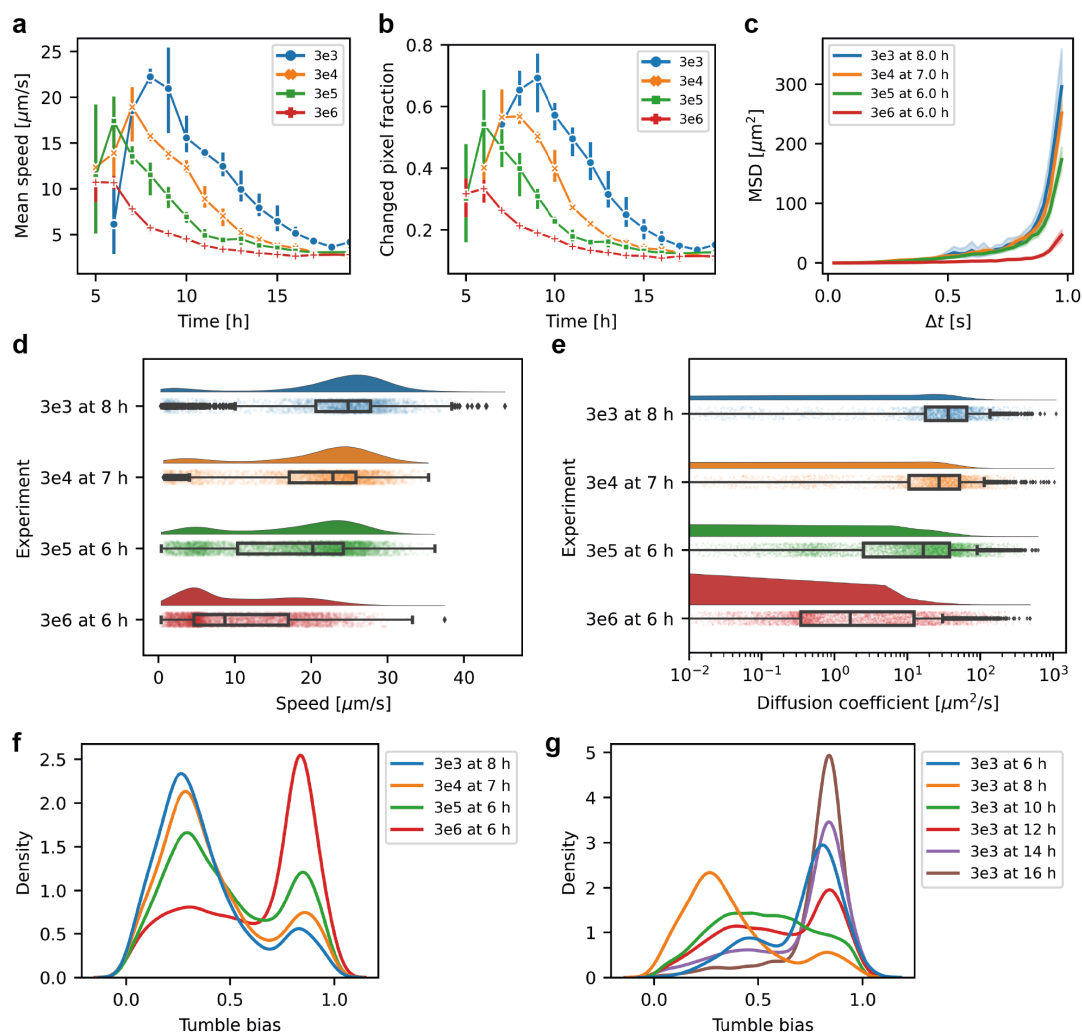


Figure 6.10 – Bacterial motility analysis for different inoculum size. (a) Mean swimming speed v_{mean} in the FOV as a function of time, derived from individual bacterial trajectories. v_{mean} peak delays and peak values increased as the inoculum concentration decreases, thus showing the same trend as the cell density curves in Figure 6.8a. (b) Fraction of pixels changed between two consecutive frames averaged over the recorded image stacks of a bacterial population traveling through the FOV. A higher number of pixels changed indicates higher overall bacterial motility. (c) MSD as a function of a time interval Δt for evaluating the effective bacterial diffusion properties at the time point of the highest v_{mean} for the corresponding inoculum size (see Figure 6.10a). Active swimming results in a strong deviation from a linear $MSD(\Delta t)$ relation expected for Brownian motion. This effect is most pronounced for the case of the lowest inoculum size (3×10^3 CFU/mL). (d) Speed v_0 distribution of all bacteria in the FOV for the time point when the v_{mean} peak occurred. Two subsequent or overlapping Gaussian distributions, depending on inoculum size, can be observed. This implies the existence of two distinct bacterial sub-populations with lower and higher swimming speeds ranges, respectively. (e) Distribution of the effective diffusion coefficient D_{eff} . D_{eff} decreases for increasing inoculum size. The y-scale indicates the density of individual D_{eff} values (arbitrary scale). (f) TB distribution showing two peaks as well. The high-TB population density rises, whereas the low-TB population decreases for lower inoculum size. Higher TB implies lower effective diffusion and mean swimming speed. Distinct TB ranges directly reflect different bacterial phenotypes. (g) TB distribution for 3×10^3 CFU/mL inoculum size observed in the FOV at different time points. High-TB sub-populations appear at later stage. Inoculum concentrations are labeled as $3e_n$ corresponding to 3×10^n CFU/mL. The error bars (or bands) stand for $\pm 2 \times SE$.

diffusion coefficient of a non-motile bacterium subjected to Brownian motion may be estimated to $0.45 \mu\text{m}^2/\text{s}$. [223] The D_{eff} median values derived here are higher than for passive diffusion for all inoculum sizes, with a clear trend to increasing D_{eff} for bacteria cultured from lower inoculum sizes.

By assigning tumble events and straight runs to each bacteria trajectory, respectively, the TB distributions for different inoculum sizes have been obtained (Figure 6.10f). A tumble event in the *E. coli* motility pattern corresponds to a sudden change of swimming direction and TB is defined as the probability that a cell is tumbling. [215] TB distributions are represented as probability density functions obtained by kernel density estimation. Analysis based on the corresponding 10 s video clips show a wide distribution of TB values over the whole range from 0 to 1.0. The TB distribution in general shows two sub-populations, *i.e.* a low-TB group centered at ~ 0.25 and a high-TB group centered at ~ 0.80 . The relative cell densities of low-TB and high-TB groups vary with inoculum size. For smaller inoculum size, *i.e.* 3×10^3 CFU/mL and 3×10^4 CFU/mL (blue and orange curves in Figure 6.10f, respectively), low-TB values dominate. As the inoculum size increases, TB values shift to the higher range, with a more balanced distribution for 3×10^5 CFU/mL (green curve in Figure 6.10f) and a clearly dominating high-TB population for 3×10^6 CFU/mL (red curve in Figure 6.10f). Figure 6.10g displays the TB distribution for an inoculum size of 3×10^3 CFU/mL at successive time points, *i.e.* for bacteria progressively migrating through the FOV. As the FOV position is fixed, the graphs in Figure 6.10g may also be interpreted as the variation of the spatial distribution of TB sub-populations in the microchannel, *i.e.* over the entire traveling band. Before the arrival of the traveling band peak, high-TB values preponderate (at $t = 6$ h, blue curve in Figure 6.10g). At the traveling band peak time point, low-TB value populations are dominating (at $t = 8$ h, orange curve). Bacteria arriving after the transient peak again feature mainly high-TB values (at $t = 14$ h or 16 h, purple and brown curves, respectively). These results reveal that an initially uniform bacterial culture self-organizes itself along the traveling band into sub-populations with different TB. TB is inversely proportional to v_{mean} and D_{eff} (Figure 6.11a and 6.11b). For instance, low inoculum size with a higher density of low-TB cells thus results in a higher v_{mean} . As bacterial inoculums have been prepared from the same overnight culture, we may assume that all bacteria have the same genotype. The peak amplitude variation therefore imply that an isogenic population generates sub-populations with different chemotactic behaviors.

6.3.4 Motility analysis for different antimicrobials

We have applied the protocols described for motility analysis under normal culture in pure MH to bacteria populations incubated with different antimicrobials. Results for *E. coli* exposed to ampicillin, ciprofloxacin and gentamicin at different concentrations are summarized in Figure 6.12 (inoculum size 3×10^5 CFU/mL). The three tested antimicrobials affected the v_{mean} distribution in different ways. Over the assay duration (up to ~ 12 h), v_{mean} was significantly lower than for normal growth conditions when subjected to 1.2 mg/L and 2.5 mg/L ampicillin (Figure 6.12a, blue and orange curves, respectively). Interestingly, for ciprofloxacin (Figure 6.12b) and gentamicin (Figure 6.12c), at sub-MIC values v_{mean} are roughly maintained at a comparable level for all conditions.

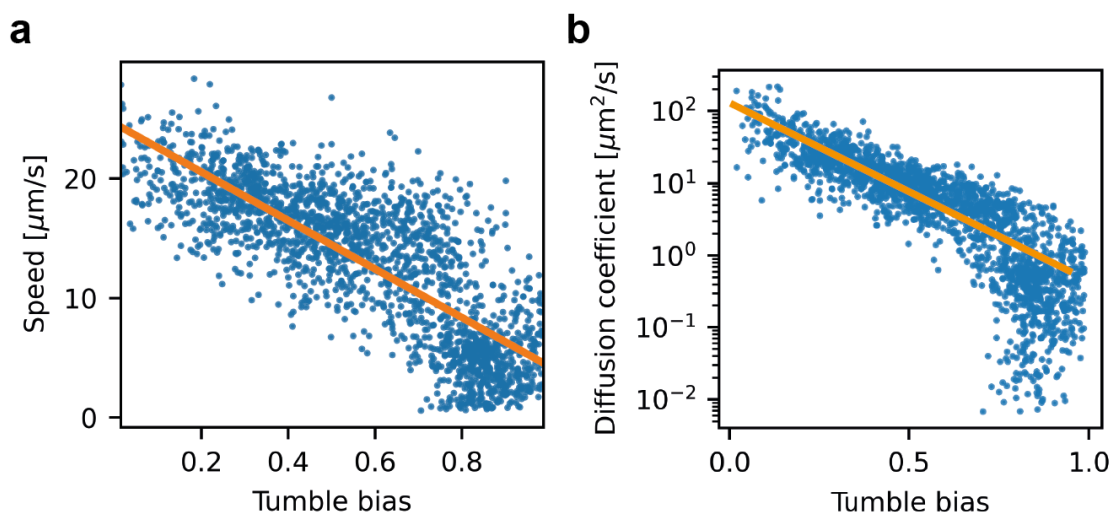


Figure 6.11 – (a) Mean swimming speed v_{mean} vs tumble bias, each dot represents the data of one trajectory. (b) Effective diffusion coefficient D_{eff} vs TB. v_0 and D_{eff} are inversely proportional to tumble bias.

A closer look to the graphs, however, revealed that v_{mean} with ciprofloxacin at 0.004 mg/L was enhanced with respect to normal conditions (Figure 6.12b, green and blue curves, respectively).

Even more surprisingly, in gentamicin an overall increase of the v_{mean} peak was observed for all sub-MIC values tested (Figure 6.12c, curves for 0.28, 0.55 and 1.1 mg/L with respect to the blue curve). For concentration values approaching MIC (see Figure 6.7), v_{mean} is strongly reduced in the case of ampicillin (Figure 6.12a, 2.5 mg/L, green curve) and ciprofloxacin (Figure 6.12b, 0.015 mg/L, purple curve). As outlined before, close to MIC, in addition to relatively strong growth inhibition (Figure 6.7a and 6.7b), filamentation occurred for ampicillin and ciprofloxacin (Figure 6.6a and 6.6b, respectively). For gentamicin tested at 1.1 mg/L such an effect was not observed (Figure 6.12c, red curve), *i.e.* that no significant elongation was observed for gentamicin (Figure 6.6c). However, *E. coli* growth was strongly delayed but not completely inhibited at 1.1 mg/L gentamicin (Figure 6.7c, red curve), which apparently did not have an impact on the speed distribution. The evaluation of motility for the three antibiotics tested based on changed pixel analysis is shown in Figure 6.12d-f.

The impact of antimicrobial exposure on the effective diffusion properties of *E. coli* was first addressed by analyzing MSD (as explained for Figure 6.10c for culture in pure MH). In the case of ampicillin, MSD (as well as the swimming speed, Figure 6.12a) dropped strongly for both concentrations tested (1.2 mg/L and 2.5 mg/L, Figure 6.12g, orange and green curves, respectively). Interestingly, in the presence of ciprofloxacin (Figure 6.12h) and gentamicin (Figure 6.12i), the effective diffusion length may be enhanced in some cases with respect to normal culture conditions. Even if for most concentrations MSD remained close to the normal $MSD(\Delta t)$ curve (blue curves in Figure 6.12h and 6.12i), for 0.004 mg/L ciprofloxacin (Figure 6.12h, green curve) and for 1.1 mg/L gentamicin (Figure 6.12i, red curve) effective diffusion is enhanced. In ciprofloxacin, as for ampicillin, MSD is strongly reduced for concentrations approaching MIC (0.015 mg/L, Figure 6.12h,

purple curve).

Overall these antimicrobial motility assays revealed a similar impact on v_{mean} and MSD . As an example, we discuss the D_{eff} and the TB distributions for ciprofloxacin for different parameters (Figure 6.13a-c). *E. coli* in ciprofloxacin at 0.004 mg/L (Figure 6.13a, green graph) shows a higher D_{eff} than at other concentrations, including normal culture conditions (Figure 6.13a, blue graph). In order to further analyze this observation, the corresponding TB distributions are shown in Figure 6.13b. The TB distribution indicates a balance between low-TB and high-TB cells for 0.004 mg/L ciprofloxacin (Figure 6.13a, green curve), whereas for other concentrations the high-TB sub-population was dominating. Eventually, according to the previous findings, this particular fact may generate higher effective diffusion and mean speeds. Figure 6.13c shows the time evolution of the TB distribution for 0.004 mg/L ciprofloxacin. Comparable to Figure 6.10g for normal conditions, bacterial self-sorting in the traveling band reveals high-TB cell ratios before and after the peak speed in the FOV, and a more balanced distribution at the time when the peak appeared (Figure 6.13c, $t = 6$ h, orange curve). Figure 6.13d and Figure 6.13g show D_{eff} reduction for 1.2 mg/L ampicillin and D_{eff} enhancement for 0.28 mg/L and 1.1 mg/L gentamicin, respectively. The corresponding TB distributions indicate a clear impact in the case of ampicillin (Figure 6.13e) and a much less pronounced effect in the case of gentamicin (Figure 6.13h). Figure 6.13f and Figure 6.13i show the time evolution of the TB distribution for 1.2 mg/L ampicillin and 1.1 mg/L gentamicin, respectively.

6.4 Discussion

Improvement of 3D particle tracking based on specific functionalities of modern microscopes[224–226] or advanced algorithms[227] has extended the possibility to study bacterial or small-molecule dynamics in more complex environments. Nevertheless, these methods are still limited to a low number of moving objects. On the other hand, sub-micron on-chip structures or constrictions enable detailed bacteria imaging with single-cell resolution.[228] However, the observation of swimming behavior and important mechanisms, such as quorum sensing for instance, are impeded in this case. By confining bacteria populations in the quasi-2D space of a 4 μm high microchannel, we were able to perform high-precision tracking for motility analysis and to visualize morphological details based on conventional microscopy, even for relatively high bacterial concentrations. In particular, we observed correlated migration properties that depend on the degree of phenotypic diversity occurring under different on-chip culture conditions.

In the studies presented in this chapter, we have chosen a composite microchip design that features an OA channel as core element. The chip provides an overall rigid and accurately defined microfluidic structure that is easier to fabricate than a full glass or polymer chip that might require more complicate etching or embossing techniques.[229] Fluidic access holes and threads for connectors could be readily machined in the PMMA top plate, whereas the bottom coverslip of the chip enables high-resolution imaging of bacteria on an optical microscope. Using OA as functional intermediate layer, into which microchannels can be directly imprinted, provides a good alternative to other assembling methods (*e.g.* glass-to-glass bonding), as it serves simultaneously as adhesion layer for leakage-free sealing of the chip. OA-based chips also have several advantages

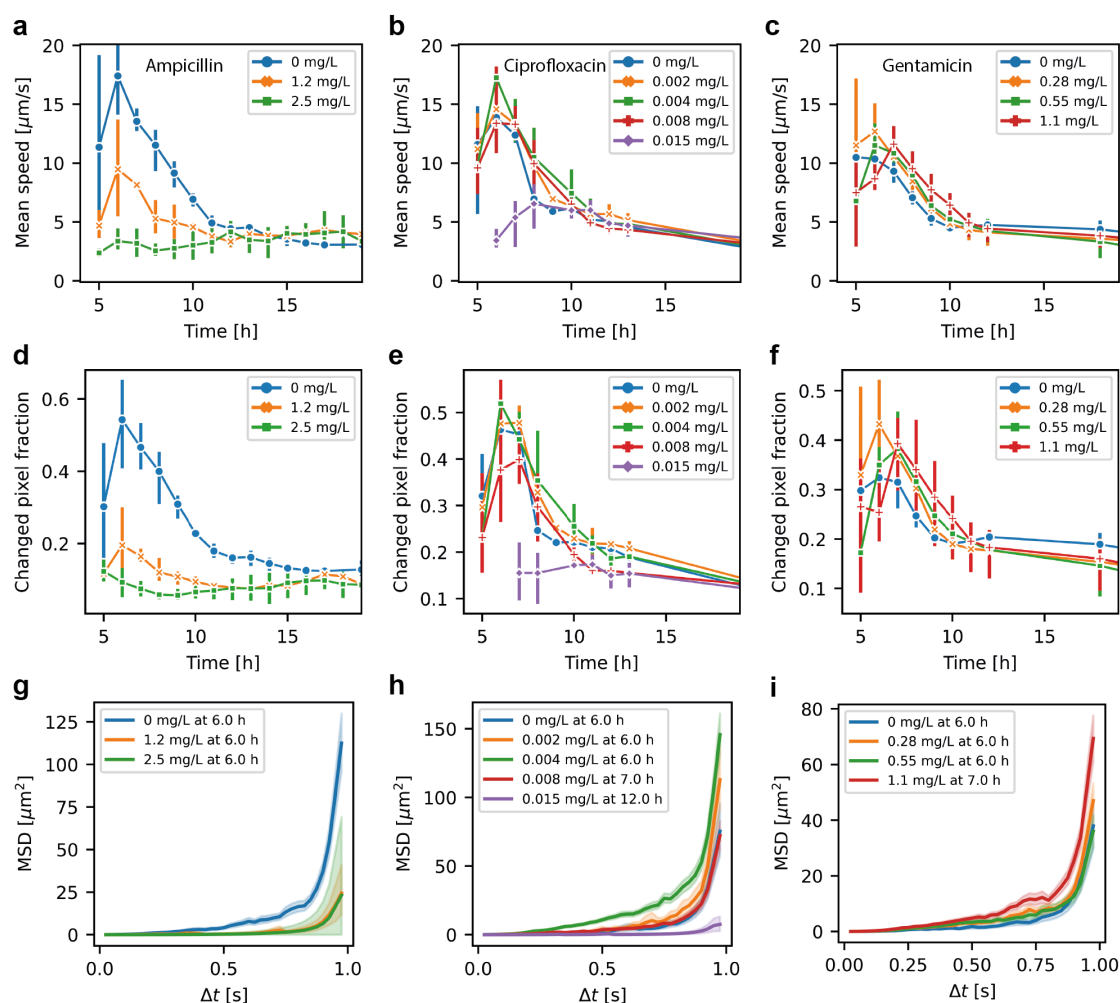


Figure 6.12 – Motility and TB analysis for bacterial growth with different antimicrobials. (a-c) Mean swimming speed v_{mean} as a function of time for bacteria incubated with ampicillin (a), ciprofloxacin (b), and gentamicin (c). Whereas sub-MIC antimicrobials do inhibit the bacterial growth and generate strongly elongated lag phases (Figure 6.7), the swimming ability of bacteria, was significantly only impeded for ampicillin, but not for ciprofloxacin and gentamicin. For 0.004 mg/L ciprofloxacin, a clear increase of the mean speed peak value compared to normal growth conditions was observed. (d-f) Corresponding changed pixel analysis for bacteria in the different antimicrobials. (g-i) MSD as a function of Δt for the time points at the highest v_{mean} in the FOV, for ampicillin (g), ciprofloxacin (h), and gentamicin (i), respectively. In the case of ampicillin, MSD dropped strongly for both concentrations tested. For 0.004 mg/L ciprofloxacin (Figure 6.12b, green curve) and for 1.1 mg/L gentamicin (Figure 6.12c, red curve) effective diffusion is enhanced. In ciprofloxacin, as for ampicillin, MSD is strongly reduced for concentrations approaching MIC. The error bars (or bands) stand for $\pm 2 \times SE$.

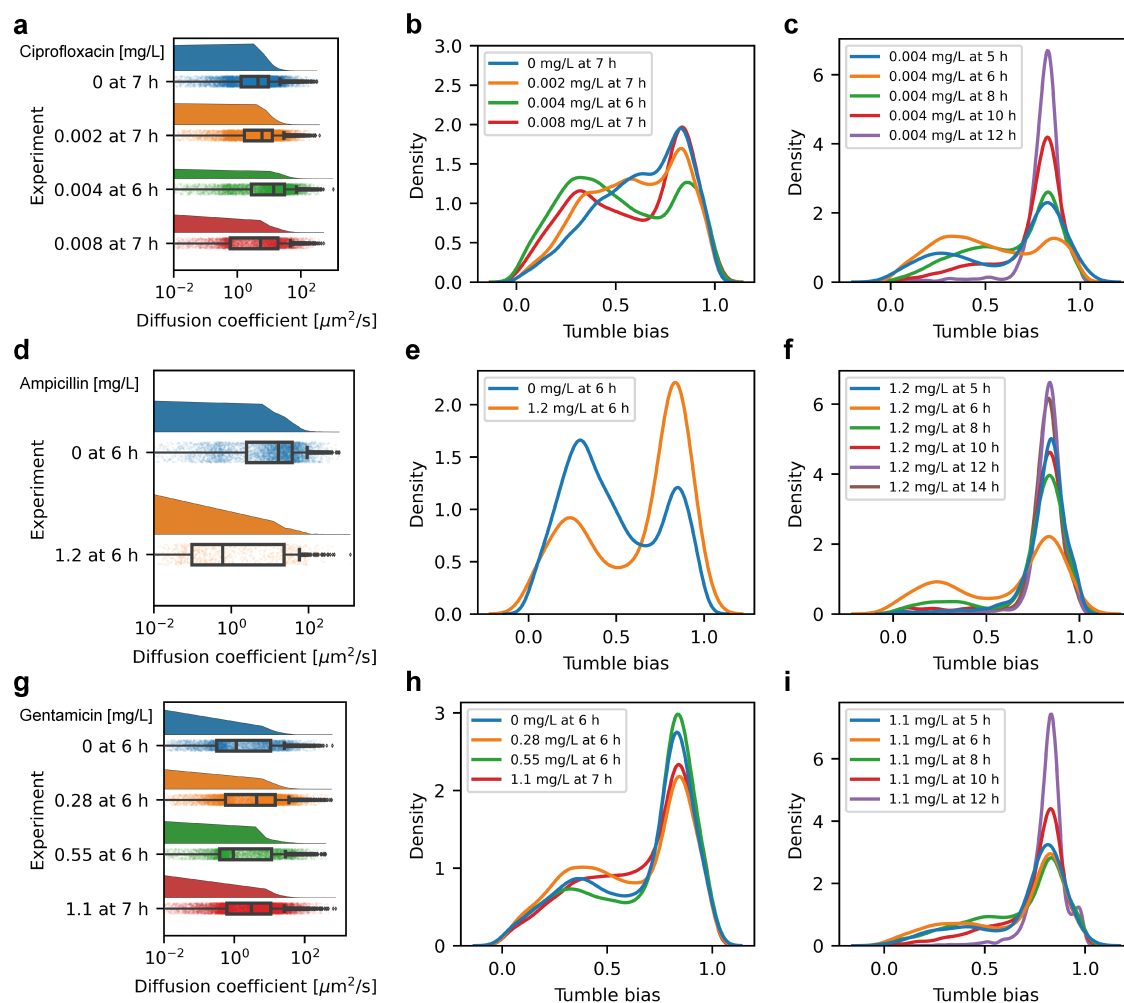


Figure 6.13 – Effective diffusion coefficient D_{eff} and TB distributions for incubation with antibiotics. (a) D_{eff} for different ciprofloxacin concentrations. The highest D_{eff} median value was found for bacteria incubated with 0.004 mg/L ciprofloxacin. (b) Bacterial TB distribution for ciprofloxacin. Two TB sub-populations (low-TB and high-TB) could be identified on all graphs. The distribution does not strongly depend on the concentration, except for 0.004 mg/L where the high-TB peak is reduced, yielding a more balanced distribution. (c) TB distribution as a function of time for bacteria in 0.004 mg/L ciprofloxacin. The rising high-TB cell fraction contributes to a decreasing v_{mean} as shown by the green curve in Figure 6.12b. (d) Effective diffusion coefficient D_{eff} and (e) TB distribution of time points with peak mean speed for bacteria in 0 mg/L and 1.2 mg/L ampicillin. (f) TB distribution as a function of migration time for bacteria in 1.2 mg/L ampicillin. (g) D_{eff} and (h) TB distribution of the time points of peak mean speed for bacteria in 0, 0.28, 0.55 and 1.1 mg/L gentamicin. (i) TB distribution as a function of migration time for bacteria in 1.1 mg/L gentamicin.

over common PDMS (polydimethylsiloxane) microfluidic chips.[230, 231] The elastic properties of PDMS, which are widely exploited in the design of on-chip valves and pumps,[13] may be a challenge for the present application, in particular for controlling residual flow in the microchannel. In our experiments using the rigid OA-based structure, we observed that residual flow instantaneously stopped once capillary filling was finished. An advantage of PDMS is that micro- and nanostructures can be accurately replicated from molds created by optical lithography in SU-8 or on Si wafers. We used this feature to define precisely the μm -size height of the OA channel by imprinting with a PDMS stamp. An additional advantage of OA-based chips is the low level of autofluorescence (about 4 times lower than PDMS), a feature that is important for assays involving fluorescently labeled organisms and molecules.[220] PDMS is gas permeable, which is a useful property in certain biological assays. However, oxygen permeability may bring about problems for certain on-chip chemical synthesis applications, which would make OA chips a more suitable choice.[232]

Our antimicrobial assays were based on compounds with different functional mechanisms, namely ampicillin, ciprofloxacin and gentamicin, respectively.[168] Ampicillin is a typical β -lactam antimicrobial, inhibiting the cell wall synthesis. Ciprofloxacin targets the topoisomerase II (DNA gyrase), thus inhibits the duplication of DNA. Gentamicin impedes the protein synthesis through binding to the A site of 16S ribosomal RNA. In a first stage, we performed a morphology study on *E. coli*. Bacteria usually do not undergo morphological changes unless strictly confined in a specific geometrical shape[233] or under impact of drug treatment. In particular, *E. coli* tends to elongate upon β -lactam antimicrobial exposure and culture, an effect known as filamentation, followed by cell lysis.[234] Genotoxic antibiotics, such as ciprofloxacin, inducing the SOS response which refers to a DNA repair network, also change the *E. coli* rod shape into multi chromosome-containing filaments.[235] In our study, we observed different degrees and forms of filamentation in *E. coli* reflecting different effects of antimicrobial stress in the cytoplasm or on the cell wall (Figure 6.6).

Subsequently, we analyzed bacterial traveling bands and individual swimming trajectories. A bacterial traveling band may be described using the classical Keller-Segel (K-S) equations[208] and an extended model based on the following equations.[236]

$$\frac{\partial b}{\partial t} = \nabla \cdot (\mu(s) \nabla b) - \nabla \cdot (\chi(s) b \nabla s) + g(b, s) - h(b, s) \quad (6.2)$$

$$\frac{\partial s}{\partial t} = D_{chem} \nabla^2 s - f(b, s) \quad (6.3)$$

where, $b(x, t)$ is the bacterial cell density at a position x and time t , $s(x, t)$ is the chemical attractant concentration, $\mu(s)$ is the bacterial diffusion coefficient due to Brownian motion, $\chi(s)$ is the chemotactic coefficient related to active swimming, $g(b, s)$ and $h(b, s)$ are functions describing cell growth and death, respectively, $f(b, s)$ is a function describing attractant degradation, and D_{chem} is the diffusion coefficient of the chemoattractant. Bacterial swimming is thus described by two components, *i.e.* passive and chemotactic diffusion, respectively. However, the swimming heterogeneities existing in a bacterial population are not reflected directly by these two equations. Fu *et al.* established a relation between the $\chi(s)$ and tumble bias, saying that $\chi(s)$ increases as the

TB decreases.[214, 215, 237] In this way, the phenotypic diversity of swimming motility is represented by TB and can be implemented in the K-S model.

Developing and maintaining phenotypic diversity can be a bet-hedging strategy in a bacterial population to ensure survival in challenging environments.[238] For instance, cells may grow at different rates or react to antimicrobial exposure in different manners, conducting to the formation of cells persisting under antimicrobial stress.[6] Non-genetic heterogeneity may also impact coordinated collective behavior of bacteria populations, with a higher degree of diversity usually implying less coordination. In our work, we observed a clear impact of inoculum size on bacterial collective migration appearing as traveling bands. Smaller inoculum size generated an enhanced coordination of migration properties resulting in traveling bands with high cell density (e.g. Figure 6.8a blue curve, inoculum size 3×10^3 CFU/mL). Expression of phenotypic diversity was found in the variation of the relative densities of high TB and low TB for different inoculum sizes (Figure 6.10f), which are correlated to the corresponding speed distributions (Figure 6.10d). For instance, straight swimming segments (runs) dominate when TB is low, resulting in an enhanced density of bacteria with higher swimming speeds (e.g. blue curves in Figure 6.10d and 6.10f, inoculum size 3×10^3 CFU/mL). Likewise, higher median or mean bacterial swimming speed is observed for low-TB populations (Figure 6.10d and Figure 6.11a, respectively). Referring to Eqn. 6.2, low TB corresponds to a high chemotactic coefficient $\chi(s)$ and thus increases effective diffusion expressed by D_{eff} in this work (Figure 6.10e and Figure 6.11b). Looking at the spatial distribution in a traveling band (deduced from observing at successive time points in the FOV), we noticed that the high-TB cells appear at higher concentration at a later stage, thus they migrate preferentially in the tail of the band due to the bacterial self-organization (Figure 6.13c,f,i).

Phenotypic diversity, reflected by the TB distributions in the present case, originates from variations of cellular gene expression and protein content.[239] The protein content inherited by daughter cells strongly depends on the protein content of the mother cells. For instance, it has been demonstrated that exponential-phase *Bacillus subtilis* cultures have a mixture of motile and non-motile cell types, depending on whether the transcription factor for motility is taking effect or not.[240] This heterogeneity manifested by the bifurcation into distinct sub-populations is usually referred to bistability. Bistability was also demonstrated in *E. coli* persister cells.[6] Bacterial population exhibit unimodal variation in the gene expression, due to environmental noise like random fluctuations in the rates of synthesis and degradation of the cognate gene product, which is at the origin of the bistability. In our study, we demonstrated the existence of low-TB and high-TB sub-populations, which can also be considered as a bistability phenomena. It seems that bacteria are able to sense the initial inoculum sizes as one of the noise sources in gene expressions and adopted a strategy to promote the low-TB cell population in the case of small inoculum size for instance (Figure 6.10f). Eventually, different inoculum sizes induced different swimming phenotypes. The underlying mechanisms on the molecular regulation level need further investigations.

Pathogen virulence is often linked to the bacterial motility.[197] Flagellar motility was shown to be important in the process of effective infection.[241, 242] Our *in vitro* study provides new insights on the motility change upon the treatment with antibiotics. The traveling bands demonstrated different

features in normal growth conditions and for growth with antimicrobials, which depend on the type of compound as well. Strong inhibition or bactericidal effect dominates when bacteria are subjected to the antimicrobials close to MIC, *i.e.* 2.5mg/L for ampicillin, 0.015 mg/L for ciprofloxacin and 2.2 mg/L for gentamicin, respectively (Figure 6.7). No dense transient bacterial migration peaks could be observed for these concentrations (Figure 6.8d-f). In the case of 1.2 mg/L ampicillin, although the lag phase was nearly the same with and without antimicrobials (Figure 6.8), the traveling band peak appeared at $t \leq 4$ h (Figure 6.8d, orange curve) before the $t \sim 7$ h of the normal case (Figure 6.8d, blue curve). For ciprofloxacin and gentamicin, the peak of the travelling band and the v_{mean} appeared nearly at the same time for all concentrations below MIC (Figure 6.12b and 6.12c), despite the confirmed growth inhibition effect of these compounds (Figure 6.7e and 6.7f). This observation indicates that there is no clear correlation between growth related properties and motility features.

In principle, the presence of a chemical repellent can induce the phosphorylation of CheY thus the clockwise activity of the flagellar motor, *i.e.* tumble, which will drive bacteria swimming away from the chemical repellent. [243, 244] However, not all chemicals that might be harmful to the bacteria can be considered as a repellent, which is the case for penicillin and streptomycin, for instance.[245] There is no clear evidence that ciprofloxacin and gentamicin act as chemorepellent for *E. coli* neither. For the ampicillin case, filamentation is the dominant effect, which strongly influences the traveling band formation. However, for ciprofloxacin and gentamicin, we hypothesize that their concentrations have limited effects on $\chi(x)$ itself, which is confirmed by the similar TB distribution curves (Figure 6.13b and 6.13h). Unlike the study on different inoculum size without drug treatment, the traveling band peak delay is not influenced by the lag phase difference. In a previous study, we proposed that, in the latter cases, the main effect that the antimicrobials bring about is promoting bacterial metabolic activity and inducing enhanced energy spilling.[98] Higher energy consumption rates during bacterial growth also increases nutrient consumption dissolved in the culture medium. Consequently, the self-generated chemical gradient, represented by $f(b, s)$ in Eqn. 6.2, may develop stronger and be formed on a shorter time scale. Here, the effect of $g(b, s)$ and $h(b, s)$ describing the growth and death become less important. Our study suggests that the motility and collective behavior correlated to bacterial virulence might potentially be promoted by the presence of sub-MIC antimicrobials. This finding further confirms the importance of correct antimicrobial prescription with appropriate doses in a therapeutic process. A more holistic quantitative study, combining bacterial chemotaxis and metabolic effects under antimicrobial stress, could reveal more interesting details in this respect.

Interestingly, the presence of traveling bands provides another method to perform fast AST for motile bacteria. The mean speed peak or cell density peak usually appears after 4 to 7 hours (Figure 6.6 and 6.12). Even if this read-out time is longer than the method based on the single bacterial growth imaging, for instance,[40] MIC values can be safely determined on a much shorter time scale than with the gold standard broth micro dilution method (typically 16 hours to read-out).[28] In the present proof-of-concept study, we performed AST starting from purified microbial colonies. AST starting from positive on-chip blood cultures might be feasible by implementing microfluidic toolboxes for sample preparation and purification.[246] Moreover, high-content information assays based on different motility parameters may eventually open the path to optimized and personalized

antimicrobial prescriptions.

6.5 Conclusion

Our microfluidic OA-based chip design provided specific advantages over other materials, enabling the fabrication of accurately defined Hele-Shaw type microfluidic channels for high-content imaging of individual bacterial trajectories in cell monolayers. By quantifying traveling band parameters in a quasi-2D plane, we revealed that isogeneic *E. coli* incubated from different inoculum sizes eventually developed different swimming phenotypes. Smaller inoculum sizes generated a higher degree of coordinated community behavior with high cell density and swimming speed. We propose that inoculum size may play the role of a noise source that influences the gene expression, resulting in different manifestations of bistability. In our study, we focused on the TB distribution as a direct phenotypic indicator and demonstrated the existence of sub-groups with low-TB and high-TB values in the migrating bacterial populations. The relative density of low-TB and high-TB sub-populations in the traveling band may explain the observed variations in cell density and swimming speed distributions. In particular, low-TB bacteria usually possess higher mean speeds and thus higher chemotactic ability associated with a higher effective diffusion coefficient. The impact of antimicrobial stress on the *E. coli* traveling bands depended strongly on the type of antibiotics and the concentration, especially in the case of ampicillin. For ciprofloxacin and gentamicin, traveling bands were less affected, or even revealed an enhancement of the chemotactic properties in specific cases. In the latter cases, traveling band peak delays were nearly independent of the antibiotic concentration, in contrast to corresponding lag phase extensions of the growth curves. We suggest that these compounds enhance the bacterial metabolic activity and as a consequence the formation of the self-generated nutrient gradient, which is at the origin of a bacterial traveling band. This observation implies a possible compensation of opposing effects due to bacterial growth inhibition, nutrient depletion (metabolic activity) and chemotactic swimming, which is also reflected in the Keller-Segel model. Replacing the rich MH culture media by better controlled chemical environments, combined with theoretical simulations, could further unravel this question.

References

6. Balaban, N. Q., Merrin, J., Chait, R., Kowalik, L. & Leibler, S. Bacterial Persistence as a Phenotypic Switch. *Science* **305**, 1622–1625 (Sept. 10, 2004) (cit. on pp. 5, 126).
13. Unger, M. A., Chou, H.-P., Thorsen, T., Scherer, A. & Quake, S. R. Monolithic Microfabricated Valves and Pumps by Multilayer Soft Lithography. *Science* **288**, 113–116 (Apr. 7, 2000) (cit. on pp. 7, 125).
19. Rusconi, R., Garren, M. & Stocker, R. Microfluidics Expanding the Frontiers of Microbial Ecology. *Annual Review of Biophysics* **43**, 65–91 (May 6, 2014) (cit. on pp. 7, 102).
22. Wu, F. & Dekker, C. Nanofabricated Structures and Microfluidic Devices for Bacteria: From Techniques to Biology. *Chem. Soc. Rev.* **45**, 268–280 (2016) (cit. on pp. 7, 102).
23. Gurung, J. P., Gel, M. & Baker, M. A. B. Microfluidic Techniques for Separation of Bacterial Cells via Taxis. *Microbial Cell* **7**, 66–79 (Mar. 2, 2020) (cit. on pp. 7, 102).
28. Jorgensen, J. H. & Ferraro, M. J. Antimicrobial Susceptibility Testing: A Review of General Principles and Contemporary Practices. *Clinical Infectious Diseases* **49**, 1749–1755 (Dec. 2009) (cit. on pp. 8–10, 104, 127).
40. Baltekin, Ö., Boucharin, A., Tano, E., Andersson, D. I. & Elf, J. Antibiotic Susceptibility Testing in Less than 30 Min Using Direct Single-Cell Imaging. *Proceedings of the National Academy of Sciences*, 201708558 (Aug. 8, 2017) (cit. on pp. 10, 11, 13, 54, 102, 127, 137).
61. Wadhams, G. H. & Armitage, J. P. Making Sense of It All: Bacterial Chemotaxis. *Nature Reviews Molecular Cell Biology* **5**, 1024–1037 (Dec. 2004) (cit. on pp. 15, 101, 102).
63. Berg, H. C. *Random Walks in Biology* (Princeton University Press, Princeton, New Jersey, 1993) (cit. on pp. 16, 101).
98. Liu, Y., Lehnert, T. & Gijs, M. A. M. Fast Antimicrobial Susceptibility Testing on *Escherichia coli* by Metabolic Heat Nanocalorimetry. *Lab on a Chip* **20**, 3144–3157 (Aug. 26, 2020) (cit. on pp. 43, 53, 74, 83, 127).
137. Van Belkum, A. *et al.* Developmental Roadmap for Antimicrobial Susceptibility Testing Systems. *Nature Reviews Microbiology* **17**, 51–62 (Jan. 2019) (cit. on pp. 54, 71, 102).
153. Stevenson, K., McVey, A. F., Clark, I. B. N., Swain, P. S. & Pilizota, T. General Calibration of Microbial Growth in Microplate Readers. *Scientific Reports* **6**, 38828 (Dec. 2016) (cit. on pp. 59, 63, 104).
155. EUCAST. "The European Committee on Antimicrobial Susceptibility Testing. Routine and Extended Internal Quality Control for MIC Determination and Disk Diffusion as Recommended by EUCAST. Version 9.0, 2019. <http://www.eucast.org>." (2019) (cit. on pp. 67, 104).
168. Kohanski, M. A., Dwyer, D. J. & Collins, J. J. How Antibiotics Kill Bacteria: From Targets to Networks. *Nature Reviews Microbiology* **8**, 423–435 (June 2010) (cit. on pp. 73, 125).
196. Berg, H. C. *E. Coli in Motion* 133 pp. (Springer, New York, 2004) (cit. on p. 101).

197. Josenhans, C. & Suerbaum, S. The Role of Motility as a Virulence Factor in Bacteria. *International Journal of Medical Microbiology* **291**, 605–614 (Jan. 2002) (cit. on pp. 101, 126, 139).
198. Pittman, M. S., Goodwin, M. & Kelly, D. J. Chemotaxis in the Human Gastric Pathogen *Helicobacter Pylori*: Different Roles for CheW and the Three CheV Paralogues, and Evidence for CheV2 Phosphorylation. *Microbiology* **147**, 2493–2504 (Sept. 1, 2001) (cit. on p. 102).
199. O'Toole, R. *et al.* The Chemotactic Response of *Vibrio Anguillarum* to Fish Intestinal Mucus Is Mediated by a Combination of Multiple Mucus Components. *Journal of Bacteriology* **181**, 4308–4317 (July 1999) (cit. on p. 102).
200. Levy, S. B. & Marshall, B. Antibacterial Resistance Worldwide: Causes, Challenges and Responses. *Nature Medicine* **10**, S122–S129 (Dec. 2004) (cit. on p. 102).
201. Scheler, O., Postek, W. & Garstecki, P. Recent Developments of Microfluidics as a Tool for Biotechnology and Microbiology. *Current Opinion in Biotechnology. Analytical Biotechnology* **55**, 60–67 (Feb. 1, 2019) (cit. on p. 102).
202. Kim, S., Masum, F. & Jeon, J. S. Recent Developments of Chip-Based Phenotypic Antibiotic Susceptibility Testing. *BioChip Journal* **13**, 43–52 (Mar. 2019) (cit. on p. 102).
203. Wang, P. *et al.* Robust Growth of *Escherichia Coli*. *Current Biology* **20**, 1099–1103 (June 2010) (cit. on p. 102).
204. Ahmed, T., Shimizu, T. S. & Stocker, R. Microfluidics for Bacterial Chemotaxis. *Integrative Biology* **2**, 604 (2010) (cit. on p. 102).
205. Lambert, B. S. *et al.* A Microfluidics-Based in Situ Chemotaxis Assay to Study the Behaviour of Aquatic Microbial Communities. *Nature Microbiology* **2**, 1344–1349 (Oct. 2017) (cit. on p. 102).
206. Clerc, E. E., Raina, J.-B., Lambert, B. S., Seymour, J. & Stocker, R. In Situ Chemotaxis Assay to Examine Microbial Behavior in Aquatic Ecosystems. *Journal of Visualized Experiments*, 61062 (May 5, 2020) (cit. on p. 102).
207. Adler, J. Chemotaxis in Bacteria. *Science* **153**, 708–716 (Aug. 12, 1966) (cit. on p. 102).
208. Keller, E. F. & Segel, L. A. Traveling Bands of Chemotactic Bacteria: A Theoretical Analysis. *Journal of Theoretical Biology* **30**, 235–248 (Feb. 1971) (cit. on pp. 102, 125).
209. Spudich, J. L. & Koshland, D. E. Non-Genetic Individuality: Chance in the Single Cell. *Nature* **262**, 467–471 (5568 Aug. 1976) (cit. on p. 103).
210. Levin, M. D., Morton-Firth, C. J., Abouhamad, W. N., Bourret, R. B. & Bray, D. Origins of Individual Swimming Behavior in Bacteria. *Biophysical Journal* **74**, 175–181 (Jan. 1, 1998) (cit. on p. 103).
211. Avery, S. V. Microbial Cell Individuality and the Underlying Sources of Heterogeneity. *Nature Reviews Microbiology* **4**, 577–587 (Aug. 2006) (cit. on p. 103).

212. Salek, M. M., Carrara, F., Fernandez, V., Guasto, J. S. & Stocker, R. Bacterial Chemotaxis in a Microfluidic T-Maze Reveals Strong Phenotypic Heterogeneity in Chemotactic Sensitivity. *Nature Communications* **10**, 1877 (Dec. 2019) (cit. on p. 103).
213. Dufour, Y. S., Gillet, S., Frankel, N. W., Weibel, D. B. & Emonet, T. Direct Correlation between Motile Behavior and Protein Abundance in Single Cells. *PLOS Computational Biology* **12** (ed Stock, A. M.) e1005041 (Sept. 6, 2016) (cit. on pp. 103, 118).
214. Fu, X. *et al.* Spatial Self-Organization Resolves Conflicts between Individuality and Collective Migration. *Nature Communications* **9**, 2177 (Dec. 2018) (cit. on pp. 103, 125, 126).
215. Waite, A. J. *et al.* Non-genetic Diversity Modulates Population Performance. *Molecular Systems Biology* **12**, 895 (Dec. 2016) (cit. on pp. 103, 120, 126).
216. Parker, D. J., Demetci, P. & Li, G.-W. Rapid Accumulation of Motility-Activating Mutations in Resting Liquid Culture of *Escherichia Coli*. *Journal of Bacteriology* **201** (ed Brun, Y. V.) e00259–19, /jb/201/19/JB.00259–19.atom (July 8, 2019) (cit. on p. 104).
217. Sim, J. H., Moon, H. J., Roh, Y. H., Jung, H. W. & Bong, K. W. Fabrication of NOA Microfluidic Devices Based on Sequential Replica Molding. *Korean Journal of Chemical Engineering* **34**, 1495–1499 (May 2017) (cit. on p. 105).
218. Wägli, P., Homsy, A. & de Rooij, N. F. Norland Optical Adhesive (NOA81) Microchannels with Adjustable Wetting Behavior and High Chemical Resistance against a Range of Mid-Infrared-Transparent Organic Solvents. *Sensors and Actuators B: Chemical* **156**, 994–1001 (Aug. 1, 2011) (cit. on p. 105).
219. Gu, H., Duits, M. H. & Mugele, F. A Hybrid Microfluidic Chip with Electrowetting Functionality Using Ultraviolet (UV)-Curable Polymer. *Lab on a Chip* **10**, 1550–1556 (2010) (cit. on p. 105).
220. Bartolo, D., Degré, G., Nghe, P. & Studer, V. Microfluidic Stickers. *Lab Chip* **8**, 274–279 (2008) (cit. on pp. 105, 125).
221. NOA68 <https://www.norlandprod.com/adhesives/NOA%2068.html> (2020) (cit. on p. 105).
222. Blair, D. & Dufresne, E. *Matlab Particle Tracking* Matlab particle tracking. <http://site.physics.georgetown.edu/matlab/> (cit. on pp. 109, 117).
223. Douarche, C., Buguin, A., Salman, H. & Libchaber, A. *E. Coli* and Oxygen: A Motility Transition. *Physical Review Letters* **102**. doi:10.1103/PhysRevLett.102.198101 (May 12, 2009) (cit. on p. 120).
224. Berg, H. C. How to Track Bacteria. *Review of Scientific Instruments* **42**, 868–871 (June 1, 1971) (cit. on p. 122).
225. Berg, H. C. & Brown, D. A. Chemotaxis in *Escherichia Coli* Analysed by Three-Dimensional Tracking. *Nature* **239**, 500–504 (Oct. 1972) (cit. on p. 122).

226. Coskun, U. C. *et al.* Nano-Resolution in Vivo 3D Orbital Tracking System to Study Cellular Dynamics and Bio-Molecular Processes in Single Molecule Spectroscopy and Superresolution Imaging XIII Single Molecule Spectroscopy and Superresolution Imaging XIII (eds Gregor, I., Erdmann, R. & Koberling, F.) (SPIE, San Francisco, United States, Feb. 13, 2020), 45. doi:[10.1117/12.2546690](https://doi.org/10.1117/12.2546690) (cit. on p. 122).
227. Taute, K., Gude, S., Tans, S. & Shimizu, T. High-Throughput 3D Tracking of Bacteria on a Standard Phase Contrast Microscope. *Nature Communications* **6**, 8776 (Nov. 2, 2015) (cit. on p. 122).
228. Mannik, J., Driessen, R., Galajda, P., Keymer, J. E. & Dekker, C. Bacterial Growth and Motility in Sub-Micron Constrictions. *Proceedings of the National Academy of Sciences* **106**, 14861–14866 (Sept. 1, 2009) (cit. on p. 122).
229. Becker, H. & Gärtner, C. Polymer Microfabrication Technologies for Microfluidic Systems. *Analytical and Bioanalytical Chemistry* **390**, 89–111 (Jan. 2008) (cit. on p. 122).
230. Halldorsson, S., Lucumi, E., Gómez-Sjöberg, R. & Fleming, R. M. T. Advantages and Challenges of Microfluidic Cell Culture in Polydimethylsiloxane Devices. *Biosensors and Bioelectronics* **63**, 218–231 (Jan. 15, 2015) (cit. on p. 125).
231. Sollier, E., Murray, C., Maoddi, P. & Carlo, D. D. Rapid Prototyping Polymers for Microfluidic Devices and High Pressure Injections. *Lab on a Chip* **11**, 3752–3765 (2011) (cit. on p. 125).
232. Bong, K. W. *et al.* Non-Polydimethylsiloxane Devices for Oxygen-Free Flow Lithography. *Nature Communications* **3**, 805 (Jan. 2012) (cit. on p. 125).
233. Takeuchi, S., DiLuzio, W. R., Weibel, D. B. & Whitesides, G. M. Controlling the Shape of Filamentous Cells of Escherichia Coli. *Nano Letters* **5**, 1819–1823 (Sept. 1, 2005) (cit. on p. 125).
234. Spratt, B. G. Distinct Penicillin Binding Proteins Involved in the Division, Elongation, and Shape of Escherichia Coli K12. *Proceedings of the National Academy of Sciences* **72**, 2999–3003 (Aug. 1, 1975) (cit. on p. 125).
235. Bos, J. *et al.* Emergence of Antibiotic Resistance from Multinucleated Bacterial Filaments. *Proceedings of the National Academy of Sciences* **112**, 178–183 (Jan. 6, 2015) (cit. on p. 125).
236. Tindall, M. J., Maini, P. K., Porter, S. L. & Armitage, J. P. Overview of Mathematical Approaches Used to Model Bacterial Chemotaxis II: Bacterial Populations. *Bulletin of Mathematical Biology* **70**, 1570–1607 (Aug. 2008) (cit. on p. 125).
237. Dufour, Y. S., Fu, X., Hernandez-Nunez, L. & Emonet, T. Limits of Feedback Control in Bacterial Chemotaxis. *PLOS Computational Biology* **10**, e1003694 (June 26, 2014) (cit. on p. 126).
238. Ackermann, M. A Functional Perspective on Phenotypic Heterogeneity in Microorganisms. *Nature Reviews Microbiology* **13**, 497–508 (8 Aug. 2015) (cit. on p. 126).
239. Frankel, N. W. *et al.* Adaptability of Non-Genetic Diversity in Bacterial Chemotaxis. *eLife* **3**, e03526 (Oct. 3, 2014) (cit. on p. 126).

-
240. Kearns, D. B. & Losick, R. Cell Population Heterogeneity during Growth of *Bacillus Subtilis*. *Genes & Development* **19**, 3083–3094 (Dec. 15, 2005) (cit. on p. 126).
241. Stecher, B. *et al.* Flagella and Chemotaxis Are Required for Efficient Induction of *Salmonella* Enterica Serovar Typhimurium Colitis in Streptomycin-Pretreated Mice. *Infection and Immunity* **72**, 4138–4150 (July 1, 2004) (cit. on p. 126).
242. Butler, S. M. & Camilli, A. Going against the Grain: Chemotaxis and Infection in *Vibrio Cholerae*. *Nature Reviews Microbiology* **3**, 611–620 (8 Aug. 2005) (cit. on p. 126).
243. Krasnopeevea, E., Barboza-Perez, U. E., Rosko, J., Pilizota, T. & Lo, C.-J. Bacterial Flagellar Motor as a Multimodal Biosensor. *Methods*, S1046202320301328 (July 2020) (cit. on p. 127).
244. Grebe, T. W. & Stock, J. Bacterial Chemotaxis: The Five Sensors of a Bacterium. *Current Biology* **8**, R154–R157 (Feb. 26, 1998) (cit. on p. 127).
245. Tso, W.-W. & Adler, J. Negative Chemotaxis in *Escherichia Coli*. *Journal of Bacteriology* **118**, 560–576 (May 1974) (cit. on p. 127).
246. Pitt, W. G. *et al.* Rapid Separation of Bacteria from Blood—Review and Outlook. *Biotechnology progress* **32**, 823–839 (July 8, 2016) (cit. on p. 127).

7 Conclusion and outlook

Combating antimicrobial resistance is an urgent global task.[2, 247] Serious bacterial infections have been increasingly reported in recent years, possibly with fatal consequences when AMR is involved. The whole society, including clinicians, researchers, companies, policy makers and eventually the public need to coordinate actions to counteract efficiently the fast-spreading AMR. Antibiotics as "magical weapons" are losing their efficiency against an ever increasing number of resistant microbial pathogens, and the stagnation of the discovery of new antimicrobial compounds makes the situation even worse.[248] Regarding the antibiotics currently available, optimum prescription is one of the keys to retard the AMR development. After identifying a patient sample positive to bacterial infection (*e.g.* blood, urine, etc.), fast AST provides valuable information on resistance and MIC of the specific bacterial strain, enabling the correct prescription of antibiotics. In this thesis, we conducted a research study on bacterial metabolism and AST with different microfluidic platforms, in order to explore fundamental concepts and innovative methods for fast AST.

Here, we first provide a short summary and some concluding remarks on the present thesis work. More extensive conclusions have been given in the respective chapters. In the outlook, we then focus on a larger extend on future perspectives in the different fields addressed in this context.

7.1 Conclusion

7.1.1 Project summary

We introduced the heat transfer theory and general classifications of calorimeters. Historically, this is a research field with rich results, of which the fundamental principles and designs are still inspiring the development of modern calorimeters. New thermoelectric material combinations further bring about new opportunities in constructing calorimeters with improved performance. In particular, we emphasized theoretical aspects of thermopile-based heat flux sensors, a technology that is largely exploited in modern nanocalorimeters, as thin-film thermocouples can be readily implemented on a sensor membrane.

The origin of bacterial heat production is the loss of energy in the central metabolic process. Heat production is influenced, for instance, by the nutrient level in the culture medium and by

chemical compounds, in particular by antibiotics. In order to monitor and to analyze microbial metabolic heat production, we developed a highly sensitive isothermal nanocalorimetric platform (INCfAST). The heat flow curves obtained from small bacterial cultures (150 μ L) reflect growth rates and provide a measurement for lag phases. Considering metabolic heat flow as a viability indicator, we performed AST on *E. coli* within several hours. This proof-of-concept study was conducted with three antibiotics (ciprofloxacin, ampicillin, and gentamicin), featuring different action mechanisms. The observed heat profiles can not only be considered as fingerprints for the activity and efficacy of the compounds at different concentrations, but they can also be used to determine correctly the MIC value ranges (*i.e.* corresponding to established standards). We also found that the heat production per biomass is promoted, implying that the energy efficiency is degrading in the presence of antibiotics. This metabolic perturbation can be interpreted of the metabolic process energy spillage in the presence of antibiotics.

Measuring microbial oxygen consumption is an indirect calorimetric method. Oxygen consumption occurs in the process of aerobic metabolic activity. In the frame of this work, we modified the isothermal nanocalorimeter platform in order to implement an on-chip bacterial oxygen consumption measurement system. The assays are based on photoluminescence oxygen measurements in the microincubator under various conditions. Oxygen consumption was promoted in a rich culture medium and delayed for decreasing culture temperatures. A clear dependence of the oxygen consumption with the applied antibiotic concentration was observed. Specifically, we found that bacteria possess a higher heat per oxygen consumption for growth in the presence of low antimicrobial concentrations with respect to higher concentrations, especially for ampicillin and ciprofloxacin. Furthermore, we established a model to describe the oxygen consumption based on bacteria doubling in the exponential growth phase and we concluded that under unfavorable cultural conditions, microbial doubling times prolong significantly. We also confirmed that indirect calorimetry is a promising new approach for fast AST and correlated oxygen consumption with metabolic heat measurements.

We further evaluated bacterial behavior under antimicrobial stress from a single-cell perspective, in particular by analyzing the swimming trajectories of individual bacteria. For that purpose, we fabricated a shallow microfluidic chip, based on a UV-curable optical adhesive microchannel with a well-defined height of only 4 μ m. By this means, bacterial suspensions could be confined in a quasi-2D plane to facilitate high-precision imaging. We were interested in collective bacterial migration patterns due to self-generated chemical gradients, so-called "traveling bands". Interestingly, different inoculum sizes of genetically identical bacterial cultures lead to different swimming behaviors. Small inoculum size results in a smaller phenotypic diversity, revealed by the corresponding tumble bias distribution, and by the higher cell density and swimming velocity in the migration peak of the band. Even if growth inhibition in the presence of antibiotics was confirmed by the optical density measurements, this feature did not inhibit the presence of the collective migration pattern. Furthermore, we took advantage of the same microfluidic system to study the morphology of *E. coli* cultured with antibiotics. Ampicillin, taking effect on the cell wall, demonstrated a pronounced filamentation effect, *i.e.* an elongation of the cell body without division. Although, ciprofloxacin influences the synthesis of intracellular DNA, elongation was also

observed to a minor extent. Gentamicin did not generate filamentation in our study.

Overall in this thesis, considering the challenging situation of AMR spreading, we intended to provide some new insights on antimicrobial activity from metabolic and motility perspectives. We developed new approaches and technologies with proven potential for fast AST. Further investigation of the platforms in clinical laboratories and with clinically relevant bacterial strains allows assessing the applicability in real health-care settings.

7.1.2 Technology readiness

For the development of *in vitro* diagnostic devices four characteristics need to be considered: (i) the robustness, (ii) the reliability, (iii) the cost per test, and (iv) the read-out time. Overall, we were able to prove robust functionalities in performing AST on *E. coli* using the INCfAST platform. The results are shown to be coherent with the conventional gold standard method. Therefore, we assume that our INCfAST prototype has accomplished the technology readiness level (TRL) 3, comprising the implementation of the critical functions and the proof-of-concept study. The current prototype is at TRL 4, *i.e.*, laboratory testing of prototype component and processes. As we have analyzed in Table 3.1 and Table 4.3, INCfAST has the same level of technical performance and read-out time as the other commercial products and calorimetry research devices. Nevertheless, although the INCfAST platform provides some advantages in terms of sample manipulation, several challenges have to be faced to further promote a possible market introduction of the current system. First, throughput needs to be improved by implementing automated modules in the product prototype. By this means, it will also be possible to reduce the cost per test, as will be discussed in the following section. The read-out time of 5-7 h is faster than for the conventional methods, however, the INCfAST platform cannot achieve the best performance of innovative methods based on single bacterial study, declaring values as fast as 30 min.[40] Further improvement of the device sensitivity would be necessary in order to improve the test speed. However, depending on the specific application, the high information content of the nanocalorimetric heat profiles can counterbalance the lack of assay speed.

7.2 Outlook

7.2.1 High-throughput calorimeters with increased sensitivity

The INCfAST nanocalorimetric platform developed in the current thesis is a prototype for proof-of-concept studies. Some aspects still have room for improvement.

(i) The dual-chip system only allows for two parallel measurements, which cannot fit the requirement of current clinical settings. Higher throughput, *i.e.* more samples tested in parallel, not only reduces significantly the turn-around time, but also reduces dramatically the cost per assay, thus the financial burden for the public health-care system. It appears to be beneficial to implement a platform with more measurement units in the future. Meanwhile, the fluidic handling system need to be optimized accordingly. Manual operations by the user should be replaced by

fully automated protocols, where only the collected clinical sample is introduced and quantitative MIC values appear as read-out at the end of the test.

(ii) In our platform the on-chip sample microincubator was not closed at the bottom, *i.e.* the biological sample was in direct contact with the sensor surface. This technique was used to maximize the thermal contact between the sample and the sensor, in order to enhance the sensitivity of the calorimeter. Even if we have proven that our sterilization procedure was efficient, it would be better to avoid this step and to develop disposable sample microincubators.

(iii) The Seebeck coefficient is of great importance for the sensor performance. The thin-film based thermopile sensor used in this work has a Seebeck coefficient of $300 \mu\text{V/K}$, which is still lower than the best p-n type thermopile sensor with a coefficient as high as $1800 \mu\text{V/K}$.^[75] The high-density integration of thermocouples for a thin-film thermopile sensor compensates the drawback of relatively low Seebeck coefficients to a certain extent. In contrast, the pillar structure of the p-n type thermopile sensor may pose difficulties with respect to the integration in dense arrays. Therefore, the investigation on packing high-density p-n junctions is of importance in order to develop high performance heat flux sensors. In addition, some other thermopile architectures may also be considered.^[65]

(iv) Interestingly, it has been shown that heat flow patterns can potentially be used for the identification of bacterial species.^[117] In order to further verify this possibility, a database of heat flow profiles of different species should be established. Building such a database would strongly benefit from high-throughput platforms. In the current study, we only used nutrient-rich culture media. As the microbial gene profiles in nutrient-limited are quite different, heat flow profiles in such culture media may further help to distinguish and establish heat flow fingerprints for different bacterial species. A platform providing both AST results and bacterial identification would clearly address the clinical needs.

7.2.2 Why not performing AST with blood samples?

As shown in the clinical workflow for a blood stream infection (Figure 1.3), a sample purification step is needed ahead of performing AST. One may ask the question why AST is not performed directly on the blood sample. For conventional clinical settings, identification of the infectious strain is a prerequisite for the drug prescription. On the other hand, AST without preliminary species identification provides a mean for antimicrobial prescription without knowing the infecting pathogens. This methodology is quite controversial, as the physician actually still relies on species identification to establish a diagnosis. The best and most efficient protocol to be applied in clinical setting may deserve more investigation. Again, as mentioned above, an AST platform enabling bacterial identification based on metabolic heat profiles would be the ideal solution. Another promising route can be single-bacterial study by isolating pathogens from the blood sample directly. This routine avoids the time-consuming purification step, and possibly also reduces the time needed for the blood culture step.

The heat measurement using the present calorimetric platform depends on the number of bacteria

in the microincubator near the sensing unit, which was typically in the range of 10^6 - 10^7 CFU/mL in the present study. Considering that in the case of blood infections the concentration of bacteria in the blood stream can be as low as 1 - 10 CFU/mL, it will be challenging to identify bacterial presence in the microincubator directly from blood samples. Therefore, a pre-concentration or pre-culture step is still required. An additional method might be to use the off-chip reservoir of the INCfAST platform for blood culture (~ 10 mL). In this case a fluidic protocol may be easily applied in order to transfer the sample periodically from the reservoir into the microincubator and *visa versa*, for successive culture and signal acquisition steps, respectively (Figure 4.4).

7.2.3 The metabolic perspective

In the current work, we only studied bacteria in nutrient-rich media, as by convention used to perform antimicrobial investigation. The microbial gene expression set is well documented for these conditions, and also for the nutrient-limited condition, the gene expression set is charted. However, in the *in vivo* infection model, the target gene expression set is much larger than for *in vitro* assays in rich or poor media. More advanced metabolic investigations of *in vivo* infection with organ-on-a-chip system is therefore another promising direction that might reveal new therapeutic features.[248]

7.2.4 Microbial co-culture

Co-culture is an important topic to study the cell micro-environment and cell-cell communication. Various micro-/nanotechnologies for cell co-culture have been developed.[249, 250] Microbial co-culture, which is somehow different from the concept of cell co-culture, is of great interest in the discovery of antimicrobials and the evaluation of their efficiency. For instance, one type of microbial strain may stimulate the secretion of chemicals of another microbial strain.[251] In the frame of this thesis, the metabolic activity is studied based on the culture of a single bacterial strain. Nevertheless, it is feasible to culture two types of bacteria simultaneously with the developed set-ups. We forecast that the obtained heat or oxygen consumption profiles would monitor an overlap of the metabolic activity of the two microbial strains. We propose the possibility of using machine learning to decompose and assist interpreting metabolic profiles recorded from co-cultures, provided a sufficient amount of data can be acquired in combination with other chemical screening technologies. On a single bacterial level, it is also possible to study co-cultured bacteria directly with optical and/or fluorescence microscopy, in particular in view of more advanced motility studies based on the work presented in this thesis. The motility chip design can easily be adapted to meet the requirements of the co-cultured species.

7.2.5 Bacterial motility

The mechanism of the bacterial flagella motor has been well established, while the role of motility on the pathogenic virulence is still a research field of great interest.[197, 252] Although in this thesis we concluded that different bacterial inoculum sizes may lead to different phenotypic diversity, the

origin of this diversity still needs further investigation. Our proposed assumption that the initial diversity in the inoculum is amplified has to be confirmed by direct assessment of the bacterial features.

7.2.6 Development of new antimicrobials

A continuous discovery of new classes of antibiotics is one of the key solution to counteract AMR. However, the limited profits of antimicrobial discovery with respect to other drug developments may not justify the investment by the private pharmaceutical companies.[253] Microfluidic-assisted technology may improve the efficiency of a drug discovery process, thus possibly decrease the cost of the antimicrobial drug discovery pipeline. More specifically, the following routes may be explored for the discovery of new antibiotics.

(i) The first approach can be realized by chemical synthesis. Modification of the chemical scaffolds of the existing antibiotics is a traditional method to evade the resistance. Although this has proven to be a great success from the 1960s until the early 1990s, it is harder and harder to apply this methodology to confront the AMR[2]. Despite the existing robotic liquid handling systems for high-throughput screening of biochemical compounds, synthesis based on microfluidics and integration with drug screening systems still deserves more attention.

(ii) The study of inter-species interaction of bacteria with high-throughput time lapse imaging may give clues for the discovery of natural antibiotics. For example, since 2008, more than 1000 compounds were isolated from marine microorganisms. Will some antibiotics be found in these compounds? Evaluating the antimicrobial properties of these compounds may rely on micro-investigation of the response of bacterial strains.

(iii) Revealing mechanisms of antimicrobial resistance may provide new impulses for antimicrobial discovery. From a more holistic point of view, revamping the way of combining mechanistic studies and drug screening can be a promising perspective. Moreover, a combinatorial approach can maximize the use of current antibiotics and even rehabilitate some obsolete drugs. This combinatorial methodology may also benefit from a problem-oriented microfluidic approach.

Here, we provided a discussion from a researcher's point of view, which is limited to fundamental or engineering aspects. However, the problem of AMR has to be addressed from a much broader societal perspective. For example, a global resistance reporting and monitoring system would be beneficial for the coordination of institutional action plans and also of global research activities. Furthermore, it is of particular importance to foster public education about the problems related to antibiotics misusing, *e.g.* by over-prescription or self-medication. Stronger regulations of antibiotic consumption in agriculture, animal husbandry, dairy industry is necessary as well. We believe that only if urgent and global actions are taken, the current trend of quickly rising AMR can be reversed.

References

2. Podolsky, S. H. The Evolving Response to Antibiotic Resistance (1945–2018). *Palgrave Communications* **4**, 124 (Dec. 2018) (cit. on pp. 1, 135, 140).
40. Baltekin, Ö., Boucharin, A., Tano, E., Andersson, D. I. & Elf, J. Antibiotic Susceptibility Testing in Less than 30 Min Using Direct Single-Cell Imaging. *Proceedings of the National Academy of Sciences*, 201708558 (Aug. 8, 2017) (cit. on pp. 10, 11, 13, 54, 102, 127, 137).
65. He, R., Schierning, G. & Nielsch, K. Thermoelectric Devices: A Review of Devices, Architectures, and Contact Optimization. *Advanced Materials Technologies* **3**, 1700256 (Apr. 2018) (cit. on pp. 23, 138).
75. Gromov, G. in *Advanced Micro and Nanosystems* (eds Dávila Pineda, D. & Rezanian, A.) 1st ed., 233–282 (Wiley, Sept. 25, 2017). doi:[10.1002/9783527698110.ch11](https://doi.org/10.1002/9783527698110.ch11) (cit. on pp. 29, 30, 138).
117. Boling, E. A., Blanchard, G. C. & Russell, W. J. Bacterial Identification by Microcalorimetry. *Nature* **241**, 472–473 (5390 Feb. 1973) (cit. on pp. 47, 138).
197. Josenhans, C. & Suerbaum, S. The Role of Motility as a Virulence Factor in Bacteria. *International Journal of Medical Microbiology* **291**, 605–614 (Jan. 2002) (cit. on pp. 101, 126, 139).
247. Bush, K. *et al.* Tackling Antibiotic Resistance. *Nature Reviews Microbiology* **9**, 894–896 (12 Dec. 2011) (cit. on p. 135).
248. Brown, E. D. & Wright, G. D. Antibacterial Drug Discovery in the Resistance Era. *Nature* **529**, 336–343 (7586 Jan. 2016) (cit. on pp. 135, 139).
249. Goubko, C. A. & Cao, X. Patterning Multiple Cell Types in Co-Cultures: A Review. *Materials Science and Engineering: C* **29**, 1855–1868 (Aug. 1, 2009) (cit. on p. 139).
250. Kaji, H., Camci-Unal, G., Langer, R. & Khademhosseini, A. Engineering Systems for the Generation of Patterned Co-Cultures for Controlling Cell–Cell Interactions. *Biochimica et Biophysica Acta (BBA) - General Subjects. Nanotechnologies - Emerging Applications in Biomedicine* **1810**, 239–250 (Mar. 1, 2011) (cit. on p. 139).
251. Jones, J. A. & Wang, X. Use of Bacterial Co-Cultures for the Efficient Production of Chemicals. *Current Opinion in Biotechnology. Chemical Biotechnology • Pharmaceutical Biotechnology* **53**, 33–38 (Oct. 1, 2018) (cit. on p. 139).
252. Butler, S. M. & Camilli, A. Both Chemotaxis and Net Motility Greatly Influence the Infectivity of *Vibrio Cholerae*. *Proceedings of the National Academy of Sciences* **101**, 5018–5023 (Apr. 6, 2004) (cit. on p. 139).
253. Plackett, B. Why Big Pharma Has Abandoned Antibiotics. *Nature* **586**, S50–S52 (7830 Oct. 21, 2020) (cit. on p. 140).

A Additional technical notes

A.1 Environmental effect on the baseline drift

We investigated the environmental effect on the heat sensor signal in the INCfAST platform. Ideally, in the case that the room temperature would be constant, heat loss from the thermostat to the surrounding environment is constant as well. Therefore, the heat power to maintain the thermostat temperature is constant as well. However in reality, for instance for an overnight measurement, the room temperature of the experimental space cannot be accurately maintained. As shown in Figure A.1a, the thermostat is maintained at 37 °C at the probing point with a variation of $\pm 200 \mu\text{K}$, however, this does not imply a constant temperature distribution all over the thermostat and the surrounding thermal shielding (foam). The room temperature (red curve in Figure A.1b) has a peak-to-peak fluctuation of 1 K. As a consequence, the temperature at the inner side of the foam box (used to isolate the thermostat from the environment) has a corresponding peak-top-peak fluctuation of 0.5 K (blue curve in Figure A.1b). The foam temperature is higher than the room temperature because the thermostat is maintained at 37 °C in this case.

The heat transfer from the thermostat to the thermal shielding foam changes upon to the fluctuation of room temperature, thus changing the boundary condition. The external heater power (green curve in Figure A.1c) to maintain the thermostat temperature varies inversely to the foam temperature (blue curve in Figure A.1c). The heater power is reflected likewise in the sensor voltage signals (purple and brown curve in Figure A.1d), *i.e.* the sensor signals vary in the same way as the heater power (green curve in Figure A.1d). Only DI water is filled in the microincubator, so there is no self-generated heat from the sample.

By controlling the ventilation of the laboratory, we can meditate the impact of air convection on the temperature perturbation in the experimental space. More sophisticated solutions have been presented in some of the recent papers.[87, 119] As shown in Figure A.2, two calorimeter studies achieved a good baseline thanks to multi-layer thermostat structures. In this configuration, the heater that is closest to the sensing unit could be maintained at a much more stable power level. The resulting high signal-to-noise level enabled stable long-term single-cell or single *C. elegans* measurements. Eventually, in our INCfAST platform we used two foam layers to minimize the effect of environmental fluctuations (Figure A.3a). Fast heat regulation could be achieved with

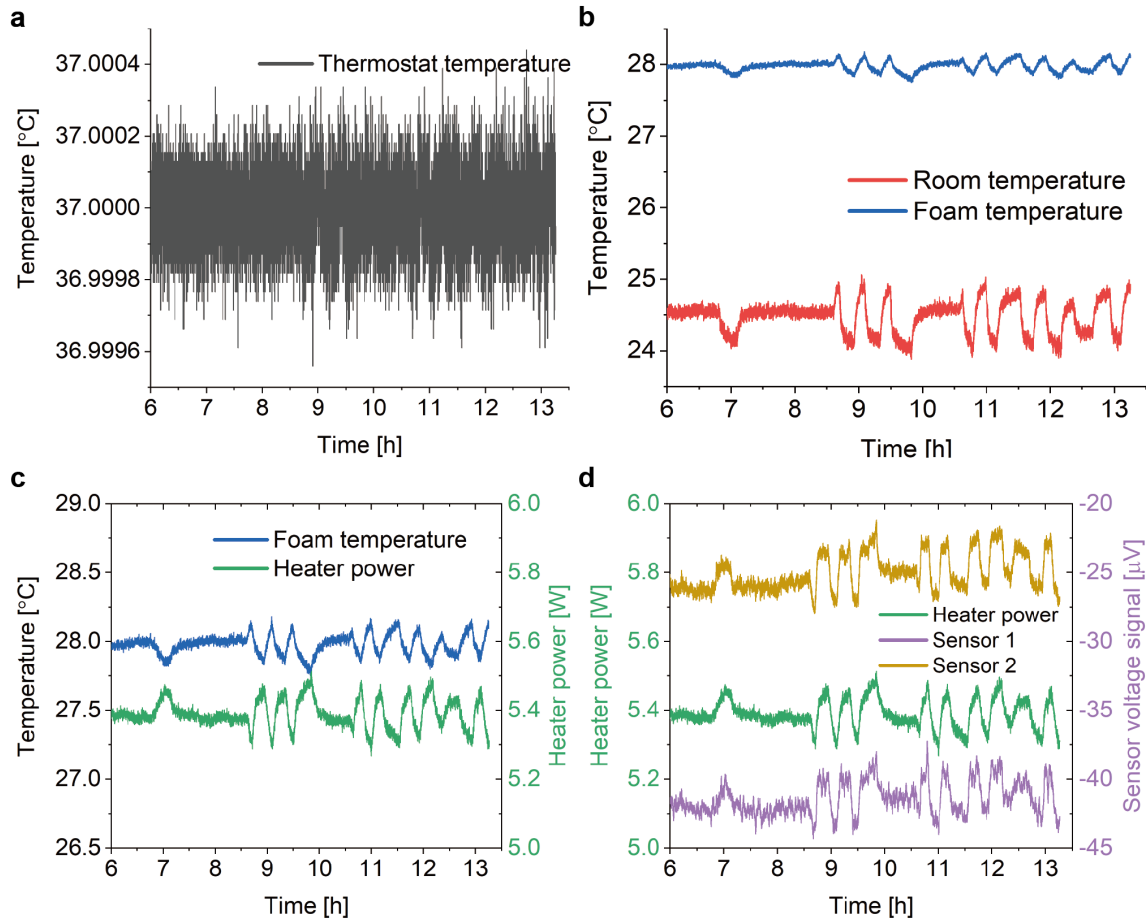


Figure A.1 – Environmental effect on heat flow. (a) Thermostat temperature at the probing point. (b) Room temperature and foam temperature. (b) Foam temperature and the heater power for the thermostat regulation. (c) Heater power and the corresponding sensors signal as a function of time. Sensor 1 and Sensor 2 are positioned symmetrically in the dual-chip nanocalorimeter platform as shown in Figure 4.1b.

three heaters at different locations of the thermostat (Figure A.3b). However, how to guarantee a homogeneous temperature distribution using the three heaters simultaneously still need further investigation.

A.2 PID controller

For temperature stabilization, a closed-loop proportional–integral–derivative (PID) controller was used to calculate the heater power output based on the measured temperature.

As shown in the Figure A.4, we define the error signal $e(t)$ as the difference between the reference

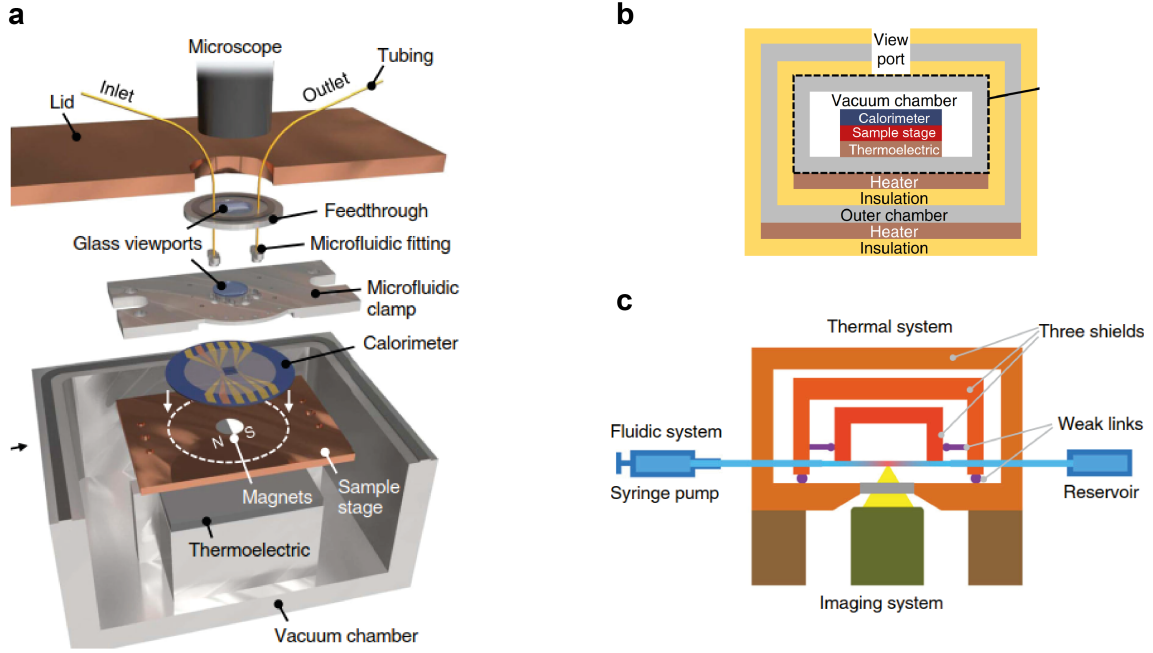


Figure A.2 – Examples for calorimeters with multi-layer thermostats. (a) Multi-layer thermostat to minimize the temperature variation and baseline fluctuation for single-cell heat power study.[87] (b) Schematic representation of the set-up in (a). (c) System with three thermal shields to prevent perturbations due to the fluctuations of the ambient temperature.[119]

signal $r(t)$ and the measured value $m(t)$.

$$e(t) = r(t) - m(t) \quad (\text{A.1})$$

PID loop consists of three terms based on the error signal: the proportional (P), the integrative (I) and the derivative (D) term, which regulate a final output $o(t)$, *i.e.* the heater power to maintain the thermostat temperature.

The proportional term imposes a correction proportional to the error signal. When the error signal is high, the proportional term takes action, however, only by proportional mode, however, this generates an $o(t)$ response that oscillates in a sinusoidal way.

$$o(t) = k_P e(t) \quad (\text{A.2})$$

where k_P is the proportional gain.

To improve the control algorithm, the integral term is introduced as:

$$o(t) = k_I \int e(\tau) d\tau \quad (\text{A.3})$$

where k_I is the integral gain. The output with respect to this term relies on the time integral of the error signal. In the case of an error offset, the integral output can further minimize the error signal.

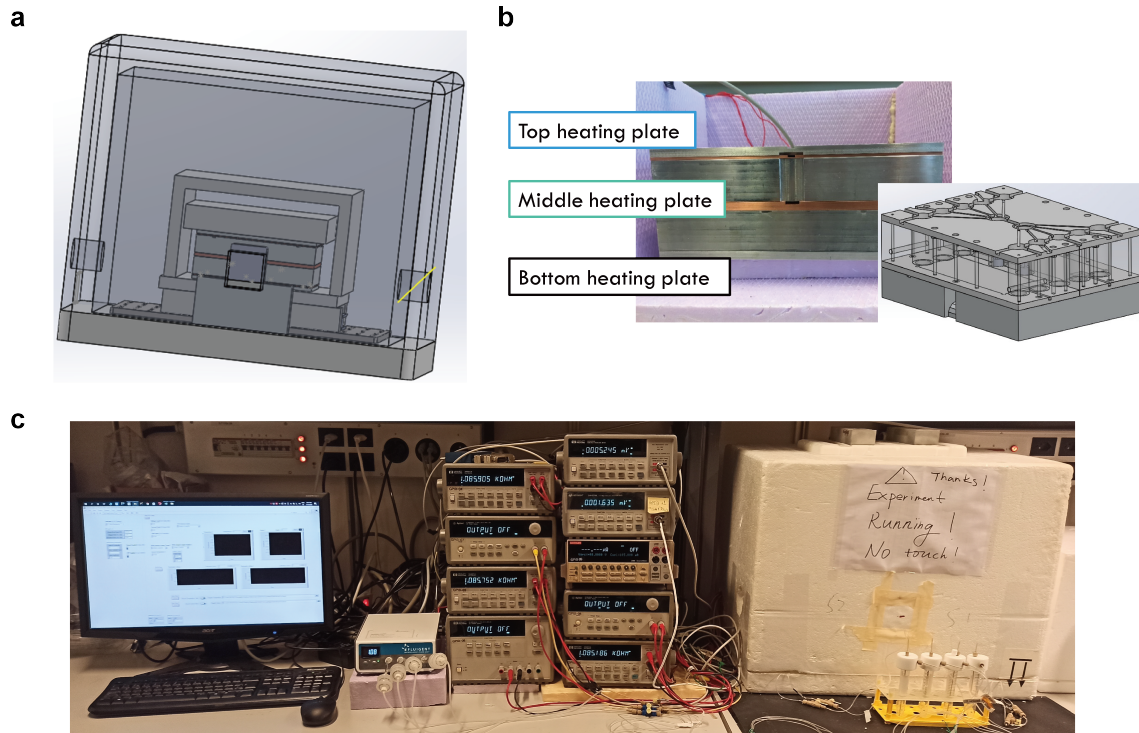


Figure A.3 – Schematic representation and pictures of the INCfAST system and the measurement set-up. (a) Two foam layers to isolate the thermostat from the environment. (b) Picture of the thermostat unit with top, middle and bottom heating plates. (c) Picture of the whole system, from left to the right: computer for the controlling softwares, MFCS air pump, electrical components (including ohmmeter, power supply, source meter, nano-voltmeter), foam box for thermal shielding, thermostat and the measurement system (inside the foam), and sample reservoirs inside the rack.

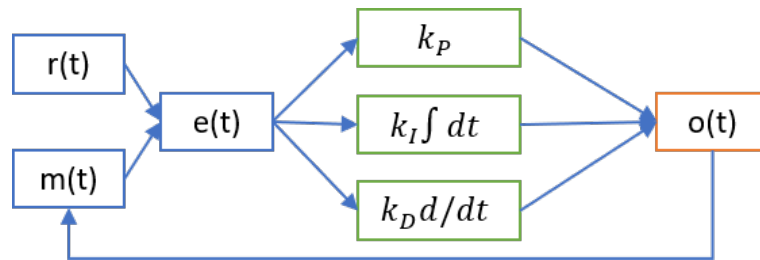


Figure A.4 – Schematic representation of the PID program. Three terms contribute to the output signal $o(t)$: the proportional term (k_P), the integrative term (k_I) and the derivative term (k_D), which are obtained based on the error signal $e(t)$ at a specific time point.

The derivative term accounts for an output variation that is proportional to temporal changes of the error signal

$$o(t) = k_D \frac{de(t)}{dt} \quad (\text{A.4})$$

This term is important when the setting point changes, as it allows the controller to follow smoothly sudden changes. This term will play an important role for developing a scanning temperature device. For fixed temperature setting as for our system, this term is not important thus not used.

In summary, the output signal $o(t)$ may be expressed in the following way:

$$o(t) = k_P e(t) + k_I \int e(\tau) d\tau + k_D \frac{de(t)}{dt} \quad (\text{A.5})$$

In our study, the PID controlling program is provided by an integrated function in LabVIEW.

A.3 ADC resolution

We have achieved a temperature stabilization of $\pm 200 \mu\text{K}$. The best performance reported in the state-of-the-art literature is higher ($\pm 80 \mu\text{K}$ [87] and $\pm 40 \mu\text{K}$ [84]). For the construction of PID-controlled heater in the current study, we used Agilent 34401A for temperature acquisition (6.5 digits) and Agilent E3645A power supply (resolution 0.01 V). The temperature resolution of Agilent 34401A is $130 \mu\text{K}$ considering a minimum measured resistance value $0.5 \text{ m}\Omega$. For a RTD PT1000 temperature sensor the conversion between the 4-wire resistance and the temperature is given by $T = (R_{4\text{wire}} - 1000)/2.85$. The limited resolution of power supply is not able to render the precision of the output value given by the PID program. For future study, a system enabling higher resolution for temperature and heater power will need to be implemented for further improvement of the temperature stability, thus the reduction of noise level and baseline drift.

A.4 Sensor datasheet

The thermopile sensor used in the current study was purchased from Xensor Integration (EJ Delfgauw, Netherlands). The technical specifications of the XEN-NCM9924 sensor can be found in the datasheet in Figure A.5. Compared to the previous study[118], we use a sensor with a thicker membrane ($45 \mu\text{m}$ instead of $22 \mu\text{m}$) in order to have a higher mechanical performance required for on-chip washing protocols. However it should be noted that the $22 \mu\text{m}$ has a better power sensitivity due to a lower thermal conductance in the lateral direction of the membrane. The sensor is packaged with a 68-pin grid array (PGA), *e.g.* for thermopile voltage outputs and for connecting the on-chip heater for sensor calibration (Figure A.6). We have designed the printed circuit board (PCB) to accommodate the sensor chip.

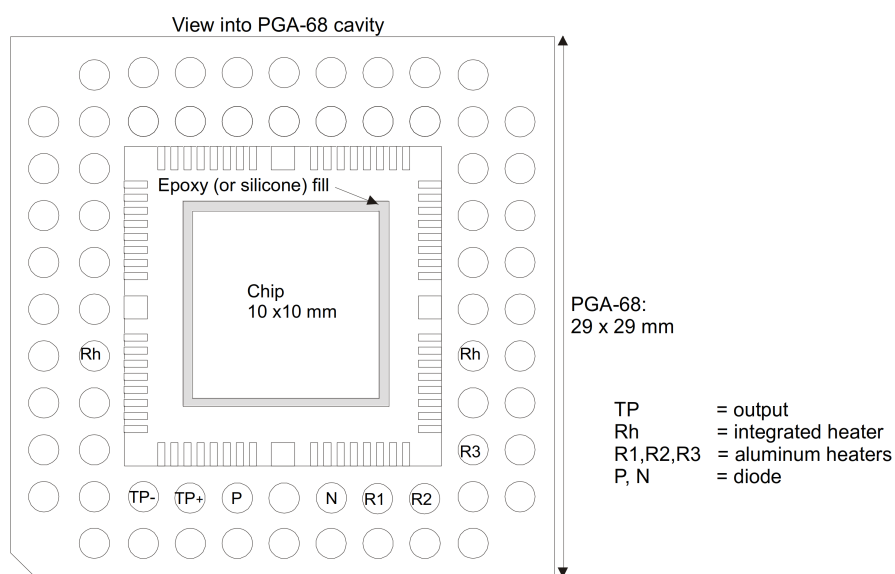
Appendix A. Additional technical notes

Table 2.1 Specifications (ambient temperature 22 °C)

	XEN-LCM 2506	XEN-LCM quad	XEN-NCM 9924	XEN-TCG 3880			
Parameter	typ	typ	typ	typ	unit	symbol	notes
Dimensions							
housing size	29x29x7	29x29x7	29x29x7	3.3x2.5x0.3	mm ³		
chip dimensions	5x5	4 of 5x5	10x10		mm ²		
membrane size	3.5x3.5	3.5x3.5	8.3x8.3		mm ²		
membrane thickness	4-8	4-8	22-45	1	µm		
Output							
in air at 1013 mbar	8	8	1.2-2.4	30	V/W		
in still water	4	4	-	-	V/W		
Time constant						τ	
in air				9	ms		
in vacuum				36	ms		
Stability							
short term				100	ppm		
long term				1000	ppm		
Thermopile							
resistance	150	150	50	55	kΩ	R _{tp}	
effective sensitivity				1.3	mV/K	S _{tp}	
intrinsic sensitivity	50-80	50-80	50	2.4	mV/K		
temp coefficient				0.05	%/K		
Heater							
resistance	0.8	0.8	0.44	0.6	kΩ	R _{heat}	
resistance R1-R2	-	-	1.0	-	kΩ	R _{heat}	Alu heater
resistance R1-R3	-	-	0.25	-	kΩ	R _{heat}	Alu heater
temperature coefficient				0.1	%/K		
Thermal resistance							
membrane				100	kK/W		
temperature coefficient					%/K		
membrane + gas				23	kK/W		
temperature coefficient				-0.08	%/K		
chip to housing					K/W		
Maximum heating voltage						U _{heat}	
in air				2.5	V		
in vacuum				1	V		
Sensor ambient temp							
minimum				-40	°C		
maximum				85	°C		
Heater max temp				250	°C		

Figure A.5 – Datasheet of the sensor XEN-NCM9924 used in this work and similar versions (not used in the frame of this work). Adapted from [78]

XEN-NCM9924: 68 pins 11x11 PGA cavity down



Electronics side of XEN-NCM9924

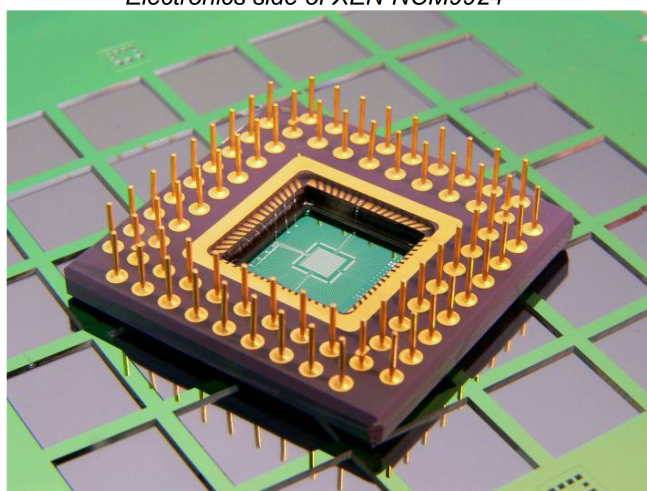


Figure A.6 – Photo of the thermopile sensor chip with PGA connector (XEN-NCM9924). Adapted from [78]

References

78. Datasheet of "Liquid Nanocalorimeters XEN-NCM9924 / -LCM2506 / -LCMquad" 2016 (cit. on pp. 33, 148, 149).
84. Lerchner, J. *et al.* Nano-Calorimetry of Small-Sized Biological Samples. *Thermochimica Acta* **477**, 48–53 (Oct. 2008) (cit. on pp. 40, 41, 147).
87. Hong, S. *et al.* Sub-Nanowatt Microfluidic Single-Cell Calorimetry. *Nature Communications* **11**, 2982 (Dec. 2020) (cit. on pp. 41–43, 47, 143, 145, 147).
118. Krenger, R., Lehnert, T. & Gijs, M. A. M. Dynamic Microfluidic Nanocalorimetry System for Measuring *Caenorhabditis Elegans* Metabolic Heat. *Lab on a Chip* **18**, 1641–1651 (2018) (cit. on pp. 47, 56, 147).
119. Hur, S., Mittapally, R., Yadlapalli, S., Reddy, P. & Meyhofer, E. Sub-Nanowatt Resolution Direct Calorimetry for Probing Real-Time Metabolic Activity of Individual *C. Elegans* Worms. *Nature Communications* **11**, 2983 (Dec. 2020) (cit. on pp. 47, 143, 145).

B Software program

In the thesis, we used various software programs for data acquisition and data processing, including LabVIEW, MATLAB, OriginLAB, and Python program language.

B.1 LabVIEW program

LabVIEW was used to create and implement different control programs, in particular for the PID heater controller, the MFCS air pump controller, and the data acquisition system with electrical instruments (Figure B.1a). Figure B.2 shows an example of the LabVIEW program interface.

B.2 MATLAB and Python code

We implemented a series of MATLAB and Python code to perform data management and data processing. The involved functionalities includes file/folder management, image/data processing, and post-processing of the results. A schematic representation is shown in Figure B.3. Figure B.4 shows a screenshot of GUI program developed with MATLAB, enabling the heat flow signal processing. At the time-being of writing the thesis, I am still organizing the code and arrange them in a consistent way. The final script and protocol will be available in near future on the author's github repositories: <https://github.com/polyyl?tab=repositories>

Appendix B. Software program

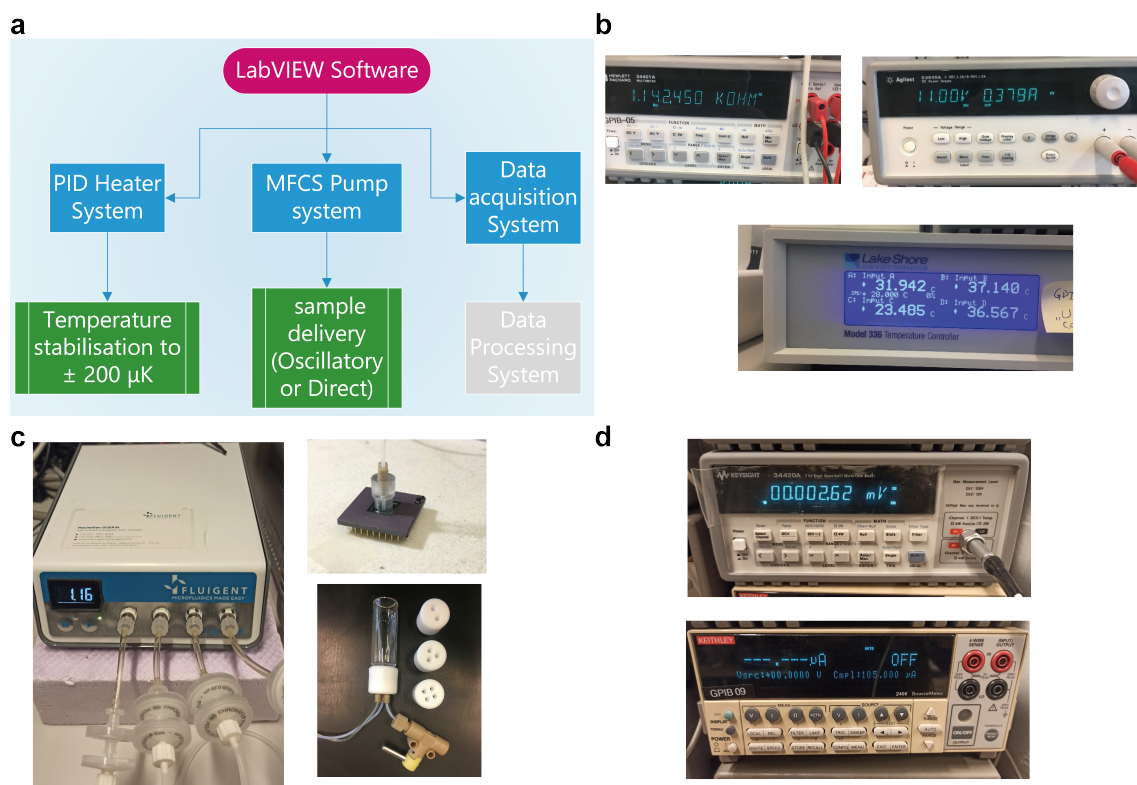


Figure B.1 – LabVIEW program and instruments used in this work. (a) Structure of the LabVIEW program, including PID controller, MFCS pump controller, and data acquisition modules. (b) Instruments for temperature controller. Upper left: Agilent 34401A for temperature acquisition based on a 4-wire resistance measurement. Upper right: Agilent E3645A as power supply for the heating pads. Lower: LakeShore Model 336® for temperature probing in different positions. (c) Left: MFCS pressure controller from Fluigent®. Upper right: Micro-incubator with the Upchurch® PEEK connectors. Lower right: Reservoir with PEEK connectors. (d) Upper: Keysight 34420A for reading the sensor signal. Lower: KEITHLEY 2400 SourceMeter applying an electrical power to the integrated heater on the thermopile sensor chip.

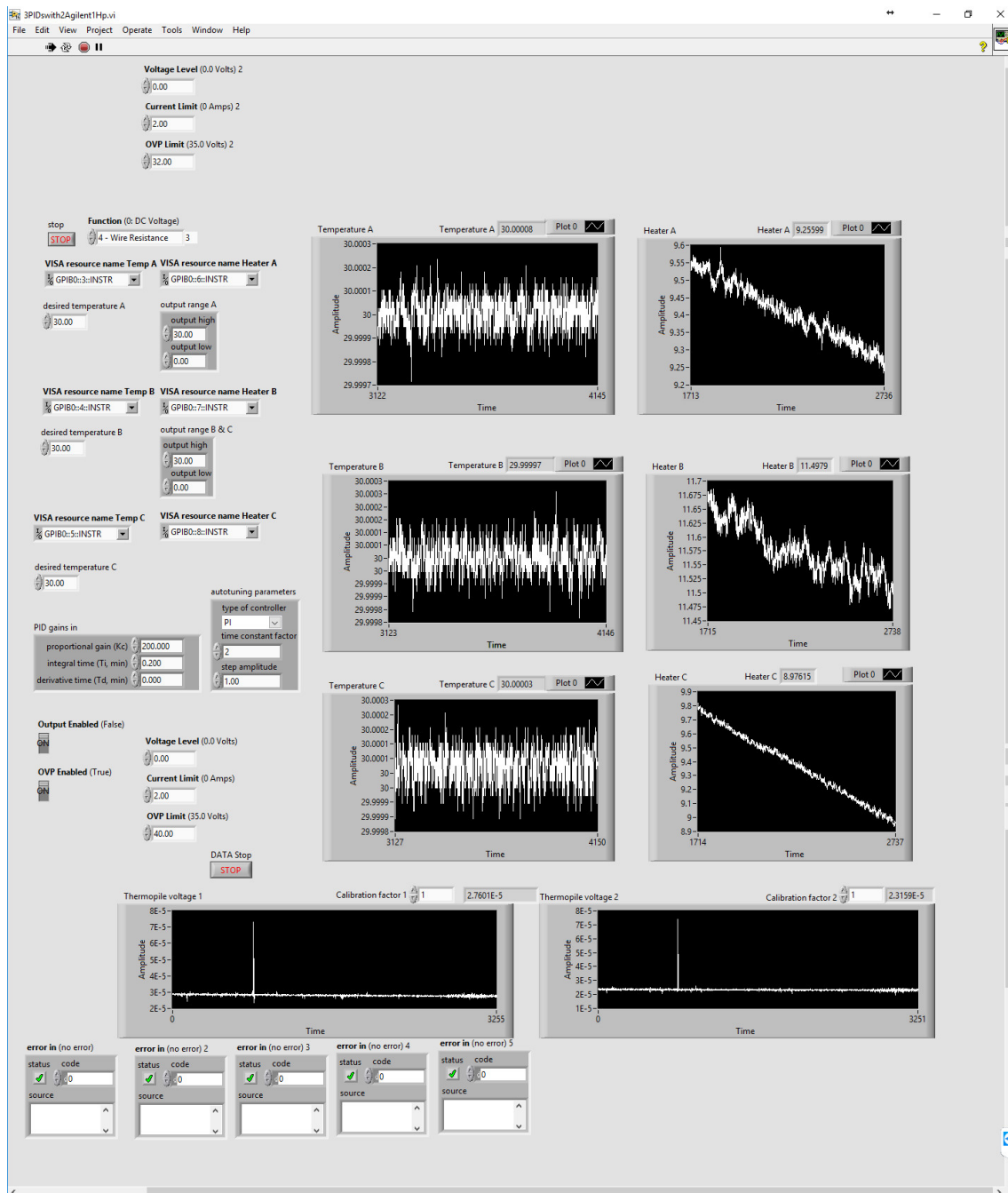


Figure B.2 – An example of LabVIEW program interface, for monitoring the temperature, heating power and acquiring the sensors' voltage signal.

Appendix B. Software program

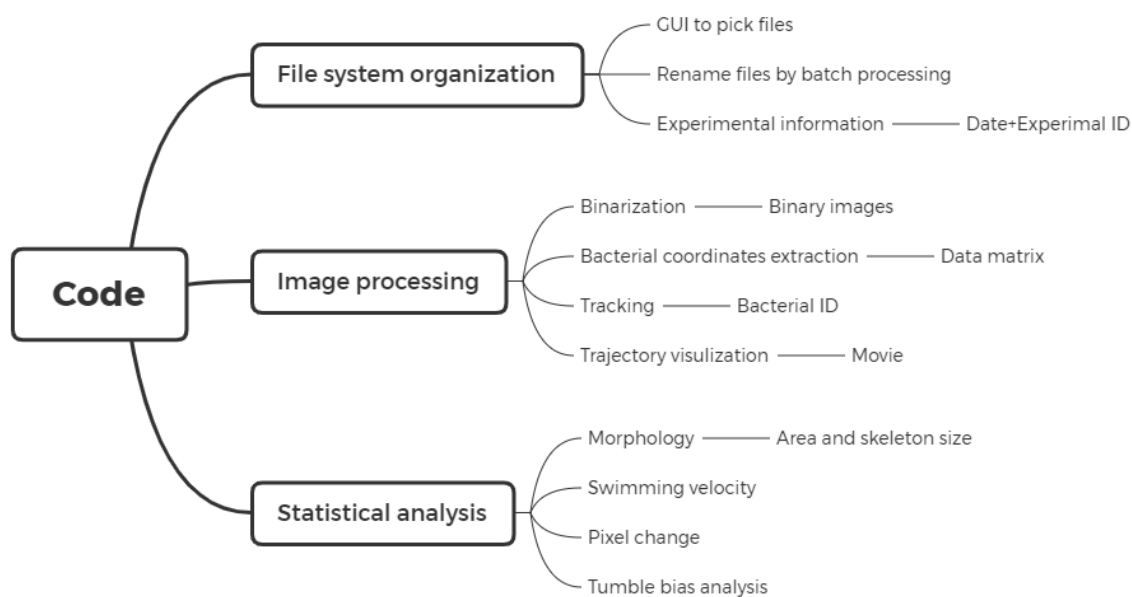


Figure B.3 – Mindmap of codes. The codes have several purposes: (i) file/folder management and organization, (ii) image/data processing, and (iii) statistical analysis of the results.

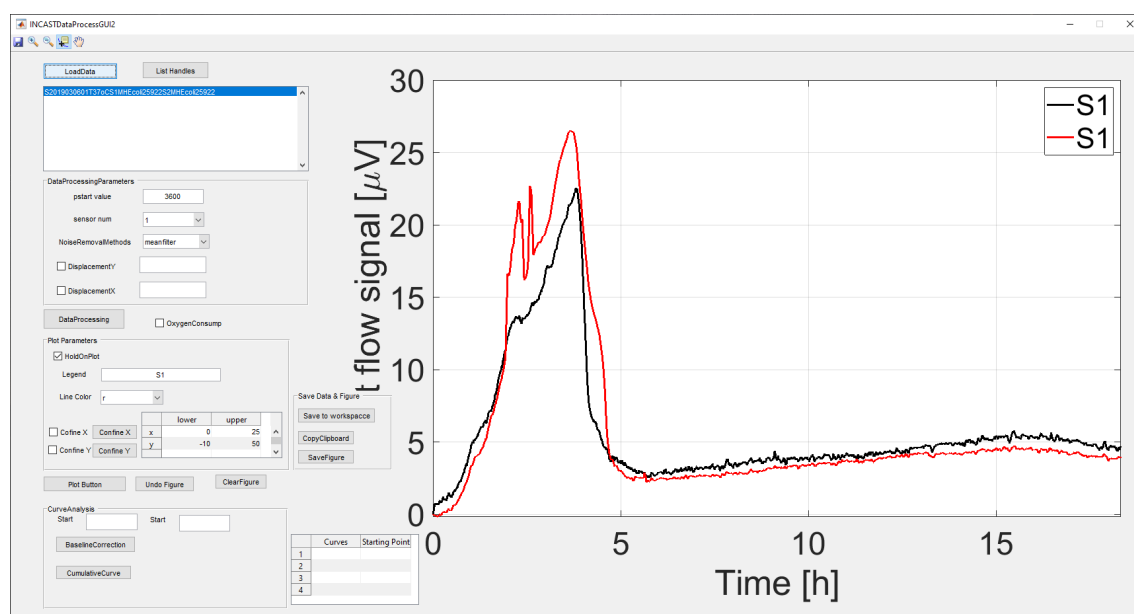


Figure B.4 – MATLAB program for the INCfAST data processing.

C Heat transfer simulations

We applied finite element analysis (FEA, COMSOL Multiphysics®) for heat transfer simulations to assist designing of the platform. Figure C.1 shows some of the important settings for the heat transfer simulation of the nanocalorimetry system (single measuring unit and in 2 dimension).

We implemented a PID controller module in the COMSOL program as shown in Figure C.1a and C.1b based on the tutorial[254]. We simplified the system to a single-unit system on a 2-D plan and attributed the correspond materials to the different parts: Aluminum thermostat, PMMA sample well, PS thin film between the sample and the thermopile, and water as liquid model for the sample. Our simulation represents an ideal situation without environmental influence. In the study of bacterial motility, we also applied a similar methodology to study the temperature distribution for the on-chip incubation.

Simulation results for the nanocalorimeter are presented in Figure C.2. After stabilization for about 1 hour, the temperature of the system is uniform (Figure C.2a and C.2b). The temperature difference between the hot and cold junctions stands for the signal baseline, which is constant when the environmental perturbations are absent (Figure C.2c).

Appendix C. Heat transfer simulations

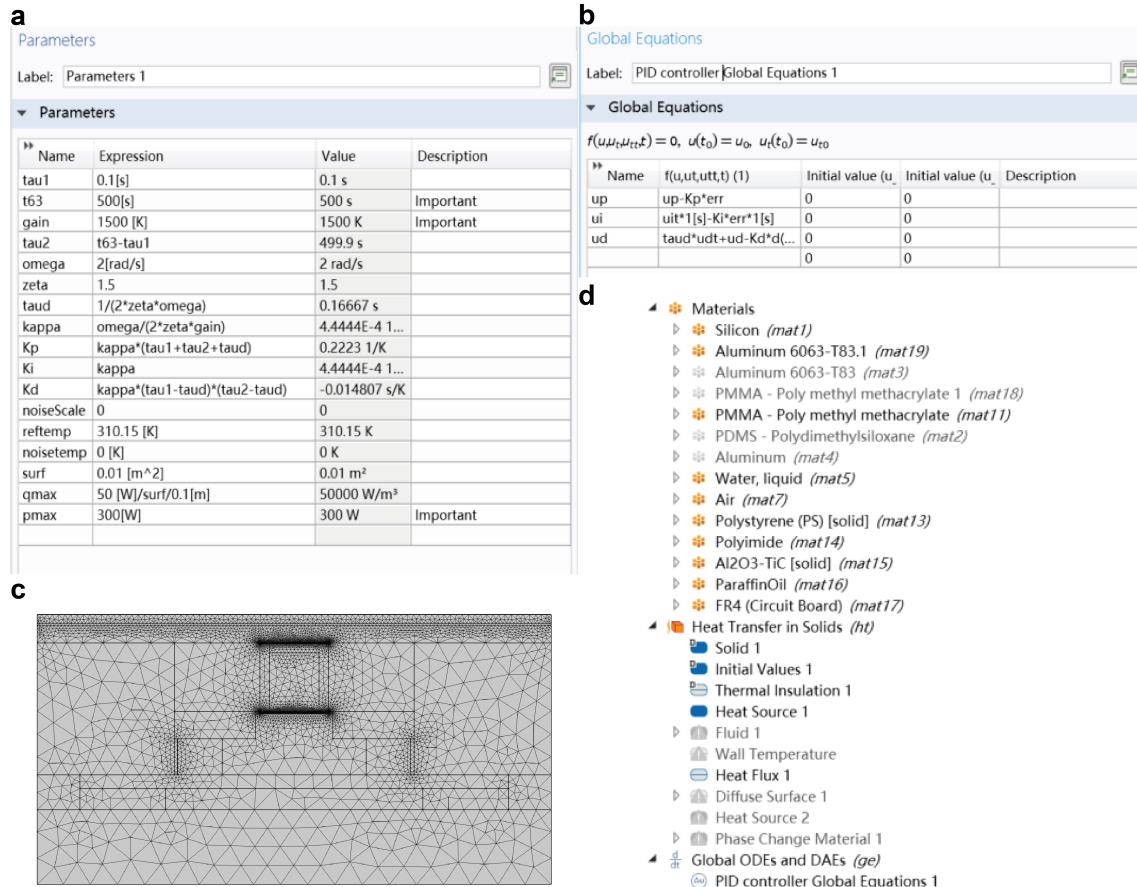


Figure C.1 – COMSOL Multiphysics® simulation snapshots. (a) Predefined parameters. (b) Global differential equations to simulate the PID controller module. (c) Physics-controlled mesh. (d) Materials and physics model involved in the study. The physical model includes a heat transfer module and the global equations to implement the PID controller.

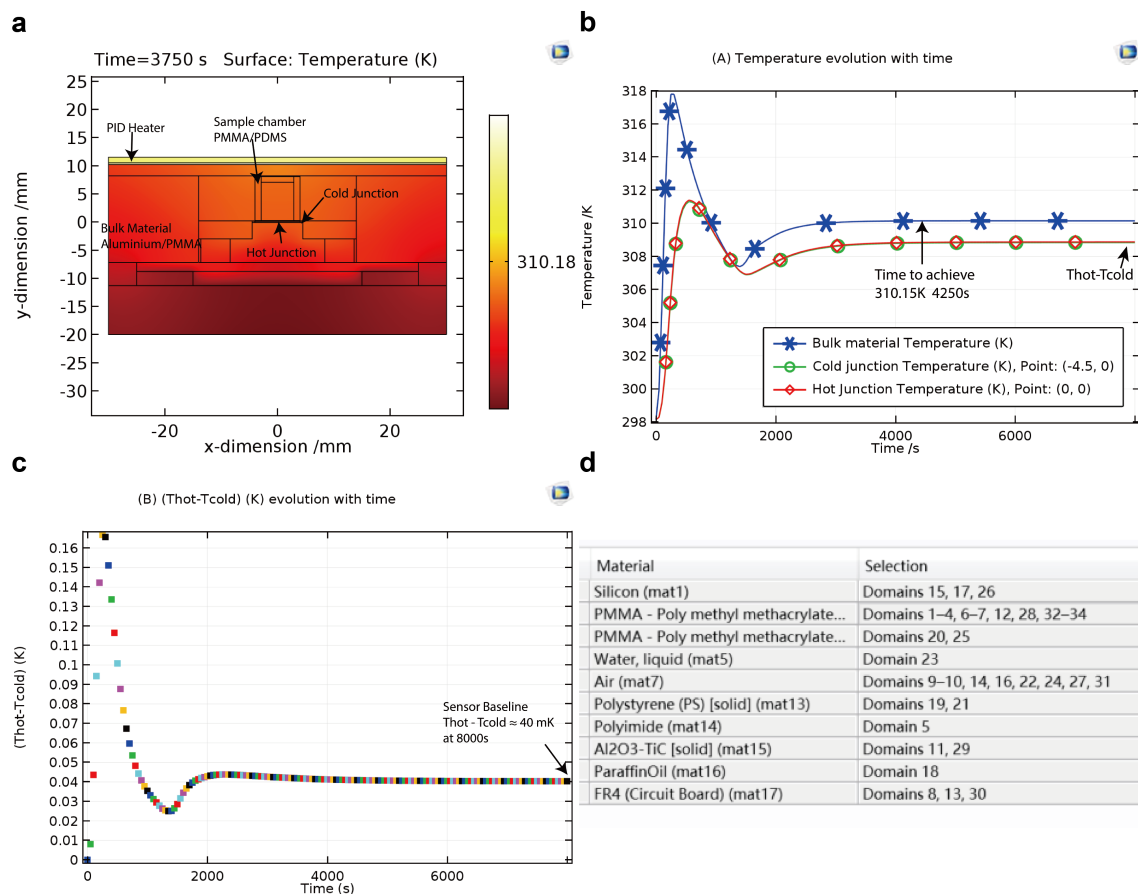


Figure C.2 – 2-D heat transfer simulation results. (a) Temperature distribution in an ideal situation, *i.e.* no ambient temperature fluctuations. (b) Temperature evolution for the bulk of the nanocalorimeter, hot and cold junctions of the thermopile. (c) Temperature difference between the hot and cold junctions, that contributes to the sensor baseline. (d) Allocation of materials in the study.

References

254. *Simulating Feedback Control of Thermal Systems* COMSOL. <https://www.comsol.eu/video/simulating-feedback-control-thermal-systems> (2020) (cit. on p. 155).

Yang LIU

Chinese with Swiss Permit B
28 years old

Chemin de la Cocarde 13
CH-1024 Ecublens, Switzerland
chimieyang@gmail.com

Skype: polyyangliu
LinkedIn: polyyangliu



CORE EXPERTISE

Microfluidics - BioMEMS - Microsystems for *in vitro* diagnostics

Cleanroom technologies

Programming skills with MATLAB and Python

Polymer science and material characterization

EDUCATION

Oct. 2016—Feb. 2021	École polytechnique fédérale de Lausanne - EPFL
Lausanne, Switzerland	Marie Skłodowska-Curie PhD fellow <ul style="list-style-type: none">Laboratory of Microsystem 2, Prof. M.A.M. GIJS, Dr. T. LEHNERTProject: "New Diagnostics for Infectious Diseases - ND4ID" (https://cordis.europa.eu/project/id/675412).Thesis: Microfluidic Platforms for the Study of Bacterial Metabolism and Antimicrobial Susceptibility TestingDevice hardware and software design and engineering, bacterial culture and testing.
2013—2016	ESPCI Paris, France
	Advanced Master's degree in Science and Technology (Diplôme d'ingénieur)
2015—2016	Paris Diderot University & Institute Pierre-Gilles de Gennes, France
	Specialized Master's degree in Complex System and Microfluidics (GPA: 1 st in 8 students)
2009—2013	Nanjing University, China
	Bachelor's degree in Chemistry (GPA: 4 th in 141 students)

EXPERIENCE

2018—2020	Teaching assistant of cleanroom technology (for 3rd year Bachelor students)
2016	Institute Curie, MMBM Group, Master's degree thesis, Prof. J.L. VIOVY (6 months)
Paris, France	<ul style="list-style-type: none">Development of a technology for reconfigurable microfluidic devices to perform DNA pre-concentration.Microfluidic chip fabrication (PDMS protocol).
2015	ESPCI Paris, EC2M Group, Prof. O. DAUCHOT (3 months)
Paris, France	<ul style="list-style-type: none">Study of self-propulsion swimming salty water droplets.Image processing experience to perform droplets tracking with MATLAB.
2014	TOTAL S.A., Physicalchemical Analysis, PERL, Dr. S. JOUENNE (6 months)
Pau, France	<ul style="list-style-type: none">Internship in a high-level industrial research setting.Set up of a protocol for measurements of extensional viscosity of polymers with microfluidic devices used in enhanced oil recovery. Mechanism of polymer degradation.
2013	Nankai University, NMR Laboratory, Prof. P. SUN (1 month)
Tianjin, China	<ul style="list-style-type: none">NMR method to characterize the phase structure of polymer blends.
2012	Nanjing University, Key Laboratory of High-Performance Polymer Materials & Technology, Bachelor's degree thesis, Prof. X. WANG (12 months)
Nanjing, China	<ul style="list-style-type: none">Discovery of a high anti-impact polymer blend that could potentially be used as high mechanical performance plastics.Application of characterization methods such as NMR, DMA, DSC, SAXS.

SKILLS

Computer	Proficient in MATLAB, Python, Origin Lab, COMSOL, SolidWorks, LabVIEW, LaTeX, MS Office Pack.
Cleanroom	Chip layout design (L-Edit), mask fabrication, photolithography, direct laser writing, dry etching, wet etching, PDMS line.
Experimental	Biosafety level 2 lab training, systematic microbiological training and experience, time-lapse imaging, Solid-State NMR and Low Field NMR machine operation, CNC micro-milling machine operation, plastics processing machine operation.
Language	Mandarin (Mother tongue), English (C1 Spoken, C2 Writing), French (C1 Spoken, C1 Writing), German (A1 module accomplished).

PUBLICATIONS / CONFERENCES

1. **Y. Liu**, T. Lehnert, M. A. M. Gijs, Measurement of oxygen consumption rate for bacterial culture with a microfluidic platform. *In preparation*.
2. **Y. Liu**, T. Lehnert, M. A. M. Gijs, Effect of Inoculum Size and Antibiotics on Bacterial Swimming and Traveling Bands in a Thin Microchannel Defined by Optical Adhesive. *In peer review*.
3. **Y. Liu**, T. Lehnert, M. A. M. Gijs, Fast antimicrobial susceptibility testing on *Escherichia coli* by metabolic heat nanocalorimetry. **Lab Chip**, 20, 3144–3157 (2020).
4. P. Illien, Charlotte de Blois, **Y. Liu**, M.N. van der Linden and O. Dauchot, Speed-dispersion-induced alignment: A one-dimensional model inspired by swimming droplets experiments. **PHYSICAL REVIEW E**, 5 (2020).
5. B. Venzac, **Y. Liu**, I. Ferrante, P. Vargas, A. Yamada, R. Courson, M. Verhulsel, L. Malaquin, J.-L. Viovy, S. Descroix, Sliding walls: a new paradigm for fluidic actuation and protocol implementation in microfluidics. **Microsyst Nanoeng.** 6, 18 (2020).
6. **Y. Liu**, T. Lehnert, M.A.M. Gijs, Antimicrobial susceptibility testing of *E. coli* based on metabolic heat measurements. **DIATECH 2020**, Oral presentation.
7. **Y. Liu**, T. Lehnert, T.P.N. Baltus, M.A.M. Gijs, Fast Antimicrobial Susceptibility Testing of *E.coli* by Oxygen Consumption Measurements in an Isothermal Microincubator Platform. **MicroTAS 2019**, Poster presentation.
8. **Y. Liu**, T. Lehnert, M.A.M. Gijs, An Isothermal Nanocalorimetric Platform For Antimicrobial Susceptibility Testing Based On Bacterial Metabolic Heat Measurements (Student travel grant prize), **MicroTAS 2018**, Poster presentation.
9. B. Venzac, **Y. Liu**, I. Ferrante, A. Yamada, P. Vargas, M. Verhulsel, L. Malaquin, J.-L. Viovy, and S. Descroix, Sliding Walls: a New Toolbox for Manually-operated Microfluidics, **MicroTAS 2017**, Poster presentation.

AWARDS

2013—2016	Scholarship by TOTAL S.A. / Scholarship by IPGG
2013	Award of Outstanding Graduate / Award of Outstanding Graduate Thesis

EXTRACURRICULAR ACTIVITIES

Oct. 2017 – July 2019	Chinese Students and Scholars Association (CSSA) Lausanne, Member, Vice-President, President.
Sports & Others	Badminton Club, Swimming, Ping-Pong, Chess Club, Poetry Writing.

REFERENCE CONTACT

Martin Gijs	EPFL full professor, EPFL STI-IMT-LMIS2, Bâtiment BM 3128, Station 17 CH-1015 Lausanne, Switzerland martin.gijs@epfl.ch +41 21 693 77 31
Stéphanie Descroix	CNRS researcher, MMBM Group, Institut Curie Research Center, CNRS UMR 168 11 rue Pierre et Marie Curie, 75005 Paris, France stephanie.descroix@curie.fr +33 1 40 79 59 11
Thomas Lehnert	EPFL Senior scientist, EPFL STI-IMT-LMIS2, Bâtiment BM 3134, Station 17 CH-1015 Lausanne, Switzerland thomas.lehnert@epfl.ch +41 21 693 66 05